Examination of surface morphology and sub-surface crystallographic changes of Si, Cu, GaP, and Ge after ultrashort laser pulse irradiation

By
Travis H.R. Crawford, B.Sc., B.Ed.

A Thesis
Submitted to the School of Graduate Studies
in Partial Fulfilment of the Requirements
for the Degree
Doctor of Philosophy

McMaster University

DOCTOR OF PHILOSOPHY (2008) McMaster University
(Department of Engineering Physics) Hamilton, Ontario

TITLE: Examination of surface morphology and sub-surface crystallographic changes of Si, Cu, GaP, and Ge after ultrashort laser pulse irradiation
AUTHOR: Travis Crawford, B.Sc., B.Ed. (University of Calgary)
SUPERVISOR: Prof. H.K. Haugen
NUMBER OF PAGES: xxi, 250

Abstract

This thesis reports the effects of ultrashort laser pulse irradiation of various materials. The morphology after irradiation was examined using several microscopy techniques. Emphasis was placed on the identification of crystallographic changes and the analysis of laser-induced periodic surface structures.

Grooves were machined in silicon by translating the target under the focussed laser beam. The resulting depths were measured as a function of pulse energy, translation speed, and number of consecutive passes, for 800 and 400 nm wavelength irradiation. The wall morphology and a corrugation along the bottom of the grooves were characterized. Various polarization configurations relative to the translation direction were compared. Such characterizations are relevant for the practical application of femtosecond laser micromachining.

Silicon and gallium phosphide exhibited periodic structures after irradiation using photon energies less than the bandgap energy, with periods as small as $\sim$20% of the irradiation wavelength. The significantly sub-wavelength periodic structures had a shallow profile on silicon, appearing as fine lines or grids of protrusions and depressions. On gallium phosphide, the surface evolved into planar-like structures with a large aspect ratio, possessing crystalline centers coated with amorphous material. These investigations, along with additional experiments, would help identify the precise physical origins of the short-period structures.

On silicon and germanium, the target crystal orientation was shown to affect the formation of certain morphological features. For multiple-pulse irradiation, the (100) and (111) surface orientations exhibited significantly different tendencies for large conical structure formation. A thin layer of defected material coated the conical structures, with some defects present within the periodic structures. The different crystalline orientations did not affect periodic structuring.

Cross-sectional transmission electron microscopy of silicon after irradiation by single pulses revealed amorphous material and dislocations in the bulk for sufficiently high pulse fluences. On a sample consisting of a metal layer on thermally-grown oxide on silicon, a range of pulse fluences was found which removed the metal layer without observed thinning of the oxide layer. Within this fluence range, above a particular fluence substantial defects were formed in the underlying silicon. Although ultrashort pulse irradiation of materials is frequently considered to be 'damage-free', attention should be paid to sub-surface modifications not evident from surface imaging.

For the drilling of holes in copper foils, the pulse duration did not strongly affect the final morphology for durations under several picoseconds. A photodiode below the foil during drilling recorded transmitted light, indicating the number of pulses required for penetration under a variety of conditions, and characterizing hole evolution during drilling. Periodic surface structuring on the walls of holes depended on the irradiation atmosphere, pulse duration, and laser polarization. These measurements provide insight into the physical processes of material modification, and for the selection of irradiation parameters in practical applications.

Acknowledgements

I would like to thank the numerous people who have helped me through to the completion of my Ph.D. While specific credit is given in the text where relevant, some people deserve special mention here.

Most of all I thank my supervisor, Dr. Harold Haugen, for his support and guidance throughout my graduate work. His attention to detail and dedication to quality research have been greatly appreciated. He was always willing and eager to discuss any aspect of the research. Harold gave me the freedom to pursue my own research ideas and the opportunity to present the work at numerous conferences.

I would like to thank Andrzej Borowiec for getting me started in femtosecond laser research and for sharing his knowledge and skills with me. He played a critical role in the development of experimental techniques, the choice of research directions, and in the discussion of results. Dr. Henry Tiedje, with his impressive combination of scientific knowledge and technical skills, has provided valuable input and experimental assistance. I have appreciated many helpful discussions with him. Dr. John Preston provided good scientific insights into the observed phenomena, and asked many thought-provoking questions along the way. I am also grateful for the scientific discussions I have had with Dr. Jörn Bonse.

I appreciate the efforts of all my collaborators and co-authors, particularly Dr. Junji Yamanaka, Arnaud Weck, and Eugene Hsu, who each did a significant amount of research and with whom I obtained many of the results in this thesis. Additionally, Dr. Gianluigi Botton and Dr. Christian Maunders contributed significantly with TEM analysis and in the interpretation of TEM results.

The staff in the Brockhouse Institute for Materials Research provided me with training and assistance in the various microscopy methods, enabling the analysis of the samples presented in this thesis. In particular, I thank Andy Duft, Steve Koprich, Chris Butcher, and Fred Pearson for their help at numerous times over the course of this research.

My lab-mates have included Andrzej Borowiec, Mike Brennan, Joel Milgram, Henry Tiedje, Paul Dube, Anna Kristoffersen, Andrew Budz, Ben Doyle, Andrew Logan, Jon Waisman, Eugene Hsu, Nick Mailman, Clare Armstrong, Derek Sahota, and several summer students over the years. In addition to their scientific help, I would like to thank these people for their friendship during my time at McMaster, and for making the lab a pleasant environment in which to work. Thank-you also to my current and former housemates at Kingsmount for moral support and friendship, and for making the grad school experience much more than just a scientific endeavour in the lab.

Finally, thanks to my family, who were supportive of me moving far from home to pursue studies beyond my undergraduate education.

Table of Contents

List of Figures

MATERIAL MODIFICATION BY ULTRASHORT LASER PULSE IRRADIATION

Examination of surface morphology and sub-surface crystallographic changes of Si, Cu, GaP, and Ge after ultrashort laser pulse irradiation

By
Travis H.R. Crawford, B.Sc., B.Ed.

A Thesis
Submitted to the School of Graduate Studies
in Partial Fulfilment of the Requirements
for the Degree
Doctor of Philosophy

McMaster University

DOCTOR OF PHILOSOPHY (2008) McMaster University
(Department of Engineering Physics) Hamilton, Ontario

TITLE: Examination of surface morphology and sub-surface crystallographic changes of Si, Cu, GaP, and Ge after ultrashort laser pulse irradiation
AUTHOR: Travis Crawford, B.Sc., B.Ed. (University of Calgary)
SUPERVISOR: Prof. H.K. Haugen
NUMBER OF PAGES: xxi, 250

Abstract

This thesis reports the effects of ultrashort laser pulse irradiation of various materials. The morphology after irradiation was examined using several microscopy techniques. Emphasis was placed on the identification of crystallographic changes and the analysis of laser-induced periodic surface structures.

Grooves were machined in silicon by translating the target under the focussed laser beam. The resulting depths were measured as a function of pulse energy, translation speed, and number of consecutive passes, for 800 and 400 nm wavelength irradiation. The wall morphology and a corrugation along the bottom of the grooves were characterized. Various polarization configurations relative to the translation direction were compared. Such characterizations are relevant for the practical application of femtosecond laser micromachining.

Silicon and gallium phosphide exhibited periodic structures after irradiation using photon energies less than the bandgap energy, with periods as small as $\sim$20% of the irradiation wavelength. The significantly sub-wavelength periodic structures had a shallow profile on silicon, appearing as fine lines or grids of protrusions and depressions. On gallium phosphide, the surface evolved into planar-like structures with a large aspect ratio, possessing crystalline centers coated with amorphous material. These investigations, along with additional experiments, would help identify the precise physical origins of the short-period structures.

On silicon and germanium, the target crystal orientation was shown to affect the formation of certain morphological features. For multiple-pulse irradiation, the (100) and (111) surface orientations exhibited significantly different tendencies for large conical structure formation. A thin layer of defected material coated the conical structures, with some defects present within the periodic structures. The different crystalline orientations did not affect periodic structuring.

Cross-sectional transmission electron microscopy of silicon after irradiation by single pulses revealed amorphous material and dislocations in the bulk for sufficiently high pulse fluences. On a sample consisting of a metal layer on thermally-grown oxide on silicon, a range of pulse fluences was found which removed the metal layer without observed thinning of the oxide layer. Within this fluence range, above a particular fluence substantial defects were formed in the underlying silicon. Although ultrashort pulse irradiation of materials is frequently considered to be 'damage-free', attention should be paid to sub-surface modifications not evident from surface imaging.

For the drilling of holes in copper foils, the pulse duration did not strongly affect the final morphology for durations under several picoseconds. A photodiode below the foil during drilling recorded transmitted light, indicating the number of pulses required for penetration under a variety of conditions, and characterizing hole evolution during drilling. Periodic surface structuring on the walls of holes depended on the irradiation atmosphere, pulse duration, and laser polarization. These measurements provide insight into the physical processes of material modification, and for the selection of irradiation parameters in practical applications.

Acknowledgements

I would like to thank the numerous people who have helped me through to the completion of my Ph.D. While specific credit is given in the text where relevant, some people deserve special mention here.

Most of all I thank my supervisor, Dr. Harold Haugen, for his support and guidance throughout my graduate work. His attention to detail and dedication to quality research have been greatly appreciated. He was always willing and eager to discuss any aspect of the research. Harold gave me the freedom to pursue my own research ideas and the opportunity to present the work at numerous conferences.

I would like to thank Andrzej Borowiec for getting me started in femtosecond laser research and for sharing his knowledge and skills with me. He played a critical role in the development of experimental techniques, the choice of research directions, and in the discussion of results. Dr. Henry Tiedje, with his impressive combination of scientific knowledge and technical skills, has provided valuable input and experimental assistance. I have appreciated many helpful discussions with him. Dr. John Preston provided good scientific insights into the observed phenomena, and asked many thought-provoking questions along the way. I am also grateful for the scientific discussions I have had with Dr. Jörn Bonse.

I appreciate the efforts of all my collaborators and co-authors, particularly Dr. Junji Yamanaka, Arnaud Weck, and Eugene Hsu, who each did a significant amount of research and with whom I obtained many of the results in this thesis. Additionally, Dr. Gianluigi Botton and Dr. Christian Maunders contributed significantly with TEM analysis and in the interpretation of TEM results.

The staff in the Brockhouse Institute for Materials Research provided me with training and assistance in the various microscopy methods, enabling the analysis of the samples presented in this thesis. In particular, I thank Andy Duft, Steve Koprich, Chris Butcher, and Fred Pearson for their help at numerous times over the course of this research.

My lab-mates have included Andrzej Borowiec, Mike Brennan, Joel Milgram, Henry Tiedje, Paul Dube, Anna Kristoffersen, Andrew Budz, Ben Doyle, Andrew Logan, Jon Waisman, Eugene Hsu, Nick Mailman, Clare Armstrong, Derek Sahota, and several summer students over the years. In addition to their scientific help, I would like to thank these people for their friendship during my time at McMaster, and for making the lab a pleasant environment in which to work. Thank-you also to my current and former housemates at Kingsmount for moral support and friendship, and for making the grad school experience much more than just a scientific endeavour in the lab.

Finally, thanks to my family, who were supportive of me moving far from home to pursue studies beyond my undergraduate education.

Table of Contents

List of Figures

List of Tables

Chapter 1

Introduction

1.1 Introduction

Ultrashort or ultrafast laser pulses are generally considered to be those with a duration on the order of or less than a picosecond (1 ps $\equiv 10^{-12}$ s). Pulses with a duration of a few hundred femtoseconds (fs) or less (1 fs $\equiv 10^{-15}$ s) are common from mode-locked and regeneratively-amplified titanium-doped sapphire laser systems. Femtosecond laser beams are characterized as having a relatively low pulse energy (or low average power), while having extremely high peak powers. For example, a 150 fs pulse of light centered at a peak wavelength λ of 800 nm is approximately 45 μm long, and corresponds to roughly 55 electric field oscillations. A one-microjoule pulse corresponds to an instantaneous power of several megawatts, although the average power (at a repetition rate of 1 kHz) would only be a milliwatt. When focussed to a small spot, these pulses will produce extremely high intensities.

The short time duration of an ultrashort laser pulse does not produce the same effects in a material as nanosecond or longer pulses. With continuous-wave (CW) lasers, the continuous input of energy at the target causes material removal due to melting and evaporation. Nanosecond or longer pulses are associated with melting, boiling, and vaporization with significant heating of the surrounding material and a large heat-affected zone. A long pulse will also interact with the vapor plume of material ejected by the leading part of the pulse. Coarse, jagged, random damage may be expected. However, with an ultrashort pulse, there is rapid ionization and plasma formation with minimal heating of the surrounding material for an individual pulse. There is no 'plasma shielding' of the pulse by the plume, since the pulse has ended before significant material begins to eject. Energy deposition is temporally separated from material removal. More precise, repeatable material removal is expected due to the localization of energy deposition and reduced heat-affected zone. Applications of ultrashort laser pulses are numerous. The short durations and thus high peak intensities lead to a range of nonlinear phenomena. Enhanced absorption occurs in materials which are normally one-photon transparent to the irradiating wavelength, and thus transparent

materials can be more easily modified by ultrashort pulses. Materials with high thermal conductivity are expected to be more easily machined with shorter pulse durations.

Many complex phenomena exist, and are not fully understood. The short time scales make the measurement and analysis of process evolution particularly difficult, as various processes must be inferred from time-resolved analysis and post-irradiation measurements, or be simulated by computer models. The application presented in this thesis is the modification of materials, providing some insight into the underlying physical processes as well as the potential for industrial applications.

1.2 Overview of the thesis

Silicon is used extensively in the microelectronics industry. It has been well characterized and significant research has been done in the processing of silicon for electronic applications. Investigations of laser-material interactions with silicon are warranted. This thesis presents results of work on the interaction of ultrashort pulses with materials, performed between Fall 2001 and Fall 2008 at McMaster University in the department of Engineering Physics, under the supervision of Professor Harold K. Haugen. Various facilities at McMaster University, particularly the microscopy facilities of the Brockhouse Institute for Materials Research, enabled a variety of studies of laser-irradiated materials. Members of the Department of Materials Science and Engineering have also contributed to the work presented in this thesis, particularly for investigations on metals. Overall, the investigation of periodic structures and the examination of changes of crystallinity after ultrashort pulse laser irradiation were the major themes present throughout most of the work presented here.

Portions of the work presented in this thesis have been published in nine refereed journal articles and several conference contributions (see appendix C for details). The first series of experiments, presented in chapter 4, was the machining of grooves on silicon under conditions potentially encountered in practical applications. Using scanning electron microscopy (SEM), groove depths and morphologies were measured as a function of various laser and sample translation parameters. A systematic investigation of the effects of these parameters on silicon had not been previously reported.

Subsequent to the groove machining experiments, a series of multiple-pulse experiments on silicon were done without translating the sample during irradiation. This included experiments using ultrashort pulses at wavelengths where silicon is single-photon transparent. The results are presented in chapter 5. The experiments revealed several previously

unobserved periodic morphologies with substantially sub-wavelength periods, only present for irradiation photon energies less than the silicon bandgap energy. Preliminary experiments on germanium did not produce the same wavelength-dependent tendencies as were observed on silicon. In chapter 5, the results of short pulse irradiation of gallium phosphide are also presented. Short-period structures on gallium phosphide were readily formed using the $\lambda = 800$ nm irradiation wavelength. In addition to the pulse energy and number of pulses, the pulse duration was varied to investigate the effects on periodic structure formation. Cross-sectional transmission electron microscopy (TEM) studies were performed on gallium phosphide, revealing the crystallinity of the structures and a high height-to-width ratio. In all cases, and consistent with previous reports for ultrashort pulse irradiation, 'classic' laser-induced periodic surface structures were observed with periods somewhat less than the irradiation wavelength.

A continuation of the periodic structure investigations is presented in chapter 6, where irradiation of Si(100), Si(110), Si(111), Ge(100) and Ge(111) surfaces is compared. The tendency to form periodic structures did not depend on the surface crystalline orientation. However, on both silicon and germanium the crystalline orientation had a significant effect on larger-scale structuring. On silicon the tendency to produce amorphous material was also affected by the orientation of the crystal lattice. These results indicate that the crystallographic nature of a target should be considered when comparing different reports of ultrashort pulse laser-material interaction. In addition to the scanning electron microscopy used for surface imaging, cross-sectional TEM investigations were performed to determine the crystalline structure of the periodic and coarse structures.

In contrast to the cross-sectional TEM results in chapters 5 and 6 for which large numbers of pulses were used, the emphasis of chapter 7 is on the final state after irradiation by single pulses and low numbers of pulses. Chapter 7 presents results for silicon, and for a multiple layer structure consisting of a metal film on thermally-grown oxide on silicon. Amorphous material was observed for certain irradiation conditions, with substantial defected material for single and small numbers of high-fluence pulses. However, single-pulse irradiation sites lacked sub-surface defects and amorphous material despite the use of peak fluences which might be expected to produce such crystallographic changes. On a multiple-layer sample irradiated by various pulse energies and wavelengths, substantial defective material can be formed in the underlying silicon at fluences which remove the metal film but do not appreciably thin the oxide.

Finally, femtosecond laser pulses were used to drill holes in thin metal foils as a fabrication step for investigations of ductile fracture. To determine ideal drilling parameters,

significant work was done with copper foils. These results are presented in chapter 8. The effects of pulse duration were examined, and the morphology of the hole walls was imaged. A photodiode placed below the foil provided information as the hole was drilled, for various pulse durations and pulse energies. For increasing pulse duration, a definite change in behaviour was observed for durations above the approximate electron-phonon relaxation time. Periodic structures were also observed on the walls of holes for certain irradiation conditions.

More detailed descriptions of my role in the research are presented near the start of each chapter presenting experimental results. With the exception of the publications of the results for metal foils and gallium phosphide, I was primarily responsible for the majority of writing of papers and preparing conference presentations, and for the relevant literature search. For these works I also did most of the optical and scanning electron microscopy. I performed the laser irradiation of the majority of the samples with the exception of the gallium phosphide, the metal foil samples used in ductile fracture experiments, and certain multilayer samples.

Chapter 2

Background

This chapter presents an overview of the processes involved in the interaction of ultrashort laser pulses with materials. A historical overview is then given for studies of crystal structure modifications, periodic structure formation, and the applications of the research. A brief summary for introductory purposes is presented here, and this section is not a comprehensive literature review of all physical processes. Further literature and background information with substantial discussion are presented in the other chapters where it is more relevant to the phenomena being discussed.

2.1 Effects of pulse duration in laser-material interaction

In the description of short pulse interaction with metal targets, the two-temperature model is generally used [1, 2, 3, 4]. This model characterizes the lattice and electron subsystems as having separate temperatures and different heat capacities. Heat diffusion equations for the lattice and electron systems are coupled by a term proportional to the electron-phonon coupling multiplied by the temperature difference between the two systems. In the model the electron-electron coupling time can be assumed to be extremely short, much shorter than for other processes. In a metal, if the pulse intensity is not exceedingly high the incident laser energy is absorbed by the free electrons via inverse Bremsstrahlung [1]. The electrons then transfer energy to the lattice through electron-phonon interactions, though some energy may also be lost by electron diffusion into the material. Heat conduction by electrons into the lattice, however, is frequently neglected as a simple approximation in the two-temperature model [1, 2, 4]. The electron-phonon coupling coefficient is normally considered to be constant, although more detailed treatments include its temperature dependence (see, e.g. reference [4]).

The pulse duration relative to the electron-phonon relaxation time distinguishes between various material evolution behaviours [3]. For femtosecond pulses, the pulse duration is much shorter than the electron-phonon coupling time which is around a picosecond to several tens of picoseconds [1, 2, 5, 6]. Fundamental physical processes for femtosec-

ond laser excitation are separated in time [6, 7], with excitation occurring on the femtosecond time scale, melting roughly on a picosecond time scale, and material removal on the nanosecond time scale [6]. Deposition of laser energy into the material is complete before substantial heat conduction or lattice heating occurs. As the electron heat capacity is much less than that of the lattice, the electron subsystem can be heated to very high transient temperatures, much higher than the lattice temperature. The electron subsystem thermalizes typically within 10 fs – 1 ps [1]. Electrons then cool by transferring energy to the lattice on a time scale corresponding to the electron-phonon coupling time. The greatly diminished heat conduction for femtosecond pulse irradiation allows highly localized material removal and requires less energy, compared to nanosecond pulses [1, 2, 3]. Highly transient thermal processes occur in short-pulse laser irradiation, and metastable thermodynamic states like supersaturated vapors and superheated liquids are likely to be present [5].

For nanosecond pulses, the pulse duration is much longer than the electron-phonon coupling time. Absorption of laser energy leads to a local temperature increase to the melting point and to the boiling point. Heat conduction into the solid target occurs while the pulse is still irradiating the surface, reducing the energy density near the surface [2, 3] and producing a significant heat-affected zone. A relatively large layer of melted material is expected, and material is evaporated from the liquid, impeding precision removal of material. The quality of microstructures that can be achieved is reduced for nanosecond pulses by the melting [3]. Picosecond or femtosecond pulses should be advantageous for low-damage patterning of materials with large thermal diffusivity [1]. Due to mechanical stresses and pressures however, on brittle materials better results may be obtained with picosecond pulses [1] and picosecond pulse trains [8]. The laser damage threshold has a $\sqrt{\tau}$-dependence with respect to pulse duration τ, but deviates from this for pulses shorter than a few tens of picoseconds [9]. For sufficiently short pulse durations, the specific pulse duration generally does not play an important role [10].

Screening of incident light can be ignored with femtosecond pulses since a vapor or plasma plume does not develop during the pulse, and ablation only takes place after the pulse [1]. However, screening often cannot be ignored for nanosecond pulses [1, 10], for which incident light in the pulse is scattered and absorbed by the vapor plume [9]. For very strong screening, overall behavior is determined more by interactions of the laser with the plume than with the substrate itself [1].

Optical absorption in metals is usually dominated by free carrier absorption [6]. In semiconductors, if the photon energy is greater than the bandgap energy, electrons are excited to the conduction band from the valence band [6, 10, 11]. Electrons in the conduction

band can absorb energy via free carrier absorption. A conduction band electron with sufficient energy can excite an additional electron from the valence to conduction band, in a process called impact ionization. A rapid buildup of electrons in the conduction band can occur as this process repeats [12], in a process known as avalanche ionization.

Modification of transparent materials is possible with picosecond and femtosecond pulses, for cases where longer pulse lasers do not provide efficient defect generation or single-photon absorption [1]. Multiphoton absorption can cause interband transitions. This and avalanche ionization occur for femtosecond structuring of wide-bandgap dielectrics [1, 6, 12]. Higher pulse intensities lead to increased probability of nonlinear absorption [10]. When the density of free electrons reaches a value on the order of 10^{19}–10^{21} per cm^3, optical breakdown within a material typically occurs [1]. For sufficiently short pulse lengths, multiphoton ionization alone creates this critical electron density [1, 12]. With shorter pulses, multiphoton ionization will contribute a greater fraction of the electron energy compared to avalanche ionization, which dominates for longer pulses [12]. Once multiphoton ionization produces a high free electron density, the material will behave like a conductor and absorb energy via inverse Bremsstrahlung heating [9]. Multiphoton ionization is a deterministic process, so short pulse material modification should have a more deterministic character compared to that from longer pulses [12].

In general, material structural modifications which take more than a picosecond consist primarily of thermal processes, while a non-thermal process regime exists for a shorter pulse duration [10, 13]. The formation of an electron-hole plasma can destabilize the lattice structure in under a picosecond, and is referred to as non-thermal melting [6, 14]. Non-thermal melting occurs when the conduction band electron density exceeds 10^{21}–10^{22} cm^{-3}, and such densities are attainable on semiconductors with femtosecond photoexcitation [10, 13, 14, 15, 16]. Absorbing solids evolve thermally on time scales of a picosecond and longer, for irradiation below the threshold for plasma formation [13].

2.2 Mechanisms of material removal in short pulse laser irradiation

Several different material removal mechanisms are expected depending on the pulse energy, wavelength, pulse duration, and the material properties. These mechanisms are still not fully understood despite many investigations [13, 17]. It is difficult to experimentally assess the transient thermodynamic states. A brief summary of the various stages of material evolution is given below. Time-resolved microscopy, second harmonic generation,

and reflectivity measurements have shown various stages of material evolution (see, e.g. references [5, 7, 10, 14, 15, 16]), in particular indicating the time scales of various processes. In such experiments, temporal resolution is limited by the duration of the probe pulse, and spatial resolution is limited by the imaging optics. Time-of-flight spectroscopy has been used to identify the species emitted from the laser irradiation (see, e.g. references [1, 16, 18]). Insight into various mechanisms of melting and material evolution, including transient temperatures and pressures, has been gained using molecular dynamics (MD) and other computer simulations (see, e.g. references [13, 19, 20, 21, 22, 23]). Due to the computational intensity required, simulations are generally done with rather small volumes of material [1], for single pulse irradiation, and materials with fast electron-phonon coupling.

Ultrafast time-resolved microscopy and reflectivity measurements have examined a variety of materials including silicon [5, 7, 10], germanium [14], and InP [15]. Within a picosecond, a high reflectivity region is formed and is attributed to the excited electron-hole plasma and the molten material. After the laser energy has thermalized, the material is in a liquid state with a high temperature and approximately solid density [7]. A dark region formed after tens to hundreds of picoseconds is attributed to the start of material removal. After roughly a nanosecond, a pattern of dark moving rings forms, and is attributed to constructive and destructive interference between an ejected surface of material and the underlying substrate, similar to Newton rings. Hydrodynamic forces then cause melt flow and carry away material [7, 15]. The pattern of dark rings has been observed on a variety of materials [5, 7, 10, 14, 15] within a few nanoseconds of irradiation, and is thus characteristic of the ultrafast material removal process. After several tens of nanoseconds the remaining material has resolidified. It should be noted that time-resolved reflectivity results are usually for somewhat low fluences, and not for those at which optical breakdown and plasma formation play a dominant role [7, 10]. In a 2D MD simulation [19] for low fluence, the matter-vacuum interface stayed relatively sharp for a long period of time. This supports the conclusion from time-resolved experiments that patterns resembling Newton rings are due to interference. For a higher fluence simulation the matter-vacuum interface is quickly destroyed [19], and Newton rings are not observed at higher fluences.

Four different ablation mechanisms were identified in the MD simulations of Perez et al. [19]: spallation, phase explosion, fragmentation, and vaporization. Distinct regions with specific expansion dynamics will occur at different depths within the target [17, 19]. In spallation [19], tensile stresses induce defects which result in internal failure. This occurs at fluences close to the ablation threshold, and is probably restricted to picosecond and

femtosecond pulse situations [19]. Relaxation of stresses has been shown to cause mechanical fracture of a solid target surface at energy densities below those required for boiling of the material [23]. For short enough pulses, laser heating occurs in a nearly constant volume condition, resulting in high compressive stresses. Tensile stress can be generated when the compressive stresses interact with the material surface, resulting in cavitation or mechanical fracture. The ejection of a layer of material occurs in this way [19, 23]. As expansion continues, the ejected layer eventually breaks up [19].

While a tensile component of a pressure wave develops at low fluences, it is small at higher fluences due to thermal softening of the material, suggesting spallation should only be observed at low fluences [19]. For somewhat higher fluences, MD simulations indicate that spallation contributes little compared to the process of 'homogeneous nucleation' or 'phase explosion' [19]. This process occurs above a particular energy threshold but below the threshold for dielectric breakdown and plasma formation. It is the rapid transition from a superheated liquid to a heterogeneous mixture of vapor bubbles and liquid droplets [1, 13, 19, 20]. The growth and coalescence of the vapor bubbles will lead to the ejection of large liquid droplets [19]. Phase explosion is able to produce the conditions under which Newton rings are expected to form [13, 19]. For sufficiently long pulses, slow material expansion and efficient heat conduction lead to an absence of explosive boiling [13, 20].

At higher energies, phase explosion is replaced by fragmentation as the dominant ablation mechanism. In fragmentation [19] an initially homogeneous medium decomposes into a collection of clusters. Material is initially put into a superheated solid state, melts and expands into a supercritical fluid state, and is followed by the formation of voids, as observed in MD simulations [19]. Constant-volume heating induces large thermoelastic stress, which causes a very high speed expansion [17]. A structural reorganization occurs, as internal surfaces form to relax internal stresses [17]. Fragmentation occurs in the breakup of the expanding supercritical fluid and is in contrast to spallation, in which strong tensile pressure waves remove material [19, 20]. Fragmentation and phase explosion are mutually exclusive processes, as different thermodynamic trajectories are involved [13, 17, 19, 20].

At high energies, the process of vaporization [19] occurs where the material surface is atomized with very few clusters, and expands at a very high speed. The material exhibits a generally gas-like behavior [17, 19]. This is not a process of slow heating followed by equilibrium melting and evaporation, as the slow heating process is not a basic material removal mechanism for femtosecond laser irradiation [21].

In femtosecond laser irradiation, the incident laser energy is absorbed by electrons which can begin to leave the material surface. An 'electrostatic ablation' process can occur

if the escaped electrons pull the ions off the target. However, this is responsible for only a small amount of material removal at the start of femtosecond irradiation of insulators [21]. A process called Coulomb explosion is however possible. If a sufficient number of electrons are excited and removed from the lattice, the lattice will have a net positive charge. The ions will strongly repel each other, and cause instability in the lattice leading to ejection of material [18, 21]. This process is expected to play a minimal role on metals, since charge separation would not be expected to occur due to the high electron mobility [21]. However, recent debate has occurred in the literature concerning the role of Coulomb explosion on metals and semiconductors [13, 16, 18]

The various material removal mechanisms described here depend on the irradiating fluence, as well as the material properties, irradiation wavelength, and pulse duration. No single mechanism alone can account for material removal. It should be noted that in a real irradiation case the pulse has a spatial profile, with local fluence varying across the focal spot. This would also play a role in the irradiation site evolution.

2.3 Post-irradiation studies of laser interactions with materials — previous work

Laser interactions with materials were studied shortly after the development of the laser. Optical components inside and outside a laser cavity would sometimes be damaged by the strong laser light electric fields [24, 25]. The laser also rapidly found application for the cutting and drilling of materials, as an alternative to mechanical processes. This section provides a brief overview of the development and history of laser-material interaction studies, with particular emphasis on semiconductors, crystalline changes, and periodic structure formation. Selected recent applications are also presented. More detailed discussion and background information are given in the thesis chapters where it is relevant.

As laser technology has evolved, the minimum pulse duration available has kept decreasing. Pulse durations entered the sub-picosecond time range in the early 1970's [26], and were used to study a variety of ultrafast processes. Mode-locked dye lasers allowed the routine production of sub-picosecond pulses. The development of mode-locked titanium-doped sapphire lasers and the chirped pulse amplification scheme [27] in the mid 1980's was a significant advance which allowed the production of femtosecond laser pulses with high peak intensities [12]. The various advantages of short pulses discussed elsewhere in this thesis led to the investigation of increasingly shorter pulses for a variety of industrial applications. Femtosecond laser machining is frequently referred to as being 'damage-

free', meaning that there is a significantly reduced heat affected zone and improved morphology in comparison to longer pulse irradiation. However, this does not necessarily mean there is an absence of unusual structuring or crystallographic changes.

2.3.1 Crystal structure studies on semiconductors

Since the early days of laser research, there has been substantial interest in the interaction of laser pulses with semiconductors and the final crystalline structure of irradiated materials. Ion implantation of dopant atoms into semiconductors provides certain capabilities in the fabrication of electronic devices, but the implantation is generally accompanied by the production of crystalline damage. Nanosecond pulsed laser irradiation was found to allow localized annealing, removing the crystalline damage and producing single crystal areas, with control over the dopant depth profile. Substantial experimentation was done during the 1970's to investigate laser annealing (see, e.g. references [28, 29] and references therein).

As laser technology evolved, shorter pulses were more easily produced, and this led to experiments on the use of shorter pulses in laser annealing of semiconductors [29, 30, 31, 32]. With fast pulse annealing, a high speed crystal growth regime was attainable in which sufficiently fast resolidification speeds led to crystal growth breakdown and an amorphous final phase [30, 32]. Rather than epitaxial recrystallization, sufficiently rapid cooling of molten semiconductor leads to the formation of amorphous material [30, 33, 34, 35]. A short irradiation wavelength was found to enhance this effect [29, 30, 32, 36], with more amorphous material for a shorter wavelength [29]. On silicon, picosecond pulses, or short nanosecond pulses of short wavelength, were able to amorphize crystalline material [29, 36]. It was found that the crystalline orientation of silicon also affected the amorphization [29, 30, 32].

Examination of crystallographic changes after ultrashort laser irradiation was a logical 'next step' after examinations of picosecond and nanosecond irradiation experiments. Until recently, there had been relatively few studies of crystalline modification for femtosecond pulse irradiation, particularly after a single laser pulse, or of multiple layer samples. TEM was used by Borowiec et al. [37, 38] after single-pulse femtosecond laser irradiation of silicon, InP, and GaAs. Amorphous material was difficult to identify due to the plan-view TEM orientation used, however polycrystalline material in crater rims and centers was observed under certain conditions. These results complement detailed studies of the surface

morphology of InP and silicon by Bonse et al. [35, 39], which included incubation effects, amorphization, and laser-induced surface structuring.

In recent years, there have been several reports from cross-sectional TEM used for observing the crystalline structure of semiconductors irradiated by ultrashort laser pulses under a variety of conditions. Focussed ion beam milling is increasingly being used for fabricating cross-sections of materials for TEM analysis, allowing a clearer observation of sub-surface changes. Amorphous material on silicon was observed for a range of ultrashort irradiation wavelengths for various numbers of pulses [40, 41, 42], with defects in some cases [42]. On InP irradiated in its transparency regime, single- and multiple-pulse irradiation sites possessed crystallographic changes [43]. For grooves machined on InP with nanosecond and femtosecond pulses, the short pulse duration created a substantial density of defects while nanosecond pulses did not [44]. In this thesis (and the corresponding journal publications [45, 46, 47]), further cross-sectional TEM studies are presented for silicon, gallium phosphide, and multiple-layer metal-oxide-silicon structures. The presence and distribution of amorphous material and defects is revealed, and discussed in the context of material evolution and periodic structure formation. In addition to TEM, complementary techniques including micro Raman spectroscopy, scanning laser microscopy, and polarization-resolved photoluminescence have been used by various authors to examine the crystallinity and strain fields in semiconductors after ultrashort pulse irradiation [33, 34, 48].

2.3.2 Periodic structure studies

The formation of periodic parallel lines on laser-irradiated material was first reported by Birnbaum [49] approximately five years after the demonstration of the first working laser. These structures appeared on a variety of semiconductor surfaces. Through the 1970's and 1980's as laser technology developed and became more common, periodic lines were reported on various materials, including semiconductors, for multiple laser types [24, 25, 28, 31, 50, 51]. Ripple formation was generally attributed to light interference effects between the incident and scattered radiation. For normal incidence, they had a period approximately equal to the laser radiation wavelength, and their direction was dependent on the polarization of the laser light. Formation of parallel lines by laser irradiation has since been called a "universal phenomenon" [52], as it occurs on a wide variety of materials for a broad range of laser wavelengths.

In the early 1980's, rigorous theories were developed for the formation of these structures [53, 54], including the theory and comparisons to experimental results of the group of Sipe et al. [52, 54, 55, 56, 57]. Within the past several years, periods substantially smaller than the irradiation wavelength for normal incidence began to be reported extensively for ultrashort pulse irradiation, particularly when the photon energy was less than the bandgap energy of the material (see, e.g. reference [58] and references therein). This included structures on various semiconductors [59], and led to subsequent further work on indium phosphide [43], silicon [58], gallium phosphide [46, 60], and zinc selenide [61] among other materials. The work in references [46, 58, 60] is presented in this thesis. Recently, Bhardwaj et al. [62] have reported formation of parallel planes of modified material within the bulk of femtosecond-irradiated fused silica. These had a period of roughly half the wavelength in the solid. The possible connection between the laser-induced surface structures and the periodic bulk structures is an ongoing field of research. Gallium phosphide was found to form significantly sub-wavelength periodic structures with large height-to-width ratios [46], somewhat resembling the planes observed by Bhardwaj et al. [62]. The origins of substantially sub-wavelength periodic structuring are still under debate in the literature. Models involving the theory of Sipe et al. [54], nonlinear mechanisms like second harmonic generation, self-organization processes, planar waveguide formation from nanoplasmonic processes, and surface free energy properties have been proposed (see, e.g. references [58, 60] and references therein).

2.3.3 Practical applications

With the increasing availability of ultrashort pulse laser systems, short pulse machining has been used to produce structures or achieve material removal not easily attainable with longer pulse durations or with mechanical techniques. They have attracted particular attention for prototyping, small quantity, and niche applications. Ultrashort pulses have been used to machine various ultrahard materials [63]. Machining of linear features with femtosecond laser pulses has been demonstrated by various groups (see, e.g. references [11, 64, 65, 66]), for applications such as forming microchannels for microfluidic devices, and for dicing of silicon wafers possessing electronic devices. In contrast to dicing with saws, laser cuts can have a narrower width and allow arbitrary shapes such as hexagons to be cut, thus allowing higher packing density. Silicon surface texturing with ultrashort lasers under various conditions has led to rough surfaces and conical spikes. These could have applications where large surface areas or pointed structures are required, such as field emission sources, improved adhesion properties, or where high light absorbance is

desired (see, e.g. references [67, 68]). Texturing of a mold surface has been demonstrated to be used for the replication of hydrophobic structures in polymers [69].

Deep holes have been drilled in metals with ultrashort laser pulses [2, 70, 71, 72, 73], and their potential use in industrial applications has been considered. In this thesis, the short pulse duration combined with post-irradiation annealing allowed precisely-located, well-defined holes and reduced the hardness of near-hole material to that of the bulk material [74]. Hole wall morphology and the laser signal transmitted through the holes were affected by the use of different pulse durations [75, 76].

A variety of electronic and optoelectronic applications involving ultrashort laser pulses have been demonstrated. Femtosecond machining of a target is an alternative to standard lithographic processes, which often involve an expensive-to-produce mask, for increased speed in prototype fabrication [66]. Laser direct-writing of a photolithography mask by selectively removing metal from a photomask substrate has been demonstrated [77]. Femtosecond laser pulses have been used for in-situ repair of optoelectronic devices [78], and show promise for the removal of nanometre-scale surface layers for nanotechnology applications [79]. Ultrashort laser pulses have allowed the direct writing of photonic band gap structures for telecom wavelengths on Si-on-SiO_2 waveguides [80]. Substantial interest has been shown for the focussing of femtosecond laser pulses inside transparent materials, including silicon via mid-IR wavelengths [81], allowing the fabrication of waveguides in the bulk material. Short-period structuring in transparent materials [62] has recently been observed. Research is currently underway using electron microscopy to investigate the modifications in bulk transparent materials which occur during ultrashort pulse excitation.

Chapter 3

Experimental Setup

This chapter describes the general experimental setup and analysis techniques used in the research presented in this thesis. Further details and information on specialized techniques are given in the thesis chapters where they are relevant.

3.1 Laser systems

The Photonics Research Laboratory at McMaster University provides the ability to irradiate materials using femtosecond laser pulses. The two complementary laser systems used in this work are summarized in table 3.1. The systems are Spectra-Physics *Spitfire* kilohertz, Ti:sapphire laser amplifiers. Such a system is shown schematically in figure 3.1.

Each system consists of four major components: the modelocked femtosecond oscillator (*Tsunami*) and its pump laser (*Millennia V* or *Vs*), and the regeneratively-amplified chirped-pulse amplifier (*Spitfire LCX* or *Spitfire*) and its pump laser (*Merlin LCX* or *Evolution X*). All components were purchased from Spectra-Physics Lasers, Inc.. The *LCX* denotes a lower-power version of a standard system sold at the time. The first system (*Millennia V*, *Tsunami*, *Merlin LCX*, and *Spitfire LCX*) is designed to produce pulses with approximate energy and duration of 300 μJ and 130 fs respectively. The second system (*Millennia Vs*, *Tsunami*, *Evolution X*, and *Spitfire*) is newer than the first, and provides complementary capabilities, such as increased pulse energy (800 μJ) and decreased pulse duration (<45 fs). The first system was tuned to a center wavelength of $\lambda = 800$ nm and was operated at a repetition rate of 1 kHz. It could be easily tuned to wavelengths in the range of 770–840 nm or operated at lower repetition rates, but this was rarely done. The newer system was sometimes used to pump an optical parametric amplifier (OPA), described later in this section. For most of the research in this thesis, experiments with irradiation by 400 nm and 800 nm wavelength pulses used the first system, while experiments at ~1300 nm and ~2100 nm were performed with the second system with the OPA.

The *Millennia* lasers use neodymium-doped yttrium vanadate (Nd:YVO_4) crystals, producing approximately 4.3 W of continuous-wave light at a wavelength of 532 nm. In each

First system

Laser	Repetition rate	Approximate pulse energy	Wavelength (nm)	Pulse duration (fs)
Ti:sapphire oscillator	~82 MHz	10 nJ	770–840	<~90
Ti:sapphire amplifier	1 Hz – 1 kHz	300 μJ	770–840	~150

Second system

Laser	Repetition rate	Approximate pulse energy	Wavelength (nm)	Pulse duration (fs)
Ti:sapphire oscillator	~75 MHz	5 nJ	800	<~45
Ti:sapphire amplifier	1 kHz	800 μJ	800	~50
OPA signal	1 kHz	90 μJ	1100–1600	~50–100
OPA idler	1 kHz	30 μJ	1600–2600	~50–100

Table 3.1: Summary of laser types used in this research

laser, two arrays of diode lasers, producing approximately 13 W of light each and operating at a wavelength near 809 nm, pump the crystal via fiber optic bundles. The 1064 nm wavelength light from the Nd:YVO_4 crystal was frequency-doubled using a lithium triborate crystal within the cavity [82].

The two Spectra-Physics *Tsunami* mode-locked laser oscillators in the lab are designed to produce linearly-polarized pulses of <~90 fs and <~45 fs duration, with average powers of approximately 600 mW and 300 mW respectively. For the first system, roughly 30% of the 600 mW output power is used to seed the regenerative amplifier. A titanium-doped sapphire crystal is used as the gain medium, which has the ability to amplify light over a large range of wavelengths (690 nm to 1080 nm [83]). From Fourier arguments, to generate a short signal in the time domain a wide range of frequencies is required. Mode-locking is the generation and amplification of many different closely-spaced frequencies of light, keeping them in the proper phase such that a short pulse is produced. The sum of the electric fields produced by each individual mode results in a peak in intensity where every mode has its maximum electric field. An acousto-optic modulator is present in the cavity, and this was used to initiate mode-locking. However, once mode-locking was occurring, the acousto-optic modulator was turned off. At this point, Kerr-lens mode-locking kept the system modelocked. In Kerr-lens modelocking, self-focussing due to the intensity-dependent refractive index in the crystal occurs, and this keeps the cavity stable. Low-intensity pulses would suffer increased loss since the lack of self-focussing would not keep them within the cavity.

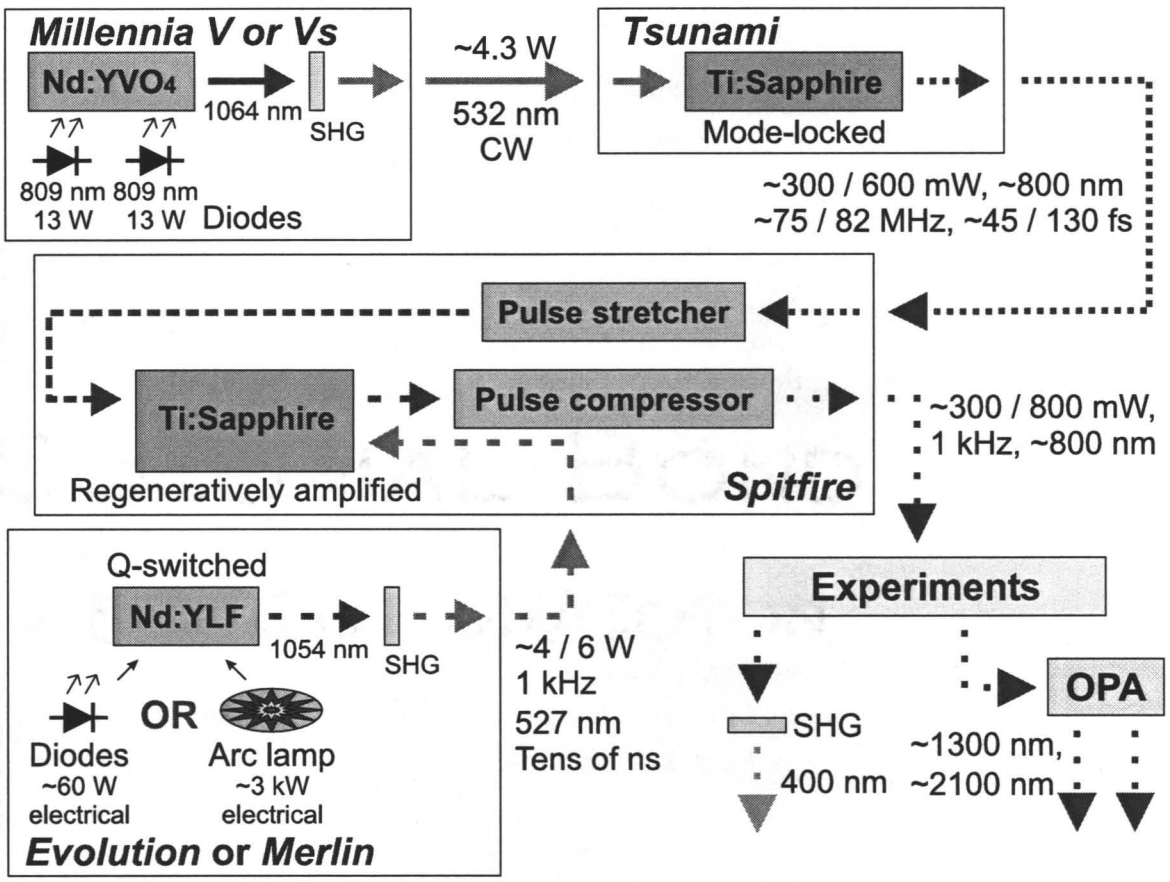

Figure 3.1: Schematic overview of a Spectra-Physics kilohertz Ti:sapphire amplified laser system used for this research.

The *Spitfire* systems work on the principle of chirped pulse amplification [27]. If a seed femtosecond pulse were amplified within a cavity containing a pumped Ti:sapphire crystal, the amplified pulse could become intense enough that it damages the cavity components or experiences distortions due to nonlinear effects. However, a laser pulse containing a range of wavelengths can be 'stretched', that is, frequencies at one end of the pulse spectrum exit the stretcher before the frequencies at the other end of the spectrum. The stretched pulse is called a 'chirped pulse' since the frequency of the waves contained within the pulse changes from one end of the pulse to the other. In chirped pulse amplification, the chirped pulse is amplified instead of the original unstretched pulse. After amplification, the pulse is compressed to bring the frequencies together again temporally.

Figure 3.2 shows how four diffraction gratings can be used to chirp a pulse via negative dispersion [84]. The bluer light comes out of the arrangement first, since it travels a shorter

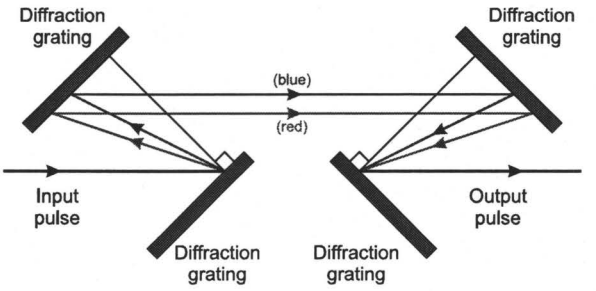

Figure 3.2: Configuration using four diffraction gratings which provides negative dispersion (shorter wavelengths travel a shorter distance). If the input pulse is unchirped, the output pulse will be stretched. If the input pulse has been chirped (via positive dispersion), this arrangement can compress the pulse if the distances between gratings are chosen properly.

path distance than the red light. In the *Spitfire* systems, additional mirrors are used so that the beam is incident on a single grating four times. Such an arrangement is used in the *Spitfire* to compress the pulse. Most materials for visible wavelengths provide positive dispersion, since the shorter wavelengths of light travel more slowly than longer wavelengths. The arrangement in figure 3.2 can be modified to provide positive dispersion by inserting telescopes (or equivalently a curved mirror in the case of the *Spitfire* stretcher) to swap the red and blue beams at certain locations, so that the redder light travels the shorter distance.

Figure 3.3 shows schematically how the stretched pulse enters the regenerative amplifier cavity, is amplified, and is ejected. Each pass of the pulse through the Ti:sapphire crystal only provides a gain of $\sim$3 [85], so multiple passes through the crystal are needed. In the configuration used, pulses are amplified from an initial energy of a few nanojoules to a final energy of a few hundred microjoules. The input seed pulses from the *Tsunami* are linearly polarized, and this polarization allows the selective transmission and reflection of the pulse depending on polarization-sensitive and polarization-manipulating optics. The Ti:sapphire rod and polarizer are at Brewster's angle, so that minimal reflection occurs for horizontally-polarized light. Vertically-polarized light on Brewster-angle surfaces experiences some reflection, however some transmission also occurs. Due to the number of Brewster-angle surfaces, the vertically-polarized light circulating within the cavity suffers high loss, although a small amount remains. The imperfect nature of these reflections can lead to satellite pulses. A slight amount of light incident on the polarizer will be reflected, leading to a pre-pulse on each round-trip of the pulse while it is trapped in the cavity. Once the second Pockels cell is turned on (typically 200–300 ns after the first cell is turned on),

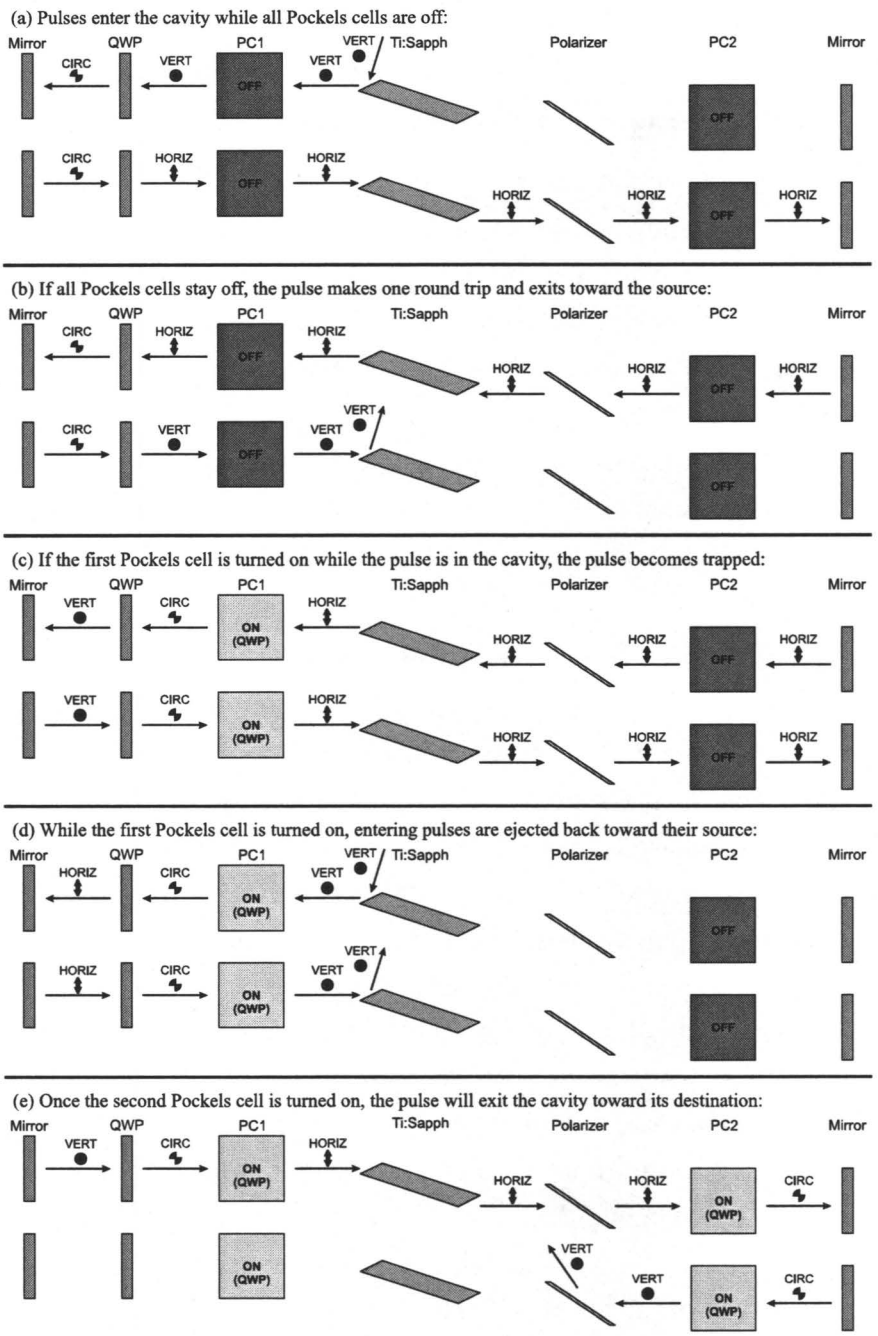

Figure 3.3: Schematic illustration of regenerative amplification, as done in the Spectra-Physics *Spitfire* systems. The polarizer and Ti:sapphire crystal are highly transmitting (minimally reflecting) for horizontally-polarized pulses. Abbreviations: QWP: Quarter-wave plate; PC: Pockels cell; HORIZ, VERT, and CIRC refer to horizontally, vertically, and circularly-polarized light respectively. In the *Spitfire* systems, a photodiode (not shown) was present behind one of the end mirrors to monitor leak-through light.

any vertically polarized light which is not initially reflected by the polarizer will be able to make another round trip in the cavity. It will suffer significant loss due to the number of Brewster surfaces in the cavity, but a small amount of light will be ejected the next time a pulse is incident on the polarizer. This produces a weak post-pulse.

The holographic diffraction gratings present in the stretcher and compressor show a polarization-dependent efficiency. Pulses with polarization parallel to the lines of the grating are attenuated more than pulses with a perpendicular polarization. A periscope is present between the stretcher and amplifier to produce the correct polarization for pulses to enter the amplifier cavity. A periscope is present between the amplifier and the compressor, to produce the lower-loss polarization for the gratings in the compressor. To some extent, this attenuates the pre-pulses caused by reflection of horizontally-polarized light off the polarizer in the cavity. The pulses which are incident on the gratings are polarized parallel to the surface of the optical table, and exit the *Spitfire* with this polarization.

On some occasions, the first *Spitfire* (*LCX*) was configured to produce pulses with durations of ~220 ps, ~7 ns, or in the range of 150 fs to 35 ps. To output the ~220 ps pulse, a mirror was placed between the output of the amplifier and the first grating of the compressor (refer to figure 3.1). In this way, the amplified pulse was not re-compressed. A polarizer was placed after the output of the *Spitfire* to suppress the vertically-polarized pre-pulses which would have formerly been attenuated by their reduced reflectivity on the gratings. The ~7 ns pulses were produced by blocking the seed input to the amplifier. In this way, pulses could be generated by 'cavity dumping'. After energy was deposited in the Ti:sapphire crystal by a *Merlin LCX* pulse, turning on Pockels cell #1 allowed horizontally-polarized spontaneous emission in the crystal to be trapped within the cavity and be amplified. At a later time, when Pockels cell #2 was turned on, the light in the cavity would be 'dumped', exiting the cavity off the polarizer. The output pulse has a duration roughly equal to the cavity round-trip time. Output of pulses with durations between 150 fs and 35 ps was possible by changing the position of a retro-reflector mirror within the pulse compressor. This has the effect of changing the distance between gratings shown in figure 3.2. The upper limit of ~35 ps was due to physical space constraints within the *Spitfire* enclosure, since the retro mirror could not be placed outside the walls of the enclosure or beyond the mounting rail. On the second laser system, due to a different physical layout of the components the upper pulse length limit using this technique was ~80 ps, and the uncompressed pulse duration was ~130 ps.

The *Merlin LCX* and *Evolution X* lasers are Q-switched, intra-cavity frequency-doubled Nd:YLF (neodymium-doped yttrium lithium fluoride or Nd:$LiYF_4$) lasers. These produced

linearly-polarized 527 nm wavelength pulses with ~3–4 W or ~5–6 W of average power to pump the Ti:sapphire crystals within the *Spitfire* systems. Although these could be operated at various repetition rates, a rate of 1 kHz was chosen for the work presented in this thesis. This repetition rate determines the repetition rate of the *Spitfire* systems, since one pump pulse is used per regeneratively amplified *Tsunami* pulse. The SDG (synchronization and delay generator) box, which controls the timings of the Pockels cells, allows a reduction of the *Spitfire* repetition rate by keeping all Pockels cells off for a chosen fraction of *Merlin/Evolution* pulses. However this function was rarely used, due to concerns of how issues such as thermal loading would affect pulse characteristics. Instead, the *Spitfire* would output at the same rate as the Nd:YLF pump, and a mechanical chopper was used on the *Spitfire* pulses, if needed, to reduce the effective repetition rate. More detail is given in section 3.2. The time scale of material evolution is much shorter than the 1 ms interval between pulses at 1 kHz.

The optical parametric amplifier (Spectra-Physics OPA-800, see reference [86]) takes input pulses from the second *Spitfire* system. Signal and idler beams centered at wavelengths of ~1280–1300 nm and ~2070–2100 nm respectively are emitted. The OPA beams are tunable, from approximately 1100–1600 nm for the signal and 1600–2600 nm for the idler, however the ~1300 and ~2100 nm wavelengths provided the highest pulse energy for this system. Parametric down conversion occurs in a type II angle-tuned beta barium borate (BBO) crystal used as the nonlinear gain medium in the OPA [86]. A white light seed pulse is generated by focussing a small amount (~1%) of the input pulse energy into a sapphire window. About 15% of the light from the input pulse is used as a pump in the BBO crystal, where the seed light collinear with the pump light generates signal and idler wavelengths. The signal and residual pump light are dumped, and the idler makes a second pass through the crystal in a 'power amplifier' stage pumped by the remaining input pulse energy. Signal and idler are produced in this step. The signal is of opposite polarization to the pump and idler, and the wavelengths are separated using polarization optics and dielectric mirrors.

3.2 Machining system

A schematic representation of the optical components after the *Spitfire* and OPA outputs is shown in figure 3.4. Mirrors M4 and M5 are silver mirrors, while the other mirrors are dielectric mirrors. When using the first laser system (*Spitfire LCX* output), three additional dielectric mirrors were used at approximately 45° incidence to direct the beam onto M1. Where these beams ran near the edges of the optical table or for long distances, they were

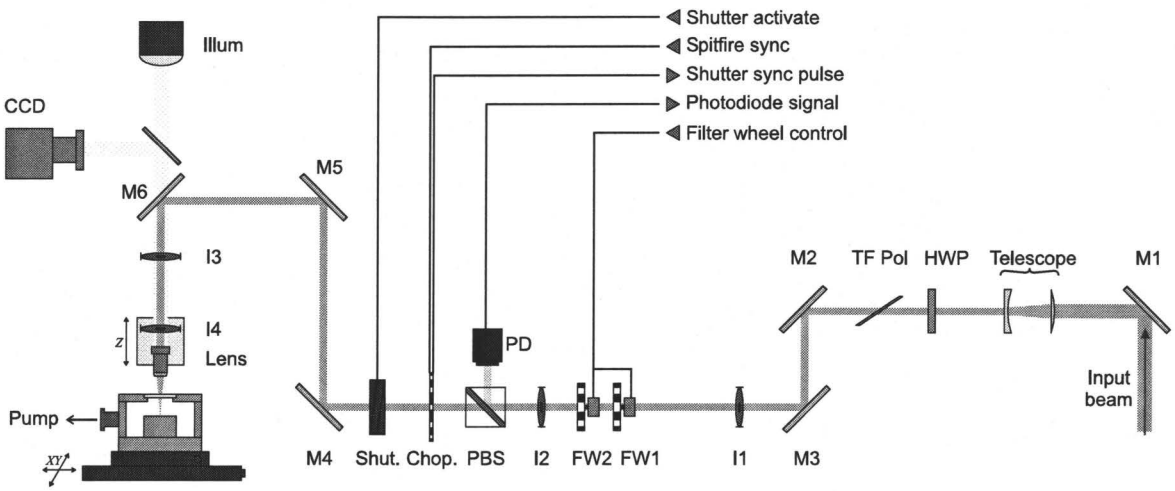

Figure 3.4: Schematic diagram of the optical components after the laser output. Components are not drawn to scale. Key: M: Mirror; HWP: zero-order half-wave plate; TF Pol: Thin-film polarizer for ultrashort pulses centered at 800 nm wavelength; I: Alignment iris; FW: Filter wheel containing neutral density (ND) filters; PBS: Pellicle beam splitter (uncoated); PD: Silicon photodiode; Chop.: Mechanical chopper; Shut.: Mechanical shutter; Illum: Incandescent or LED illumination source; CCD: CCD video camera.

enclosed in one-inch-diameter beam tubes to improve beam stability. Additionally, for later experiments using the *LCX* system, mirror M1 was replaced with an ultrafast beam splitter which reflected approximately 20% of the beam. In part, this was to reduce the possibility of overly intense pulses reaching the target which could generate significant amounts of x-rays. Reducing the pulse energy here also reduced that possibility that undesirable pulse distortions would occur in downstream optical components due to nonlinear effects. When using the second *Spitfire* system, four or more dielectric or gold mirrors were used to route the beam onto M1, or M1 was removed.

When pulses from the optical parametric amplifier (OPA) were being used, M1 was removed and a combination of dielectric mirrors (reflective at the OPA wavelengths) and gold mirrors was used to route the beam into the setup shown in figure 3.4. The half-wave plate and thin film polarizer were not used. For OPA wavelengths, mirror M6 and one or both of M3 and M2 were replaced with dielectric mirrors appropriate for those wavelengths.

When irradiation with 400 nm wavelength pulses was desired, a BBO crystal was placed between the thin film polarizer and M2. The crystal generates light polarized perpendicular to the incident longer-wavelength light. In some cases, the polarization of the 400 nm wavelength light was made to be the same as the usual polarization of the 800 nm wave-

length light. This was done either by placing a half wave plate for 400 nm immediately after the BBO, or by placing a half wave plate for 800 nm immediately before the BBO crystal. Mirrors M2, M3, and M6 were replaced by dielectric mirrors for 400 nm wavelength light. This also served to remove residual 800 nm light from the beam, as it was not strongly reflected by those mirrors. The very strong attenuation of $\lambda = 800$ nm light was confirmed by removing the BBO followed by using the power meter at a sensitive setting after the 400 nm mirrors.

The telescope consisted of a positive and negative lens, to reduce the diameter of the beam from approximately 10 mm to approximately 4 mm. This is primarily so that the beam would pass through the thin film polarizer and other downstream optics without being clipped spatially at the edges. The zero-order half-wave plate in a rotation mount, and ultrafast laser thin film polarizer (Newport 11B00UP.26) allowed continuous variation of laser power to points downstream. In later experiments, an additional ultrafast thin film polarizer was placed immediately before the half-wave plate to help ensure the polarization was linear with minimal pre- and post-pulses of perpendicular polarization. In cases where extremely low pulse energies were desired, some attenuation was achieved by using additional neutral density filters and beam splitters, rather than trying to achieve near-total attenuation with the waveplate and polarizer alone. Total attenuation with the waveplate and polarizer requires very tight tolerances for the components and their alignment, and in the purity of the pulse polarization.

The two filter wheels are each mounted on a motor and controlled via an RS-232 interface (designed and built by A. Shiner). Each wheel has six positions. The wheels hold metallic neutral density filters (New Focus, set 5249). The transmission of a filter is $10^{-\mathrm{OD}}$, where the OD of consecutive filters is summed. The first wheel has an empty position, and filters with optical densities of 0.5, 1.0, 1.5, 2.0, and 2.5. The second wheel contains an empty position, a beam block, and filters with optical densities of 0.1, 0.2, 0.3, and 0.4. The combination allows net attenuations from OD of 0.0 to 2.9, in increments of 0.1.

The pellicle beam splitter (ThorLabs, BP108) consists of an uncoated 2 μm thick nitrocellulose membrane which has an approximate splitting ratio of 8:92. The weak reflected beam is directed toward a high speed silicon photodiode (ThorLabs DET210) behind a flashed opal diffuser. The photodiode has a rise time of approximately 1 ns. It is connected to a boxcar integrator (Stanford Research Systems, SR250) which is triggered by the SDG box for each laser pulse. The boxcar integrator outputs the average signal within a gate period, which is chosen and synchronized using the boxcar front panel controls and observing the gate and photodiode signal on a two-channel oscilloscope. Provided the photodiode is

not saturating, the voltage output is proportional to the pulse energy. This voltage was logged by the data acquisition computer. In early experiments, the pellicle beam splitter was not present, and instead the photodiode collected scattered light off the shutter when it was closed.

A motorized 'spinning' zero-order half-wave plate was sometimes placed between the pellicle beam splitter and the chopper. This wave plate was mounted on a hollow shaft, which allowed the beam to travel along the axis of rotation within the motor, and pass through the wave plate. The waveplate was spun at a relatively high speed (roughly 20-30 degrees per millisecond), so that each pulse passing through the waveplate had its polarization rotated relative to the pulse which preceded it. This 'scrambled' the polarization, reducing the effect of laser polarization on sites requiring many pulses. This technique was utilized primarily for the drilling of deep holes in copper, and was not used in the study of ripples or grooves on silicon.

The mechanical chopper (ThorLabs MC1000, with 10-slot blade) was sometimes used to reduce the repetition rate of pulses reaching the sample. Nine of the ten slots are blocked with a thin metal sheet glued to the blade. The mechanical shutter cannot open and close rapidly enough to let pass a single pulse from the 1 kHz stream of pulses from the *Spitfire*. However, the mechanical chopper, when synchronized properly, blocks 19 out of every 20 consecutive pulses. The resulting 50 Hz repetition rate is low enough for single pulses to be selected by the shutter.

The chopper controller takes as input the trigger signal from the *Spitfire* SDG box, locking the spin speed to the repetition rate of the laser. A phase-adjust trimpot allows the opening in the blade to be shifted in time slightly, so that the blade opening does not clip the pulses. An LED and photodiode are mounted adjacent to the blade, to detect the time that the blade opening passes. This signal is delivered to the data acquisition computer. To allow a single pulse to pass through the shutter, the following sequence occurs:

- The user clicks a button in the software to request a single pulse, or the system is ready for a single pulse as part of a predefined pattern.
- The data acquisition board (National Instruments PCI-6024E) inside the computer is triggered by the detection of the blade gap from the LED and photodiode combination (i.e. a voltage transition from the photodiode).
- The data acquisition board waits for a specific period of time. This time was calibrated as the time for the opening in the blade to return to the beam location, and pass

that location. The data acquisition delay is very precise, using a 100 kHz timebase within the data acquisition board.

- The data acquisition board, which normally outputs a 0 V signal to the shutter controller, outputs a +5 V signal for the desired shutter-open time. For a single pulse, this is 20 ms, corresponding to the period of the 50 Hz repetition rate. The shutter takes ~3–4 ms to open, during which time the laser pulses are blocked by the chopper blade and thin metal sheet.

- The opening in the chopper blade passes through the beam location, allowing a single pulse through.

- When the shutter-open time is finished, a 0 V signal is returned to the shutter. The shutter closes in ~3–4 ms, and is closed by the time the chopper blade opening reaches the beam position again.

This process maintains synchronization with the laser, since the chopper controller keeps the blade synchronized to the laser (via the SDG box), and the shutter is synchronized to the chopper blade via the LED and photodiode. The fact that the pulses are not being clipped by the chopper blade is confirmed using a CCD beam profiler after the chopper. The fact that only a single pulse is being let through the system is confirmed by a temporary photodiode (connected to an oscilloscope) placed in the beam after the shutter. The shutter (UNIBLITZ, Vincent Associates VS25S2S1, controller VMM-D1) possesses two actuated blades, driven by the controller. The controller opens the blades as long as a +5 V signal is applied to the controller.

At various points in this research, different beam focussing elements were used to focus the beam on the sample. The most frequently used elements were a 5× microscope objective (Newport M-5x) and a 15 cm focal length plano-convex BK7 singlet lens (Newport KPX100). Plano-convex lenses were mounted such that the pulse entered the curved side, to reduce spherical aberration. The focussing element was mounted on a precise motorized translation stage (Newport MFN25PP) connected to a translation stage controller (Newport ESP300) under GPIB control (National Instruments PCI-GPIB). A small vacuum chamber was mounted on an *xy* translation stage (two Newport UTM100PP.1 stages) connected to the ESP300. The *xy* stage was capable of a minimum step size of 0.1 μm, but was typically moved in increments of one micrometre or more.

The machining chamber could be evacuated to a rough vacuum of less than approximately 100 mTorr using a roughing pump (BOC Edwards 8). For later research a Pirani

vacuum gauge (Kurt J. Lesker model KJL912001 with KJL2000D display) was attached to the side of the vacuum chamber, while for earlier research (before 2006) a thermocouple gauge (Varian Model 531 with 801 display) was used. A 1 mm-thick fused silica window (1-inch diameter) was used for most experiments. The walls of the chamber were aluminum (for earlier work) or stainless steel. The sample was typically placed on an aluminum cylinder or disk within the chamber.

Various measures were taken to protect the operator and others from x-rays which can be produced by the interaction of sufficiently intense laser pulses on a target (see, e.g. references [87, 88]). The steel walls and lid of the machining chamber were ~1/4-inch thick, to provide attenuation of emitted x-rays. A transparent acrylic-based shield effective to around 50 keV was mountable at the edge of the optical table between the sample chamber and the operator who typically stands at the computer. A short ~3 mm thick C-shaped x-ray shield, fabricated by cutting a short length of copper or iron pipe along its length and forcing the sides of the cut apart, could be placed on the machining lid with the window in the center. This allowed the chamber to move without the shield hitting the focussing elements or intercepting the beam. Iron sheets, painted with matte black paint to reduce the potential for scattered laser light, were later mounted above, behind, and to the side of the machining back-panel. The usual 1 mm thick fused silica window could be replaced with 2 mm or 3 mm windows to provide additional attenuation. The expected attenuation (as a function of x-ray energy) was calculated by $\exp((\mu/\rho)\rho x)$, using the density ρ, tables of μ/ρ, and the thickness x of the material. In early experiments, x-ray measurements were made with a hand-held Bicron x-ray monitor. For later experiments, an Eberline RO-20 ion chamber was used to check for evidence of x-ray penetration through the shielding during experimental runs.

A silicon photodiode-based laser power meter (Ophir Optronics NOVA display and PD300-3W head) with RS-232 interface was used to measure the average laser power. During alignment and calibration, it would be placed immediately after the focussing optic and fused silica window, to measure the power after any losses from those components. A computer program was able to log the power and boxcar integrator output voltage for a predefined period of time (often a couple minutes) to look for instability in the laser power. Short-term instability, if present, could often be observed visually on the oscilloscope trace showing the non-averaged photodiode output from the boxcar integrator. The computer program could also record the average power and boxcar voltage for each position of the filter wheel.

During alignment, a CCD-based beam profiler (Ophir Beamstar) could be placed below the position of the focussing optic. This could confirm that the beam passes through the centers of the alignment irises, and was not being clipped by some component. It allowed the confirmation that the beam spatial profile was acceptable.

An Ocean Optics PC2000 spectrometer was used routinely to verify that the spectrum of the *Tsunami* possessed sufficient bandwidth (full-width half-maximum of roughly 10 nm or more for a ~150 fs pulse) and was free of significant anomalies. The *Spitfire* spectrum was observed with the same spectrometer. While the *Tsunami* spectrum was usually measured immediately at the laser output, the spectra of the *Tsunami* and *Spitfire* were sometimes taken after the focussing optic to check that the spectrum was still appropriate. An Ocean Optics USB2000 spectrometer was sometimes used, particularly for taking the spectra of the *Tsunami* and *Spitfire* in the second laser system near its outputs. Both Ocean Optics spectrometers employ a fixed grating and a one-dimensional CCD sensor. To measure the spectra of the OPA pulses, a Sciencetech 9050 monochromator with moving grating under computer control was employed with a photodiode appropriate for the wavelength being examined.

3.3 Pulse analysis tools

Photodiodes cannot be used to directly measure the duration of femtosecond laser pulses, since the photodiode response time is much longer than the pulse itself. However, short distances can be measured relatively easily. Most ultrashort pulse measurement techniques rely on interfering a pulse with a temporally delayed copy of itself, created with a beam splitter or other techniques. An autocorrelator, shown schematically in figure 3.5, was frequently used to measure the duration of the pulses used in this work. A gold mirror could be placed between M2 and M3 (see figure 3.4) to divert the beam into the autocorrelator. An ultrafast beam splitter reflects some of the pulse, and a movable retro-reflector causes the reflected pulse to travel a different path length than the transmitted pulse. Each retro-reflector consisted of two square gold mirrors positioned at 90° with respect to each other. The pulses are recombined via a lens at a small angle in a KDP crystal. The light generated in the crystal is recorded by a silicon photodiode as a function of the delay distance. To acquire the autocorrelation data, the photodiode would be connected to the boxcar integrator input, and one of the roof mirrors on a motorized translation stage (Newport UTM100CC1HL) would move under control of the ESP300 controller. The computer would record the photodiode data, and calculate a pulse duration from the resulting trace.

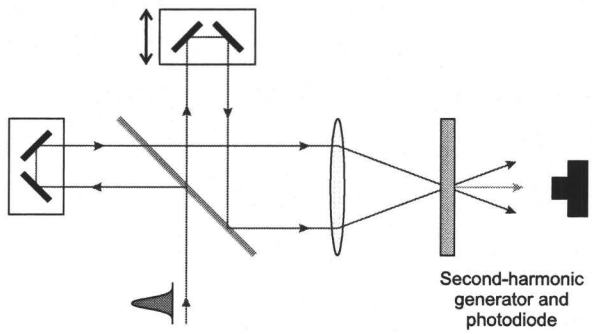

Figure 3.5: Schematic diagram of a non-collinear autocorrelator.

The trace is actually a convolution of the two temporal pulse shapes, and is therefore longer than the actual pulse length. A deconvolution factor, dependent on the pulse shape, is used to convert the trace width to a pulse duration. An assumption must be made about the pulse shape, in order to calculate the duration. Two frequently used shapes are a Gaussian shape, or a sech^2 shape. In this work, a Gaussian was assumed.

A variation of the configuration shown in figure 3.5 is to have the two exit beams collinear along the same axis. The autocorrelator is configured as a Michelson interferometer in this way, and the photodiode records the interference pattern as one of the arms is translated. As an alternative to the second harmonic generator crystal, a photodiode or other device may be used as the nonlinear detector. This detector should not respond to photons at the laser wavelength, but give an output proportional to the square of the intensity incident on it. This was the technique used to determine pulse durations of OPA wavelengths, using a silicon or InGaAs photodiode. For the 800 nm wavelength, a GaP photodiode was occasionally used. A 'solar-blind' UV phototube (Hamamatsu R6800U-26) with a diamond photocathode was used as a nonlinear detector in autocorrelations of $\lambda = 400$ nm pulses. With careful positioning and after greatly attenuating the beam, the output of a Michelson interferometer could be focussed onto a detector to directly measure the pulse duration at the focus.

The autocorrelator/interferometer technique above moves the stage between each incident pulse and records a data point for each pulse, building the trace from a sequence of pulses. A 'single-shot' (single-pulse) autocorrelator may be built, schematically shown in figure 3.6. In this case, two replicas of the pulse are made to cross in a nonlinear crystal. The intensity along a line perpendicular to the output is the autocorrelation. A CCD camera

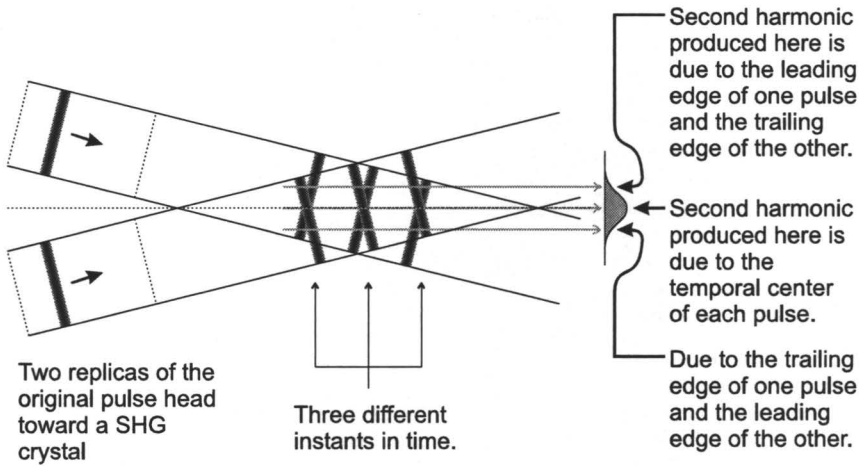

Figure 3.6: Schematic diagram of a single-shot autocorrelator.

may be placed at the output, and with calibration, the width of the trace on the camera is proportional to the duration of the pulse.

A further refinement of the single-shot autocorrelator is shown in figure 3.7. The system is named 'GRENOUILLE' [89] (GRating-Eliminated No-nonsense Observation of Ultrafast Incident Laser Light E-fields), and is a variation of the FROG (Frequency-Resolved Optical Gating) technique. Along one axis a Fresnel bi-prism splits the two (spatial) sides of the beam, and overlaps them. This produces a single-shot autocorrelation similar to that shown in figure 3.6. Along the other axis the spectrum at each point in time is produced. For a thick crystal, at each light propagation direction the phase-matching condition will produce substantial second harmonic radiation for a specific wavelength, resulting in a second-harmonic spectrum emitted along one axis. The inclusion of the spectrum permits a more complete characterization of the pulse. The GRENOUILLE also provides information on various spatio-temporal distortions of the pulse such as tilt in the laser pulse front or a spatial (wavelength) chirp across the pulse front. A tilted pulse-front autocorrelator [90] was also used to detect and minimize pulse-front tilt. This operates similarly to the single-shot autocorrelator shown in figure 3.6, except that after the initial pulse has been split one of the replicas is inverted using a third mirror. A pulse and its inverted replica then cross inside the nonlinear crystal, and a shear of the output light is related to the amount of pulse-front tilt. Two commercial devices ('TFP Autocorrelator' or TFPA by Light Conversion Ltd., and a GRENOUILLE device (UPM-8-20) from Swamp Optics LLC) were used in the later stages of the research presented in this thesis, to examine and minimize

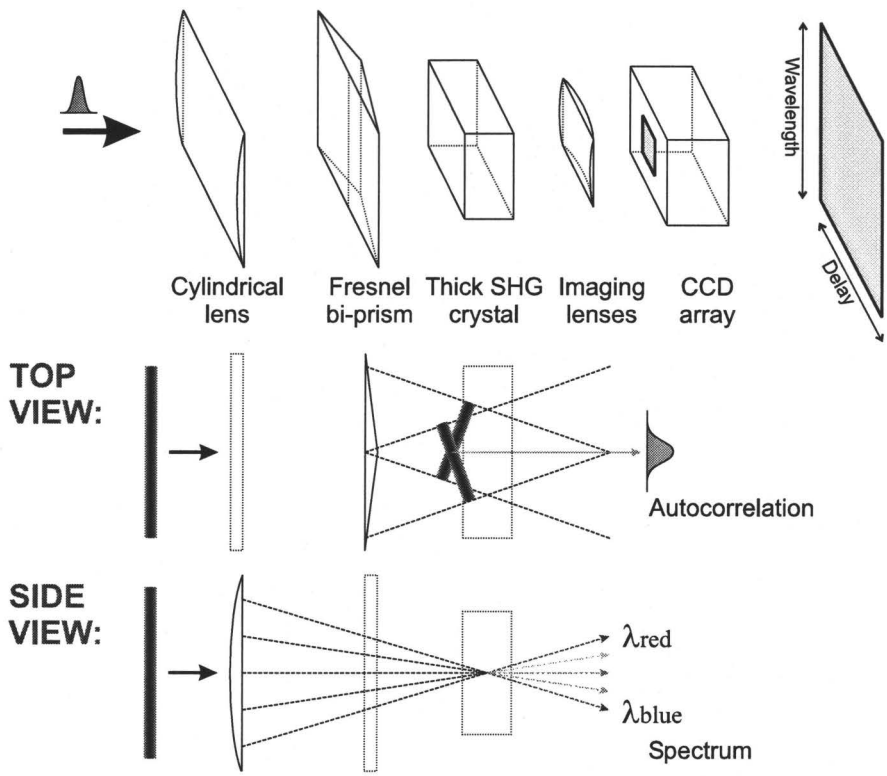

Figure 3.7: Schematic diagram of a GRENOUILLE, adapted from reference [89].

spatio-temporal distortions. It is important to minimize pulse-front tilt and spatial chirp, as they can affect the pulse duration at the focus and affect the size of the focussed spot (see, e.g. reference [91]). Although spatio-temporal distortions can be produced in various ways, one origin of pulse-front tilt in regeneratively amplified femtosecond laser systems is a misalignment of the gratings and mirrors in the pulse stretcher and compressor. However, if these components are properly aligned, it is unlikely that the pulses will have substantial pulse front tilt.

For pulse durations of several tens of picoseconds or longer, a New Focus 1454-50 fast photodiode with a manufacturer-quoted rise time of 18.5 ps was used with a Tektronix CSA 803 communications signal analyzer. This photodiode was also used to confirm the calibration of the autocorrelator. Additionally, different second harmonic generation crystals (including 50 and 150 μm thick BBO) were used in the autocorrelator to confirm the autocorrelation results. A 1 ns risetime reverse-biased photodiode and a 400 MHz oscilloscope were used to measure the 7 ns pulse duration. At one point, photodiode results were confirmed using a streak camera on loan from Hamamatsu.

3.4 Sample analysis tools

An optical (light) microscope (Zeiss Axioplan 2) in reflected-light mode was used for observation and measurement of many of the features in this work. The 50× and 100× objectives with an additional 2.5× magnification lens were most frequently used. The microscope includes a CCD camera connected to a computer, for recording images. A glass calibration slide with a 10 μm ruling period was available, and was used with the image acquisition software (Northern Eclipse) to calibrate the number of pixels per micrometre on the saved images. This allows the measurement of various spatial features on the irradiated sites, such as the site diameter and the space between periodic features. The calibration process first required acquiring an image of the calibration slide with the desired objective and lens. In the software a line could be drawn on the image from one calibration ruling to the next. The number of pixels between the start and end of the line was then defined to be 10 μm. When choosing the predefined calibrations stored in the computer, I would check the calibration by taking an image of the calibration slide in the same mode used for imaging of the target (usually Nomarski DIC mode), and verifying that the reported distance between two rulings was 10 μm.

Compared to standard brightfield optical microscopy, the Nomarski differential interference contrast mode [92] makes more visually prominent small changes in sample height, and gives enhanced visibility of edges. This was particularly important in the case of fine ripple structures, which were rather shallow. Amorphization and shallow features were difficult to observe under scanning electron microscopy but were more visible under optical microscopy. As discussed further in section 5.3.2, different modes of optical microscopy were sometimes compared to measurements of the same target with other techniques, to check for possible imaging artifacts and scale calibration errors.

Scanning electron microscopy (SEM, Philips model SEM515) with image acquisition software (UltraRapid Spectral Analyzer or 'URSA' by Mektek) was used extensively for imaging features showing high aspect ratios, such as after the cutting of grooves, drilling of holes greater than a few micrometres in depth, and coarse structures. Compared to optical microscopy, SEM has a much greater depth of field. This allowed good imaging of structures with significant depth modulations. The secondary electron imaging mode was used for the images presented in this thesis. A calibration specimen was available consisting of a grid with lines 9.87 μm apart. This was occasionally imaged, to confirm that the magnifications reported by the SEM were correct. An uncertainty of approximately 5% was determined via comparisons to the calibration specimen. A sample holder was made which could clamp the sample, enabling its easy removal after SEM analysis. This holder

also allowed holding a sample on end, so that the cleaved surface was upward in the SEM, enabling easy viewing of a groove cross-section. This sample holder is described in more detail in section 4.3.1. Under scanning electron microscopy, for samples of poor electrical conductivity a 'charging' phenomena exists in which electrons do not drain quickly enough from the sample, and cause a distortion of the beam incident on the sample. A electron-beam sputterer metallization chamber was available, to deposit a very thin gold layer on the sample before SEM analysis. This was done for some examinations of grooves, but infrequently for other samples.

The SEM included an EDXS (energy dispersive x-ray spectroscopy) analysis mode (Link Analytical 'PentaFET'), with data acquisition using the URSA software. The electron beam incident on the sample causes some atoms at that location to emit x-rays with a spectrum characteristic of that atomic species. An x-ray detector (lithium-drifted silicon) recorded the energies of these x-rays. It was used, for example, to confirm the chemical composition of the samples (in case materials had been accidentally switched), and to determine if a gold or thermally-grown oxide layer had been removed within a site. For the calibration of x-ray energies in EDXS, the technician used a sample containing a variety of materials to ensure the reported x-ray energies were correct. This could also be used to calibrate quantitative EDXS, however percent compositions of the target materials were not necessary in this research.

The atomic force microscope (AFM) used in this work (Veeco Instruments, Nanoscope IIIa) allowed the determination of the depths of shallow features. An Olympus AC160TS AFM tip was used, with a quoted tip radius of less than 10 nm. Along the axis of symmetry (along the cantilever), the tip is quoted as having an angle of around 18° relative to the normal to the cantilever. In the geometry generally used in the AFM, this sets a limiting angle along the vertical axis of the image, meaning that it should not be possible to correctly image any feature with an angle of more than roughly 72° relative to the substrate normal. Along the other axis (in the direction usually used as the fast scan axis, along horizontal scanlines), the tip is not symmetric. In the direction in which the tip is moving during data acquisition (the 'trace' direction), the angle is 25°, while in the opposite (or 'retrace') direction the tip angle is 10°. This results in sample angle limitations of approximately 65° and 80° respectively. The maximum range of heights measurable with this system was a few micrometres, and thus the AFM was not used on deep holes or coarse structures. The AFM was used primarily in the experiments measuring certain periodic surface structures, whose heights were typically less than half a micrometre. The software allowed measure-

ment of surface distances and heights, and also provided a measure of the spatial frequency of periodic structures via Fourier analysis.

A focussed ion beam milling technique was used to prepare thin cross-sectional samples for transmission electron microscopy (TEM) analysis. The majority of these were prepared by Fibics, Incorporated, in Ottawa, Canada, while a few were prepared by Junji Yamanaka at the University of Yamanashi in Japan. These samples allowed the observation of crystallographic changes below the surface of laser-irradiated material. A small amount of the TEM operation was done by myself using a Philips CM12 microscope at McMaster, but the majority of the TEM work was done by Junji Yamanaka and Christian Maunders. The microscopes were a Philips CM12 operating at 120 kV for obtaining bright-field images and diffraction patterns, Hitachi HD-2300C for HAADF (high-angle annular dark-field) at 200 kV, and JEOL 2010F equipped with Gatan imaging filter (GIF) for HREM (high-resolution electron microscopy) and EDXS analysis. The specific details of the TEM technique and the person who did the imaging are given in the thesis sections where the corresponding results are presented.

3.5 Spot size determination

The diameter D of a laser-induced damage region is related to the spot size $\omega_\circ$ (spatial radius at $1/e^2$ of peak intensity), the pulse energy E, and the threshold energy E_{th} by

$$D^2 = 2\omega_\circ^2 \ln\left(\frac{E}{E_{th}}\right) \tag{3.1}$$

(see reference [39]). This equation was derived from analogous equations for a $1/e$ radius from reference [93]. The peak fluence $\phi_\circ$ (fluence at the center of a Gaussian spatial profile, with units typically given as J/cm^2 or mJ/cm^2) in terms of pulse energy E is

$$\phi_\circ = \frac{2E}{\pi\omega_\circ^2}\,. \tag{3.2}$$

According to equation 3.1, a plot of D^2 versus the natural logarithm of the pulse energy E should be a straight line. Curve fitting algorithms can be used with equation 3.1 to calculate the spot size and threshold energy.

Figure 3.8 shows the squared diameter D^2 as a function of pulse energy E, for a certain single-pulse run using a $5\times$ microscope objective. Prior to the experiment, the laser power (from the power meter head immediately below the focussing element) and corresponding

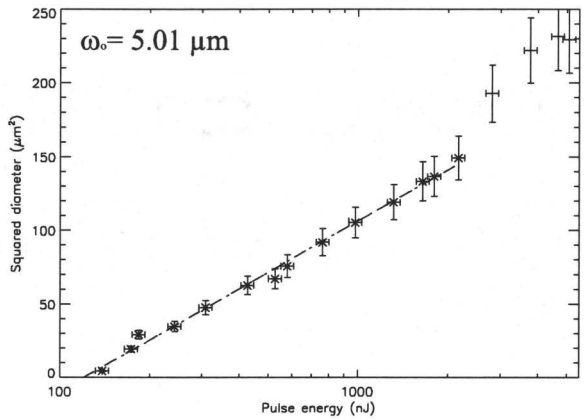

Figure 3.8: Graph showing the squared diameter of sites in a typical single-pulse run, as a function of pulse energy.

boxcar integrator voltage were logged by the computer, for each filter wheel setting. In a typical single-shot run, the following steps occurred:

- Using the synchronized shutter and chopper, a single laser pulse was allowed to pass through the focussing element onto the sample.
- The computer recorded the boxcar integrator voltage, corresponding to the pulse energy.
- The neutral density filter wheel position was advanced, to increase the optical density by 0.1.
- The computer commanded the translation stage to move to the next site.
- This process was repeated for the specified number of sites.

Runs similar to this were performed on most samples, and site diameters from multiple runs were measured on each sample. The mean spot size from multiple runs was used to determine the peak fluence for each pulse energy via equation 3.2. A linear least-squares curve fitting algorithm which considers uncertainties in both the x and y values was employed. The results were also compared to those from multiple linear regression and non-linear least-squares fit algorithms. Further details on the curve fitting algorithms are given in section 4.3.3. All fluences reported in this thesis are incident fluences, not considering the reflectivity of the target surface.

The spot size varied slightly from sample to sample, due to uncertainty in the precise location of the focal point. Additionally, changes in the laser system over a period of several months could affect the unfocussed beam radius and divergence slightly, thus affecting the focussed spot size. To ensure the sample surface was near the focal point, the following procedure was typically carried out near a corner of a sample during alignment. The laser energy was reduced to a value such that only slight modification occurred on the target while translating the target under the beam. The height of the lens was then adjusted. By iteratively moving the lens and lowering the pulse energy, a lens position and pulse energy could be found such that moving the lens vertically away from this position would cease the production of visible sample modification. In this way, a lens position was set for which it was assured that the sample surface was approximately at the position of tightest laser focus. The CCD camera's focus was then adjusted so that the image on the video monitor was in focus. The translation stages and sample holder held the sample at a constant distance from the focussing element, such that it did not go out of focus as the sample was moved laterally. This could be confirmed by observing that opposite edges of the sample were in focus, as seen on the monitor. This also ensured that the spot size would be the same at all locations on the sample, provided that the sample was flat. The semiconductor wafer surfaces were very flat. Additionally, on some samples multiple D^2 runs were performed separated by large distances, to check that the spot size was similar at different locations on the sample.

The optical microscope, typically in Nomarski mode and using a $50\times$ or $100\times$ objective, was used for measuring the diameters of irradiated sites. To estimate the diameter of a particular site, the computer software provided with the optical microscope was used along with a calibration done at the start of the microscope session. Measurements were made to the outside of any observable material modification, as this was the most readily and repeatable observable feature. A measure along the horizontal axis of the image was made, and a measure along the vertical axis was made. The arithmetic mean ($(D_{\mathrm{H}}+D_{\mathrm{V}})/2$) of the two measurements (D_{H} and D_{V}) was taken to produce the value of D used in the curve fitting. Single-pulse sites generally did not show a great deal of ellipticity, and thus the geometric mean ($\sqrt{D_{\mathrm{H}}D_{\mathrm{V}}}$) did not differ substantially from the arithmetic mean.

It should be noted that the D^2 method makes the assumption that a specific local fluence on the Gaussian beam profile always corresponds to the same physical modification or feature on the target surface. The same physical modification feature must be measured at several irradiation sites formed by several different pulse energies. This assumption breaks down if there is substantial lateral heat or material transport, particularly if the amount of

transport varies with incident pulse energy. In multiple-pulse sites, phenomena such as incubation and the masking of features by debris reduces the reliability of the D^2 method so it was generally not used for multiple-pulse sites. At sufficiently high pulse energies, significant 'splatter' (appearing as ejected droplets) was present at the edges of the sites. This produced poor measurements of the diameter since it was no longer possible to measure the outside of a rim, as the violently ejected material obscured it. Any deviations in the Gaussian beam profile in the wings of the spatial profile would also play a greater role when high energy pulses are used, as the material modification fluence would be within the wings. As in the example shown in figure 3.8, high-energy sites were generally omitted from the fitting. Although there are some potential issues with the D^2 fitting method, alternative methods for focussed spot size determination also suffer from potential problems. A knife-edge could be scanned through the spot while the amount of light not blocked by the edge is measured by a large photodiode below the edge. As an alternative, a CCD beam profiler with sufficiently small pixels could be placed in the beam focus. However, both these techniques risk damaging the knife-edge or CCD with too high a pulse energy, and it is difficult to be certain that the sample would be placed in the same plane as the knife-edge or CCD. This is particularly true in the case of the $5\times$ microscope objective due to its small Rayleigh length. Ultimately, the D^2 method was used due to the fact that it is relatively straightforward to use and does not have the uncertainty of trying to position the sample in the same plane as a separate measurement technique. Experiments with the $5\times$ objective on different materials irradiated under similar conditions (within a few months of each other) produced similar spot sizes, within uncertainty. When comparing irradiation of germanium at $\lambda \approx 1300$nm (where it is opaque) to silicon at the same wavelength (which requires two or more photon absorption), the D^2 fitting yielded similar spot sizes on the two materials. Additionally, different microscopy techniques were confirmed to give similar D^2 values [94].

For most experiments, the sample was typically placed in the machining chamber with one of its cleavage planes parallel to a translation direction of the translation stages. The machining software would make rows of irradiated spots or lines by moving only along one translation stage axis. Under the optical microscope, the sample was positioned so that the horizontal axis of the microscope camera was parallel to one of the grid lines of irradiated features. This ensured that microscope images had the same orientation as the images on the CCD when machining, and allowed each image to be compared directly without having to rotate certain images. Irradiation sites were separated by a predefined distance (usually 50 μm when the $5\times$ objective was used). This also provided a simple check on the calibration of the microscopical techniques. In the SEM or optical microscope, the

distance between sites was frequently measured, to check that it matched that moved by the translation stage (which has a quoted accuracy of less than a micrometre).

Chapter 4

Femtosecond Laser-machined Grooves

4.1 Introduction and motivation

A variety of laser types are used industrially to cut materials [1]. Due to the short duration of ultrashort laser pulses, high peak intensities can be achieved while using low pulse energies, thus minimizing energy input and heating of the target. For femtosecond laser-based machining to be used industrially or as a research tool, it is useful to characterize the depth, width, and morphology of a laser-cut line or groove, as a function of various laser and machining parameters. These parameters include:

- the pulse energy
- the translation speed of the sample under the stationary focus
- the number of consecutive passes of a region under the beam
- the polarization of the incident light (linear, circular, elliptical, or 'spinning' in which a rotating half-wave plate in the beam causes each incident pulse to have a linear polarization in a different direction than for the previous pulse), and the electric field direction relative to the translation direction
- the wavelength of the laser light
- the irradiation atmosphere (air, vacuum, or other chemical compositions)
- the focussed laser beam spot size
- the pulse duration
- the pulse repetition rate.

Some of these parameters may have minimal effect depending on what other parameters are in use. Some additional configurations, such as a non-normal angle of incidence, could also

enable certain applications. The desired outcome, such as the final feature sizes, feature quality, and throughput would affect the choice of parameters. The parameters would also depend on the material properties.

The results from the published journal paper [65] and the conference oral presentation [95] presented in this thesis chapter were my first major research contributions. Much of the experimental approach for these two works was conceived by Andrzej Borowiec, who published results on groove cutting on InP in an earlier paper [64] and in his Ph.D thesis [96]. In particular, the Borowiec work [64] measured and discussed the groove depth and material removal rate as a function of pulse energy, translation speed, and number of passes, and compared the cutting of deep grooves with different polarizations. The software for controlling the machining apparatus for these experiments was also written mainly by A. Borowiec. Some of my experiments on silicon followed the same approach as for InP (measuring depths as a function of various parameters, and comparing the effects of different polarizations) using the same equipment, to provide a direct comparison between silicon and InP. The InP and silicon data were analyzed separately and independently (I did not use the same analysis software as A. Borowiec). However, as a check, on a few occasions the raw data from a silicon experiment was also analyzed by A. Borowiec, and I analyzed InP data using my routines. The differences in results were insignificant.

The results presented in the silicon paper [65] and the conference oral presentation [95] include some types of investigations which were not presented in the InP paper [64], such as examination of the groove wall morphology, uniformity of the groove depth, and the comparison of irradiation with 800 nm and 400 nm light. The results presented in this chapter and in the paper [65] provided a basis from which further machining experiments would begin, such as giving an idea of how much energy is required for certain features to form. It helped determine the set of parameters which provide a desired result, given a particular set of constraints. Such surveying of parameters and results is useful when applying the laser machining technique in other experiments and material configurations, and was valuable as previous systematic and straightforward treatments were lacking.

4.2 Pages from the silicon grooves paper [65]

The pages from the paper on grooves in silicon (Applied Physics A **80**, 1717 (2005), reference [65]) are reproduced on the following pages[1]. The paper outlines some details of the experimental setup and approach used, and presents the results and discussion. Fol-

[1] See appendices C and F for copyright and permission information.

lowing the paper are additional comments on the work presented in the publication, results from the 2003 CLEO conference contribution [95], and further unpublished results.

It should be noted that there are some minor wording issues and technical inconsistencies (such as ϕ and φ being used interchangeably) in the published article [65]. In the typesetting and proofing process a second proof was generated due to issues in the first proof, and errors occurred in the subsequent proof correction. However, these issues do not affect the scientific results presented in the paper. Additionally, for a period of time this paper was available online with very low-resolution images, greatly obscuring the details. The subsequent online version (presented here) does not have this resolution issue.

Appl. Phys. A 80, 1717–1724 (2005)
DOI: 10.1007/s00339-004-2941-2

Applied Physics A
Materials Science & Processing

T.H.R. CRAWFORD[1,✉]
A. BOROWIEC[1]
H.K. HAUGEN[1,2]

Femtosecond laser micromachining of grooves in silicon with 800 nm pulses

[1] Department of Engineering Physics, McMaster University, Hamilton, Ontario, Canada, L8S 4L7
[2] Also with the Department of Physics and Astronomy, the Brockhouse Institute for Materials Research, and the Centre for Electrophotonic Materials and Devices; McMaster University

Received: 28 October 2003 / Accepted: 18 May 2004
Published online: 31 August 2004 •

ABSTRACT Femtosecond laser micromachining of grooves in silicon is investigated using 150 fs pulses with a center wavelength of 800 nm. Ablation rates are investigated as a function of pulse energy, translation speed, and the number of consecutive passes. The effect of the laser polarization relative to the translation direction is observed, and the morphologies of the groove walls are examined. In addition, the uniformity of the groove depth is investigated as a function of the number of passes of the sample under the beam.

PACS 42.62.Cf; 79.20.Ds; 81.20.Wk

1 Introduction

Laser-based machining of materials with femtosecond light pulses has attracted considerable attention in recent years [1]. The reduction of the temporal width of pulses from the nanosecond to the femtosecond regime limits the thermal diffusion into the surrounding material during ablation and increases the quality of the machined surface [2]. With many 'user-friendly' integrated ultrafast systems recently coming onto the market, material processing with femtosecond laser pulses is becoming increasingly common in industrial applications.

Several studies have been conducted on the ablation thresholds, dynamics, and morphologies of metals [3–6], dielectrics [7–9], and semiconductors [10, 11] processed with single and multiple femtosecond laser pulses. Linear features ('grooves' or 'trenches') in silicon and tunnels in silicon under SiO_2 films have been fabricated using argon-ion lasers in a Cl_2 atmosphere [12–15]. However, relatively few systematic studies have been performed on the fabrication of linear features in semiconductors with femtosecond laser pulses (see e.g., [16–19]). Laser machining presents a variety of parameters which may be adjusted, making possible a wide range of surface structures. Knowledge of the dependence of groove depth and morphology on laser cutting parameters can lead to further manufacturing applications and techniques. In this work, we have not tried to find optimal parameters for a particular application. Instead we have performed a systematic investigation with simple, well-defined parameters.

✉ Fax: 905-527-8409, E-mail: crawftr@mcmaster.ca

2 Experimental details

The experimental approach has already been described in a separate paper concerning studies of grooves in indium phosphide [19] but is briefly outlined here. A commercial amplified Ti:sapphire laser system (Spectra-Physics Spitfire LCX) produced linearly polarized ~ 150 fs pulses with a peak wavelength at 800 nm and at a repetition rate of 1 kHz. The laser beam was focussed onto the sample by a 5× microscope objective. The spot size ω_o (spatial radius at $1/e^2$ of peak intensity) on each sample was determined by measuring the diameters of single-pulse craters as a function of pulse energy, then by fitting the data to the appropriate equations as described previously [19]. As in reference [19], the diameters were measured to the outside of the crater rim, since this was the most readily and consistently observable feature. Measurements to other locations might lead to a somewhat different spot size. Due to the small spot sizes used (5–6 μm), the total uncertainties in the spot size and pulse energy measurements cause an uncertainty in the fluence calculation of approximately ±30%.

Silicon samples ((100)-oriented, phosphorus-doped with a resistivity of 2–6 Ω-cm) were placed inside a small vacuum chamber equipped with a 1 mm thick fused silica window. The chamber was mounted on a computer-controlled xy translation stage and was evacuated to a rough vacuum of ~ 0.1 mbar. Unless otherwise specified, the laser polarization was chosen to be perpendicular to the translation direction. After machining, the sample was cleaved perpendicular to the grooves near the middle of the grooves. The sample was then analyzed using scanning electron microscopy (SEM).

The depth d of an ablation crater produced by pulses of peak fluence φ_o is often described by the relation [1, 5, 10]

$$d = d_o \ln\left(\frac{\varphi_o}{\Phi_{th}}\right). \quad (1)$$

We will adopt this equation as a framework for data analysis in the machining of grooves, with the parameters d_o and

Φ_{th} determined by curve fitting. The value Φ_{th} can be interpreted as a generalized ablation threshold fluence whose value depends on the particular cutting parameters used. An incubation effect has been observed in various materials including semiconductors [10, 11], which leads to an ablation threshold fluence which is a function of the number of pulses N incident on the sample. For a target moving at a linear speed v with a pulse repetition rate of f, the value of N is not clearly defined. One approach to finding an effective N_{eff} is to determine the 'accumulated' fluence at a point along the center of the groove. This is the sum of the individual fluences of equally spaced points along a Gaussian pulse profile which has a peak fluence of φ_o. The equivalent number of pulses of uniform fluence φ_o required to equal this accumulated fluence can be derived to be

$$N_{eff} = \sqrt{\frac{\pi}{2}} \times \frac{\omega_o f}{v} \tag{2}$$

when we assume the spacing between pulses (v/f) is much less than the spot radius ω_o.

3 Results and discussion

3.1 *Depth vs. energy*

In order to determine the effect of laser pulse energy on the depth and morphology of a micromachined groove, a set of grooves was cut using a single pass of the translation stage at each of the pulse energies available using a reflective neutral density filter set. For each energy within this set of grooves, the same translation speed was used. Three sets of grooves were cut: one set each at translation speeds of 100 μm/s, 250 μm/s and 500 μm/s. The depth d and width W of each groove was measured as indicated by the inset diagram of Fig. 1.

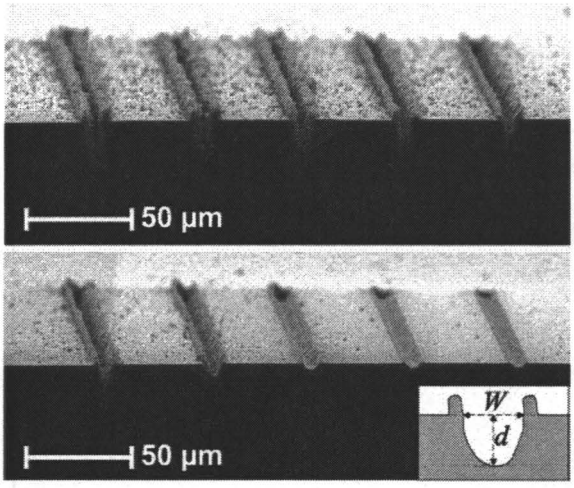

FIGURE 1 SEM images of a series of grooves cut with different pulse energies. One pass for each groove at 250 μm/s was used in this image. The images are taken at an angle of 5° from the normal to the cleaved surface. Single-pulse fluences range from 11 J/cm² to 4.9 J/cm² (*top*) and from 3.9 J/cm² to 1.6 J/cm² (*bottom*). *Inset*: definition of the groove width W and the depth d, as used in this paper

Figure 1 shows a representative series of grooves cut at 250 μm/s at various pulse energies. The depths were measured under SEM, and are plotted in Fig. 2a. The spot size was $\omega_o = 5.3 \pm 0.2$ μm, where the uncertainty is that given solely by the curve fitting algorithm based on estimated SEM and power meter uncertainties of 5% each. An explanation for some of the scatter in the data points in Fig. 2 will be given in Sect. 3.5.

For multiple-pulse ablation of stationary targets, two fluence regimes are often observed [4, 5, 16, 19, 20], with a third regime occurring at very high fluences [16]. The regimes are characterized by different per-pulse material removal rates and ablation thresholds. For metals, Nolte et al. [5] associated

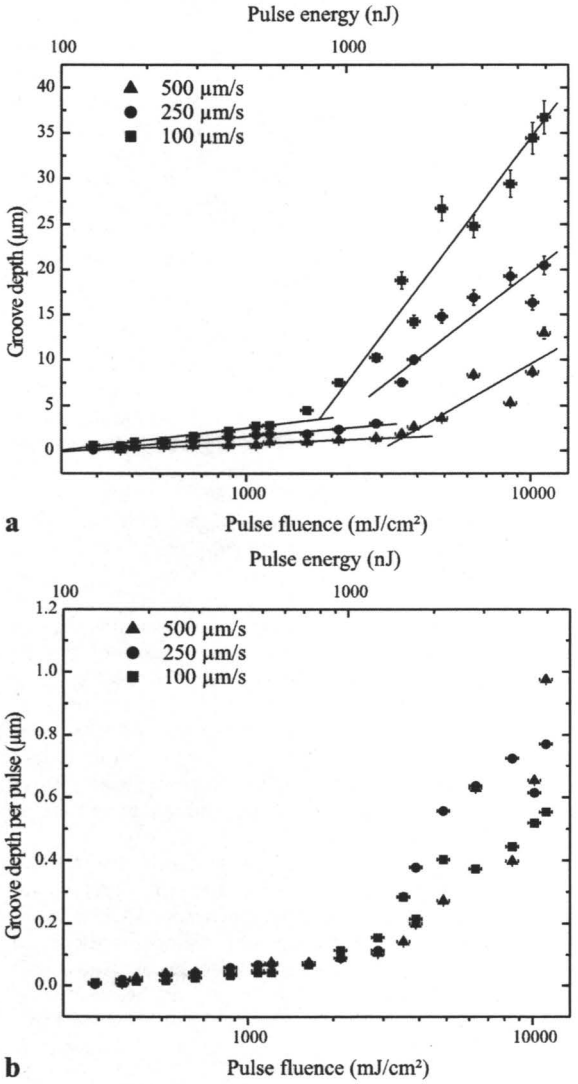

FIGURE 2 **a** Depth vs. energy plot for translation speeds of 100 μm/s, 250 μm/s, and 500 μm/s. **b** Depth per pulse for translation speeds of 100 μm/s, 250 μm/s, and 500 μm/s. Pulse energy measurements and SEM distance measurements have an uncertainty of 5% each. Horizontal error bars represent uncertainty in pulse energy

Cutting speed (μm/s)	N_{eff}	Low-fluence regime d_o (μm)	Low-fluence regime Φ_{th} (mJ/cm^2)	Low-fluence regime d_o/N_{eff} (nm)	High-fluence regime d_o (μm)	High-fluence regime Φ_{th} (mJ/cm^2)	High-fluence regime d_o/N_{eff} (nm)
100	66.5±1.5	1.7±0.1	220±70	25±1	18.1±0.9	1490±730	270±15
250	26.6±0.6	1.2±0.1	250±70	43±2	10.5±0.8	1530±1120	390±30
500	13.3±0.3	0.6±0.1	270±80	43±2	7.8±0.6	2960±2270	590±45

TABLE 1 Depth vs. energy fit parameters and calculated values for single-pass grooves. Note that the values of d_o/N_{eff} are for a fluence $\phi = e \times \Phi_{th}$. Errors in fit parameters are those from the curve-fitting routine based on instrumental uncertainties only, and do not consider errors such as the nonuniformity in the groove depth or laser energy fluctuations

the ablation depth in the low-fluence regime with the optical penetration length, while in the high-fluence regime the ablation depth was associated with the heat diffusion length. In silicon, the penetration depths are the same for *n*- and *p*-doped samples with resistivities of 10–30 Ω-cm [16]. However, the optical penetration depth may be strongly intensity-dependent due to the high intensities of femtosecond laser pulses [11, 16].

In Fig. 2a, the data for each speed was divided into two fluence ranges and a line was fit to each range. The dividing point for the two ranges (and thus the two ablation regimes) was chosen such that it minimized the sum of the chi-squares of the two lines. For each translation speed, (1) was then fit to the data in each regime, and the parameters d_o and Φ_{th} were determined. These are tabulated in Table 1, along with the values of N_{eff} calculated using (2).

The parameter d_o is different for each translation speed since the time spent by the laser spot over a particular area changes. For each speed, it is also expected that the parameter Φ_{th} will change since Φ_{th} is related to N_{eff}, and N_{eff} is related to v by (2). Slower translation speeds allow for more incubation, and thus a lower ablation threshold fluence at lower speeds is predicted. This trend is suggested by the Φ_{th} values in Table 1, although the uncertainties are large enough to prevent the confirmation of this prediction.

Figure 2b shows the same data as Fig. 2a, but with the depths divided by the appropriate N_{eff} for each translation speed. It can be seen that the depth per pulse is not strongly dependent on the translation speed, as the data from each speed lies around the same line in each regime. This can be quantified by calculating d_o/N_{eff} for each translation speed, as shown in Table 1. This value can be interpreted as an ablation depth per pulse when the fluence $\phi = e \times \Phi_{th}$ ($e = 2.718...$). In the low-fluence ablation regime, the values at 250 μm/s and 500 μm/s are the same. The lower value at 100 μm/s is likely due primarily to increased redeposition of debris within the groove, increased energy loss due to the increased groove depth and possibly other effects. These effects are reduced in grooves cut at higher speeds.

While applying (1) directly to a multiple-pulse scenario provides a useful framework for analysis, it neglects several factors which could prove important in a more detailed analysis. Stoichiometric or crystallographic changes in the target would cause changes in d_o for each pulse. Each incident laser pulse changes the geometry of the target, and thus each pulse would have its energy distributed over a different surface area and at different incident angles over much of the wavefront. As a consequence, the effective fluence would change somewhat for each pulse. There is a potentially big difference between single or few pulse irradiation versus many pulse irradiation, whether or not the target is moving. For grooves the ablation depths and rates would not generally be the same as for stationary targets. All fluences reported in this work are those on the original sample surface.

For translated targets, it is reasonable to expect that two regimes would be present since such regimes have been observed for ablation of stationary targets. However, the two-regime model may not be completely appropriate for the cutting of grooves. In some cases, particularly at low translation speeds, a plot of the groove depth as a function of the pulse energy suggests that the groove depth may be proportional to the pulse energy, not the logarithm of the pulse energy, and that two regimes are not present in such cases. Significant scatter or noise in the data points (due to nonuniformity of the groove depth and debris redeposited within the groove) can make it difficult to decide which model best fits the data: a linear model, or a logarithmic two-regime model. However, we feel that our data overall fits better to a logarithmic two-regime model.

The effect of changing pulse energy is much more dramatic on the depth of a groove than on the width of the groove. For the pulse energies used in this study (less than ~ 5000 nJ), the smallest width is generally greater than 50% of the largest width. An upper limit on the groove width is expected simply due to the profile of the near-Gaussian laser beam.

3.2 *Depth vs. translation speed*

An SEM image of the first few grooves from a typical depth vs. translation speed set is shown in Fig. 3. In each set, twenty single-pass grooves are cut at the same pulse en-

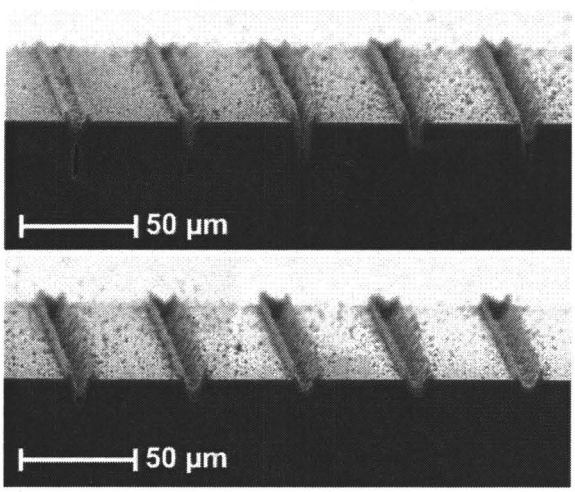

FIGURE 3 SEM images of a set of grooves cut with different translation speeds. One pass each at a pulse energy of 2160 nJ (fluence 4880 mJ/cm^2) was used. The translation speed varies from 50 μm/s to 250 μm/s (*top*) and from 300 μm/s to 500 μm/s (*bottom*)

ergy, at speeds from 50 to 1000 μm/s, in 50 μm/s increments. The depths of the grooves as a function of the translation speed v are graphed in Fig. 4a. Empirically, the groove depth has been found to roughly obey the equation

$$d(v) = \frac{A}{v} \tag{3}$$

where A is a fit parameter. This relation is in agreement with the results of Ameer-Beg et al. for grooves cut in fused silica [18]. The values of the parameter A are given in Table 2. The spot size was $\omega_o = 5.3 \pm 0.2$ μm.

By substituting v from (2) into (3), it is expected that a plot of the groove depth as a function of N_{eff} would be linear. The same data as in Fig. 4a is plotted in Fig. 4b, but with the value of N_{eff} for each point calculated from v and ω_o via (2). To a good approximation, the groove depth appears to be linearly proportional to the effective number of pulses, with greater depths obtained using greater pulse energies. We find that the translation speed has little effect on the width of grooves in silicon, with this effect being difficult to quantify due to groove roughness and debris.

Pulse energy (nJ)	Fluence (mJ/cm^2)	A (μm^2/s)	Depth/pulse (nm)
2160	4880	2100 ± 50	320 ± 10
730	1640	510 ± 20	77 ± 3
230	520	200 ± 10	31 ± 1

TABLE 2 Depth vs. translation speed fit parameters for single-pass grooves. The pulse energy uncertainty is 5%. Errors are those from the curve-fitting routine

3.3 *Depth vs. number of consecutive passes*

Multiple passes of the sample under the focussed laser spot can be used to produce deeper grooves. Figure 5 shows grooves cut at 500 μm/s with a pulse fluence of 4880 mJ/cm^2 at various numbers of passes. The sample passed back-and-forth under the same focal spot, rather than always translating in the same direction [19]. The spot size was $\omega_o = 5.3 \pm 0.2$ μm.

Figure 6a shows the measured groove depth as a function of the number of passes for three different pulse fluences at a translation speed of 500 μm/s. After many passes, the groove depth does not increase with the number of passes. However, for fewer than ~20 passes the depth increases linearly. This is more clearly seen in Fig. 6b, in which only the low number of passes region of Fig. 6a is shown. A similar effect in silicon has been observed by Ameer-Beg et al. [18],

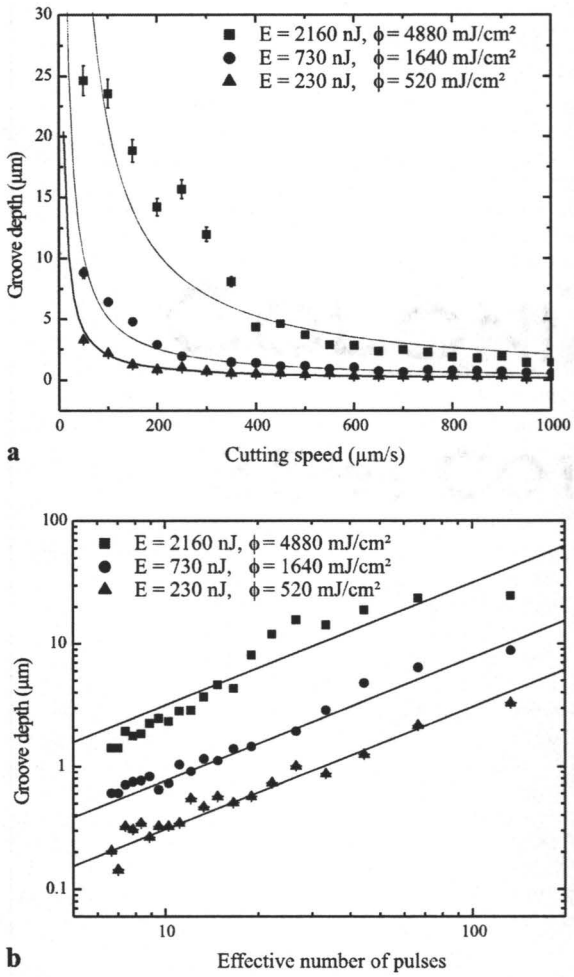

FIGURE 4 **a** Depth vs. translation speed for pulse energies of 2160, 730, and 230 nJ (fluences of 4880, 1640, and 520 mJ/cm^2). **b** Depth vs. effective number of pulses for the same data as in (**a**). Groove depths have an uncertainty of 5%

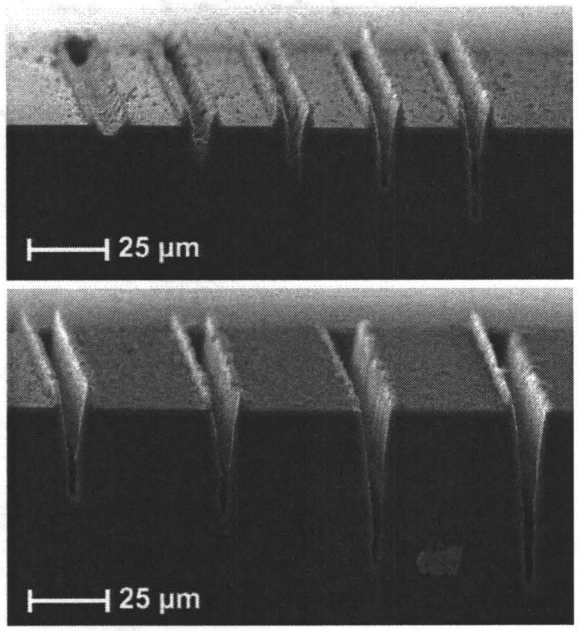

FIGURE 5 SEM images of a set of grooves cut with various numbers of passes. The numbers of passes (from *left* to *right*) are 1, 2, 4, 8, and 10 (*top*) and 20, 40, 80, and 100 (*bottom*). Cutting speed was 500 μm/s and pulse energy was 2160 nJ (fluence 4880 mJ/cm^2)

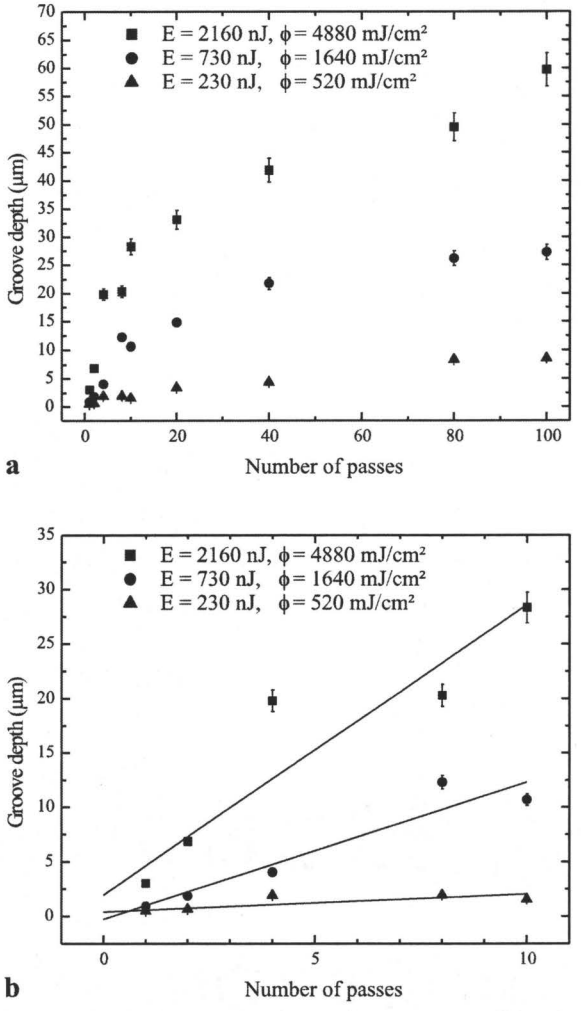

FIGURE 6 **a** Depth vs. number of passes for grooves cut at 500 μm/s. **b** The data from (**a**) for 1 to 10 passes. Depth uncertainties are 5%

in which the depth increased linearly while overscanning the beam by up to 20 passes.

Table 3 shows the slopes of the best fit lines to the depths at each of the three pulse energies for the number of passes ranging from zero to 10. A data point of zero depth for zero passes was included in each fit. At each pulse energy, an ablation depth per pulse was obtained by dividing the slope by the effective number of pulses $N_{\text{eff}} = 13.3$ per pass (at a specific point). The ablation depths per pulse are similar to those from the depth vs. translation speed experiments (see Table 2) at each fluence, but some differences are expected. In the multiple-pass case, for every pass after the first the laser beam is incident on a surface whose shape has been changed by the previous pass.

Pulse energy (nJ)	Fluence (mJ/cm^2)	Slope (μm)	Depth/pulse (nm)
2160	4880	2.7±0.5	200±35
730	1640	1.3±0.2	95±13
230	520	0.17±0.06	12±5

TABLE 3 Depth vs. number of passes parameters for grooves cut at 500 μm/s. The slope is obtained from a fit to data points from zero passes to 10 passes. The pulse energy uncertainty is 5%

The depth limit is to be expected since energy is lost via several mechanisms as the pulse propagates down the groove. A limit is reached where the fluence at the bottom of the groove is no longer sufficient to cause ablation [19]. Competition between ablation and material redeposition may also be significant. A similar depth limit has been observed for the drilling of holes in metals and sapphire with femtosecond and picosecond pulses and with high repetition rate picosecond pulse bursts [3, 21–23]. In these studies, for a given sample thickness there was a threshold fluence below which it was not possible to drill through the sample, even when using a high number of pulses.

3.4 *Ablation depth per pulse: Comparisons with other studies*

The apparatus used in the present study has been used to fabricate and analyze grooves in indium phosphide [19]. Qualitatively, the same trends as for silicon were observed in the depth vs. energy, speed, and number of passes experiments. Less scatter in the depth data points was observed for InP, which we attribute to different material properties. Silicon requires a higher fluence than InP before ablation occurs, and the fluence which delineates the two ablation regimes is lower for InP than it is for silicon. To some extent this complicates the comparisons between the two materials. In the high-fluence ablation regime of indium phosphide, the ablation rates were 144 and 100 nm per pulse (at a fluence $e \times \Phi_{\text{th}}$) for speeds of 100 and 250 μm/s respectively. These are approximately double the rates found for silicon, although at the corresponding fluences silicon is still in its low-fluence ablation regime. For depth vs. translation speed and depth vs. number of passes experiments on InP, the resulting ablation rates were between 195 and 80 nm per pulse for fluences between approximately 1900 and 650 mJ/cm^2 respectively. These are roughly 2 – 4 times the ablation rates for silicon at the same fluences.

Ameer-Beg et al. [18] machined grooves in silicon using a 1 kHz stream of ≈ 170 fs pulses at a center wavelength of 790 nm. Using a scanning galvo system they overscanned a 60 μm spot at ~ 10 mm/s over the same region 20 times with 50 μJ pulses and obtained a groove with a depth of approximately 15 μm. Using these values in (2) and by calculating the fluence using the equation $\phi = 2E/\pi\omega_o^2$ (where E is the pulse energy), we can estimate an ablation depth per pulse of ≈ 200 nm at a fluence of ≈ 3500 mJ/cm^2. This depth compares well with our data from the depth vs energy experiments at roughly the same fluence (Fig. 2b), and fits reasonably well with the depth per pulse values from our depth vs. translation speed and depth vs. number of passes results (see Tables 2 and 3). It should be noted that this estimation assumes the given spot size of 60 μm is a $1/e^2$ diameter.

Ngoi et al. [17] report a 0.2 μm deep groove machined in silicon with a 1 kHz stream of 300 fs pulses at a center wavelength of 400 nm and 100 nJ per pulse. They calculate a spot diameter of 5 μm and translate the sample at 400 μm/s. From these values, we can calculate an ablation depth of ≈ 25 nm per pulse, at a fluence of ≈ 1020 mJ/cm^2. Although their wavelength and experimental setup is not the same as in the present experiment, the resulting depth is within a factor of 2–3 of ours for a similar fluence.

There is great variation in the ablation depths per pulse reported in the literature for stationary silicon targets. For 150 fs pulses at a wavelength of 267 nm, Zhao et al. [24] obtain an ablation depth of ~ 2 nm for a single pulse at a fluence of 6.4 J/cm^2. Kautek and Krüger [25] used 300 fs pulses at a wavelength of 612 nm on Si(111). At fluences of approximately 500 mJ/cm^2 and 1600 mJ/cm^2, they indicate ablation depths of approximately 22 nm and 45 nm respectively. Kim et al. [26] used 150 fs pulses of wavelengths of 780–800 nm and a fluence of 210 mJ/cm^2 and obtained an ablation rate of 0.48 nm per pulse. This fluence however is only slightly above their reported threshold fluence of 200 mJ/cm^2. Bärsch et al. [16] used 150 fs pulses with 780 nm center wavelength. For fluences below 2.3 J/cm^2, corresponding to pulse energies of 450 μJ, they obtain an ablation rate of up to 5 nm per pulse. For fluences above 2.3 J/cm^2, they determine an ablation rate of 35 nm per pulse when using pulse energies of almost 1 mJ. The differences between various groups' results are likely due in part to the different ablation atmospheres and spot sizes employed, as well as the wide range of wavelengths and pulse energies used. Comparing these depths to our results from grooves at a wavelength of 800 nm, we find that our depths are similar in magnitude to those of Kautek and Krüger, while we obtain much higher values than the groups of Zhao et al. and Bärsch et al.

The ablation rates we obtain for silicon are similar to those obtained by some other groups on various materials. Bonse et al. [10] ablated stationary indium phosphide targets in air with 800 nm wavelength, 130 fs duration pulses. They obtained an ablation depth of 86 nm per pulse at a fluence of 0.58 J/cm^2. At this fluence, we can estimate from our data an ablation depth per pulse of between 15 and 40 nm. After 100 pulses at a fluence of approximately 2000 mJ/cm^2 they obtain a depth of approximately 90 nm per pulse. This is close to our values of approximately 70–100 nm near this fluence. Dumitru et al. [27] ablated various stationary ultrahard materials in air with 150 fs, 800 nm wavelength pulses. At a fluence of approximately 6.2 J/cm^2, they obtain ablation depths of between 90 and 185 nm per pulse. The rates we obtain are only approximately 2–5 times the ablation rates of these ultrahard materials at the same fluence.

3.5 *Qualitative observations*

For the results presented thus far, the laser polarization was perpendicular to the translation direction, resulting in the laser being *p* (TM) polarized relative to the sidewalls of the groove. Figure 7 shows grooves cut with the laser light (a) linearly polarized perpendicular to the translation direction, (b) linearly polarized parallel to the translation direction, and (c) circularly polarized. Half- and quarter-wave plates were used to change the laser polarization state, but all other parameters were the kept the same for each groove. While multiple-pass grooves cut with polarization parallel to the translation direction tend to be narrower, a great deal of 'branching' occurs near the bottom of such grooves. Branching is rarely seen in grooves cut with the polarization perpendicular to the translation direction. However, such cuts tend to have a small rib along the length of the groove, approximately half-way down the groove. This rib will be discussed later in this section. Grooves cut with circularly polarized light generally have widths comparable to those cut with perpendicular polarization, but tend to show some branching. This branching is generally less dramatic than that which occurs with parallel-polarized light.

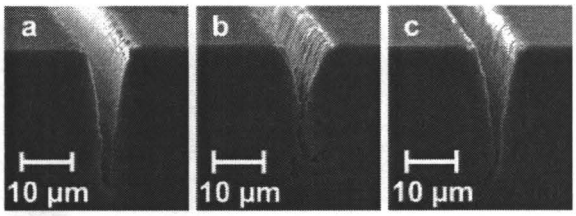

FIGURE 7 Grooves cut with the laser polarization **a** perpendicular and **b** parallel to the translation direction, and with **c** circularly polarized light. For each groove, the translation speed was 500 μm/s, the pulse fluence was 1600 mJ/cm^2, and 100 passes were used

The fact that the choice of polarization relative to the translation direction has a major effect on the groove morphology could be expected. There is a significant difference in reflectivity between *p* and *s*-polarized beams incident on an angled surface. We have observed similar polarization-dependent effects when machining grooves on InP [19], and we present a more detailed discussion of these effects in that work.

The stated uncertainties in our data points reflect only the absolute errors in the accuracy of the measurement equipment. However, the depth of a groove is generally not uniform, and consequently there is an additional level of uncertainty in determining a 'true' depth. The depth measured at the location of the perpendicular cleave may have been different if the cleave had been at another location. The cross-section of the groove bottom may also be uneven, causing some ambiguity as to where the depth should be measured. For irradiation of stationary targets, laser-induced periodic surface structures (LIPSS) have long been known to occur [28, 29]. These 'ripples' typically are aligned perpendicular to the polarization of the incident laser beam. Structures highly similar to LIPSS occur for translated targets, provided that the pulse energy and number of pulses are not so high that the structures themselves are ablated away. An example of such LIPSS produced at low fluence on a translated target is shown in Fig. 8a. However, for most grooves cut with the parameters stated in this paper, the surface is generally much less periodic than the one shown.

At higher pulse energies and lower translation speeds, considerable debris is produced. Figure 8b shows a single-pass groove cut at the same speed as the groove in Fig. 8a but with a significantly higher pulse energy. Debris accumulated within the groove itself, partially sealing it. A great deal of debris has also accumulated around the top of the groove.

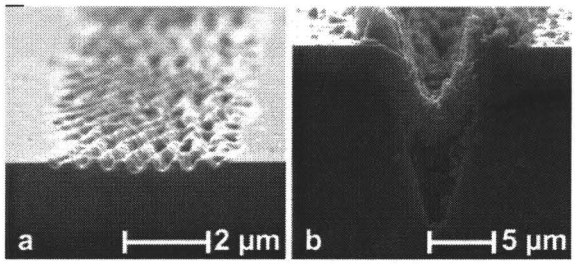

FIGURE 8 Cross-sectional SEM images of single-pass grooves cut at 250 μm/s with $\omega_o \approx 5$ μm. **a** Groove cut at low pulse energy (≈ 100 nJ). LIPSS are present along the entire groove. **b** Groove cut at high pulse energy (≈ 2000 nJ). Debris has deposited inside and around the groove

The unevenness in the groove depth can be seen more clearly by cleaving the groove along its length. Figure 9a shows a 225 μm long groove, cut with 8 passes. The depth varies by $\lesssim 50\%$, excluding the ends of the groove where the increased depth is due to the deceleration and momentary stopping of the translation stage between passes. The unevenness in this case does not appear to be the same phenomenon as LIPSS, but resembles the corrugation observed by Kautek and Krüger [25]. As the number of passes is increased, the difference in groove depth between the tops and bottoms of the bumps reaches a maximum at around 4 to 8 passes, at which point the difference decreases and the groove depth becomes more uniform. The lack of uniformity in groove depth is likely the primary cause of scatter in the data points in Fig. 6, and could contribute to the scatter shown in Figs. 2 and 4. Figure 9b shows a groove cleaved along its length for which 100 passes have been made, but the other laser parameters are the same as those which produced the groove in Fig. 9a. A rough periodicity still exists along the bottom of the groove, but the height of the bumps is roughly 10% of the depth of the groove.

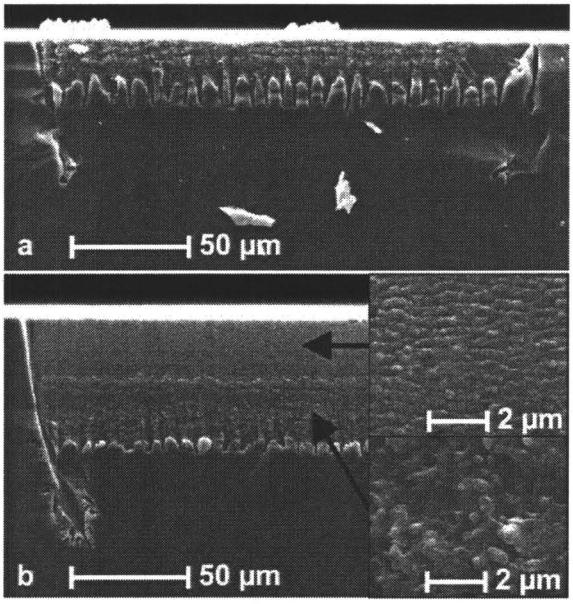

FIGURE 9 SEM images of grooves cleaved along their length. **a** Eight consecutive passes and **b** 100 consecutive passes under 2000-nJ pulses at 500 μm/s were used. *Inset*: magnification of two regions of the groove wall, showing a periodic and a semi-random rough structure

The features shown in Fig. 9 for a scan speed of 500 μm/s might suggest that 60 Hz power line noise contributes to the observed structures in the groove. In order to verify that the unevenness is not attributable to such technical issues, a number of sensitive tests were subsequently conducted by patterning surfaces with long rows of single shot ablation craters. Analysis of the samples indicates that neither general vibrations nor nonlinearity in the translation speed are important issues. Moreover, additional multiple-pass groove cutting experiments at a number of different translation speeds led to various structure periods which did not correspond to a 60 Hz fluctuation.

As can be seen in Fig. 9b, a rough line halfway down the groove (corresponding to the rib feature observed in Fig. 7a) and running along the length of the groove separates two different groove-wall surface structures. This line generally forms after approximately 10–20 passes, and remains approximately half-way down the groove even as the number of passes (and thus groove depth) increases. Magnified images of the regions above and below the line are shown in the insets of Fig. 9b. For a laser beam incident with p (TM) orientation relative to an angled surface, the period Λ of the resulting LIPSS is given by [30]

$$\Lambda = \frac{\lambda}{1 \pm \sin\theta} \tag{4}$$

where λ is the wavelength of the incident light, and θ is the angle of incidence measured from the normal to the surface. The upper inset of Fig. 9b shows a relatively periodic structure, with a feature period of approximately 350 nm. This period is in quite good agreement with (4) for $\theta \approx 90°$, $\lambda = 800$ nm, and using the positive sign in the denominator. This, along with the fact that the laser polarization is in the p (TM) orientation relative to the groove wall, and the observation that the resulting ripples are perpendicular to the laser polarization, suggests that these ripples along the groove wall are of the same origin as the LIPSS frequently encountered elsewhere. It should be noted that (4) might tend to overestimate Λ slightly. Even for $\theta = 0°$ and $\lambda \approx 800$ nm, the value of Λ on silicon was observed to be around 650–750 nm [11].

The lower inset of Fig. 9b shows the groove wall near the bottom of the groove. This image has the same scale as the upper inset image. The periodic structure is no longer present, and is instead as a semi-random rough structure. A possible explanation is that at this depth within the groove, the incident beam has scattered a great deal and no longer has a smooth wavefront. Such scattering would also tend to scramble the laser polarization, hindering the formation of LIPSS.

A burr or 'rim' is frequently formed along the top of a groove. The rim is prominent at translation speeds above approximately 250 μm/s. Figure 10 shows grooves cut with 20 and 100 passes while all other laser parameters were kept unchanged. This rim is generally tallest when large pulse energies are used for between 10 and 20 consecutive passes. At higher numbers of passes, the rim is smaller and often not present.

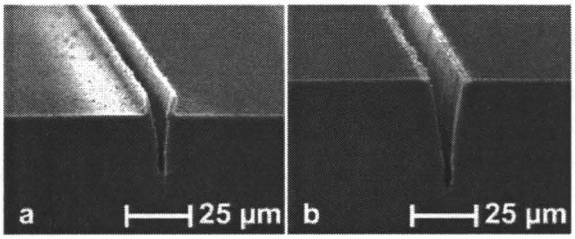

FIGURE 10 Grooves cut with pulse energy of 2000 nJ, 750 μm/s, and **a** 20 passes and **b** 100 passes

For the first few passes of the laser, large amounts of material are removed per pass. This material can redeposit on the rim and increase its height. For passes beyond the ~20th pass, the amount of material ejected per pass decreases (as implied by the plot in Fig. 6a). At this point, the growth of the rim due to material redeposition competes with material removal by the edges of pulses incident directly on the rim. Although the removal rate is small at the edges of the groove (due to the lower fluence at the edges of the pulse), the redeposition rate may eventually become less than the removal rate. Thus, after a large number of passes, we would expect the rim to be largely eroded away.

4 Summary

We have presented the results of micromachining of silicon with 800 nm femtosecond pulses. We have systematically varied the pulse energy, translation speed, and number of sample passes under the laser beam. The depth of a single-pass groove is consistent with a logarithmic dependence on the incident pulse energy, with two ablation regimes observed. The characteristic ablation depths per pulse in the low-fluence ablation regime are 25–43 nm for translation speeds ranging from 100–500 μm/s respectively. In the high-fluence ablation regime the analogous ablation rates range from 270–590 nm for these same speeds. A groove's depth is inversely proportional to the speed at which it is cut. This corresponds to an approximately linear relationship between the ablation depth and the effective number of pulses incident on the sample. For these single-pass grooves the ablation rates at pulse fluences of 4880, 1640, and 520 mJ/cm^2 are 320, 77, and 31 nm respectively. For multiple passes over the same region, the resulting depth increases linearly with the number of passes up to approximately 20 passes, at which point the depth increases progressively slower. For the first ten passes, the ablation rates at fluences of 4880, 1640, and 520 mJ/cm^2 are 200, 95, and 12 nm respectively.

The polarization of the laser beam relative to the translation direction has a significant effect on the cross-sectional profile of deep grooves, with significant branching in the case of the polarization parallel to the translation direction. The walls of a groove exhibit a great deal of unevenness. For low numbers of passes, the depth is somewhat periodic with a large variation in height, while for large numbers of passes (greater than approximately 20), the depth remains somewhat periodic but with less variation. The wall of a deep groove exhibits two primary morphologies. In the upper half of a groove, the wall exhibits small ripples with a period of approximately 350 nm, in this case almost half of the wavelength of the incident radiation. In the lower half, the morphology appears as a somewhat random rough pattern. During machining with multiple passes, a tall rim forms at the sides of the groove, which subsequently erodes away with more passes.

ACKNOWLEDGEMENTS The authors thank H. F. Tiedje for helpful comments on this work. They would also like to acknowledge the Natural Sciences and Engineering Research Council of Canada (NSERC) and Materials and Manufacturing Ontario (MMO) for financial support of this work.

REFERENCES

1 D. Bäuerle: *Laser Processing and Chemistry*, 3rd Ed. (Springer-Verlag, Berlin, 2000)
2 B.N. Chichkov, C. Momma, S. Nolte, F. von Alvensleben, A. Tünnermann: Appl. Phys. A **63**, 109 (1996)
3 X. Zhu, A.Yu. Naumov, D.M. Villeneuve, P.B. Corkum: Appl. Phys. A **69** [Suppl.], S367 (1999)
4 K. Furusawa, K. Takahashi, H. Kumagai, K. Midorikawa, M. Obara: Appl. Phys. A **69** [Suppl.], S359 (1999)
5 S. Nolte, C. Momma, H. Jacobs, A. Tünnermann, B.N. Chichkov, B. Wellegehausen, H. Welling: J. Opt. Soc. Am. B **14**, 2716 (1997)
6 J. Güdde, J. Hohlfeld, J.G. Müller, E. Matthias: Appl. Surf. Sci. **127–129**, 40 (1998)
7 D. Ashkenasi, G. Müller, A. Rosenfeld, R. Stoian, I.V. Hertel, N.M. Bulgakova, E.E.B. Campbell: Appl. Phys. A **77**, 223 (2003)
8 J. Ihlemann, B. Wolff, P. Simon: Appl. Phys. A **54**, 363 (1992)
9 J. Krüger, W. Kautek: Appl. Surf. Sci. **96–98**, 430 (1996)
10 J. Bonse, J.M. Wrobel, J. Krüger, W. Kautek: Appl. Phys. A **72**, 89 (2001)
11 J. Bonse, S. Baudach, J. Krüger, W. Kautek, M. Lenzner: Appl. Phys. A **74**, 19 (2002)
12 G.V. Treyz, R. Beach, R.M. Osgood, Jr.: J. Vac. Sci. Technol. B **6**, 37 (1988)
13 M. Müllenborn, H. Dirac, J.W. Petersen: Appl. Surf. Sci. **86**, 568 (1995)
14 B. Shen, M. Allard, S. Boughaba, R. Izquierdo, M. Meunier: Can. J. Phys. **74** [Suppl.], S54 (1996)
15 M. Allard, S. Boughaba, M. Meunier: Appl. Surf. Sci. **109–110**, 189 (1997)
16 N. Bärsch, K. Körber, A. Ostendorf, K.H. Tönshoff: Appl. Phys. A **77**, 237 (2003)
17 B.K.A. Ngoi, K. Venkatakrishnan, E.N.L. Lim, B. Tan, L.H.K. Koh: Opt. Las. Eng. **35**, 361 (2001)
18 S. Ameer-Beg, W. Perrie, S. Rathbone, J. Wright, W. Weaver, H. Champoux: Appl. Surf. Sci. **127–129**, 875 (1998)
19 A. Borowiec, H.K. Haugen: Appl. Phys. A. Published online March 16, 2004. DOI: 10.1007/s00339-003-2377-0
20 K. Venkatakrishnan, B. Tan, B.K.A. Ngoi: Opt. Las. Technol. **34**, 199 (2002)
21 A.E. Wynne, B.C. Stuart: Appl. Phys. A **76**, 373 (2003)
22 M. Lapczyna, K.P. Chen, P.R. Herman, H.W. Tan, R.S. Marjoribanks: Appl. Phys. A **69** [Suppl.], S883 (1999)
23 D. Ashkenasi, A. Rosenfeld, H. Varel, M. Wähmer, E.E.B. Campbell: Appl. Surf. Sci. **120**, 65 (1997)
24 J. Zhao, B. Huettner, A. Menschig: Opt. Las. Technol. **33**, 487 (2001)
25 W. Kautek, J. Krüger: Mater. Sci. Forum **173–174**, 17 (1995)
26 M.K. Kim, T. Takao, Y. Oki, M. Maeda: Jpn. J. Appl. Phys. **39**, 6277 (2000)
27 G. Dumitru, V. Romano, H.P. Weber, M. Sentis, W. Marine: Appl. Phys. A **74**, 729 (2002)
28 J.E. Sipe, J.F. Young, J.S. Preston, H.M. van Driel: Phys. Rev. B **27**, 1141 (1983)
29 J.F. Young, J.S. Preston, H.M. van Driel, J.E. Sipe: Phys. Rev. B **27**, 1155 (1983)
30 Z. Guosheng, P.M. Fauchet, A.E. Siegman: Phys. Rev. B **26**, 5366 (1982)

4.3 Additional comments on the results and techniques presented in the paper

4.3.1 Approach to sample preparation

Figure 4.1 shows a schematic layout of a typical grooves sample, and images of actual samples. Before laser irradiation, the sample is cleaved along crystal axes, and is placed in the machining chamber such that the x translational direction is parallel to a cleave. This allows the cleaving of the sample perpendicularly through the grooves, which are typically machined by moving the sample in the y direction. Cleaving a machined sample exposes cross-sections of many grooves without requiring the use of a dicing saw or other techniques. For selected experiments a target with a non-(100) surface orientation was used, and the y translational direction was sometimes chosen to be parallel to a cleave. Due to the difficulty in predictably and accurately cleaving non-(100) materials, all groove cross-sections presented here are for materials of (100) surface orientation. In a lower corner of the sample, once the chamber window was in place and the roughing vacuum pump turned on, a few low-energy lines were machined while adjusting the height of the lens (typically a 5$\times$ microscope objective for grooves experiments). This was to ensure that the sample was at the point of tightest laser focus, as described in section 3.5. Pulses with a 400 nm peak wavelength were generated by placing a BBO crystal in the beam, typically immediately after the half wave plate and polarizer. Residual 800 nm wavelength light was removed by multiple dielectric mirrors highly reflective at the 400 nm wavelength.

The procedure for machining samples used in grooves experiments was typically as follows. A sample label, consisting of the sample machining date and possibly other information, was machined using low power in two locations on the sample surface, so that each piece could be identified after cleaving through the grooves. Two or more single-pulse runs (a run consisting of one pulse at each of the pulse energies available using the neutral density filter set, to a pulse energy below the visible modification threshold) were performed on the sample so that the spot size could be later determined via microscope measurements and the D^2 fitting technique described in the paper [65] and section 3.5 of this thesis. At least two D^2 runs were measured and compared, to guard against the possibility that one run was flawed in some way. One or more depth vs. energy groove runs were made on the sample, starting with the highest energy (OD 0.0) and decreasing in 0.1 OD steps to energies which no longer produced visible modification. The pulse energy at OD 0.0 was typically $\sim$2 μJ or $\sim$5 μJ. As with the single-shot runs, an additional space was placed between groups of

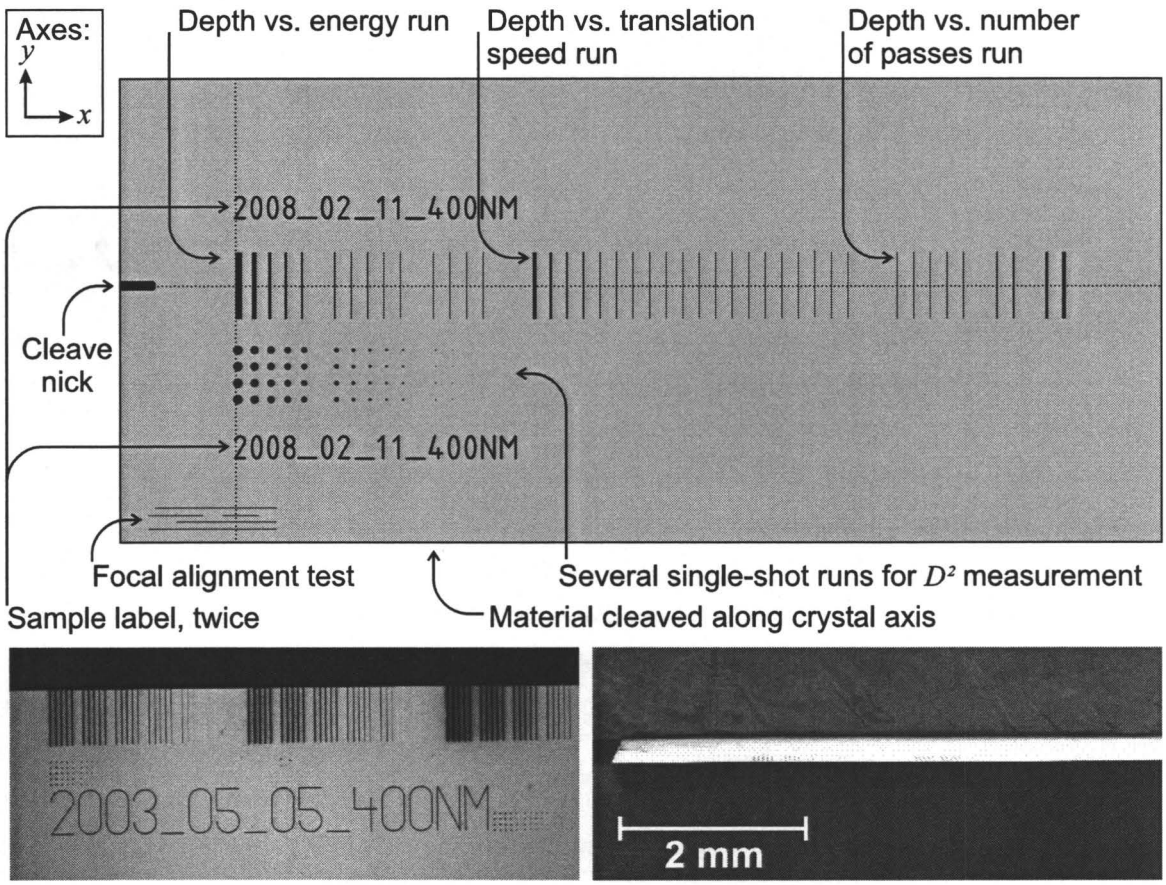

Figure 4.1: *Upper*: Schematic diagram of the typical layout of a sample used in grooves investigations. *Lower left*: Optical microscope image of a portion of a sample after cleaving through the grooves, looking in 'plan-view' mode at the surface of the wafer. *Lower right*: SEM image of a portion of the same sample held end-up for measuring the depths of grooves.

five grooves. This space made it easier to keep track of which groove was being imaged in the SEM. If a site was accidentally skipped in the SEM, the space would show up unexpectedly. One or more depth vs. translation speed runs were usually performed next, starting with a groove machined at a speed of 50 μm/s and followed by grooves at speeds up to 1000 μm/s, increasing in steps of 50 μm/s between grooves. Finally, one or more depth vs. number of passes runs were usually performed, at 500 μm/s and for three different OD filter settings. These settings usually differed by 0.5 OD, for example, 0.4, 0.9, and 1.4 OD. The numbers of passes were 1, 2, 4, 8, 10, 20, 40, 80, 100, with additional numbers occasionally used. In all groove runs, grooves had a length of 1000 μm each, separated by 50 μm, with somewhat larger spacing sometimes used between grooves machined with high num-

bers of passes. Most grooves were produced while translating the sample along the y axis, meaning that the $\lambda = 800$ nm laser polarization was approximately perpendicular to the translation direction, and producing 'classic' LIPSS running along the length of the groove at particular pulse energies and translation speeds. Occasionally, a polarizer was used just before the focussing element to confirm the direction of the polarization.

A 'cleaving nick' was machined at the edge of the sample using the laser, so that the nick ran perpendicular to the center of the rows of grooves. The nick did not reach the grooves. More than 100 passes was used, with the translation stage moving along the x axis. Cleaving was accomplished by placing the sample machined-side down on a lens tissue, placed on several Kimwipes tissues. A thin wooden dowel (from a cotton swap stick) would be positioned at the location of the nick, running in the direction of the desired cleave. Downward force was applied to the stick, with somewhat more force near the nick, until the sample cleaved. This successfully forced a cleave running perpendicular through the grooves the majority of the time, although a small jog in the cleave would sometimes occur at deep grooves. Runs producing deep grooves were typically performed near the end of the experiment, not near the nick, so that if a severe jog occurred at the deep grooves the shallower ones would already have been cleaved near their centers. An additional lens tissue was placed between the sample and the wooden dowel before cleaving so that a silicon piece could not fly into the air at the moment of cleaving. The grooves were typically cut in a set along the middle of the sample, as making cleaves near the edge of a piece of silicon is generally less successful. Most machining of features to be measured was done at least 1–2 mm from the edges of the sample, to decrease the likelihood of features being damaged by tweezers during handling. The left side of the text, the first (OD 0.0) single-shot site, and the first groove were all aligned along the y axis, to make finding the sites easier in the SEM. Some features, particularly the single-shot craters, were difficult to observe in the SEM until the focus and SEM 'gain' and 'black level' settings were adjusted well. However, the sample text was much easier to see in the initial stages of SEM setup. Samples were usually cleaned before machining, but were not cleaned after machining. This allowed observation of any debris produced by the machining process.

A custom sample holder was used for holding samples cleaved-end-up in the SEM for groove depth measurements, or for holding samples in plan-view ('top-down' imaging of the wafer surface) mode. Photographs of the holder are shown in figure 4.2. The use of this holder meant that electrically conductive tape or silver epoxy were not needed, thus avoiding almost-permanent bonding of the samples and allowing the samples to be later analyzed with other techniques (AFM, TEM, and optical microscopy). Removal of epox-

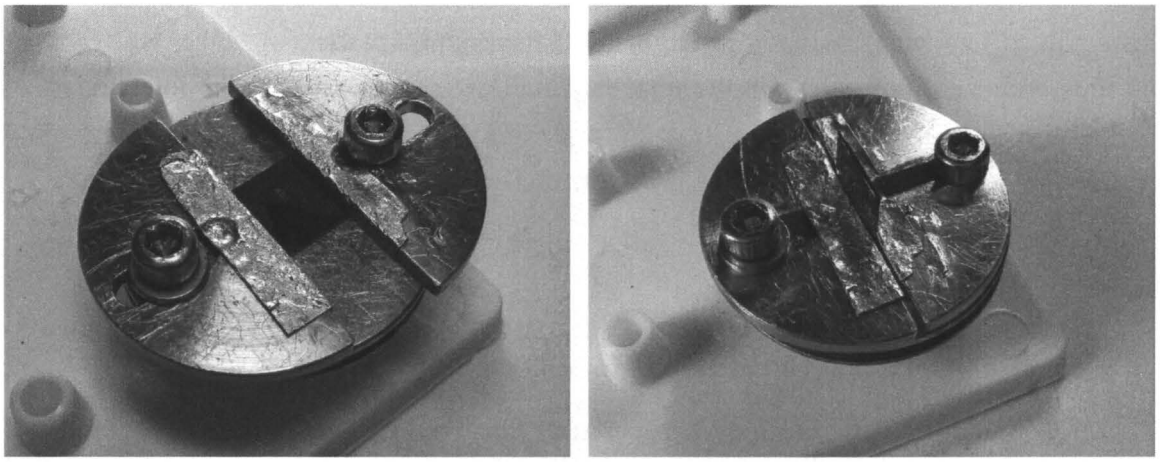

Figure 4.2: Photographs of the custom SEM sample holder, showing the sample mounting for *(left)* plan-view observation and *(right)* edge observation for cleaved grooves.

ies or tape would require chemical rinses or risk breaking or contaminating the sample. The sample holder consists of a standard 1-inch-diameter SEM stub, two slotted semicircular disks approximately 1.5 mm thick, and two screws for affixing the semicircular disks to the upper stub surface. Each screw would pass through a slot into a threaded hole on the stub. The sample could be placed between the straight portions of the semicircles, the semicircles pushed toward each other, and then the screws tightened to hold the semicircles in place. Pieces of indium foil were placed along the straight sections of the semicircles, as it was very malleable and aided the holding of the sample, and provided good electrical contact between the sample and the sample holder. The majority of samples did not have a gold sputter coating applied, as the conductivity of the silicon generally was good enough to avoid 'charging' artifacts in the SEM. Silicon with relatively low resistivity and with n-type doping was chosen for most experiments, to reduce the possibility of charging. Within the SEM, the sample was tilted to an angle of approximately 5° relative to the normal of the cleaved surface. A corresponding scale adjustment of 5° was set on the SEM image acquisition system to match. Depths of grooves were measured to the point shown in the inset of figure 1 of the paper [65], i.e. from the location of the original substrate surface perpendicularly down to the bottom of the groove. In some cases there was ambiguity in the location of the bottom of the groove, for example for grooves clogged with debris (in this case the bottom of visible material removal was measured), or when LIPSS were present (the approximate midpoint of the LIPSS was measured). Due to the lower atomic number of silicon compared to many other researched materials such as indium

phosphide, gallium phosphide, germanium, and copper, a lower secondary electron signal was obtained for imaging silicon in the SEM. This required the use of higher SEM gain, and thus produced more noise in the images. Shallow features such as the lower-energy single-pulse sites were particularly difficult to see in SEM, and thus Nomarski Differential Interference Contrast optical microscopy was usually used for measuring crater diameters for the D^2 fitting technique.

4.3.2 Derivation of the effective number of pulses for grooves

Equation 2 in the silicon grooves paper [65] (also appearing in the InP grooves paper [64]) for the 'effective' number of passes N_{eff} was derived myself as follows. A one-dimensional Gaussian curve $G(x)$, centered at $x = 0$, with a maximum of 1 (i.e. $G(0) = 1$), and a $1/e^2$ half-width of $\omega_\circ$ is defined by

$$G(x) = e^{\frac{-2x^2}{\omega_\circ^2}}. \tag{4.1}$$

The sum of points equally spaced along the x axis of this Gaussian can be calculated, where each point n is at $x_n = nk$. The spacing between each point (measured along the x axis) is k, and n is any integer from $-\infty$ to $+\infty$. For the application to a Gaussian pulse profile traveling at a speed υ, the centers of pulses at a repetition rate f will be spaced a distance $k = \upsilon/f$ apart. The sum S is

$$S = \sum_{n=-\infty}^{\infty} e^{\frac{-2(nk)^2}{\omega_\circ^2}}. \tag{4.2}$$

The definition $\Delta n = 1$ can be made, since this is the change in n from one integer to the next. Every term in the sum can be multiplied by Δn without affecting the sum:

$$S = \sum_{n=-\infty}^{\infty} \left[e^{-\left(\frac{2k^2}{\omega_\circ^2}\right)n^2} \cdot (\Delta n) \right]. \tag{4.3}$$

This can be approximated by an integral when taking the limit as Δn becomes 'small'. The Δn becomes 'small' when the width of the Gaussian becomes 'large'. This approximation will break down as $\omega_\circ$ becomes small relative to k (i.e. as k becomes 'large', i.e. as the speed υ becomes large or the repetition rate f becomes small). Taking the limit S_{lim},

$$S_{\text{lim}} = \lim_{\Delta n \to \text{small}} \sum_{n=-\infty}^{\infty} \left[e^{-\left(\frac{2k^2}{\omega_\circ^2}\right)n^2} \cdot (\Delta n) \right]$$

$$
\begin{aligned}
&= \int_{-\infty}^{+\infty} \mathrm{e}^{-\left(\frac{2k^2}{\omega_\circ^2}\right)n^2} dn \\
&= \sqrt{\frac{\pi}{2k^2/\omega_\circ^2}} \\
&= \sqrt{\frac{\pi}{2}} \cdot \frac{\omega_\circ f}{v} \,.
\end{aligned} \tag{4.4}
$$

In this derivation, the integral

$$
\int_{-\infty}^{+\infty} \mathrm{e}^{-az^2} dz = \sqrt{\frac{\pi}{a}} \tag{4.5}
$$

is used. While this derivation is not mathematically rigorous, the resulting equation with its $\sqrt{\pi/2} \approx 1.2533$ factor agrees with numerical simulations involving summing many adjacent Gaussian curves separated by a distance k along the x axis. Since the Gaussian G had a maximum value of unity, it can be related directly to the peak fluence $\phi_\circ$ at the center of a (two-dimensional) Gaussian profile. Consider the line, running in the x direction along the center of a groove machined by translating a pulsed Gaussian pulse profile along the x axis, with the pulse profile (along the x axis) being described by $\phi_\circ \cdot G(x)$. The peak fluence of such a pulse is $\phi_\circ$. The sum $\phi_\circ \cdot S_{\mathrm{lim}}$ would give (approximately) the total accumulated fluence at any point along that line. In the papers [64, 65] we refer to the value of S_{lim} as the effective number of pulses N_{eff}. As noted in the papers [64, 65] there is some assumption made about the true physical effect of multiple pulses. For example, at a particular point a single pulse of local fluence ϕ might not be expected to produce the same physical effect as two (temporally) separated pulses each with a local fluence of $\phi/2$, or of several pulses with fluences summing to ϕ. However, this equation for N_{eff} provides a useful starting point for the analysis of multiple pulses on a translated target.

Somewhat different results would be expected in a comparison between a translated sample and a stationary sample, for a similar number of incident pulses. For example, there are effects such as the constant introduction of unmodified surface material into the focussed spot, and the possibility of debris from one part of a groove depositing in a previously-formed part of the same groove. However, due to their length, cross-sections of grooves are much easier to prepare than cross-sections of sites irradiated when the sample was stationary. Because of the imprecision in predefining the location of a cleave, attempts at cleaving through single-pulse and multiple-pulse locations were generally not successful. For depth measurement, AFM is somewhat more time consuming in comparison to SEM, is not usable for deep features or with high aspect ratios, and does not provide

information on features such as the 'branching' described in certain deep grooves in the paper [65].

4.3.3 Consideration of uncertainties in the grooves calculations

Uncertainty in a calculated value is determined using a standard method, as follows. If Z is a function of A and B, and these have uncertainties of ΔA and ΔB respectively, then ΔZ (the uncertainty in Z) is calculated from

$$(\Delta Z)^2 = \left(\frac{\partial Z}{\partial A}\right)^2 (\Delta A)^2 + \left(\frac{\partial Z}{\partial B}\right)^2 (\Delta B)^2. \tag{4.6}$$

For example, the peak fluence $\phi_\circ$ is $(2E)/(\pi\omega_\circ^2)$, and thus the uncertainty in $\phi_\circ$ is given by

$$(\Delta\phi_\circ)^2 = (\phi_\circ)^2 \left[\left(\frac{\Delta E}{E}\right)^2 + \left(2\frac{\Delta\omega_\circ}{\omega_\circ}\right)^2\right]. \tag{4.7}$$

The manufacturer-quoted uncertainty in the power meter readings was 5%, and a 5% uncertainty was estimated for the SEM length and optical microscope crater-diameter measurements.

For the curve fitting in the depth vs. energy experiments, a linear least-squares method was used which considers uncertainties in both the x and y values. This calculation was done in the 'IDL' programming language using the `fitexy.pro` routine written by Frank Varodi, NASA/GSFC, September 1992. The fit values were also compared to those produced by the built-in IDL routines `curvefit` (non-linear least-squares fit), and `regress` (multiple linear regression), however these routines do not consider uncertainties in the x data (pulse energy). The three routines generally produced similar fit parameters. The `fitexy` routine is based on that given in section 15.3 of *Numerical Recipes in C: The Art of Scientific Computing (Second Edition)* by W.H. Press *et al.*. Fit parameters from the `fitexy` routine were also used in the depth vs. translation speed experiments, for which a 1% uncertainty in the translation speed was assumed. Diagnostic tests such as the one shown in section 4.7, figure 4.7, showed that the speeds had this accuracy or better outside of the short acceleration and deceleration regions. The IDL `regress` routine was used for fitting the low number of passes data in the depth vs. number of passes experiments, as there was no uncertainty in the x (number of passes) values. For all fit methods, a 5% uncertainty in SEM measurements (y values) was used.

4.3.4 General comments

A point which is implied in the paper but worth emphasizing is that for shallow features, it can frequently be reasonably assumed that each successive pulse of the same local fluence removes approximately the same amount of material. However, this becomes a poor assumption as the features become deeper. Taking the final depth and dividing by the number of pulses would give a 'depth per pulse' value which changes as a function of depth for sufficiently deep features. As seen in section 3.3 of the paper [65], the groove depth no longer increases after a sufficiently high number of passes. However, this calculation is more reasonable for shallow features and low numbers of pulses. Measurements of a 'depth per pulse' are reported frequently in the literature, and care must be taken in their interpretation. In material removal the incubation effect, in which the material removal threshold fluence depends on the number of pulses, could play a role especially in the wings of the pulse spatial profile where the local fluence is near the material removal threshold.

As noted in the paper, InP and silicon qualitatively followed many of the same trends, but some differences exist between the machining of InP and of silicon. InP had machining rates of 2–4 times those of silicon, although comparisons are complicated by a different fluence regime dividing point for the two materials. In general, InP was 'easier' to machine, requiring lower fluences, and exhibiting less scatter in the the depth data points. Comparing the graphs presented in reference [64] for InP and [65] for silicon, data points are typically closer to the best-fit lines fitted to them on InP. The exact cause of this difference in scatter was not investigated, but would be related to the material properties, as the experiments on InP and silicon were each done repeatedly with the same apparatus and around the same time. The trends for data point scatter are further demonstrated by some of the results presented later in this thesis chapter.

4.4 Depth vs. pulse energy for 100-pass grooves

In the InP grooves paper by A. Borowiec et al. [64], a plot of depth vs. pulse energy was made for grooves cut with 100 passes of the sample under the beam. A similar plot for 100 passes on silicon is presented in figure 4.3 in this thesis, using the same data analysis and curve fitting approach as in the silicon grooves paper [65]. For both InP and silicon, a two-regime behaviour was observed as a function of pulse energy, however the regimes appear more distinct in InP. On silicon, while the high fluence cases fit well to a logarithmic dependence on pulse energy, there is a not a sharp bend in the data where the fit lines intersect. As in the paper [65], the separation point between the regimes was chosen by finding

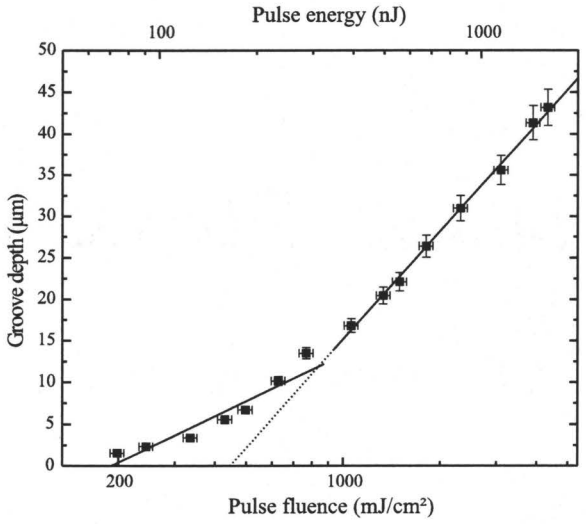

Figure 4.3: Depth vs. energy plot for a translation speed 500 μm/s, after 100 passes for each pulse energy. The graph and fit lines were obtained via the same method used for depth vs. energy plots in the silicon grooves paper [65]. The error bars on the x-axis represent the uncertainty in pulse energy.

the two curves which minimized the sum of the chi-squares of the two fit lines. Here, the seven lowest energy points were calculated to be in the low-energy regime. However, judging 'by eye' the low-energy slope might look more reasonable the line only included the lowest five points, thus giving a smaller slope and lower x-intercept value. The data shows a similar trend as has been observed in other comparisons between silicon and indium phosphide, namely that data points on graphs for silicon do not typically lie as close to best-fit curves as they do for InP. In the silicon grooves paper [65] for depths as a function of pulse energy for single-pass grooves, it was difficult to decide if the data best fits a linear model or a two-regime logarithmic model due to scatter in the data. For the 100-pass data in figure 4.3, a good logarithmic fit is made for only the high-fluence data. As noted in the silicon grooves paper [65], Nolte et al. associated a two-regime logarithmic behaviour on metals to optical penetration and heat diffusion depths. However, for semiconductors like silicon there could be additional or different phenomena which would cause a deviation from a two-regime logarithmic behaviour, and perhaps cause a more continuous change in the dynamics.

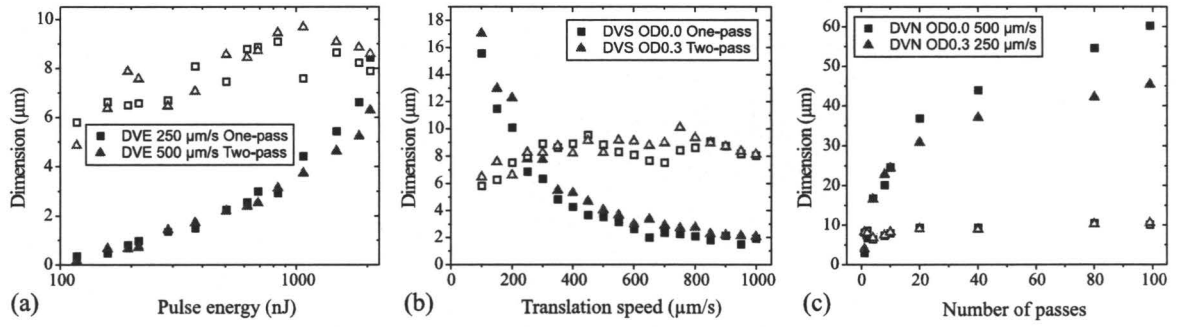

Figure 4.4: Depth (solid symbols) as a function of various laser parameters for configurations in which the net energy per spot is approximately equal. Also shown in hollow symbols are the groove widths. Each plot compares two different configurations. 'DVE' means *'depth vs. energy'*, 'DVS' means *'depth vs. translation speed'*, and 'DVN' means *'depth vs. number of passes'*. The per-pulse energy for the OD 0.0 case is 2.06 µJ while for OD 0.3 it is 1.07 µJ. The peak laser wavelength was 800 nm.

4.5 Comparisons of equal net fluence via different machining parameters

By varying the pulse energy, translation speed, pulse repetition rate, and number of passes there are a variety of combinations by which one can obtain a particular net energy per location on the sample. In an industrial application, the question arises as to whether two different methods of applying the same energy would produce different results, particularly if one method provides additional benefits such as reduced machining time. Figure 4.4 shows the results of an experiment to compare various methods. In the case where the speed was doubled and the number of passes doubled (figure 4.4(a)), the two cases produced very similar depths, although the one-pass case tended to produce somewhat deeper grooves for the highest pulse energies. In the case where the pulse energy was approximately halved and the number of passes doubled (figure 4.4(b)), the two-pass case was usually slightly deeper than the one-pass case. In the third comparison, in which the pulse energy was approximately doubled and the translation speed doubled (figure 4.4(c)), the depths are similar for low numbers of passes but are significantly deeper for the higher translation speed and energy. This could be due to the lower pulse energy not being sufficiently high enough to cause material removal at the bottom of a groove once the pulse has reached the groove bottom. In all three comparisons, the groove widths did not show any significant, consistent differences. From SEM imaging (not shown here), other than the significant difference in depth for the high number of passes case, the groove morphology did not show any significant qualitative differences. This examination has only looked at a small area of

parameter space. To determine if the trends observed here apply to a wide range of irradiation conditions (different energies, speeds, and numbers of passes), extensive further work would be needed.

4.6 Further investigation of polarization effects

In the two grooves papers [64, 65], three polarization configurations were considered. Two cases used linear polarization, one of which was parallel and the other perpendicular to the translation direction. The third case used circularly polarized light, where it is not expected that the translation direction is relevant. A fourth case, not presented in the grooves papers [64, 65] but which was used extensively in the drilling of holes in copper foils (see chapter 8) used linearly polarized light which had previously passed through a half wave plate, with the wave plate rotating approximately 15° between each pulse. This 'spinning wave plate' or 'polarization trepanning' was found to produce less elliptical entrance and exit holes on stationary copper samples.

Preliminary experiments on the machining of grooves in silicon with the 'spinning' polarization were also performed. With the spinning polarization, the groove had relatively straight sides, as was the case for the perpendicular polarization and for circularly polarized light shown in figure 7 of the paper [65]. The curved walls seen in figure 7(b) of the paper [65] for parallel-oriented linearly polarized light did not form for the spinning polarization. A small amount of 'branching', in which the the lower portion of the groove tended to split into multiple regions, existed at the bottom of the grooves when the spinning polarization was used. These results were all for a translation speed of 500 μm/s and 100 passes, with a per-pulse fluence of 1600 mJ/cm^2.

The groove cutting experiment using the four polarization configurations was repeated with blue light (actually $\lambda = 417$ nm, due to the way the laser was configured at that time for a different experiment). A translation speed of 500 μm/s was used, with 100 passes and a per-pulse fluence of 2300 mJ/cm^2. The general trends for groove morphology exhibited in the $\lambda = 800$ nm experiments for the four polarization configurations were present in the blue light case. Blue light polarization parallel to the translation direction led to curved sides and some branching at the bottom of the groove, although the spinning and circular polarizations exhibited a small amount of branching too (as in the 800 nm case). The $\lambda = 800$ nm cases tended to exhibit more branching than the blue light cases.

A groove-cutting experiment (at a translation speed of 500 μm/s) was also performed with the polarization at 45° relative to the translation direction, and was compared to results

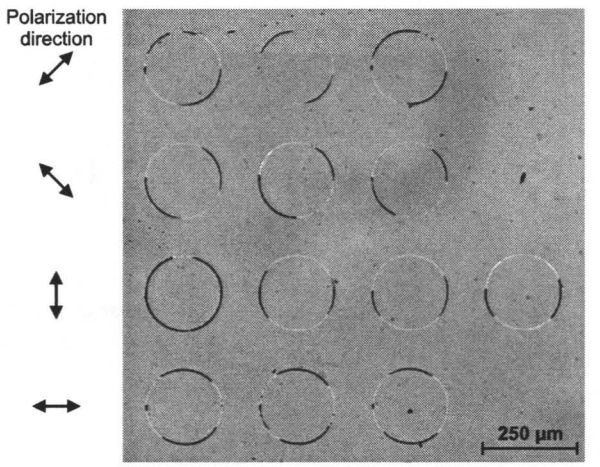

Figure 4.5: Optical microscope image of silicon translated in a circular motion, for four different directions of incident laser polarization. The 800 nm wavelength was used with a vacuum atmosphere, 150 fs pulse duration, and 1 kHz repetition rate. Three or four circles for each polarization were produced, to show repeatability. The dark lines correspond to LIPSS, while the higher-reflectivity lines are a shallower modification.

using linear-perpendicular, linear-parallel, and circularly polarized light in the same experimental run. In the cases of $\lambda = 400$ nm (fluences of 5500 mJ/cm^2 and 1700 mJ/cm^2) and $\lambda = 800$ nm (fluences of 4600 mJ/cm^2 and 1600 mJ/cm^2), some branching was produced near the bottom of the grooves with 45° polarization, with the amount of branching similar to that obtained with circularly polarized light. Under the 45° polarization, the grooves did not show any particular tendency to curl or branch in a specific direction.

From depth vs. energy grooves experiments, a narrow range of incident pulse energies existed for which the irradiated material had a higher reflectivity than unmodified material, but minimal material was removed. Below this range, no visible modification occurred, while for energies above this range LIPSS (with a period somewhat less than the 800 nm irradiation wavelength) and significant material removal occurred. In later studies within this narrow energy range it was observed that LIPSS had a slightly greater tendency to form when the sample was moving in a direction parallel to the polarization direction. When the translation was perpendicular to the polarization, material of higher reflectivity would be produced instead for the same pulse energy. Figure 4.5 demonstrates this case, where a half wave plate was placed in the beam to set the polarization direction, and the sample was translated in a large circular motion so that all translation directions relative to the polarization were sampled. A possible explanation for the results in figure 4.5 is that the

LIPSS tend to more strongly scatter incident laser light in a direction perpendicular to the direction along which each LIPSS ripple runs, similar to how a diffraction grating diffracts incident light. Thus, increased material modification would occur when translating in the direction of diffraction. This phenomenon was only observed for a small range of pulse energies, and the cases shown in figure 4.5 took several attempts at adjusting the pulse energy (with the waveplate and polarizer combination for fine adjustment) before the appropriate energy was found. Thus, this phenomenon is not expected to have a major effect in the results presented in this chapter. It should be noted that LIPSS could be produced extending coherently in grooves regardless of the translation direction for sufficient pulse energy, as shown in figure 8(a) of the silicon grooves paper [65] and figure 4.9(b) of this chapter. In additional experiments, conditions could be found in which opening the shutter followed by commencing sample translation would produce a dark region (LIPSS). However, if the laser was blocked and subsequently unblocked while the sample continued to translate, the dark material would not begin to be produced again. This suggested that structuring initiated (or 'seeded') at the start of translation, when the sample had not yet reached its final speed, helped nucleate further structuring adjacent to already-structured material. Again, this was only observed for a small range of pulse energies.

4.7 Further analysis and discussion of the coarse corrugation at the bottom of grooves

Figure 4.6 shows SEM images of grooves cut with 800 nm wavelength irradiation, cleaved along their length, with the light polarization perpendicular to the translation direction. For these sites the sample was translated in a back-and-forth fashion, instead of starting each pass from the same end of the groove. These images show the evolution with number of passes of a corrugation along the bottom of the groove, with the 8- and 100-pass cases also presented in figure 9 of the silicon grooves paper [65]. As described in the paper [65], the severity of modulation increases up to 4–8 passes, then decreases with further passes. Even in the 1- and 2-pass cases some periodicity can be seen, and resembles the corrugation reported by Kautek and Krüger for two passes on silicon [97]. The ridge described in reference [65], running approximately half-way down the groove wall, can be seen after 10 passes.

In an additional test, sets of five grooves were machined with all grooves in a set using the same laser and translation parameters. Pulse energies of 2.0, 0.68, and 0.22 μJ were used for 100 passes with a 500 μm/s translation speed. For each set, the average depth and

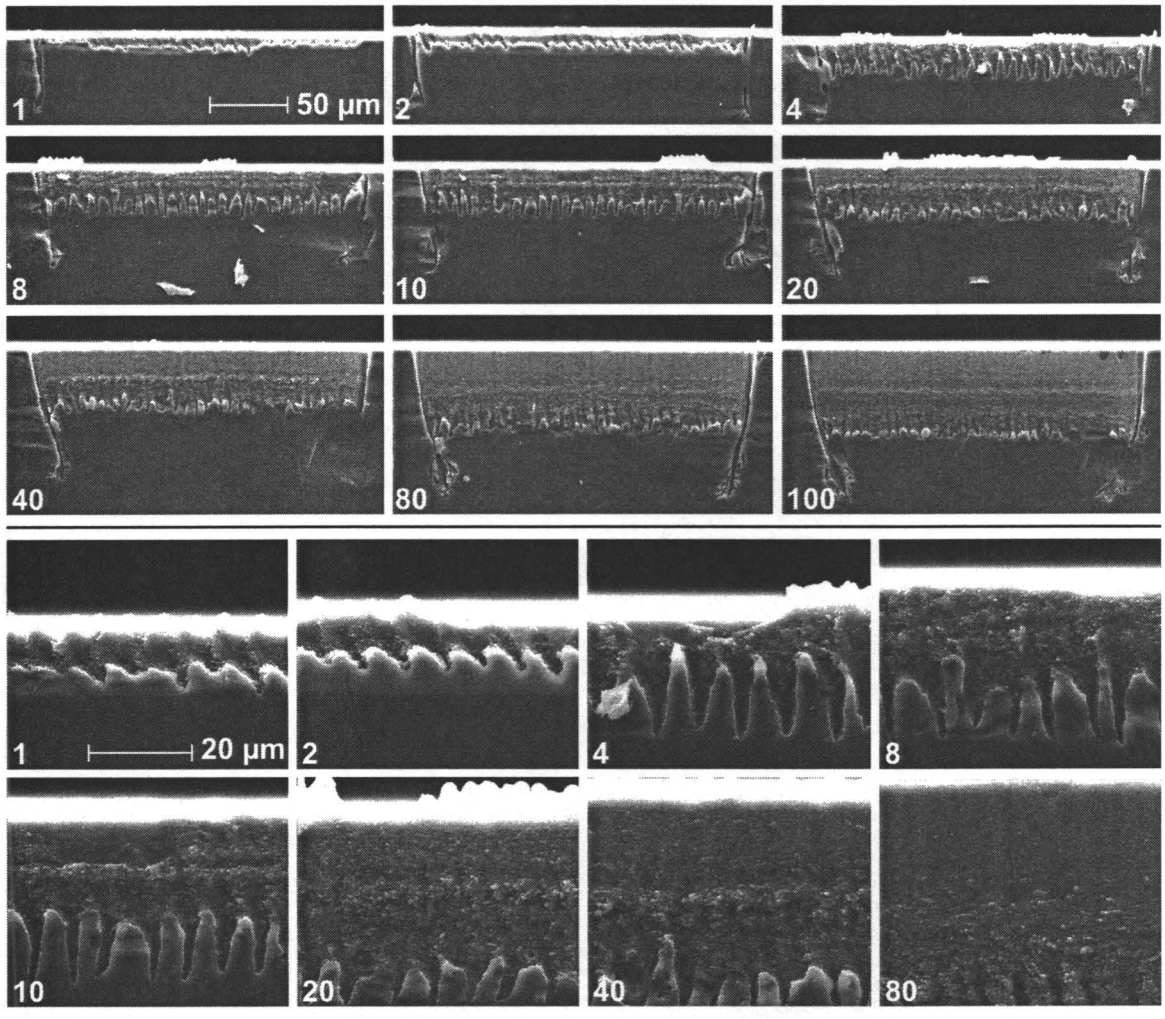

Figure 4.6: SEM images of grooves cleaved along their length, showing corrugation. The number in the lower corner of each image indicates the number of passes. The grooves were cut using $\lambda = 800$ nm, the $5\times$ objective, and a translation speed of 500 μm/s. The lower group of eight images shows higher magnification views of cases from the upper group of nine images. Within each group, all images use the same scale.

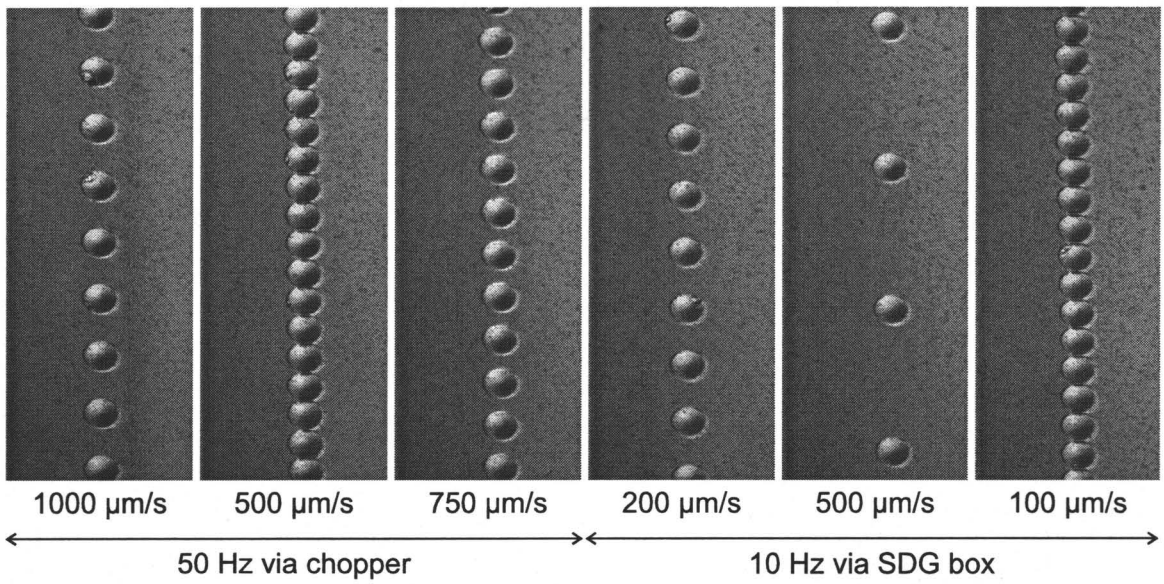

Figure 4.7: Plan-view Nomarski-mode optical microscope images of silicon samples translated at various speeds under a low repetition rate beam. All images use the same scale.

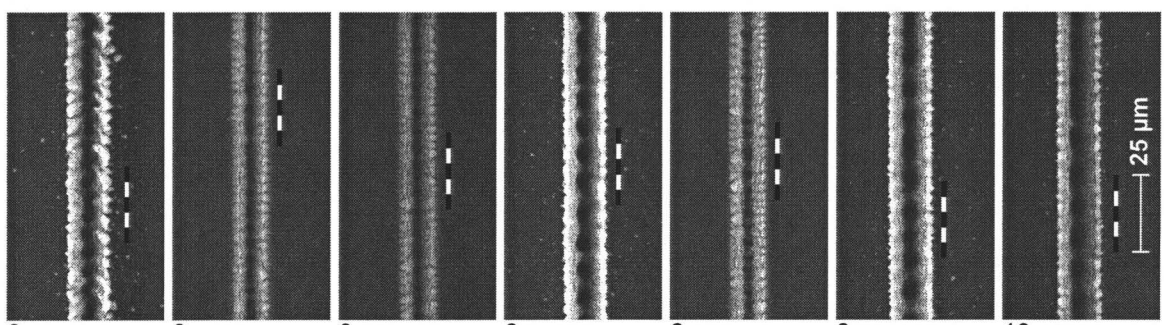

Figure 4.8: Plan-view SEM images of selected grooves irradiated with $\lambda = 800$ nm pulses, showing the rough corrugation at a variety of translation speeds and pulse energies. All images use the same scale. Each black or white line segment has a length of 5 μm.

standard deviation were calculated. The average depths were 52.5, 27.1, and 5.7 μm and the standard deviations were 2.1, 1.0, and 0.5 μm respectively for the three pulse energies. The two highest energy cases in this test can be compared to the experiment whose results are shown in figure 4.6, where 2.0 and 0.68 μJ pulses were used for grooves cleaved along their length (0.68 μJ results not shown). The standard deviations are roughly half the heights of the corrugations. It should be noted that the spot sizes were not measured in this case, although they are expected to be similar for the two experiments. The position of the ridge did not vary significantly between the different grooves within the same set.

A possibility which was investigated was that the beam was changing its pointing direction significantly during machining or that the translation speed was not constant. Figure 4.7 shows rows of craters produced by the laser, either running at a low repetition rate (10 Hz, set using the SDG box which triggers the Pockels cells in the laser cavity), or by using the mechanical chopper (50 Hz, by blocking 19 out of every 20 pulses with the laser running at 1000 Hz). From the image, there does not appear to be significant variation in stage speed or beam position. In similar tests, imaging larger areas and measuring the crater separation at multiple points along the line indicated a rather constant and accurately specified translation speed. For locations on the optical table where the beam was traveling a significant distance, beam tubes were mounted through which the beam propagated. These hollow metal tubes prevented air currents from disturbing the propagation (via variations of air index of refraction with temperature), and reduced the likelihood of accidentally interrupting the beam due to moving a cable or other equipment. The images in figure 4.7 also help to show the repeatability of the profile of the single-pulse irradiation sites. The lack of significant variation in crater size implies there was not a major fluctuation in pulse energy.

As noted in the paper [65], the period of the corrugation presented in the paper matched that which would be produced by a near-60 Hz modulation of laser energy or translation speed. This possibility was further investigated by cutting shallow grooves at a variety of translation speeds. Figure 4.8 shows some selected plan-view SEM images. The corrugation tends to have a shorter period for slower translation speeds, but is not always of a 60 Hz temporal period. Also of note, if a 60 Hz fluctuation in laser pulse energy was causing modulation, this would need to be approximately synchronized with the stage motion during multiple passes. Otherwise, the modulation would be out-of-phase with the modulation on the previous pass, though it is possible an initial strong modulation from the first pass would seed deeper holes on subsequent passes.

Preliminary experiments investigating corrugation formation in grooves were done with other laser wavelengths, spot sizes, crystalline orientations, and on germanium. Light with a wavelength of 400 nm was used to cut grooves which were then cleaved along their length. The polarization for $\lambda = 400$ nm relative to the translation direction was the same as in the 800 nm wavelength experiments, and a translation speed of 500 μm/s was used. Similar to the 800 nm case, the unevenness in the groove depth was most pronounced for between 4 and 8 passes, and the corrugation period was around 8 μm. The modulation was similar to or somewhat less severe in the 400 nm case than the 800 nm case. Due to the nonlinear nature of second harmonic generation, if a laser energy fluctuation was the cause of the corrugation, it would be expected that the corrugation would instead be more severe at $\lambda = 400$ nm.

Plan-view imaging of the grooves in the SEM, rather than cleaving the grooves along their length, is useful for observing corrugation. Cleaving is not always successful, and the number of grooves along a cleave is limited to a low number (fewer than ~15–20) due to the space required. Imaging of the results of many different laser parameters is easier in this plan-view configuration. Such imaging of grooves cut in silicon with ultrashort pulses at other wavelengths (specifically, ~2100 nm obtained from the OPA, and 417 nm, obtained via frequency doubling of the laser beam at a time when it was adjusted to 835 nm for a different experiment in the lab) also revealed some corrugation along the bottom of multiple-pass grooves. Three surface crystalline orientations of silicon ((100), (110), and (111)) were investigated, and all showed some cases of corrugation for irradiation with λ =800 nm via a 5× microscope objective. The conditions for corrugation formation did not vary greatly between the different orientations for this focussing condition. Machining of germanium with (100) and (111) surface orientations using the 5× microscope objective produced corrugation viewable in plan-view orientation in the SEM. When a 12.5 cm focal length lens was used to focus the pulses onto germanium, a periodicity could occasionally be observed along the bottom of some grooves (as shown in section 6.3.2).

In general, the periodicity looks somewhat similar to what might be caused in a 'stick-slip' type of phenomenon observed when two objects are in contact with each other. A plausible explanation for the corrugation in laser machining goes along the following lines. A slight depression exposed to laser light is expected to grow deeper, since incident light would tend to reflect into the depression, and greater erosion will be experienced at the bottom of the depression. (A similar idea exists in the evolution of LIPSS and blunt conical structures, whereby greater erosion occurs in the 'valleys' due to increased light absorption there and increased light scattering into the 'valley', while there is reduced fluence on the

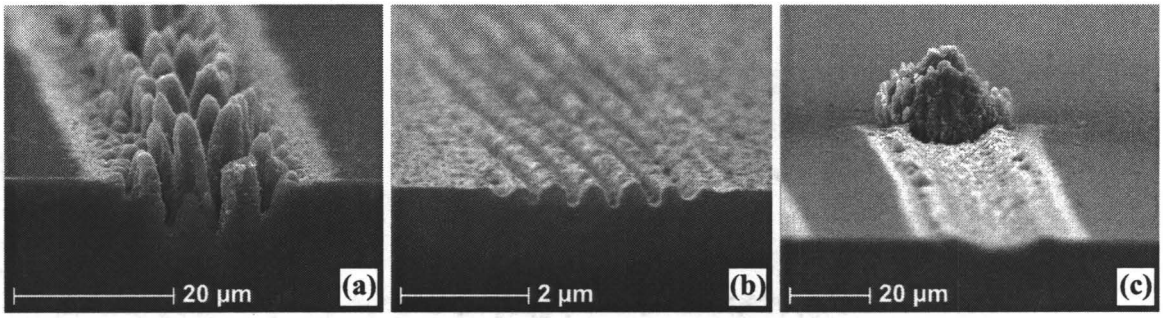

Figure 4.9: Various protruding structures formed by laser machining of silicon with $\lambda = 800$ nm pulses. (a): Blunt conical structures. (b): LIPSS. (c): Debris accumulating at the end of a groove. All cases shown are for a single pass of the laser. Cases (a) and (c) were produced by focussing with a 15 cm focal length achromat lens, while (b) was from a $5\times$ microscope objective.

angled sidewalls. See chapter 6 for more details.) While the sample is translated under the focussed beam, numerous pulses are incident near a depression, and the depression becomes deeper. As the sample translates sufficiently far from the depression, only the weak spatial edges of the beam will be near the depression, and that depression will no longer grow deeper. A subsequent depression can form and will begin to be eroded, and the process will repeat. On each pass of the beam, each depression formed by the previous pass will be deepened. After several passes, the depressions are deep and no longer growing substantially deeper, but the shallower material will still be slowly eroded by the pulses. Such an explanation would explain why the large corrugations become shorter for higher numbers of passes. This is analogous to the eventual erosion of blunt conical structures with a sufficiently high number of pulses. The process is also reminiscent of the erosion of the rim mentioned in the paper [65], whereby the slow removal rate in the wings of the pulse is expected to eventually exceed the decreasing redeposition rate. However, it is difficult to conclusively determine if the process described here is the cause of the corrugation, and further investigations could be performed to test the validity of this explanation. This process would likely be affected by the spot size, however systematic experiments varying the spot size were not performed. Increased debris accumulation at the material surface occurs with increased ambient gas pressure (see, e.g. chapter 8 and reference [98]), and would probably impede corrugation formation. This possibility was not examined experimentally. Unlike in the case of LIPSS formation, it is not expected that the coherent nature of laser light affects the formation of the coarse corrugated structure.

Of final note, corrugation is not the only phenomena which can contribute to an uneven groove depth. Figure 4.9 shows some examples of features which protrude above the original sample surface after machining of grooves. Blunt conical structures protruding from the groove are shown in figure 4.9(a), for which an achromatic lens of 15 cm focal length was used (pulse energy 4.9 μJ, translation speed 100 μm/s). Significant material exists above the original sample surface, showing that the laser irradiation does not solely consist of material removal. The structures shown in the grooves are expected to be similar to some of those shown in section 6.3.2, although side-views of cross-sections (like the one shown in figure 4.9(a)) were not done for the grooves in section 6.3.2. LIPSS running along along the length of the groove are shown in figure 4.9(b), showing that the tops of the ripples protrude slightly above the original substrate surface. Similar protrusion is shown in figure 8(a) of the silicon grooves paper [65], and in a TEM study (see section 4.9, figure 4.16 of this thesis). The LIPSS in figure 4.9(b) were produced using a 5× microscope objective, 100 μm/s translation speed, and 0.089 μJ per pulse. A 'shoveling' effect was observed in the experiment where the 15 cm achromat lens was used, in which material accumulated at the end of a groove. A representative case is shown in figure 4.9(c), for a 1000 μm/s translation speed and 20.3 μJ per pulse. Less 'shoveled' debris was present for significantly slower translation speed. It is not clear to what extent this 'shoveled' material could affect the formation of the coarse corrugation discussed earlier. As noted in the paper, material protrusion is also evident under certain sets of parameters such as the rims shown in figure 10 of the paper [65], and debris near the groove shown in figure 8(b) of the paper [65].

4.8 Groove depth measurements for 400 nm wavelength irradiation and comparison to 800 nm irradiation

The various depth measurement experiments presented in the silicon grooves paper [65] were also performed for $\lambda = 400$ nm irradiation. The majority of these results were presented in the 2003 CLEO conference contribution [95]. The same qualitative trends for depth as a function of the energy, speed, and number of passes parameters observed for the $\lambda = 800$ nm case (two-regime logarithmic, reciprocal, and linear-with-saturation) were also observed for $\lambda = 400$ nm irradiation, although the data and resulting fit parameters were different. For the depth vs. energy experiment, the data for the three translation speeds is shown in figure 4.10, with the corresponding calculated values and fit parameters in table 4.1. The 800 nm data is the same as that in the paper, and is repeated here to enable easier comparison. In the 400 nm case the spot size ω_o was 3.4 ± 0.1 μm, while in the

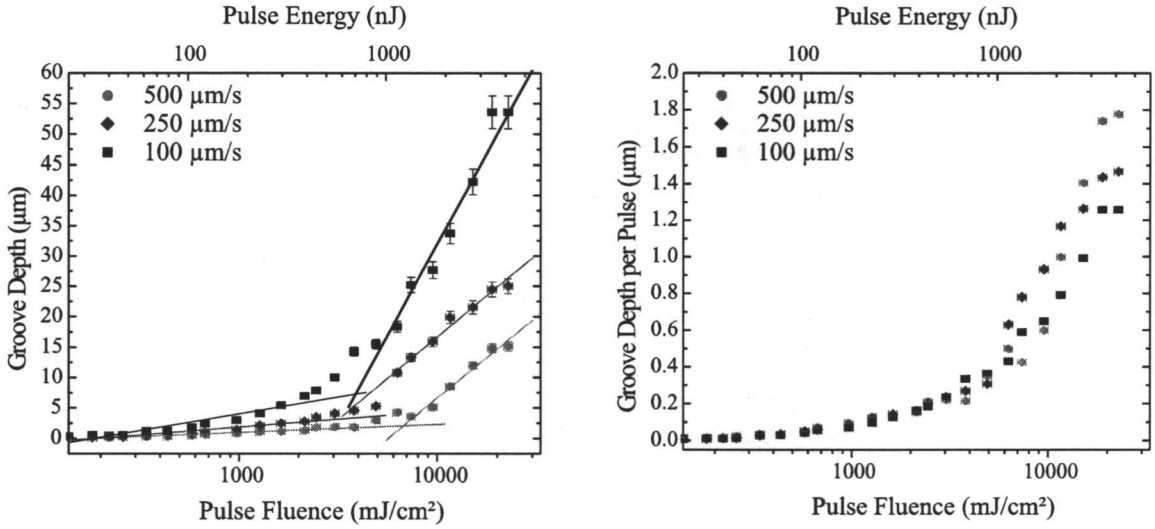

Figure 4.10: Depth vs. energy plots for translation speeds of 100, 250, and 500 μm/s, and depth per pulse at those translation speeds, for 400 nm wavelength irradiation.

800 nm case it was 5.3 ± 0.2 μm. The differences in spot size cause a difference in N_{eff} for the same translation speed at different wavelengths. With the exception of the 100 μm/s translation speed, the $d_\circ$ values are similar for the two wavelengths in the low-fluence regime. As with the 800 nm case, the two higher translation speeds resulted in similar $d_\circ/N_{\text{eff}}$ at 400 nm in the low-fluence ablation regime. The reduced $d_\circ/N_{\text{eff}}$ at 100 μm/s in both wavelength cases could be due in part to increased deposition of debris and depth saturation for sufficiently deep grooves. As in the $\lambda = 800$ nm silicon case, there is not an obvious sharp 'kink' in the depth data separating the two fit regimes. Although scatter in the data would make a delineation less obvious, it is possible that a somewhat continuous change in dynamics exists for silicon and that a two-regime logarithmic dependence does not fully describe the material removal processes (as described in section 4.4).

The results of the depth vs. translation speed experiment at $\lambda = 400$ nm are presented in figure 4.11, with the results from the corresponding fit parameters and analysis in table 4.2. For the depth vs. number of passes experiments, the groove depths from the 400 nm irradiation wavelengths are plotted in figure 4.12. The fit parameters and calculated parameters are shown in table 4.3. Note that unlike in the 2003 CLEO presentation [95], the data in table 4.3 is only for the number of passes up to 10, and includes a data point of zero depth for zero passes in the fit. This is for consistency with the data analysis technique used in the paper [65].

Low-fluence regime

λ (nm)	Speed (μm/s)	N_{eff}	$d_\circ$ (μm)	Φ_{th} (mJ/cm^2)	$d_\circ/N_{\text{eff}}$ (nm)
800	100	66.5 ± 1.5	1.7 ± 0.1	220 ± 70	25 ± 0.1
	250	26.6 ± 0.6	1.2 ± 0.1	250 ± 70	43 ± 0.2
	500	13.3 ± 0.3	0.6 ± 0.1	270 ± 80	43 ± 0.2
400	100	42.6 ± 0.8	2.4 ± 0.1	180 ± 30	56 ± 0.2
	250	17.1 ± 0.3	1.1 ± 0.1	190 ± 30	66 ± 0.2
	500	8.52 ± 0.16	0.6 ± 0.1	180 ± 30	67 ± 0.3

High-fluence regime

λ (nm)	Speed (μm/s)	N_{eff}	$d_\circ$ (μm)	Φ_{th} (mJ/cm^2)	$d_\circ/N_{\text{eff}}$ (nm)
800	100	66.5 ± 1.5	18.1 ± 0.9	1490 ± 730	270 ± 15
	250	26.6 ± 0.6	10.5 ± 0.8	1530 ± 1120	390 ± 30
	500	13.3 ± 0.3	7.8 ± 0.6	2960 ± 2270	590 ± 45
400	100	42.6 ± 0.8	26.0 ± 1.6	2930 ± 1740	610 ± 41
	250	17.1 ± 0.3	11.8 ± 0.9	2430 ± 1830	690 ± 57
	500	8.52 ± 0.16	11.6 ± 0.8	5650 ± 4130	1360 ± 104

Table 4.1: Comparison of groove cutting parameters for 400 nm and 800 nm irradiation wavelengths in depth vs. energy experiments.

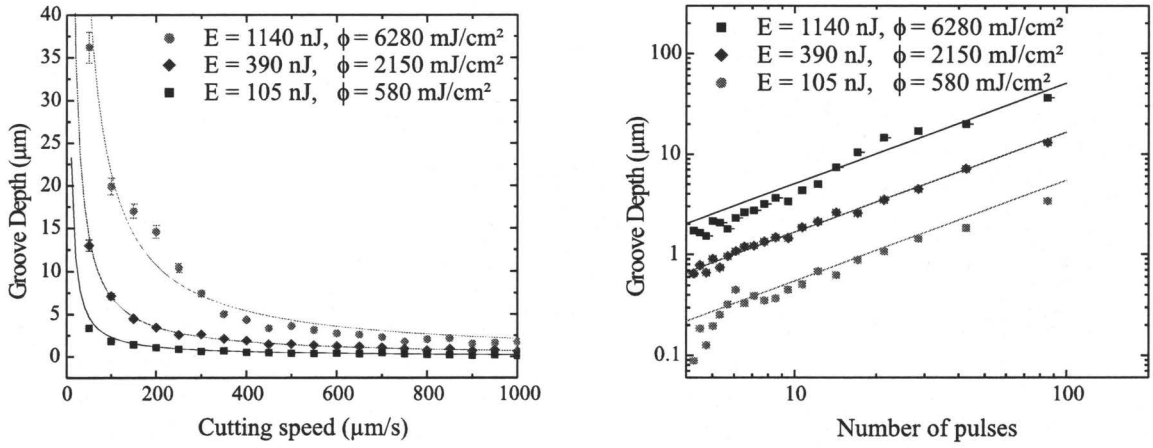

Figure 4.11: Depth vs. translation speed plots for three different pulse energies and 400 nm wavelength irradiation. Also shown are the corresponding depths as a function of the effective number of pulses N_{eff}.

λ (nm)	Pulse Energy (nJ)	Fluence (mJ/cm^2)	Fit parameter A (μm^2/s)	Depth/pulse (nm)
800	2160	4880	2100 ± 50	320 ± 10
	730	1640	510 ± 20	77 ± 3
	230	520	200 ± 10	31 ± 1
400	1140	6280	2150 ± 50	500 ± 19
	390	2150	710 ± 20	170 ± 6
	110	580	230 ± 10	55 ± 2

Table 4.2: Comparison of groove cutting parameters for 400 nm and 800 nm irradiation wavelengths in depth vs. translation speed experiments.

λ (nm)	Pulse Energy (nJ)	Fluence (mJ/cm^2)	Slope (μm)	Depth/pulse (nm)
800	2160	4880	2.7 ± 0.5	200 ± 35
	730	1640	1.3 ± 0.2	95 ± 13
	230	520	0.17 ± 0.06	12 ± 5
400	1140	6280	2.4 ± 0.2	280 ± 30
	390	2150	1.4 ± 0.1	160 ± 9
	105	580	0.35 ± 0.01	41 ± 2

Table 4.3: Comparison of groove cutting parameters for 400 nm and 800 nm irradiation wavelengths in depth vs. number of passes experiments. The curve fits include a point of zero depth for zero passes, and includes the number of passes from 1 to 10.

Graphically, the depth per pulse values for grooves experiments at the two wavelengths are plotted in figure 4.13. For the depth vs. translation speed data and for the depth vs. number of passes ($\leq$10) experiments, the depth per pulse is generally greater for 400 nm light than for 800 nm light. The exception to this trend is the $\lambda = 400$ nm, 6280 mJ/cm^2 data point from the depth vs. number of passes experiment which appears low. For a given wavelength, at low fluences the depth per pulse values do not differ strongly when comparing the translation speed and the number of passes experiments. This is true for both wavelengths. The highest fluence depth per pulse values differ substantially, with the lower value occurring in the depth vs. number of passes experiment for both wavelengths. It is perhaps not surprising that the highest fluence cases behave more anomalously, as the material removal processes under these conditions are more violent and produce more debris, and the grooves are deepest which (as mentioned earlier) complicates a simple description of machining.

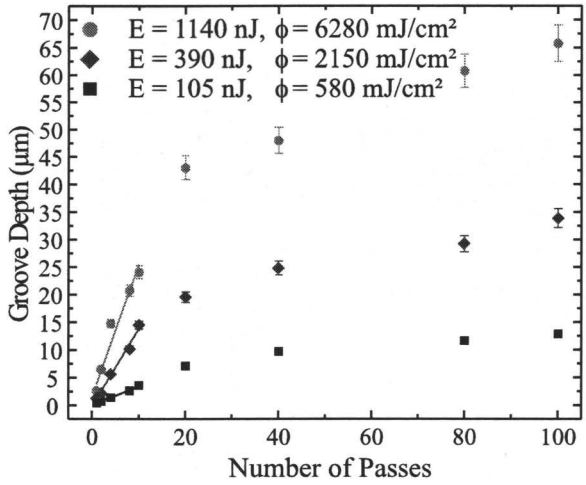

Figure 4.12: Depth vs. number of passes plots for three different pulse energies and 400 nm wavelength irradiation.

In general, there was less scatter in the depth data points for machining with 400 nm wavelength pulses, compared to with 800 nm shown in the paper [65]. Best fit lines tended to be closer to their corresponding data points for 400 nm plots. The 800 and 400 nm experiments were done multiple times, without a significant period of time elapsing between the experiments. Thus, it is unlikely that any variations in the laser performance could cause the reduced scatter at the shorter wavelength. If the laser pulse energy was unstable, it would be expected that the 400 nm data points would show more scatter since the nonlinear second harmonic generation process would make small energy variations in the original 800 nm beam more prominent. The difference in behaviour between 400 and 800 nm wavelength light might be related to the significant difference in (linear) optical penetration depth in silicon between the two wavelengths ($\sim$82 nm vs. $\sim$10.6 μm for $\lambda = 400$ and 800 nm respectively [99]), although the nonlinear (intensity-dependent) penetration depths are also relevant. Preliminary results (see section 4.7) suggest that there is somewhat less corrugation at the bottom of the grooves in the $\lambda = 400$ nm case. On InP [64, 96], data points at both wavelengths tended to lie close to the fit lines. A useful set of experiments would to be to repeat the depth measurement experiments on silicon at other wavelegths. If certain wavelengths give a more predictable depth and/or produce significantly less corrugation, this would be useful to know for a practical application of this research. A preliminary groove cutting experiment was performed using $\lambda \approx 2100$ nm pulses from the OPA, however the light polarization was parallel to the translation direction. This complicates direct comparisons to the 400 and 800 nm wavelength data since the 2100 nm wavelength grooves

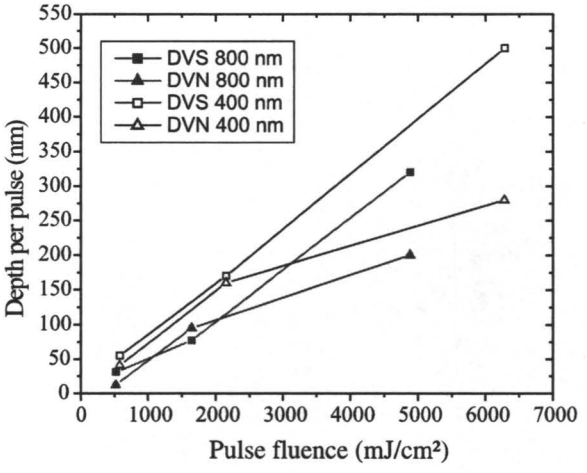

Figure 4.13: Comparison of depth per pulse values from the *depth vs. translation speed* (DVS) and *depth vs. number of passes* (DVN) experiments at 400 and 800 nm wavelengths. The data points are from tables 4.2 and 4.3, in the linear depth per pulse regimes.

showed significant 'branching' with curved sides, similar to that discussed in section 4.6 but more prominent than at $\lambda = 800$ nm.

The geometry of the grooves can be compared for 400 nm and 800 nm wavelength irradiation. Figure 4.14 shows grooves cut with 100, 8, and 1 pass at 400 nm and 800 nm irradiation wavelengths. In both wavelength cases the incident laser polarization was perpendicular to the translation direction. However, it should be noted that different per-pulse fluences were used in the 400 nm and 800 nm cases, in part because it is difficult to know the spot size (and thus fluence) accurately until after the single-pulse craters have been measured and the D^2 fits performed. For the single-pass case it is expected that the groove would be narrower, since the laser spot size for the shorter wavelength is smaller. The somewhat narrower nature of the grooves persists for higher numbers of passes as well. The thesis of Andrzej Borowiec [96] presented preliminary experiments comparing irradiation of InP with 800 nm and 400 nm light. The same qualitative trends for depth were observed (two-regime logarithmic dependence on pulse energy, inversely proportional to translation speed, and initial linear increase followed by saturation with number of passes). As with silicon, InP at 400 nm irradiation produced higher aspect ratio (depth to width) grooves [96].

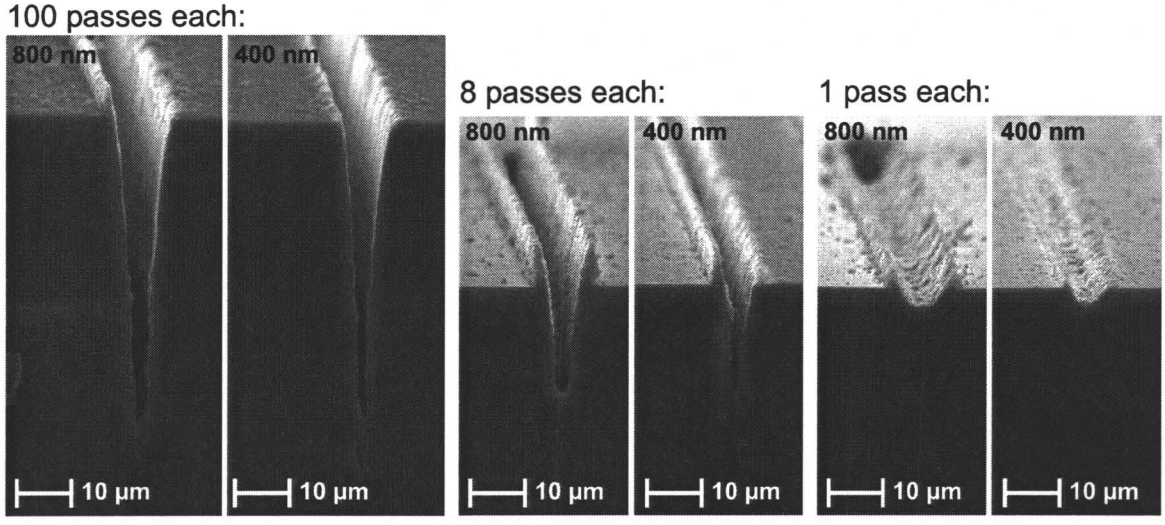

Figure 4.14: Visual (SEM image) comparisons of grooves cut with the same number of passes but different wavelengths and pulse energies. The grooves cut with 400 nm wavelength light tend to be narrower. The fluences for 800 and 400 nm wavelength irradiations were 4880 and 6280 mJ/cm^2 respectively.

4.9 Tripod polishing technique for TEM analysis of grooves

In early 2003, Junji Yamanaka and Garrett Deyne did preliminary cross-sectional investigations of femtosecond laser-machined grooves in silicon, for which focussed ion beam (FIB) milling was used to produce cross-sectional TEM samples. Results from that work (see reference [100]) showed dislocations, polycrystalline material, and amorphous silicon. FIB preparation and subsequent TEM examination of grooves in InP was used successfully by Andrzej Borowiec and Martin Couillard to observe crystalline defects and nanocrystalline material [44]. The expense of preparing a FIB sample, which requires a specialized FIB machine and skilled operator, tends to limit the number of different sites that can be examined. An alternative TEM preparation method, the 'tripod polishing' technique, allows the possibility of obtaining cross-sectional samples of several grooves simultaneously.

In the summer of 2004, Mark Luttikhof and Martin Couillard used the tripod polishing technique with subsequent cross-sectional TEM examination of femtosecond laser-machined grooves in silicon (see reference [101]). By tripod polishing, a thin wedge-shaped sample (shown schematically in figure 4.15) is obtained which can be imaged in TEM. I prepared several samples using ~500 μm and ~700 μm thick silicon wafers, since

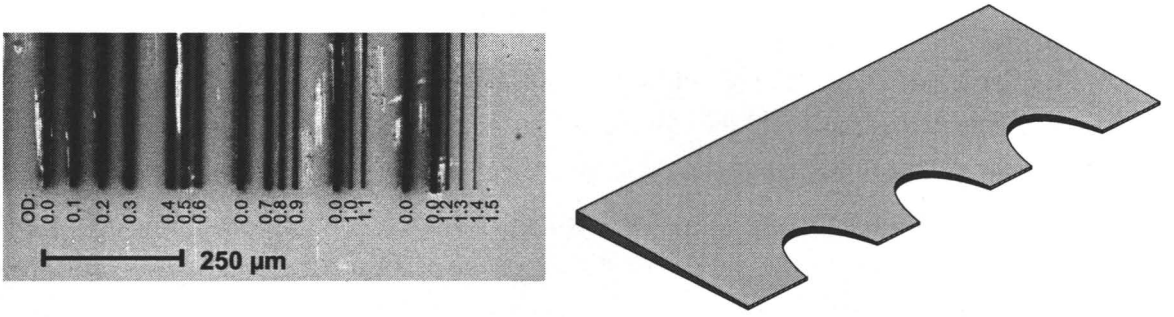

Figure 4.15: *Left*: Optical microscope surface image of various single-pass grooves cut in ~500 µm thick silicon, in preparation for tripod polishing. *Right*: Schematic diagram of a sample after tripod polishing, showing the cross-sections of three grooves.

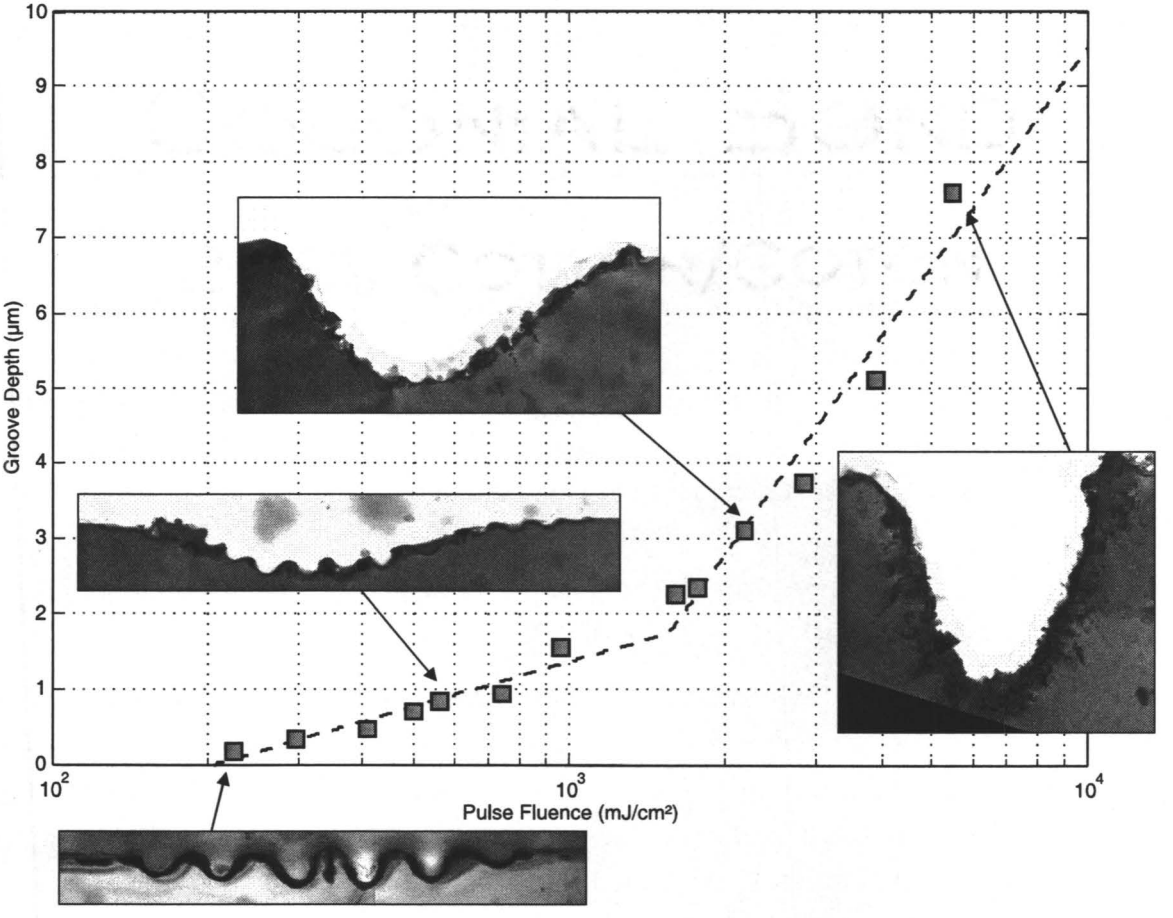

Figure 4.16: Depth vs. pulse fluence graph and cross-sectional TEM images of grooves in silicon, prepared for TEM using the tripod polishing technique. This graph and the TEM images were prepared by M.J.H. Luttikhof and M. Couillard.

the usual ~300 μm thick silicon used in most other experiments had a strong tendency to break during the tripod preparation. The left image in figure 4.15 is an optical microscope image of the surface of a sample before tripod polishing, showing deep (OD 0.0) grooves interspersed with shallower (higher OD) grooves. Since very shallow grooves were difficult to locate, the additional deep grooves were made to aid in finding the shallow grooves. Additionally, rather than using the same spacing between every groove, various spacings were used. This allowed the easier identification of each groove in the TEM imaging. The surface of the grooves was coated with epoxy to prevent damage during mechanical polishing. An Allied Multiprep system polished the sample using a diamond-impregnated plastic lapping film, and produced a 2° wedge. Figure 4.16 shows a plot of groove depth vs. pulse fluence and some selected TEM images, prepared by M.J.H. Luttikhof and M. Couillard. Sub-surface changes can be seen in the TEM images, with the cross-section of LIPSS visible in the lower fluence cases. A nonuniform, resolidified polycrystalline layer was produced which was thicker for higher pulse energies [101]. Higher pulse energies also produced more defects under the layer, extending up to 3 μm below it [101]. This TEM sample preparation technique is a useful alternative to FIB preparation, since many grooves can be prepared on the same TEM specimen simultaneously. The tripod polishing technique however cannot precisely pre-determine the location of the final slice, which severely limits its ability to obtain cross-sections of highly localized laser modifications such as single- and multiple-pulse craters. While the tripod polishing method works on sufficiently long grooves, the FIB technique still allows more precise determination of the desired slice location. The polishing approaches used in the tripod technique could also be useful for examining cross-sections of grooves on material with (111) and (110) surface orientations, as these pose difficulties in cleaving through the grooves.

4.10 Fabrication of waveguides

Silicon-on-insulator (SOI) material can, using photolithography, have a rib etched on it which allows the material to act as a waveguide. The light guides in the thin silicon layer under the rib, confined by the lower refractive index of the air at the surface and by the buried oxide below. In preliminary tests performed in collaboration with A. Knights and his students (D. Walters, N. McGaw, J. Milgram, and J. Lannan), I produced pairs of parallel shallow grooves on the surface silicon layer of an SOI sample, defining a rib. Under certain combinations of groove separation, pulse energy, translation speed, and number of passes, a successful waveguiding structure was produced. However, further work remains to be done in this investigation. The laser direct-write technique gives the ability

to do rapid prototyping of waveguide structures, without needing the prior fabrication of the masks required in photolithography. Another potential advantage is the ability to make arbitrary waveguide shapes, such as curved waveguides, provided appropriate trajectories are performed by the translation stages. Likely the largest problem in this investigation is the roughness of the grooves. This produces much higher losses than waveguides formed with conventional photolithography. Minimal attempts were made to make the walls or bottoms of grooves smooth, although it may be possible using various sequences of machining parameters. If smooth walls were possible, this could find application in a variety of areas in addition to making rib waveguides, such as polishing the facets on the edges of a semiconductor device. As a preliminary test, after machining the SOI wafer was soaked in a potassium hydroxide solution to preferentially etch the machined areas along a specific crystalline axis. While this yielded flat sections along the bottom of a groove, the effect on waveguiding was not determined. A potential problem may be any generation of defects or polycrystaline material within the waveguide, as was suggested in cross-sectional InP studies [44].

4.11 Angled and V-grooves

For the majority of the results presented in this thesis, the laser pulses were incident on the target at approximately normal incidence. However, machining can be done with a non-zero angle of incidence so that a high number of passes will produce a groove which can undercut the original surface of the target wafer. Since the width of a groove decreases along the depth of the groove, the walls of a groove cut at normal incidence are not at a 90° angle relative to the sample surface. However, using an angle of incidence of several degrees could produce a groove wall extending approximately perpendicular to the sample surface. This could be useful in certain applications like milling or cutting edges.

Figure 4.17 shows grooves cut using $\lambda = 800$ nm pulses at various angles of incidence. As with previous experiments, the grooves were cut near the center of the sample, and the sample was then cleaved, so that a cross-section of the grooves could be observed in SEM. Due to limitations of the mounting hardware and the size of the sample chamber at the time the experiment was done, this sample was irradiated in air atmosphere. A plastic hose connected to the fume hood suction had its end positioned near the machining site to minimize the amount of debris entering the lab environment. However, substantial debris was left on the sample surface. Much of this debris was removed by wiping the sample

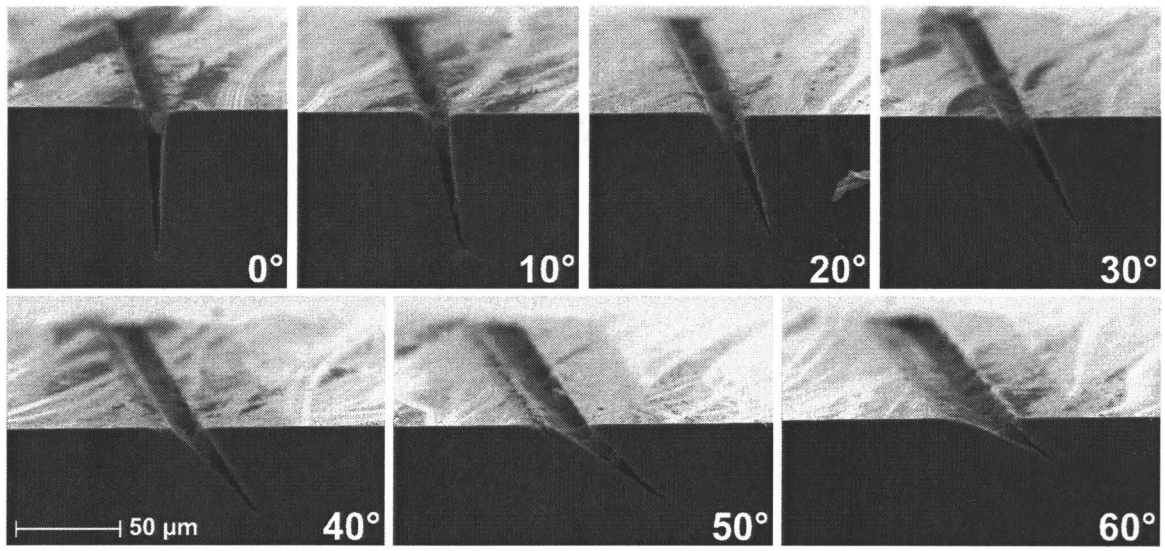

Figure 4.17: SEM images of grooves cut in silicon at angles of incidence from 0 to 60 degrees, using $\lambda = 800$ nm pulses. All images use the same scale. The sample was irradiated in air, and cleaned with three wipes from methanol-soaked lens tissue. The $5\times$ microscope objective was used, with 100 passes, 500 µm/s translation speed, 2.0 µJ/pulse, at 1 kHz repetition rate.

surface with a lens tissue soaked in methanol, three times. Significant debris remained inside the grooves shown in figure 4.17.

Various grooves made by irradiation by 400 nm wavelength light, at 45 degree angle of incidence, are shown in figure 4.18. Two grooves, each at a non-normal angle of incidence and intersecting each other could be used to produce a V-shaped cantilever which would be difficult to manufacture using standard photolithographic or chemical etching techniques. An aluminum mount designed for holding mirror mounts at 45° was placed inside the vacuum chamber. This was used to hold the silicon target at approximately 45 degrees relative to the incoming laser beam direction, and did not prevent the use of a vacuum atmosphere in the chamber. Machining done in vacuum left very little debris on the sample surface or within the groove, compared to cases (such as in figure 4.17) where machining was in ambient atmosphere. Similar results in the comparison of air and vacuum atmospheres for debris generation were observed for drilling of holes in copper (see chapter 8 for more details).

Figures 4.18(a) and (b) are images of grooves for which the edge of the sample was translated in and out of the laser beam, rather than by cleaving through a groove near the

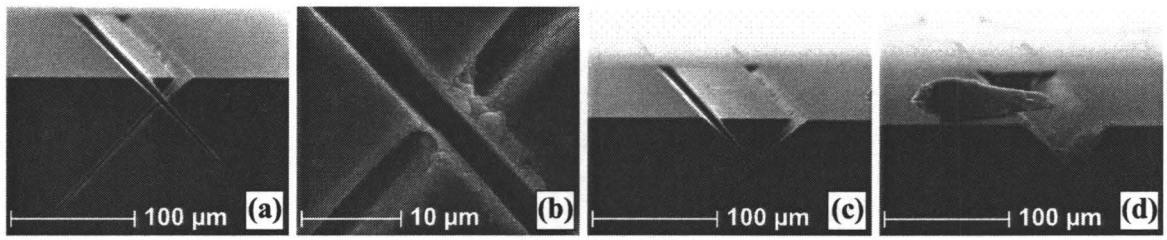

Figure 4.18: Various SEM images of angled grooves cut in silicon, using $\lambda = 400$ nm pulses, to produce large V-shaped structures. The sample was irradiated in rough vacuum environment, with a 45° angle of incidence in all cases. The 5× microscope objective was used, with 100 passes, 500 µm/s translation speed, 1.0 µJ/pulse, at 1 kHz repetition rate.

center of the sample. Grooves for which the focussed laser beam passed beyond the end of the sample tended to have a very large depth at the edge of the sample. This is presumably because material removed from within the groove could easily escape out the side, and the laser light was at some times incident (at grazing incidence) on the side of the sample. Figure 4.18(a) shows a rather narrow V-shaped cantilever. Figure 4.18(b) shows a higher magnification of the bottom of a V-structure, showing that material from the second cut has been pushed into the first cut, somewhat plugging the first cut. It could be the case that the recast material has attached the bottom of the V to the substrate, thus inhibiting its movement as a cantilever. Potentially, the material could be removed by re-cutting the first cut with a few more passes, provided the sample could be precisely re-aligned to the position of the first cut. Alternately, some sort of chemical etchant could conceivably be used to remove the recast material while not removing substantial amounts of the V itself, provided the chemical exposure time was sufficiently short. Some chemical etchants, such as potassium hydroxide used in section 4.10, have higher material removal rates along certain crystalline directions, and this may be advantageous.

Angled grooves which were cut near the middle of the sample and cleaved are shown in figures 4.18(c) and (d). In (c), the bottoms of the grooves are touching, although due to variation in the groove depth there may be many points at which the V piece is still connected to the underlying substrate. This reflects the uncertainty in precisely predicting the depth of a groove under predefined laser parameters, particularly since there is some uncertainty in setting the focal position precisely at the surface of an angled target. It is difficult to determine if the bottoms of two angled grooves touch, without inspection in SEM or optical microscopy. In figure 4.18(d), the V piece has broken away from the original target at the end of the V, leaving a large trench. It is not clear if the piece of

material sitting on the surface was originally part of the V. For producing a freely-vibrating cantilever, cleaving may not be the best option since it would be difficult to control where on the V the cleave occurs.

One of the initial motivations for cutting angled grooves and V-grooves was to be able to rapidly remove large quantities of material. Focussed ion beam milling has the ability to achieve very fine and precise removal of material, but is less feasible for the removal of many cubic micrometres of material. Femtosecond laser-based removal of macroscopic quantities, followed by finishing with FIB could be a useful manufacturing process, particularly for prototyping or for low quantities of samples. It would avoid the need for development of masks and chemical etching in photolithography which are typically more effective for highly parallel processing. Preliminary work on angled grooves in InP was also performed by A. Borowiec and presented in his thesis [96]. This yielded qualitatively similar results, showing the applicability to multiple materials.

Several important points needed to be addressed in the sample setup in order to produce angled grooves, and certain techniques were developed. For a variable angle of incidence, the sample was taped to a glass microscope slide, which was held by a clip designed for holding glass filters. This clip was attached to a rotation stage, in turn attached to the translation stage, so that the angle of incidence could be set by rotating the rotation stage. Approximately normal incidence was determined by finding where the collinear sample illumination (the light source for observing the sample with the CCD camera) was reflected most strongly back toward the CCD camera. Under non-normal incidence the sample was very difficult to observe since the usual illumination source did not reflect back to the camera. In such cases, a 6 V light bulb on the end of a rod was positioned near or inside the chamber such that light from the bulb was reflected by the sample into the camera. A later variation of this configuration used the end of a flexible fiber optic light pipe positioned near the sample. A white piece of paper positioned inside the chamber, with a bright light source shining on the paper, could also be used as it scattered sufficient light toward the sample to observe the sample on the CCD camera. In this configuration light could be shone through the window onto the paper, allowing machining to be done in a vacuum without a light source within the chamber. X-ray shielding was mounted around the sample and illumination, requiring careful positioning of the light source and shielding so that there were no collisions between them and the stage or objective during translation stage movement. The sample was angled such that reflected laser light was reflected away from the user and onto a dark surface.

Significant care was required to ensure that the sample was positioned correctly, so that movement along a translation stage axis (usually the y axis) did not cause the position of the sample to vary vertically under the focussed beam. Otherwise, the sample would move in-and-out of focus during translation. The sample would ideally be allowed to rotate on the glass slide itself, so that two separate grooves could more easily be aligned to be parallel to each other. Multiple connected small rotation stages (half-inch-diameter mounting surface and rotating around perpendicular axes) were later purchased to enable more careful positioning, however they were not yet available when the angled experiments presented in this thesis were performed. A larger machining chamber, built after the experiments presented here were performed, was available for later work. It allowed complex mounting hardware to be placed within the chamber, avoiding the need to do machining of angled grooves in the air atmosphere.

A strategy which was used in later angled surface work was to make single-pass low-energy grooves on the sample as markers while the sample was positioned at normal laser incidence. The desired positions of angled grooves would be indicated by these shallow marks. These marks were relatively easily located when the sample was at an angle, reducing the probability that incorrect locations were machined, and helping ensure that the desired groove location was positioned such that it did not move in-and-out of focus.

4.12 Conclusions

In addition to the conclusions presented in the silicon grooves paper [65], additional conclusions can be made from the results of the experiments presented here. Grooves cut in silicon with 100 passes show a dependence on pulse energy qualitatively similar to that for single-pass grooves and for indium phosphide [64]. For relatively shallow grooves, various combinations of laser parameters which give the same net accumulated energy produce a similar groove depth. However, for deep laser-cut grooves the depth does not depend solely on the total accumulated energy. The trends due to varying the laser polarization relative to the translation direction at $\lambda = 800$ nm also exist for $\lambda = 400$ nm laser pulses. Polarization trepanning and $\sim$45° polarization conditions also produce small amounts of branching near the bottom of a groove, but with relatively straight sides and no observed tendency to branch in a particular direction. A corrugation or modulation in groove depth, especially strong for between 4 and 8 passes of the laser, is produced under numerous conditions, including different irradiation wavelengths, target crystalline orientations, materials (silicon and germanium), and focal spot sizes. The corrugation period depended somewhat on laser

and translation parameters. In groove production, femtosecond laser machining does not solely remove material, but can redistribute material causing it to extend above the original substrate. Machining with $\lambda = 400$ nm pulses can produce narrower grooves with a generally higher material removal rate. Less variability exists in the depth data for the shorter wavelength, potentially allowing more predictable groove depth. Multiple techniques can be successfully used to image cross-sections of laser-machined grooves, including cleaving, the tripod polishing technique, and focussed ion beam milling. Each method has particular advantages and disadvantages, such as the cost and the applicability to certain substrate thicknesses and orientations. Grooves can be cut with a non-normal angle of incidence, although some technical aspects of the machining process still need to be solved before reliable fabrication of structures like V-shaped cantilevers can be attained. Numerous further investigations would be of value to more completely describe the behaviour of femtosecond laser machining of grooves. Additionally, the cross-sectional groove depth measurement experiments from Si(100) could easily be repeated on Ge(100) or other materials of (100) surface orientation using the same experimental approaches, as they would cleave easily through grooves.

Chapter 5

Periodic Surface Structures on Semiconductors

5.1 Introduction and motivation

Formation of laser-induced periodic surface structures (LIPSS) on solid surfaces after laser irradiation has been called a "universal phenomenon" [52], as it occurs for a broad range of laser wavelengths and wide variety of materials. The pattern is generally considered to result from interference between the incident beam and a surface scattered field [52], resulting in inhomogeneous energy deposition. For normal laser incidence, they usually have a period roughly equal to the in-air wavelength of the light, and for semiconductors, the structures generally form lines running perpendicular to the incident laser polarization [1].

On InP, GaP, and GaAs, Andrzej Borowiec observed a periodic structure with a period roughly 4.2–5.1 times smaller than the laser wavelength [59], but only for photon energies less than the bandgap energy of the semiconductor. These were named high spatial frequency LIPSS, or HSFL. In addition to HSFL, more 'classic' LIPSS formed on InP, GaP, GaAs, InAs, silicon, germanium, and sapphire with periods close to (but less than) the free space wavelength of the laser pulse. These were named low spatial frequency LIPSS, or LSFL, to differentiate them from HSFL. Examination of germanium and silicon did not reveal HSFL under the condition used in the paper [59]. The 800 nm wavelength ultrashort pulses of the Ti:sapphire laser system with a 5× microscope objective were used in the experiments [59], along with the ~1300 and ~2100 nm wavelengths produced by an optical parametric amplifier (OPA) pumped by a $\lambda = 800$ nm Ti:sapphire system.

In late 2002, as part of an experiment for silicon groove machining using $\lambda \approx 2100$ nm pulses and the 5× microscope objective, I observed a small region of a fine periodic structure in SEM on a 100-pulse site. The previous experiments [59] were typically done for fewer than 100 pulses, and by only 20 pulses HSFL were generally prominent on III-V semiconductors. The fine structures on silicon had a substantially different morphology than the HSFL on other materials (silicon showing shallow surface changes rather than

gaps extending significantly into the substrate), and required a higher number of pulses. This observation led to subsequent experiments using much higher numbers of pulses (up to 10 000 or more) and larger spot sizes to increase the area over which the fine structures were formed. Similar experiments with $\lambda \approx 1300$ nm irradiation were also begun, and multiple structure types were found to form solely for the below-bandgap photon energy irradiation of silicon. Both Si(100) and Si(111) wafer surface orientations were used, and experiments were repeated to confirm the repeatability of the phenomena. The results were presented in a conference poster [102] at CLEO 2004, and later published in a peer-reviewed journal article [58]. Preliminary experiments on Ge(111) were performed along with the silicon experiments, however due to time constraints more rigorous LIPSS experiments on germanium were not performed and the results were not published. In the silicon and germanium work, I did all the laser irradiation, SEM, and optical microscope work, and all data analysis. I also did the literature review, preparation and presentation of a poster [102], and the writing of the article [58]. I performed many of the AFM scans and analysis, while AFM imaging early in the research was done by A. Duft.

Further investigations on the formation of LIPSS were later done by Eugene Hsu on GaP. The choice of GaP, which has a bandgap energy greater than the 800 nm photon energy, allowed further HSFL experiments to be performed at $\lambda = 800$ nm without the complications introduced by the use of the OPA. It also provided additional experimental possibilities such as the variation of pulse duration over four orders of magnitude, not easily implementable with the OPA output. Cross-sectional transmission electron microscopy studies on GaP HSFL and LSFL structures were performed by Eugene Hsu with Gianluigi Botton and Christian Maunders. The GaP results were published in two peer-reviewed journal letters [46, 60]. My role was in providing laser training and assistance in the earlier stages of the GaP research, and I contributed to scientific discussions during the data analysis and writing of the GaP papers.

5.2 Pages from the silicon ripples paper [58]

The pages from the silicon ripples paper (Applied Surface Science **253**, 4970 (2007), reference [58]) are reproduced on the following pages[1]. The experimental approach and techniques are outlined, and the results are presented and discussed. Additional comments on the work presented in the publication are then given after the paper, along with other unpublished results and results obtained after the publication of the silicon paper. Results

[1] See appendices C and F for copyright and permission information.

from the work on gallium phosphide, done with Eugene Hsu, are also presented after the paper.

Available online at www.sciencedirect.com
ScienceDirect
Applied Surface Science 253 (2007) 4970–4977
applied surface science
www.elsevier.com/locate/apsusc

Sub-wavelength surface structures on silicon irradiated by femtosecond laser pulses at 1300 and 2100 nm wavelengths

T.H.R. Crawford [a,*], H.K. Haugen [a,b]

[a] *Department of Engineering Physics, McMaster University, Hamilton, Ontario, Canada L8S 4L7*
[b] *Department of Physics and Astronomy, McMaster University, Canada*

Received 3 June 2006; received in revised form 29 October 2006; accepted 4 November 2006
Available online 14 December 2006

Abstract

We present periodic ripples and arrays of protrusions formed on the surface of silicon after irradiation by low-fluence linearly polarized femtosecond laser pulses. Laser-induced periodic surface structures (LIPSS) are observed for irradiation at center wavelengths of 800, ~ 1300, and ~ 2100 nm, with the structure periods somewhat less than the incident wavelengths in air. Additionally, we observe structures with spatial periods substantially less than the incident laser wavelengths. These sub-wavelength periodic structures form only when the photon energy is less than the silicon bandgap energy. We discuss a number of factors which may contribute to the generation of this surface morphology.

PACS : 61.80.Ba; 78.30.Am; 79.20.Ds

Keywords: Femtosecond pulsed laser; Silicon; Surface morphology; Sub-wavelength period

1. Introduction

The formation of parallel grooves on laser-irradiated surfaces was first reported by Birnbaum [1] in 1965. In several subsequent investigations using neodymium-doped and CO_2 lasers, ripples with periods roughly equal to the laser wavelength were observed (see, e.g. [2] and references therein). Formation was typically attributed to the interaction between incident and scattered radiation. Similar laser-induced periodic surface structures (LIPSS or 'ripples') have since been observed on a wide variety of materials from a range of laser sources, and their formation processes have been explained [2–6]. These structures consist of parallel ripples, and, for semiconductors, generally form lines aligned perpendicular to the polarization of the incident laser radiation [7]. For irradiation at normal incidence, they usually have a period roughly equal to the wavelength of the incident laser light in air.

Within the past few years, many groups have observed structures after femtosecond pulse irradiation whose periods were substantially shorter than the irradiation wavelength (see, e.g. [8–29]). In some investigations involving multiple laser wavelengths, the presence of such structures depended on the irradiating wavelength [8–10]. For femtosecond pulse irradiation, we have reported substantially sub-wavelength periods which formed only when the incident photon energy was less than the bandgap energy of the material [8,9]. In our first study [8], lines running perpendicular to the incident laser polarization formed on compound semiconductors. Fewer than 20 pulses were generally sufficient for this ripple formation, and fewer than 100 pulses were typically used. These structures were not observed on silicon or germanium at any wavelength [8]. In this work we report and discuss several periodic structures on silicon which were not observed under the conditions of our first study [8]. These structures do not appear to be the same as those reported by other groups. Small ripples and arrays of 'bumps' and 'pits' are produced by several hundred low-fluence pulses, but only when the laser photon energy is less than the bandgap energy. The periods of these structures are roughly ~ 50% or ~ 20–25% of the laser wavelength, depending on the structure type [9].

The use of femtosecond laser pulses for material modification has a number of advantages over longer pulses, such as the

* Corresponding author. Tel.: +1 905 525 9140x24859; fax: +1 905 527 8409.
E-mail address: crawftr@mcmaster.ca (T.H.R. Crawford).

0169-4332/$ – see front matter © 2006 Elsevier B.V. All rights reserved.
doi:10.1016/j.apsusc.2006.11.004

smaller heat-affected zone and a reduction of the plasma screening effect [7]. The precision of laser machining with femtosecond pulses is generally better than that produced by longer-pulse lasers [7]. Surface patterning has a variety of potential applications, for example where increased surface area is desired. Surface roughening could be used to improve adhesion of other materials [30]. A textured surface can have high optical absorption and in some applications could be used as an alternative to anti-reflecting coatings [31]. Pointed structures can be used as field-emission sources [26,28,30,31]. Additionally, long-range ordering is relevant to the use of nanostructures in electronic materials applications [32]. Most femtosecond laser modification experiments to date have been performed with a photon energy greater than the bandgap energy of silicon ($\sim$ 1.11 eV, corresponding to a wavelength of $\sim$ 1120 nm). In contrast, material irradiation with femtosecond pulses at longer wavelengths is a relatively unexplored area. Such pulses can be generated using optical parametric amplification and by ultrafast fiber and 'all-diode-pumped' solid-state lasers incorporating certain rare-earth dopants. As these evolve and become more commercially available, their use in material modification applications is likely to increase.

2. Experimental

A commercial sub-50 fs Ti:sapphire regenerative amplifier produced linearly polarized pulses with a peak wavelength λ of 800 nm and a repetition rate of 1 kHz. These pulses were used for sample irradiation, or were used to pump an optical parametric amplifier (OPA). This produced linearly polarized beams at center wavelengths of 1280–1300 and 2070–2100 nm, with typical pulse durations between 50 and 120 fs. These durations are determined from interferometric autocorrelations performed near the OPA output, using the two-photon response of a silicon or InGaAs photodiode. Spectra were measured using a linear CCD-based spectrometer or a scanning monochromator with a photodiode for the OPA wavelengths.

A set of $\sim$ 1 mm thick reflective metallic neutral density filters was used to vary the pulse energy by increments of $\sim$ 0.1 OD (transmission $=10^{-\mathrm{OD}}$). For experiments at $\lambda = 800$ nm, a zero-order half-wave plate and a thin-film polarizer were placed before the filters to provide additional attenuation. When fewer than 50 pulses were desired on the sample, a mechanical chopper was used to reduce the repetition rate to 50 Hz. This rate was low enough to allow the selection of individual pulses with a synchronized computer-controlled mechanical shutter. For higher numbers of pulses, only the mechanical shutter was used. On each sample a grid of irradiation sites was produced, with varying pulse energies along one axis and varying numbers of pulses along the other axis [33].

The pulses were focused onto polished crystalline silicon surfaces at nominally normal incidence. A 150 mm focal length BK7 plano-convex singlet lens was used, unless otherwise noted. The resulting on-sample spot size ω_0 (spatial radius at $1/e^2$ of peak intensity) with this lens was $\sim$ 20 to $\sim$ 35 μm, depending on the wavelength and radius of the original beam. Two types of silicon wafers were used. Samples with (1 0 0) surface orientation were phosphorus doped with a resistivity of 2–6 Ω-cm, and (1 1 1) orientation were boron doped with a 7–13 Ω-cm resistivity. Both were approximately 300 μm thick, with a rough back surface and typical lateral dimensions of approximately several millimetres. Wafers were cleaned in acetone, methanol, and an HF solution several months before the experiments and stored in air atmosphere inside plastic trays. For irradiation, samples were placed on an aluminum cylinder inside a small vacuum chamber equipped with a 1 mm thick fused silica window. The chamber was mounted on a computer-controlled xy translation stage and evacuated to a rough vacuum of less than $\sim$ 0.1 mbar. Observation of the sample was accomplished with a confocal incandescent light source and CCD camera with video monitor.

A CCD beam profiler relying on multi-photon effects for the OPA wavelengths confirmed that the far-field intensity distribution was Gaussian, to a reasonable approximation. The laser power at $\lambda = 800$ nm was measured using a silicon photodiode power meter, while at longer wavelengths a low-power thermal surface absorbing head was used. The peak pulse fluence $2E/\pi\omega_o^2$ (where E is the pulse energy) was estimated after measuring the spot size on sample, using a D^2 method on single-pulse and low multiple-pulse craters. This method also allowed an estimation of the modification threshold fluence. Further details are given in a previous work [34]. The D^2 method assumes a Gaussian spatial profile. However, the irradiated regions tended to appear somewhat elliptical, particularly after irradiation by hundreds of pulses. To obtain a simple estimate of the diameter D, we took the arithmetic mean of the major and minor axes of the ellipse. These measurements were to the outer edge of any observable surface modification under optical microscopy, as this was the most readily and consistently observable feature. Due to uncertainties in the pulse energy and spot size, the fluences reported here have an uncertainty of approximately $\pm$ 30%. We report the incident fluences, not considering reflection at the silicon surface.

After irradiation, the modification sites were imaged using Nomarski-mode differential interference contrast optical microscopy. Some sites were also imaged using scanning electron microscopy (SEM) to improve the resolution. Atomic force microscopy (AFM) was used on some sites for imaging, to measure feature heights and depths and to obtain cross-sectional profiles. A Nanoscope IIIA AFM with an Olympus AC160TS AFM tip was used, with a manufacturer-quoted tip radius of <10 nm and tip full-angle of 35°. This system provided a lateral resolution of less than $\sim$ 10 nm and vertical resolution of $\sim$ 1 nm.

3. Results

LIPSS with periods somewhat less than the laser wavelength were observed on Si(1 0 0) and Si(1 1 1) after irradiation by 800, $\sim$ 1300, and $\sim$ 2100 nm wavelength light. We will call these 'low spatial frequency LIPSS' (LSFL) after Ref. [8].

These run along an axis perpendicular to the laser polarization, meaning that the normal to the ripples (i.e. the wave vector of the ripples) is oriented parallel to the electric field direction. They have a period which is around ~ 80% of the in-air laser wavelength. The LSFL observed in this work are qualitatively similar to the LSFL shown in reference [8], although the larger spot size used in the present work provides LSFL covering a larger area. They form for a wide range of fluences, in the center of irradiation sites where the local fluence is highest. For low numbers of pulses, the LSFL formation threshold is slightly above the single-pulse modification threshold, but decreases with increasing number of pulses. For a constant fluence, as the number of pulses increases the areas of LSFL eventually become rough and lose any obvious long-range periodicity. For sufficiently high fluences and numbers of pulses, a rough, deep hole begins to form. In this study, we only characterized rather shallow surface modifications and we did not analyze structures formed within holes.

An 'intermediate' or 'medium-sized' type of ripple forms between ~ 100 and ~ 1000 pulses, in a narrow fluence range near the single-pulse modification threshold. At both ~ 1300 and ~ 2100 nm wavelengths the ripples have a period which is approximately half the incident radiation wavelength, and run parallel to the laser polarization. These structures form more readily at ~ 1300 nm than at ~ 2100 nm, and were not observed after $\lambda = 800$ nm irradiation under our experimental conditions. They are present only in the center of laser-modified areas, and were not observed forming a ring around some other feature. On both Si(1 0 0) and Si(1 1 1) the same type of structure formed. The fluence range for the formation of these ripples is narrower than that of the LSFL and of the fine ripples and fine bumps discussed later. Fig. 1 is a Nomarski microscope image showing intermediate ripples at the center of the irradiation area. An AFM cross-section of similar ripples is shown in Fig. 2. These structures have a peak-to-valley height on the order of

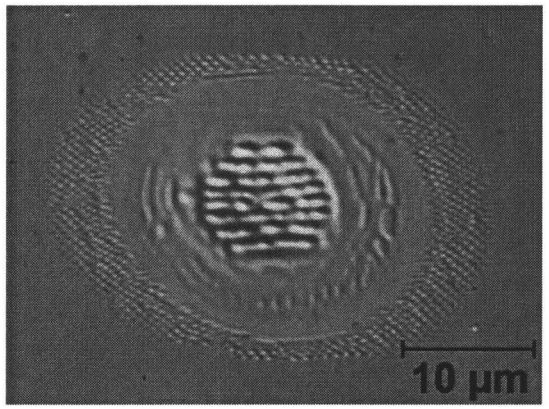

Fig. 1. Nomarski image of Si(1 0 0) irradiated by 350 pulses of ~ 2100 nm wavelength light. A pulse energy of 1900 nJ (peak fluence 190 mJ/cm^2) was used. The laser polarization was approximately horizontal in this image. Intermediate ripples formed in the center of the crater, while fine bump arrays formed around the edge.

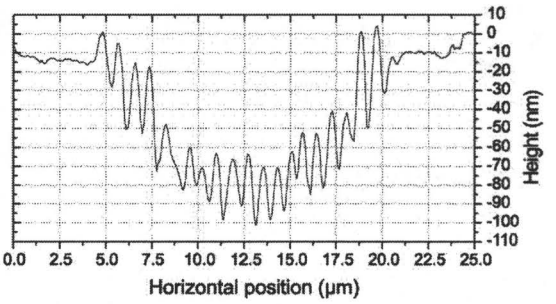

Fig. 2. AFM cross-section of intermediate ripples, formed by irradiation of Si(1 0 0) by 200 pulses of ~ 1300 nm wavelength light. A pulse energy of 3200 nJ (peak fluence 200 mJ/cm^2) was used. Note the different scales on the two axes of the plot.

tens of nanometres. They do not coexist with LSFL. As the number of pulses increases, the structure becomes disordered, and LSFL begin to cover the area.

Between ~ 100 and ~ 2000 pulses, rows of periodic 'pits' and 'bumps' are present for fluences near and below the single-pulse modification fluence. These periodic structures form at both ~ 1300 and ~ 2100 nm, and the row spacing is ~ 20–25% of the laser wavelength in air. They are found in the center of sites for low-fluence irradiation, and near the edges of the higher-fluence modification regions where the local fluence was low. They are shown in Fig. 1 in a ring surrounding longer-period ripples. Small patches of disordered bumps can also be found in a narrow region at the edge of irradiation sites for higher fluences and numbers of pulses. Irradiation of both Si(1 0 0) and Si(1 1 1) resulted in these structures. The rows run parallel to the laser polarization, with the bumps out-of-phase by ~ 180° between adjacent rows. Large areas of these bumps can show structures resembling dislocations in a crystal, where one row ends within the grid. Fig. 3 shows an example of a large array, and Fig. 4 shows AFM cross-sections of fine bump structures. Along the laser polarization (along the center of a row), there is a relatively smooth variation in height. Perpendicular to the laser polarization, the rows are separated by a flat surface in approximately the same plane as the unmodified substrate. The bumps themselves extend several tens of nanometres above the original surface of the sample, and the pits extend a few tens of nanometres below the original surface. It is possible under optimal energy and focusing conditions to make large arrays of these structures. However, it is difficult to repeatedly obtain these conditions during irradiation due to uncertainties in the laser energy and focal positioning. When the fine ripples (discussed later) are present near the bumps, the rows of bumps are typically colinear with these ripples. For high enough fluence or number of pulses, the surface becomes disordered and somewhat smoother, followed by the formation of longer-period ripples. This progression as the local fluence increases toward the center of an irradiation site can be seen in Figs. 1 and 3.

Arrays of fine bumps were not observed on silicon after irradiation at $\lambda = 800$ nm. However, scattered bumps lacking

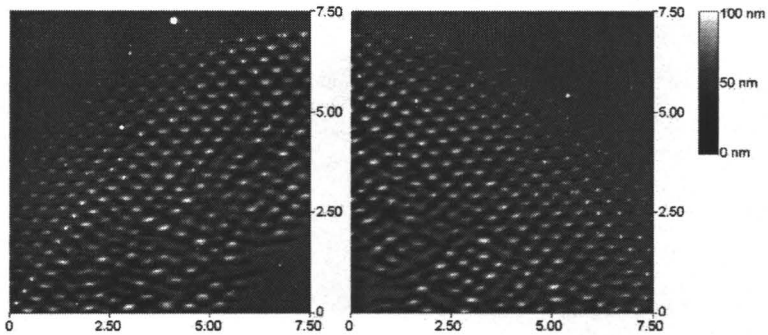

Fig. 3. AFM images of fine bump arrays on Si(1 0 0). The sample was irradiated by 650 pulses of ~ 1300 nm wavelength light. The pulse energy was 2700 nJ, corresponding to a peak fluence of 170 mJ/cm^2. The laser polarization was approximately horizontal in these images. Axis dimensions are in microns, and both images use the same height scale. The center of the irradiation area is beyond the lower right corner of the left image, and beyond the lower left corner of the right image.

obvious long-range order were occasionally formed at 800 nm near the edges of irradiation sites involving thousands of pulses. Under SEM imaging the elongated bump shapes resemble the protrusions formed by ~ 1300 and ~ 2100 nm wavelength irradiation, and have a length of ~ 200 nm. The range of fluences required for their formation is much smaller than for the other wavelengths, and they were rarely observed under our experimental conditions.

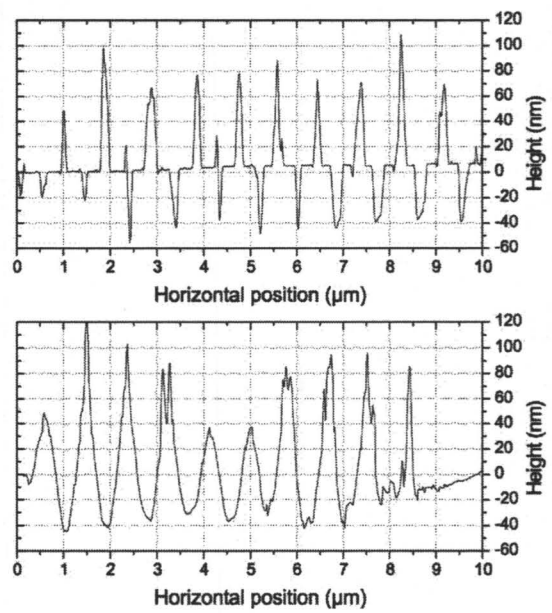

Fig. 4. Cross-section plots from a fine bump array formed at ~ 2100 nm wavelength after irradiation by 750 pulses. The pulse energy was 3800 nJ, corresponding to a peak fluence of 140 mJ/cm^2. In this case the focusing element was a 200 mm focal length lens. (Top) Cross-section perpendicular to a line of bumps (perpendicular to the laser polarization); (bottom) cross-section along a line of bumps (parallel to the laser polarization). Note the horizontal axes have a different scale than the height axes.

A type of thin, 'fine' ripples forms aligned parallel to the laser polarization, for irradiation by ~ 100 to ~ 300 pulses. The required fluences are near the single-pulse modification threshold. AFM images and an *averaged* cross-section of these ripples are shown in Fig. 5. Fine ripples are sometimes located near the outer edges of the regions of fine bumps described above. They form more readily at ~ 2100 nm than at ~ 1300 nm, though at both wavelengths the spacing is ~ 20–25% of the laser wavelength in air. These structures were not observed after irradiation by $\lambda = 800$ nm light. We attribute the random debris seen in Fig. 5 primarily to redeposited material from irradiation sites on the sample. The ripples consist of protruding ridges with a slight dip on either side of a ridge. Near the outer ends of the long ripples shown in Fig. 5 they evolve into a structure resembling a string of particles along the center of a trench. The average height of the particle strings is ~ 8 nm, with a trough on either side of the ridge only 2–4 nm deep. From the AFM scan, it is not possible to conclusively determine if the 'particles' are truly particles, or if they are protrusions attached to the substrate. Based on simple AFM cross-sections, they have heights of 10–15 nm and widths of 30–40 nm. In preliminary experiments using a 5 × microscope objective at $\lambda \approx 2100$ nm it was possible to produce fine ripples, though over a small area due to the smaller spot size compared to that obtained with the lens.

Using the D^2 fitting method described earlier, single-pulse modification threshold fluences in the range of ~ 100–200 mJ/cm^2 were found for each wavelength. However, it is important to note that there is a substantial uncertainty in the specific values, since the accurate determination of modification thresholds was not the primary purpose of this experiment. Many factors, such as different spot sizes and pulse lengths at each wavelength could complicate a fair comparison of these fluences.

On laser-textured areas with an elliptical shape, the major axis of the ellipse was typically parallel to the polarization of the original laser beam. As an additional test performed at $\lambda = 800$ nm, a half-wave plate was placed in the beam before

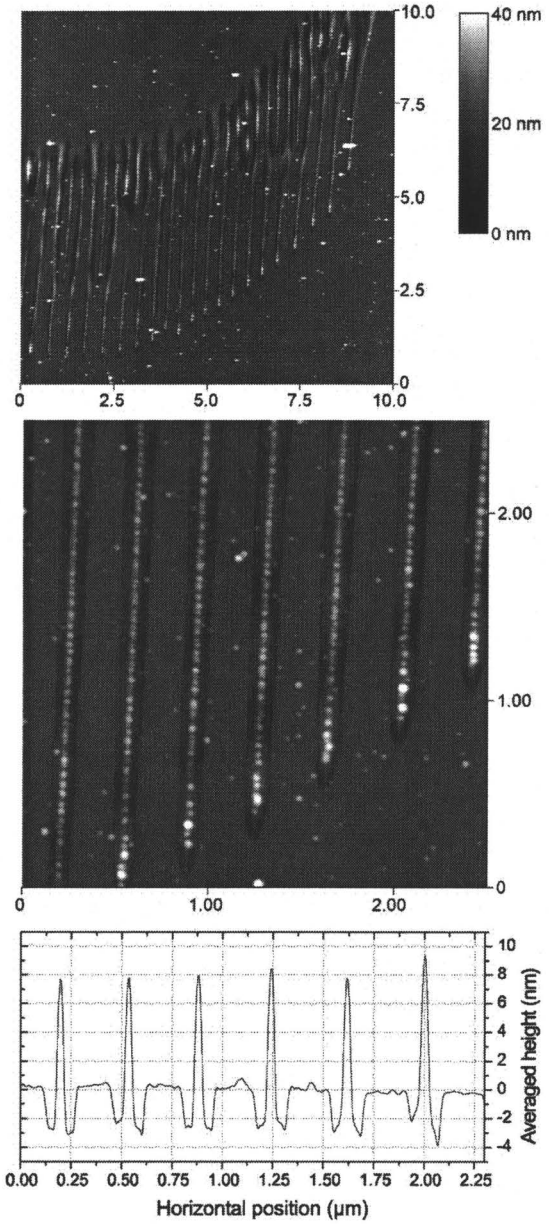

Fig. 5. Fine ripples formed on the surface of Si(1 0 0) by ~ 2100 nm wavelength pulses. The middle image is a smaller-area scan of an area shown in the upper image. Image axis dimensions are in microns, and both images use the same height scale. The graph is an *averaged* cross-section of the ripples from the middle image over many scanlines. Irradiation was by 200 pulses of energy 1200 nJ (peak fluence 120 mJ/cm^2). The laser polarization was approximately vertical in the images.

the lens. The resultant ellipticity of the roughened silicon changed depending on the orientation of the wave plate axes. This suggests that the ellipticity was not due solely to factors such as the initial spatial profile, astigmatism, lens aberrations, or spatio-temporal distortions [35] of the beam. Since our structures show a polarization dependence, the causes of the ellipticity could be related to the structure formation processes. Elliptical irradiation spots have been reported for femtosecond irradiation of copper at normal incidence [36], and images in that work also show a tendency for the major axis of the ellipse to be parallel to the incident polarization direction.

4. Discussion

4.1. Low spatial frequency LIPSS (LSFL)

'Classic' LIPSS have been observed on many materials, and mechanisms for their formation have been presented [2–6]. They are generally explained as being due to an inhomogeneous distribution of energy on the material surface due to interaction between incident light and 'surface-scattered waves' or 'radiation remnant' field structures. The resulting spatial modulation of energy leads to modulated modification of material. For normal incidence, the period is often approximately equal to the incident laser wavelength. We observe LSFL only after multiple-pulse irradiation, as other works have previously reported for femtosecond pulse irradiation of semiconductors [11,37].

In our work, the LSFL period is sometimes as small as 80% of the laser wavelength. A similar deviation has been observed in femtosecond irradiation by other groups. For $\lambda = 800$ nm, structures on silicon [37], InP [11], several ultrahard materials [38], and ceramics [12] had periods of 650–750 nm, ~ 590–750 nm, ~ 0.60 μm, and ~ 700 nm respectively. On silicon, ripples with periods 800–900 nm have been observed for scanned $\lambda = 1040$ nm pulses [13]. Thin polymer films containing metal nanoparticles produced a period obeying $(0.70 \pm 0.03)\lambda$ for irradiating wavelengths from 266 to 800 nm [39].

4.2. Substantially sub-wavelength periods on silicon

For $\lambda = 800$ nm femtosecond irradiation of silicon, Costache et al. [14] reported ripples of ~ 200 nm period in addition to structures with a period of ~ 600–700 nm. They note the two types of ripples were also present on dielectrics (see, [15,16]), however the orientations were rotated 90° compared to the features on silicon. Comparing to our results, the longer-period silicon ripples of Costache et al. [14] appear qualitatively similar to LSFL. Their shorter-period structures however have a different shape than those we present here. They report the coexistence of both types of structures on top of each other, while our structures were spatially separate. The different results could be due to several differences which exist between the two experiments. In particular, their irradiation occurs in an ultra-high vacuum, and involves tens of thousands to hundreds of thousands of pulses. Their silicon was cleaned in HF shortly before transfer to the vacuum chamber, while our silicon would have possessed a native oxide (see Section 4.6).

Silicon is transparent at the wavelengths produced by CO_2 lasers ($\lambda \approx 10.6$ μm) as well as at the OPA wavelengths used in

this work. If the factors causing sub-wavelength periodic structures are not unique to femtosecond irradiation, we might expect similar results after CO_2 laser irradiation. In one study of silicon irradiated with 1 μs duration CO_2 laser pulses, square-shaped rods with 200–700 nm separations were reported [40]. Parallel fringes with a period of about 0.8 μm were observed by Trtica and Gaković [41]. Of particular relevance to our work, they also show structures which look somewhat similar to the fine bumps we observe (see their Figs. 1(e), 2(d) and 3). Their structures have an elongated 'lump' shape which generally forms on top of a long ripple, and had an increased oxygen atomic percentage. We note this increase also suggests that oxidation or a native oxide may have a role in the formation of our structures.

Fluid confinement has been reported to produce substantially sub-wavelength structures for femtosecond irradiation of silicon. In air irradiation with $\lambda = 800$ nm pulses, Daminelli et al. [17] observed a $\sim$ 700 nm ripple period, while a periodicity of $\sim$ 100 nm could be formed on silicon in water. The shorter period was attributed to self-assembling processes, related to ripples observed on dielectrics (see, [15]) and ceramics (see, [12]).

4.3. Periods close to the second harmonic wavelength

After femtosecond pulse irradiation of InP at $\lambda = 800$ nm, ripples with periods between 330 and 360 nm coexisting with LSFL were observed [11]. The period was attributed to second harmonic generation at the rough surface [11]. For a GaN layer on sapphire irradiated at $\lambda = 775$ nm, ripples could be formed on the underlying sapphire with a period as short as 235 nm [18]. On the GaN, a period of 160 nm was observed. The authors [18] postulated that the short ripples are related to the production of second harmonic waves. For a material with refractive index n, the second harmonic wavelength within the material is $\lambda/2n$. Jia et al. [10] report a $\lambda/2n$ period on ZnSe for femtosecond pulse irradiation. With $\lambda = 800$ nm (photon energy below the bandgap energy of ZnSe), structures with a period of 160–180 nm formed, while these did not form for above-bandgap irradiation ($\lambda = 400$ nm). They note the absence of nanostructure formation for above-bandgap photon energy is similar to what our group observed on InP and GaAs (see, [8]).

In our previous work [8], we noted that the dimension of the small ripple periods can approach the second harmonic wavelength in the material, leading to some considerations of second harmonic generation. However, the periods were between λ/n and $\lambda/2n$, and the observations could not be explained by simple considerations based on parameters for the unmodified materials. Bulk centrosymmetric crystals such as silicon should not create second harmonic radiation, although this is allowed at the surface. However, amorphization, crystallite formation and other laser-produced phenomena should be taken into account [8,11]. Moreover, a detailed analysis should consider how the dielectric function behaves during intense irradiation (see, e.g. [42]). Calculations by Jia et al. [10] for ZnSe and GaP predict how the refractive index decreases with increasing density of conduction band electrons. It was suggested that $\lambda/2n$ should be larger than what would be expected using values of n for non-excited materials. A decrease in n (from $\sim$ 3.5 for silicon) due to electron excitation could bring the value of the period closer to the $\sim\lambda/5$–$\lambda/4$ we observe. In addition, our $\sim\lambda/2$ period structures are a close match to the second harmonic in air.

After focusing $\lambda = 800$ nm pulses inside silica glass, Shimotsuma et al. [19] observed thin stripes with a period of 140–320 nm. For fused silica translated under femtosecond pulses, Bhardwaj et al. [20] observed thin arrayed planes spaced by approximately $\lambda/2n$ for free-space laser wavelengths of 800 and 400 nm. The plane orientation was controlled by the laser polarization direction. Bhardwaj et al. [20] propose an alternative to the theory presented by Shimotsuma et al. [19], based on local field enhancements occurring during inhomogeneous breakdown. Growth of underdense nanoplasmas into sheets would cause light to adopt modes similar to those in planar waveguides. In contrast to second harmonic generation, this process could also provide a $\lambda/2n$ plane spacing [20].

4.4. Examples of substantially sub-wavelength periods on other materials

Reif and co-workers report on femtosecond laser irradiation of various dielectrics [15,16,21]. Typically, they used several tens of thousands of $\lambda = 800$ nm pulses. On BaF_2 and CaF_2 they present coarse structures superimposed on fine structures with a period of 200–300 nm [16]. A strong dependence of the ripple period on the local intensity was observed [21]. Reif and co-workers argued that the classical model of LIPSS fails in the case of their results [15,16,21] due to the insensitivity to incident wavelength (400 nm versus 800 nm) and angle of incidence [16]. They speculate that the periodic fine structures are due to self-organization during relaxation of surface instability [21]. Some structures attributed to 'classic' LIPSS show what might be called bifurcations (see, for example Fig. 8 in Ref. [37]), although bifurcations are sometimes given as a reason in support of a self-organization model instead of a light-interference model (see, for example [16]). Concerning the wavelength dependence of structure formation for our results, it is conceivable that different optical penetration depths for each wavelength affect the energy deposition distribution. However, in [15] it was noted that the polarization-dependent orientation of patterns is not completely explained by the self-organization picture.

For femtosecond pulse irradiation of TiN and diamond-like carbon (DLC) at 267 and 800 nm wavelengths, the mean spacing of fine structures was 1/10–1/5 of the wavelength [22]. The spacing was later found to increase with fluence on films of DLC [23], TiN, and CrN [24]. On TiN films, Bonse et al. [25] observed different structure sizes and morphologies under two different applied fluences, suggesting that varying mechanisms were involved [25]. Recently, Kautek et al. [43] have discussed the physico-chemical issues associated with the formation of surface structures by femtosecond pulses on selected ceramics

and silicon. The surface chemical conditions were proposed to be more relevant for fluences near the ablation threshold.

4.5. Comparisons to the theory of Sipe et al. [4]

For chemical vapor deposited (CVD) diamond irradiated by $\lambda = 248$ nm femtosecond pulses, ripples formed with a period on the order of 50–100 nm in addition to periods near the wavelength of the light [26,27]. Wu et al. [28] reported three periodic structure types on CVD diamond after femtosecond laser irradiation. For a 5° angle of laser incidence, the shortest-period ripples had a period of $\sim$ 90 nm and $\sim$ 0.21 μm for 400 nm and 800 nm wavelength irradiation, respectively. They perform calculations based on the theory of Sipe and co-workers (see, [4,5]) and compare these to the experimental results [28].

In the theory of Sipe et al. [4], a function η is developed which describes the efficacy with which inhomogeneous energy absorption occurs just beneath a material surface. For nanosecond pulse irradiation, very good semiquantitative agreement with the positions of peaks in η and the spatial periods of structures was reported [5]. A plot of η for InP predicted ripples with $\lambda/\Lambda = 3.0$–3.5 oriented parallel to the laser polarization [11], where Λ is the structure period. The peak was rounded and such ripples were not observed experimentally [11]. We have made some preliminary estimates of η for normal laser incidence on silicon. The complex refractive index $n_o + ik$ varies with wavelength [44]. For all three wavelengths, the plot for light polarization parallel to the ripple orientation (i.e. ripple wave vector perpendicular to polarization direction) has a peak corresponding to $\Lambda \approx \lambda/n_o$. However, the peak for the $\lambda = 800$ nm case is smaller than for 1300 and 2100 nm, and is somewhat less sharp. For silicon at the two OPA wavelengths, the linear absorption is approximately zero (i.e. $k \approx 0$), while silicon is not transparent at $\lambda = 800$ nm (i.e. $k > 0$). The theory of Sipe et al. [4] indicated that structures with these predicted λ/n_o periods are strongly suppressed when the absorption of the light is large [45]. In our work, the predicted periods are larger than the periods of fine structures we observe, but smaller than the intermediate-sized structures. As with our consideration of second harmonic periods (see Section 4.3), a thorough analysis using the theory of Sipe and co-workers for femtosecond irradiation should consider how the material optical constants change under high electron excitation. Formation of amorphous material could affect the calculations, as the optical properties of amorphous silicon differ from those of crystalline silicon and depend on the preparation conditions [44].

4.6. Other issues

The native oxide layer on silicon is $\sim$ 1–3 nm thick [46,47], which may not be negligible compared to some of the vertical dimensions of structures we observe. McDonald et al. [47] report that oxide-free silicon has a lower femtosecond laser damage threshold and a different morphology, for irradiation at grazing incidence inside an ultra-high vacuum system. Oxidation has been discussed for femtosecond pulse modification of certain ceramics [43] and TiN films [25]. Other groups have reported effects of oxide on silicon under laser irradiation (see, e.g. [32,40,46,48]). For irradiation at a $Si–SiO_2$ interface, oxygen diffusion can occur which can decrease the melting points and reflection coefficients [49]. This could result in a feedback mechanism which enhances formation of periodic structures [49]. In the rough vacuum we use, it is expected that the freshly exposed silicon surface becomes contaminated by oxygen or other species between pulses.

The surfaces of fused silica and an $Er:BaTiO_3$ film have been scanned under a focused $\lambda = 800$ nm femtosecond beam [29], producing a structure period of 200–300 nm. The structures extended coherently over many overlapping laser pulses. Formation of periodic structures on translated materials has been reported in several other investigations (see, e.g. [2,20,50]). For the structures we observe, translation of the target under focused OPA beams could give insight into structure formation mechanisms. For example, the intermediate ripples presented here have only been observed at the center of an irradiated region. Lack of these ripples on a translated sample would imply the importance of a crater-shaped irradiation area. Bonse has suggested [51] that multiple reflections at the crater walls could produce two-beam interference in the center of the crater. This would explain the lack of $\sim\lambda/2$ structures near the edges of irradiated areas [51].

Recessed test patterns have been used to help characterize phenomena underlying ripple formation mechanisms [48]. Scratches [5] and other substrate pre-patterning [52], irradiation through a mask [53], and interception of the laser beam with a fine wire [52] have been previously used to investigate structure formation. The disruption of the periodic structure, or a change in its period or orientation, could provide insight into the formation mechanisms involved.

Yasumaru et al. [24] noted periodic nanostructure at the periphery of a femtosecond laser-irradiated spot on stainless steel. However, we did not find other reports of substantially sub-wavelength periodic structures on metals in the literature. In contrast, substantially sub-wavelength periods have been observed on many materials which are single-photon transparent at the irradiating wavelengths.

5. Conclusions

Crystalline silicon was exposed to femtosecond laser pulses of 800, $\sim$ 1300, and $\sim$ 2100 nm wavelengths. Low spatial frequency laser-induced periodic surface structures were observed for all wavelengths. For the $\sim$ 1300 and $\sim$ 2100 nm wavelengths, additional morphologies of periodic structures formed. An 'intermediate-sized' ripple structure occurred at the center of some low-fluence irradiation sites, with a spatial period of roughly half the irradiating wavelength. Lines and 'bump' arrays, with periods $\sim$ 20–25% of the irradiating wavelength also formed near the material modification threshold fluence.

The physical origins of the structure formation in the current study are still an open question. In their simplest forms, none of the mechanisms discussed can fully explain our results. More experiments would be required to more conclusively identify the formation mechanisms. A complete explanation for the substantially sub-wavelength structures we observe would have to address at least the following points:

- orientation of the structures relative to the incident light polarization;
- variation of the structure sizes with irradiation wavelength;
- relative lack of structures for 800 nm wavelength light;
- similarity of structures on Si(1 0 0) and Si(1 1 1);
- any effects of laser incidence angle on the structure period.

In conclusion, sub-wavelength laser-induced structure formation may have a variety of technological applications, but a number of investigations remain to be done in order to elucidate the key mechanisms.

Acknowledgements

The authors thank J. Bonse, A. Borowiec, J.S. Preston, and H.F. Tiedje for helpful discussions of these results, and A. Duft for assistance with AFM work. In particular, we would like to thank J. Bonse for his input on calculations based on the theory of Sipe. The authors would also like to acknowledge the Natural Sciences and Engineering Research Council of Canada (NSERC) and Materials and Manufacturing Ontario (MMO) for financial support of this work, and the Canada Foundation for Innovation (CFI) and the Ontario Innovation Trust (OIT) for infrastructure.

References

[1] M. Birnbaum, J. Appl. Phys. 36 (1965) 3688.
[2] P.M. Fauchet, A.E. Siegman, Appl. Phys. Lett. 40 (1982) 824.
[3] Z. Guosheng, P.M. Fauchet, A.E. Siegman, Phys. Rev. B 26 (1982) 5366.
[4] J.E. Sipe, J.F. Young, J.S. Preston, H.M. van Driel, Phys. Rev. B 27 (1983) 1141.
[5] J.F. Young, J.S. Preston, H.M. van Driel, J.E. Sipe, Phys. Rev. B 27 (1983) 1155.
[6] J.F. Young, J.E. Sipe, H.M. van Driel, Phys. Rev. B 30 (1984) 2001.
[7] D. Bäuerle, Laser Processing and Chemistry, 3rd ed., Springer-Verlag, Berlin, 2000.
[8] A. Borowiec, H.K. Haugen, Appl. Phys. Lett. 82 (2003) 4462.
[9] T.H.R. Crawford, A. Borowiec, H.K. Haugen, CLEO/IQEC and PhAST 2004 Technical Digest on CD-ROM, The Optical Society of America, Washington, DC, 2004, CTuP40.
[10] T.Q. Jia, H.X. Chen, M. Huang, F.L. Zhao, J.R. Qiu, R.X. Li, Z.Z. Xu, X.K. He, J. Zhang, H. Kuroda, Phys. Rev. B 72 (2005) 125429.
[11] J. Bonse, M. Munz, H. Sturm, J. Appl. Phys. 97 (2005) 013538.
[12] P. Rudolph, W. Kautek, Thin Solid Films 453/454 (2004) 537.
[13] R. Le Harzic, H. Schuck, D. Sauer, T. Anhut, I. Riemann, K. König, Opt. Exp. 13 (2005) 6651.
[14] F. Costache, S. Kouteva-Arguirova, J. Reif, Appl. Phys. A 79 (2004) 1429.
[15] J. Reif, F. Costache, M. Henyk, S.V. Pandelov, Appl. Surf. Sci. 197/198 (2002) 891.
[16] F. Costache, M. Henyk, J. Reif, Appl. Surf. Sci. 208/209 (2003) 486.
[17] G. Daminelli, J. Krüger, W. Kautek, Thin Solid Films 467 (2004) 334.
[18] X.C. Wang, G.C. Lim, F.L. Ng, W. Liu, S.J. Chua, Surf. Rev. Lett. 12 (2005) 651.
[19] Y. Shimotsuma, P.G. Kazansky, J. Qiu, K. Hirao, Phys. Rev. Lett. 91 (2003) 247405.
[20] V.R. Bhardwaj, E. Simova, P.P. Rajeev, C. Hnatovsky, R.S. Taylor, D.M. Rayner, P.B. Corkum, Phys. Rev. Lett. 96 (2006) 057404.
[21] F. Costache, M. Henyk, J. Reif, Appl. Surf. Sci. 186 (2002) 352.
[22] N. Yasumaru, K. Miyazaki, J. Kiuchi, Appl. Phys. A 76 (2003) 983.
[23] N. Yasumaru, K. Miyazaki, J. Kiuchi, Appl. Phys. A 79 (2004) 425.
[24] N. Yasumaru, K. Miyazaki, J. Kiuchi, Appl. Phys. A 81 (2005) 933.
[25] J. Bonse, H. Sturm, D. Schmidt, W. Kautek, Appl. Phys. A 71 (2000) 657.
[26] A.M. Ozkan, A.P. Malshe, T.A. Railkar, W.D. Brown, M.D. Shirk, P.A. Molian, Appl. Phys. Lett. 75 (1999) 3716.
[27] A. Malshe, D. Deshpande, J. Mater. Process. Technol. 149 (2004) 585.
[28] Q. Wu, Y. Ma, R. Fang, Y. Liao, Q. Yu, X. Chen, K. Wang, Appl. Phys. Lett. 82 (2003) 1703.
[29] R. Wagner, J. Gottmann, A. Horn, E.W. Kreutz, Proc. SPIE 5662 (2004) 168.
[30] T.-H. Her, R.J. Finlay, C. Wu, S. Deliwala, E. Mazur, Appl. Phys. Lett. 73 (1998) 1673.
[31] S.I. Dolgaev, S.V. Lavrishev, A.A. Lyalin, A.V. Simakin, V.V. Voronov, G.A. Shafeev, Appl. Phys. A 73 (2001) 177.
[32] A.J. Pedraza, J.D. Fowlkes, Y.-F. Guan, Appl. Phys. A 77 (2003) 277.
[33] Specifically, the numbers of pulses included 10, 25, 50, 100, 200, 350, 500, 650, 750, 850, 1000, 2000, 5000, and 10000. In addition to these, other numbers were sometimes included.
[34] A. Borowiec, H.K. Haugen, Appl. Phys. A 79 (2004) 521.
[35] G. Pretzler, A. Kasper, K.J. Witte, Appl. Phys. B 70 (2000) 1.
[36] S.E. Kirkwood, A.C. van Popta, Y.Y. Tsui, R. Fedosejevs, Appl. Phys. A 81 (2005) 729.
[37] J. Bonse, S. Baudach, J. Krüger, W. Kautek, M. Lenzner, Appl. Phys. A 74 (2002) 19.
[38] G. Dumitru, V. Romano, H.P. Weber, M. Sentis, W. Marine, Appl. Phys. A 74 (2002) 729.
[39] A. Kiesow, S. Strohkark, K. Löschner, A. Heilmann, A. Podlipensky, A. Abdolvand, G. Seifert, Appl. Phys. Lett. 86 (2005) 153111.
[40] D.-Q. Yang, E. Sacher, M. Meunier, Appl. Surf. Sci. 222 (2004) 365.
[41] M.S. Trtica, B.M. Gaković, Appl. Surf. Sci. 205 (2003) 336.
[42] K. Sokolowski-Tinten, J. Bialkowski, D. von der Linde, Phys. Rev. B 51 (1995) 14186.
[43] W. Kautek, P. Rudolph, G. Daminelli, J. Krüger, Appl. Phys. A 81 (2005) 65.
[44] E.D. Palik (Ed.), Handbook of Optical Constants of Solids, Academic Press Inc., Boston, 1985.
[45] J.S. Preston, Private communication.
[46] M. Weingärtner, R. Elschner, O. Bostanjoglo, Appl. Surf. Sci. 138/139 (1999) 499.
[47] J.P. McDonald, A.A. McClelland, Y.N. Picard, S.M. Yalisove, Appl. Phys. Lett. 86 (2005) 264103.
[48] G.K. Giust, T.W. Sigmon, Appl. Phys. Lett. 70 (1997) 3552.
[49] Y. Liao, J.-Y. Degorce, M. Meunier, Appl. Phys. A 82 (2006) 679.
[50] T.H.R. Crawford, A. Borowiec, H.K. Haugen, Appl. Phys. A 80 (2005) 1717.
[51] J. Bonse, Private communication.
[52] J.D. Fowlkes, A.J. Pedraza, D.A. Blom, H.M. Meyer III, Appl. Phys. Lett. 80 (2002) 3799.
[53] M.Y. Shen, C.H. Crouch, J.E. Carey, R. Younkin, E. Mazur, M. Sheehy, C.M. Friend, Appl. Phys. Lett. 82 (2003) 1715.

5.3 Additional comments on the results and techniques presented in the paper

5.3.1 Approach to sample preparation and analysis

The sample layout and approach to irradiation were generally as follows. The sample was cleaved from a larger wafer piece, and placed in the machining chamber such that one of the cleave planes was approximately parallel to a stage translation direction. A focal alignment test was typically done in a corner of the sample, as described previously (sections 3.5 and 4.3.1). The sample label was then machined at a low power, with text running along the x axis. A few to several hundred micrometres above the start of the sample label was where the grid of irradiation sites began. As in the grooves experiments, aligning the side of the irradiated grid with the start of the text label made finding the irradiation sites easier in the early steps of SEM setup.

A grid of irradiation sites consisted of decreasing pulse energies along the x axis, and increasing numbers of pulses along the y axis. The order in which the sites were produced was as follows. Starting with the lowest number of pulses (usually a single pulse), the highest energy site (usually OD 0.0) was irradiated. The translation stage moved along the x axis to the location of the next site, and the pulse energy was reduced by increasing the filter OD by a 0.1 step. This site was irradiated, and the process repeated until the predefined maximum OD was reached, corresponding to a pulse energy much below that at which visible modification occurred. The sample and chamber were translated back along the x axis to the location of the first site of that run, then was translated along the y axis to the next site location. A higher number of pulses was used for the next run. The process was repeated until the run with the highest number of pulses was complete. In this way, the sites for which the highest number of pulses was used were machined last. Since a higher number of pulses produced greater amount of debris (due to a larger volume of material removal), these were saved for last so that minimal debris would be present on the sample when irradiating with low numbers of pulses. Also, although whole-sample heating was not expected to pose a major problem (see appendix A), this order of irradiation reduced the potential impact of heating on the lower number-of-pulses sites. The D^2 method, described in section 3.5, was used to determine the spot sizes. Due to the different wavelengths and initial beam radii, the spot size was not the same for all three wavelengths. The D^2 method was not used on sites with substantial numbers of pulses, since incubation effects

and a complicated morphology (debris, substantial expulsed material, etc.) would impede the tracking of the same surface feature among sites.

Sites were usually spaced 250 μm apart, although other spacings were occasionally used depending on the sample dimensions. A large spacing helped reduce the amount of debris from one site depositing on adjacent sites. Irradiation was done in a rough vacuum, which greatly reduced the amount of debris settling on the sample in comparison to irradiation in air, and helped reduce possible nonlinear phenomena which may occur in the air near the focus. The 5× microscope objective used in many other experiments was typically not used in experiments for silicon ripple production, since the spot size of the 5× objective was rather small and would produce only a small area of ripples, reducing the area of measurable periodic structures. Lenses with focal lengths of 15 or 20 cm were used for the majority of ripples experiments. As noted in the paper however [58], fine ripples were first observed after irradiation at $\lambda \approx 2100$ nm via the 5× objective, so the use of a particular lens is not a requirement for the formation of at least some of the structures reported here. The spot size did not seem to affect the ripple periods.

The highest pulse energy available from the OPA was usually used for the OD 0.0 site, as this pulse energy was not particularly high (generally $<\sim$10 μJ at the target). At the time the experiments were done, there were no half-wave plates or polarizers for the two OPA wavelengths for continuously varying the pulse energy. In some experiments, the pulse energy was still higher than necessary, so a few of the lower OD sites simply had the laser beam manually blocked, as it was known from the results of previous experiments that these energies would produce deep holes and substantial debris, without any significant periodic structuring.

The infrared viewer and the 'standard' orange IR detector cards (Newport F-IRC1 and similar) in the lab were not capable of viewing or detecting the $\lambda \approx 2100$ nm beam, although they worked for the $\lambda \approx 1300$ nm beam. The very weak green and orange beams emitted from the OPA outputs were not collinear with the infrared beams, so while they provided a rough indication of the location of the IR beams they could not be used for alignment. They had a somewhat different propagation direction, diverging from the IR beams and were easily blocked a sufficient distance from the OPA. A reverse-biased InGaAs photodiode could be used to detect the ~1300 nm wavelength light, while an InAs photodiode was sensitive to ~2100 nm wavelength light. The use of a photodiode for $\lambda \approx 2100$ nm beam alignment required large irises to be placed in the beam. By making the iris small and placing the photodiode after the iris, or by placing a white piece of paper after an iris with the photodiode picking up the light scattered by the paper, the beam could be steered to the

position at which the photodiode produced the highest output. This implied that the center of the beam was passing through the iris, as the beam had an approximately Gaussian spatial profile. A portion of a liquid crystal sheet, which is black at room temperature but has a different colour at a somewhat higher temperature, made a reasonable beam detector for the $\lambda \approx 2100$ nm light. At average powers of a few milliwatts it would take several seconds of being in the beam before it would change colour, though for lower powers or sufficiently diverged beams the fluence would not be high enough to induce a colour change. Care also needed to be taken as the surface of the liquid crystal sheet is smooth, and thus could reflect the beam to inappropriate locations. It was also flexible, so a concave bend could focus the beam.

The CCD beam profiler had some sensitivity to the $\lambda \approx 2100$ nm pulses (and stronger sensitivity to the $\lambda \approx 1300$ nm pulses) despite silicon detectors not being one-photon sensitive to these wavelengths. This allowed the confirmation that the $\sim$1300 and $\sim$2100 nm wavelength beams had an approximately Gaussian beam profile. To test that residual 800 nm light was not present in the longer wavelength beams, the white seed light generation inside the OPA was blocked. This prevents the generation of the $\sim$1300 and $\sim$2100 nm wavelengths, while the majority of the 800 nm light continues to follow the same paths in the OPA as before. If residual 800 nm wavelength was present in the output beams, the majority of it would continue to be present when the white seed light was blocked. However, no light was detected on the CCD when the white light was blocked.

5.3.2 Comparison of optical microscopy with AFM

The periods of the fine structures produced by the OPA wavelengths are often in the region of $\sim$250–350 nm. In optical microscopy these can be resolved, but their size is near the limits attainable using light-based measurements. Nomarski differential interference contrast (DIC) mode was typically used since it enhances contrast for small differences in structure height, making structures easier to observe and measure. Atomic force microscopy was used on many sites, not just to measure the depths of features but to measure the periods and to confirm that the period measurements from optical microscopy were correct. Figure 5.1 shows a Nomarski image of a site irradiated by $\sim$1300 nm pulses, in which fine bump arrays are present. 'Manual' measurement of Nomarski images involved measuring a certain region of ripples, and dividing the width of this region by the number of complete ripples within it, providing an approximate average of the ripple period in that region. Depending on the site, this could be repeated for multiple locations on the same ir-

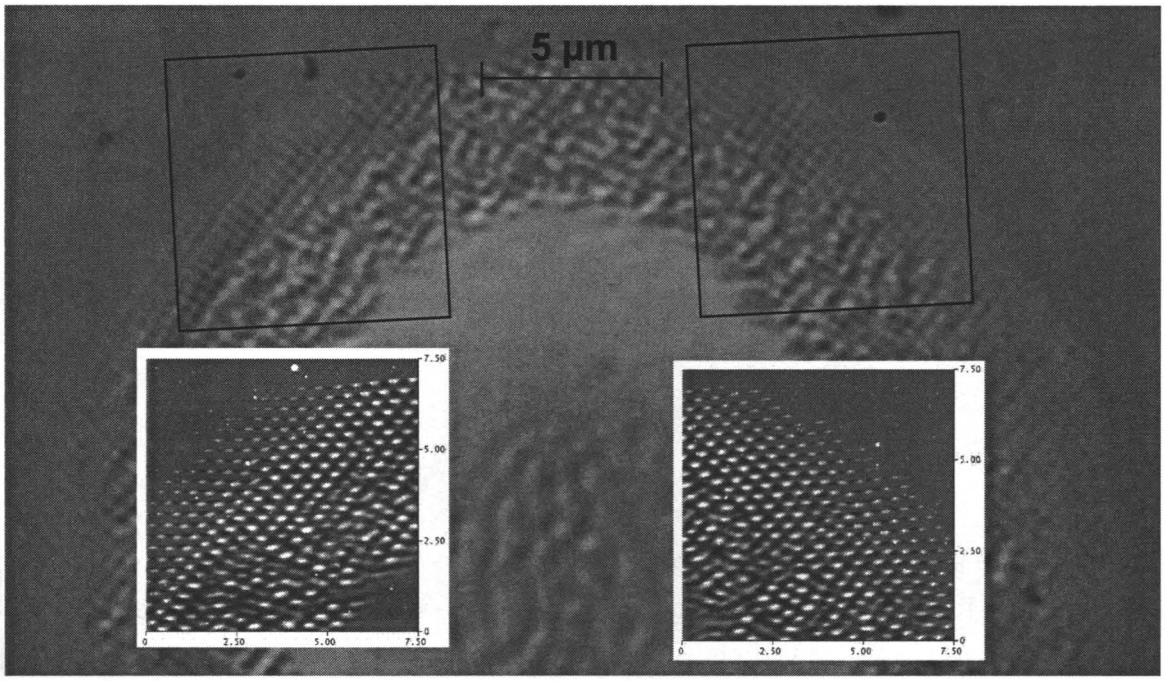

Figure 5.1: Nomarski DIC optical microscope image of Si(100) irradiated by 650 pulses of $\lambda \approx 1300$ nm light at a peak fluence of 170 mJ/cm^2. The scale bar (5 μm) is from the optical microscope calibration. Also shown *(inset)* are the corresponding AFM images (from figure 3 in the silicon ripples paper [58]) with axis units of micrometres. The approximate locations of AFM scans are indicated by the black squares in the optical microscope image. Periodic structures can be resolved in the optical image, with the same period as indicated by the AFM scans.

radiation site. For example, in the left square of the optical image, 12 rows were measured from top to bottom over a distance of 3.30 μm, giving a period of 275 nm. In the right square, 12 columns were measured horizontally over a distance of 3.50 μm, giving a period of 292 nm. These are approximately the same as the periods measured in the AFM scans. Care was taken to ensure that entire structures were enclosed within the measured distances, so that inclusion of a partial structure would not count as an entire period. In some cases, the distance between two adjacent rows of features was measured, directly giving the period at that location. Similar comparisons were made for the intermediate-size ripples and the low spatial frequency LIPSS. Some AFM scans were done with the AFM tip moving parallel to the ripples, while other scans were done with the tip moving perpendicular (i.e. with the sample rotated 90°). Comparing the results ensured that the AFM results were not due to abnormal tip behaviours or other AFM artifacts (figure 5.4 in section 5.4 shows

a comparison between Nomarski imaging and an AFM scan in which the tip moved in a different direction relative to the ripples in figure 5.1). The AFM software also provided a Fourier transform of the scan, showing peaks at the periods of structures for comparison. In Nomarski DIC mode, the calibration slide discussed in section 3.4 was measured to ensure the optical microscope calibration was correct. It was found that switching between Nomarski DIC mode and standard brightfield mode did not affect the calibration. Additionally, measurements using optical microscopy, AFM, and SEM were sometimes compared (see, e.g. reference [94]) to ensure they were similar within experimental uncertainties.

5.3.3 Parameter space maps

Figure 5.2 schematically shows the conditions for the number of pulses and the peak pulse fluence for which the various structures form for ~1300 and ~2100 nm wavelengths. Each map is from a single experimental run, and some variations may exist between runs. For the higher fluences and numbers of pulses, the structures indicated on the map formed at the edge of a deep, rough hole, and the morphology deep within these holes could not be imaged in plan-view SEM or AFM. Since only certain fluences and numbers of pulses were used in the experiments (see reference [58] for details), the boundaries of the regions on the figure are approximate. Due to an incubation effect present in laser irradiation, it is generally possible for surface modification to appear after many pulses at a particular fluence, while a small number of pulses at the same fluence would not visibly modify the surface [35]. This is suggested by the somewhat slanted (non-constant fluence) boundary near the left side of the graphs in figure 5.2.

5.3.4 Translated samples

As noted in the silicon ripples paper [58], translating a silicon target under a focussed OPA beam could potentially give insight into the structure formation mechanisms. The machining of the sample label and the focal alignment test involve translating the sample under the beam, providing some preliminary results. Fine ripples and fine bump formation were observed on some of these translated sites, with an example shown in figure 5.3 for $\lambda \approx 2100$ nm. However, more rigorous tests would need to be conducted to more accurately determine to what extent and under what experimental conditions these structures form. It was speculated in the silicon ripples paper [58] that a crater-shaped irradiation site could produce the intermediate-size ripples, and translating the sample would spoil this geometry.

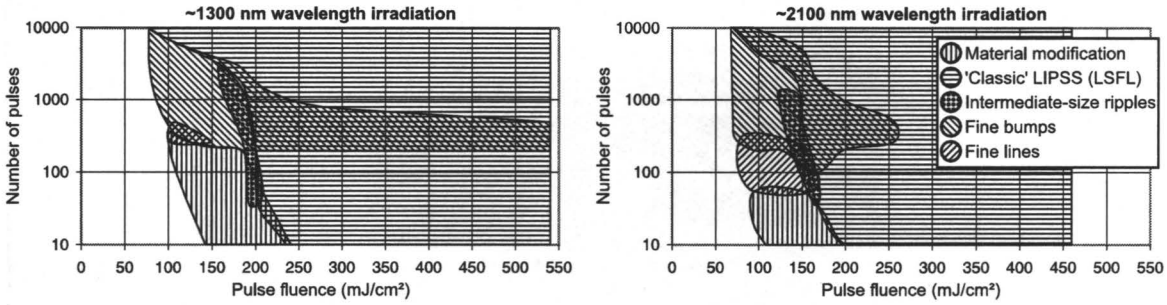

Figure 5.2: Maps showing the number of pulses and per-pulse fluences for formation of various structures on Si(100) at *(left):* ~1300 nm and *(right):* ~2100 nm irradiation. 'Material modification' refers to observed changes which did not visibly show any periodicity. The right fluence boundary marks where no higher fluences were used in the experimental run. The boundaries between regions are approximate, due to the coarseness of the grid of fluences and numbers of pulses employed. The legend within the ~2100 nm map also applies to the ~1300 nm map.

The direction of laser polarization relative to the translation direction could also affect the structure formation if scattering from the walls of a shallow groove was relevant. In light of the results on graphite (see section 5.5) and for very low fluence grooves (see section 4.6), it is uncertain to what extent a certain ripple type, once its direction has been seeded, would maintain its orientation as the incident light polarization was rotated while translating the sample. Some potential industrial applications of laser-induced surface roughness are noted in the silicon ripples paper [58]. Such applications could be enhanced if a large area of fine bumps on silicon or HSFL on III-V materials could be produced by raster scanning the laser beam. For adjacent laser passes with sufficient spatial overlap, ripples in one laser pass may form coherent with the ripples produced in the previous pass, leading to large regions of coherent structures.

5.3.5 Feasibility of laser diffraction for observations of laser-induced periodic structures, and for time-resolved imaging

In some papers (e.g., reference [56]), a low-power HeNe or Ar-ion laser beam was incident on the irradiation sites. This would diffract off the periodic structures, forming a diffraction pattern on a screen. The periods and orientations of gratings could then be deduced from the pattern of diffracted light. While diffraction of room lights off LSFL could be frequently observed, systematic laser diffraction was not attempted in the research. The

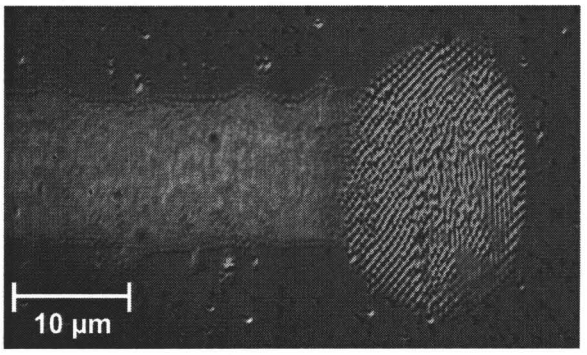

Figure 5.3: Nomarski image of Si(100) irradiated by $\lambda \approx 2100$ nm pulses while the sample was translated. The image has had its dynamic range strongly altered (digitally), to more clearly show the fine structures in the translated area. The translation stopped near the right edge of the image, where the sample was stationary for a moment before the laser was blocked. Small areas of fine ripples and fine bumps are present along the upper and lower edges of the region irradiated while the sample was in motion.

use of low-power irradiation of lasers to create a diffraction pattern from HSFL on silicon is complicated by the small period of the HSFL. To produce a diffraction pattern, the low-power laser wavelength should be less than the period of the grating. The use of an even shorter wavelength would allow the screen to be more distant from the sample, otherwise the first-order diffraction pattern would form at large angles from the sample normal. For the fine ripples and fine bump arrays, diffraction would require laser wavelengths in the blue or ultraviolet regions of the spectrum, which would complicate the imaging of the diffraction pattern. Due to their larger period, laser diffraction from the intermediate-sized ripples and LSFL would be easier to accomplish.

In principle, time-resolved imaging or diffraction could be performed to examine the formation of ripples. Similar to time-resolved imaging of single-pulse sites (see, e.g. reference [5]), this would involve a short-wavelength probe pulse being incident on the sample at a predetermined (but adjustable) delay after the incidence of the main pulse. Such experiments would require the generation of an ultrashort pulse with sufficiently short wavelength, such that ripples could be resolved optically or that a diffraction pattern would be formed. In time-resolved measurements, each image from different evolution times comes from a different site. However, due to the somewhat random nature of material evolution for multiple-pulse irradiation, two separate 500-pulse sites (for example) would possess similar structures but would not generally look identical. Thus, images or diffraction patterns from time-resolved evolution could be difficult to interpret. A pulse-to-pulse evolution 'video' of

a single site, with a diffraction pattern or microscope image taken after each pulse, would show how the final state of material changes with increasing number of pulses, although imaging may be more difficult to achieve experimentally. Material irradiation within the vacuum of an SEM chamber would allow the acquisition of a high-resolution image after each pulse, however the SEM system would need to be customized to avoid material redeposition within the SEM column.

The AFM software featured built-in one- and two-dimensional Fourier transform calculations, allowing the calculation of ripple periods and also showing the orientations in the 2D case. The Fourier transform (spectrum) feature was used frequently to obtain periods, and to compare them to those measured 'manually' on the optical microscope images and on the AFM images. Separate software is available which is capable of performing a Fourier transform of SEM and optical microscope images, although required extra care to ensure the calibrations of physical distance per image pixel are translated properly into frequency components. This approach is shown (for example) by Bonse et al. [103] for SEM images of ripples on InP.

5.3.6 More detailed comparison to the theory of Sipe et al. [54]

Section 4.5 of the silicon ripples paper [58] makes some general, qualitative comparisons to the theory of Sipe et al. [54]. These comparisons are based on more detailed work. The further details are presented in appendix B.

5.4 TEM of substantially sub-wavelength ripples on silicon

As shown for several samples in this thesis, focussed ion beam milling can be used to prepare a cross-sectional sample of material irradiated by femtosecond laser pulses, allowing examination by TEM of the resulting crystal structure. Figure 5.4 shows optical and AFM images of a fine bump array on silicon for which a FIB sample was prepared. The milling was performed by Fibics, Incorporated in Ottawa, Canada, in July 2003, and preliminary TEM imaging was performed shortly after by Martin Couillard. M. Couillard also performed high-resolution TEM imaging at a later date.

Figure 5.5 shows TEM images of the sample shown in figure 5.4. Unfortunately it was not clear exactly where on the original sample the FIB slice was prepared, or at what angle relative to the bump array the slice was obtained. While it looks somewhat periodic, it does

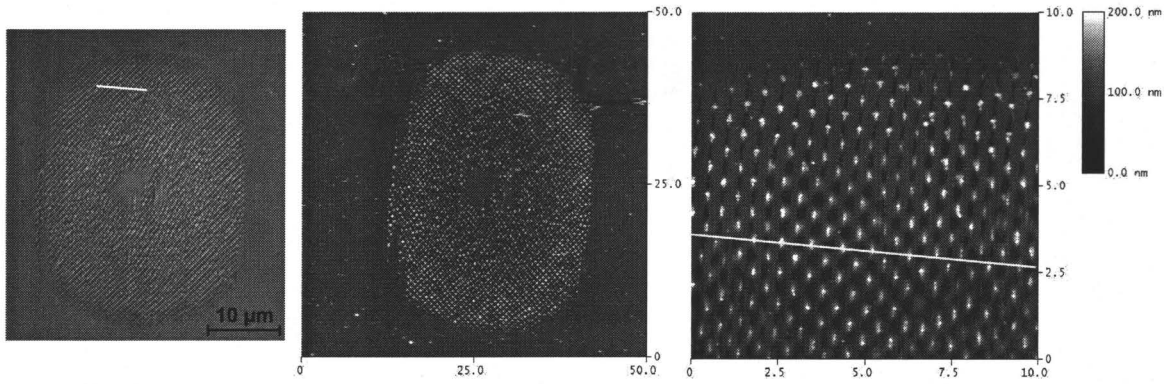

Figure 5.4: Nomarski optical microscope image *(left)* and two AFM scans of a Si(100) site irradiated by 750 pulses of $\lambda \approx 2100$ nm light (per-pulse energy 3.8 µJ, fluence 140 mJ/cm^2). The AFM images are from separate scans (one is not a rescaling of the data from the other). Fine bump arrays are present. The line in the images indicates where FIB preparation was desired for TEM examination. The AFM x and y axis units are micrometres.

not clearly show the peaks and depressions visible in AFM scans (such as the cross-section plots in figure 4 in the silicon ripples paper [58]). It could be that the protective palladium coating is hiding somewhat the tips of the protrusions. In later investigations of LSFL and HSFL on InP by M. Couillard and A. Borowiec (see reference [43]), a polymer layer was deposited before the protective metal layer to avoid the potential of strong masking of features by a largely electron-opaque metal layer. It could be possible to place some sort of markers on the sample surface for future samples, so that the desired location of the FIB slice could be more precisely defined relative to the markers. Using the laser to make markings is likely impractical, as the dimensions of the ripples are much smaller than the typical laser-modified area or spot size. One option would be to have the person who prepared the sample be present with the FIB operator before and during FIB preparation, to discuss and observe the precise location in the SEM mode of the FIB machine. Despite the problems in this first attempt at cross-sectional investigation, some conclusions could still be made. A polycrystalline surface layer with small grain size (not amorphous) was produced by the laser irradiation, and the interface between the layer and substrate appears to follow the topography of the surface.

The oxide composition and distribution was not analyzed in the structures presented here, but determining this could help explain the observed morphological changes. Trtica and Gaković [104] used CO_2 laser pulses to irradiate silicon in air and found an increased

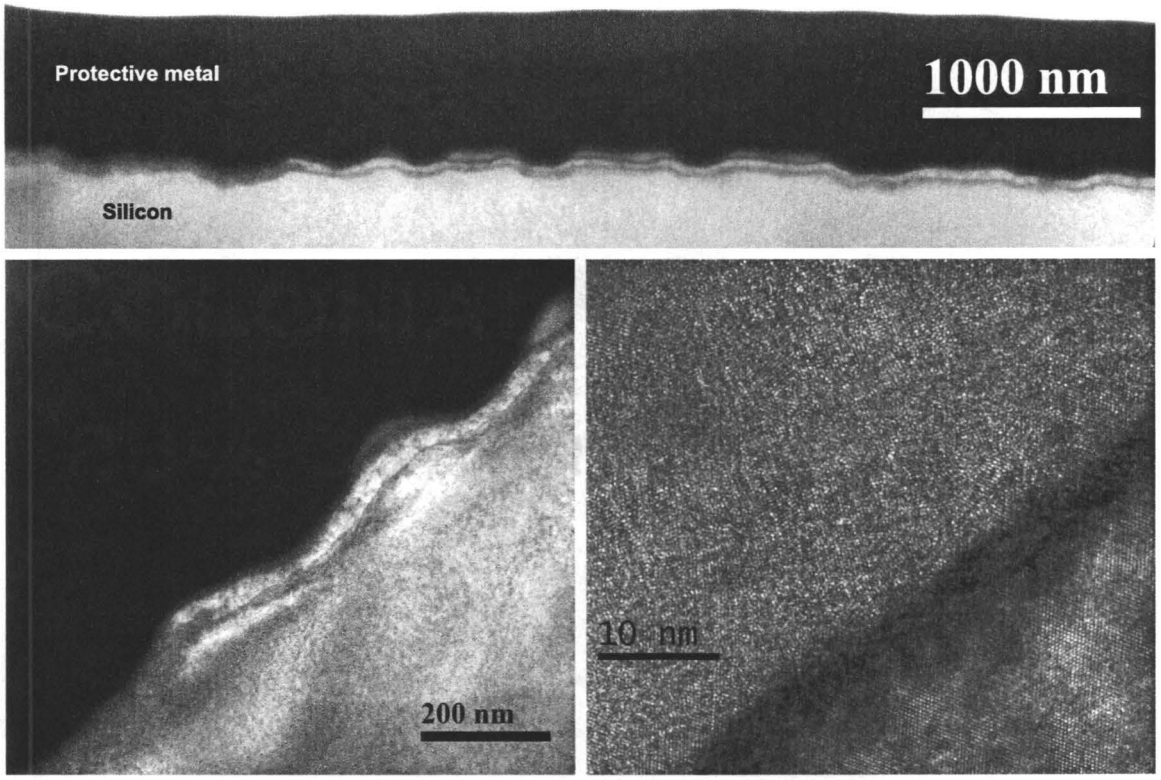

Figure 5.5: TEM images of the surface layer and layer/substrate interface of the sample shown in figure 5.4. These images were obtained by M. Couillard. The top image shows an overview of the TEM sample. The lower right image is a HRTEM (high-resolution TEM) image.

oxygen percentage in the ripple (6.0%) compared to 0.8% in the surface before laser irradiation. Investigations in the TEM may be able to indicate if the surface layer of the fine bumps presented in this thesis have a different chemical composition than the bulk, as was done for InP [43]. After material removal by one laser pulse, the freshly exposed silicon surface can become contaminated by oxygen or other species in the rough vacuum before the next pulse arrives at the sample. This contamination could then affect the material modification process. An irradiation experiment performed in an inert atmosphere or an ultrahigh vacuum could indicate the role of atmospheric species on structure formation. For further comparison of these silicon TEM results, LSFL on silicon were examined in cross-sectional TEM with the results presented in section 6.3.3, while cross-sections of ripples formed in the machining of grooves are presented in chapter 4.

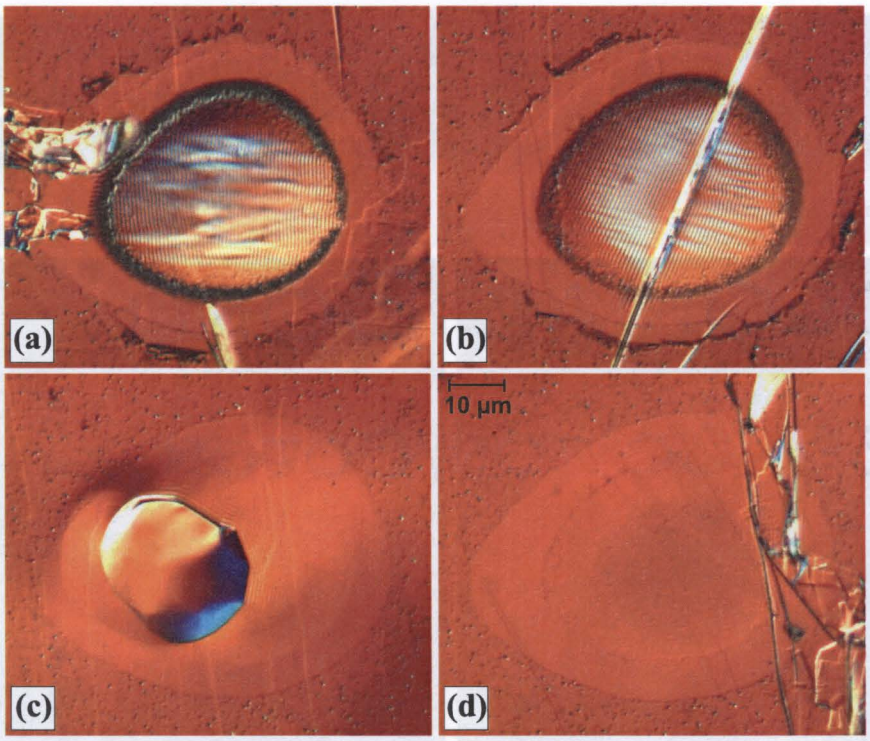

Figure 5.6: Nomarski DIC optical microscopy images of crystalline flake graphite irradiated by 50 fs laser pulses at $\lambda = 800$ nm. A 15 cm focal length lens was the focussing element. (a): 50 pulses, 930 mJ/cm^2; (b): 25 pulses, 1050 mJ/cm^2; (c): 5 pulses, 930 mJ/cm^2; (d): 1 pulse, 1050 mJ/cm^2. All images use the same scale and orientation, with the incident laser polarization approximately horizontal in the images.

5.5 Investigation of graphite, and consideration of pre-existing structure

As noted in the silicon ripples paper [58], substrate pre-patterning has been used by some groups to affect ripple formation. A crystalline flake graphite sample, provided by Gianluigi Botton, enabled an examination of the effect of pre-existing surface structure. Figure 5.6(a) shows classical LIPSS on graphite with minimal graphite flake edges running through the irradiation site. The LIPSS in this image run perpendicular to the incident laser polarization. Figure 5.6(b) shows a large diagonal feature running though the site, with LIPSS running parallel to the diagonal feature rather than perpendicular to the incident laser polarization. A somewhat round graphite feature was present in the irradiation area of figure 5.6(c), with LIPSS parallel to its edges near the center of the irradiation site. In some cases, only a single laser pulse incident near a ridge or flake-edge was sufficient to produce

a small region of shallow-looking ripples parallel to the flake immediately adjacent to it. Such ripples had a period around 700–800 nm, with a large uncertainty due to the small ripple area and rarity of ripple formation. An example is shown in figure 5.6(d), where very shallow ripples can be seen adjacent to the flake in the right side of the image, although the ripples are very faint in this image. All ripples in figure 5.6 have a period around 700 nm, somewhat less than the wavelength of the incident light.

For ultrashort pulse irradiation the absence of LIPSS after a single pulse has been observed previously for a variety of semiconductors (see, e.g. references [35, 39, 58, 59, 60, 103]). The existence of single-pulse ripples at edges on graphite further suggests that scattering locations are important in the nucleation of ripples. The semiconductor wafers used in this thesis have a very smooth flat surface. It could be that after the first pulse on these smooth targets, the resulting slight variations in surface smoothness provide enough scattering for ripples to begin forming for subsequent pulses. Bonse et al. [103] make a similar suggestion for the observation of ripples on InP after two pulses but not after one pulse. After single-pulse femtosecond irradiation of copper, Kirkwood et al. [79] report ripples on a rough foil target but not on a smooth thin film. Mannion et al. [105] observed that the ripple direction on metals is affected by grain boundaries in the irradiated region.

SEM, TEM, and AFM measurements of sites on graphite was not performed, but would be useful for further research. The observed effect of ridges on graphite suggests that prepatterning of other materials could be done, to investigate the tendencies for ripple formation. On some semiconductor sites LSFL near the edge of the irradiated material were sometimes slightly arc-shaped, particularly for low numbers of pulses. In these cases the LSFL somewhat followed the curvature of the crater rim where the laser polarization was close to perpendicular to the rim direction. As a further investigation, focussed ion beam milling could be used to inscribe a fine diagonal line on a silicon wafer surface. To help determine if HSFL formation is due to light interference effects, it would be useful to examine if the substantially sub-wavelength ripples would align parallel to the line, as it is likely that LSFL would do so. It could also be possible to cause a ripple period to have a somewhat different value than would naturally occur, by making an array of fine FIB-included lines with the desired period. In addition to providing more information on ripples, the TEM could reveal to what extent the crystalline structure of the graphite changed, perhaps forming small regions of diamond structure or amorphous carbon. Such an investigation was the original intention for preparing the graphite sample shown, although TEM was not done due to time constraints.

5.6 Investigations on gallium phosphide

After most of the indium phosphide and silicon ripples experiments were completed, the primary material for which the investigation of ripples was performed was gallium phosphide. The bandgap energy of GaP is above the ~1.55 eV photon energy of the $\lambda = 800$ nm laser pulses, and thus investigations could be performed more easily as the OPA would not need to be used, and the majority of the lab equipment (silicon photodiodes, CCD spectrometers, GRENOUILLE, etc.) operates at this wavelength. Eugene Hsu performed the laser irradiation of the GaP samples, and did most of the writing for the two papers which presented the results [46, 60]:

- E.M. Hsu, T.H.R. Crawford, H.F. Tiedje, H.K. Haugen: *Periodic surface structures on gallium phosphide after irradiation with 150 fs–7 ns laser pulses at 800 nm*, Applied Physics Letters **91**, 111102 (2007) [60]
- E.M. Hsu, T.H.R. Crawford, C. Maunders, G.A. Botton, H.K. Haugen: *Cross-sectional study of periodic surface structures on gallium phosphide induced by ultrashort laser pulse irradiation*, Applied Physics Letters **92**, 221112 (2008) [46]

The pulse duration results were also presented in the poster presentation:

- E.M. Hsu, T.H.R. Crawford, H.F. Tiedje, H.K. Haugen: *Near and sub-wavelength ripples on gallium phosphide irradiated at various laser pulse durations*, 9th International Conference on Laser Ablation (COLA) 2007, Poster presentation PTU-65

The GaP graphs and images in this thesis section come from these publications[2]. Some additional results on GaP not present in the two publications were presented in the M.A.Sc. thesis of Eugene Hsu [106].

5.6.1 Pulse duration effects

The first GaP paper [60] investigated the formation of LSFL and HSFL as a function of pulse duration, number of pulses, and pulse energy. A wide range of pulse lengths are easily obtainable from the Ti:sapphire laser systems at $\lambda = 800$ nm (see chapters 3 and 8 for further details). A wide range was not easily attainable from the OPA and thus pulse duration experiments were not done for silicon or InP in their transparency regimes. The

[2]See appendices C and F for copyright and permission information.

investigation of pulse duration effects could give insight into the formation mechanisms of substantially sub-wavelength periodic structures. For example, if the fine periodic structures were primarily due to (intensity dependent) second harmonic effects in the material, the formation would be expected to drop off rapidly with increasing pulse duration, unless only a very small amount of second harmonic is required. The threshold fluences for surface modification and ablation do not generally rise rapidly as the pulse duration is increased [107].

The double-side polished, ~430 μm thick *n*-GaP(100) samples had a quoted doping of 1.85×10^{16} cm^{-3} and a mobility of 160 cm^2/Vs. GaP was irradiated using a similar technique as for silicon using the same machining apparatus. For each pulse duration, a grid of sites with decreasing pulse energy along one axis and increasing number of pulses on the other axis was produced. Since LSFL and HSFL tend to be prominent on III-V materials like GaP for a wide range of conditions, the 5× objective generally provided a sufficiently large spot size for the observation of these structures. Scanning electron microscopy was used for imaging the periodic structures on GaP, as their high aspect ratio (in comparison to small structures on silicon) made them easily imaged. Nomarski optical microscopy was also used, however neither technique could successfully image the bottoms of deep holes.

No LIPSS were observed on GaP after irradiation by only a single laser pulse at any of the pulse durations employed, similar to other semiconductors under femtosecond pulse irradiation (see, e.g. references [35, 39, 58, 59, 103]). Figure 5.7 shows the number of pulses and pulse energy conditions under which various surface structures on GaP formed, for two different pulse lengths. The graphs are analogous to those shown for silicon (figure 5.2 in section 5.3.3), although the graphs for GaP use pulse energy instead of fluence. The graph for GaP shows the specific numbers of pulses and pulse energies examined, with different symbols for each structure type, while the silicon graph (figure 5.2) instead shows regions due to the higher number of symbols which would have been required. On GaP, as for the other III-V materials reported in reference [59], the HSFL were parallel to the LSFL. However on silicon, the fine lines and intermediate-size ripples ran perpendicular to the LSFL. Some similar trends exist for the silicon and the GaP. For example, the incubation effect can be observed in both cases, for which surface modification is observed at lower energies as the number of pulses is increased. Some sites showing multiple structure types at the same site are present for both materials, with the shorter period structures occurring nearer the edges of the irradiation site where the local fluence is lower.

A significant difference between silicon and GaP is the behaviour with increasing number of pulses. On GaP, with increasing number of pulses for a fixed fluence, the surface at

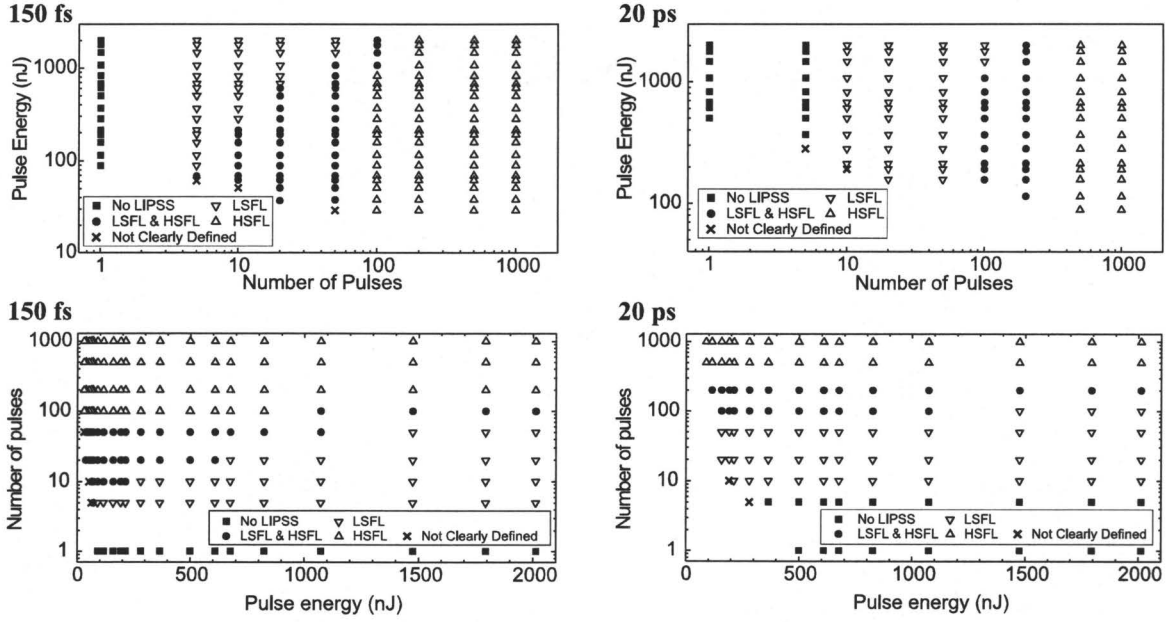

Figure 5.7: Maps of selected number of pulses and pulse energy conditions, showing the types of structures formed on GaP under these conditions. The top two graphs are from reference [60] and were prepared by E.M. Hsu. The bottom two graphs show the same data as the upper two, but are reorganized to more closely match the format used in figure 5.2.

the center of a site evolves from no LIPSS to LSFL, then to HSFL. With more pulses, a deep hole forms, with HSFL on the walls of the hole (such a case is shown in figure 5.8 later in this chapter). For silicon however, fine structures have a small height and form while the irradiation site is not particularly deep. As the number of pulses on silicon increases, an absence of periodicity is replaced by fine structures, then by coarse structures, and eventually a deep hole with some LSFL on the surface near the edge. Unlike GaP, fine surface structures on silicon are easily eroded by too high a number of pulses, while for GaP a higher number of pulses increases their presence. Since the irradiation of GaP typically used a smaller laser spot size, additional work would be needed to confirm that the differences reported here are not due to the difference in spot sizes. As noted in the paper on GaP discussing pulse duration [60], a larger spot size on GaP would have enabled clearer identification of features near threshold.

The images shown in section 6.3.2 show the evolution with number of pulses for silicon and germanium. The LSFL on silicon and germanium do not extend from the surface down along the sides of a deep hole (as the HSFL in GaP do). Instead, on silicon larger structures looking somewhat like remnants of eroded large cones exist at the upper edges of the

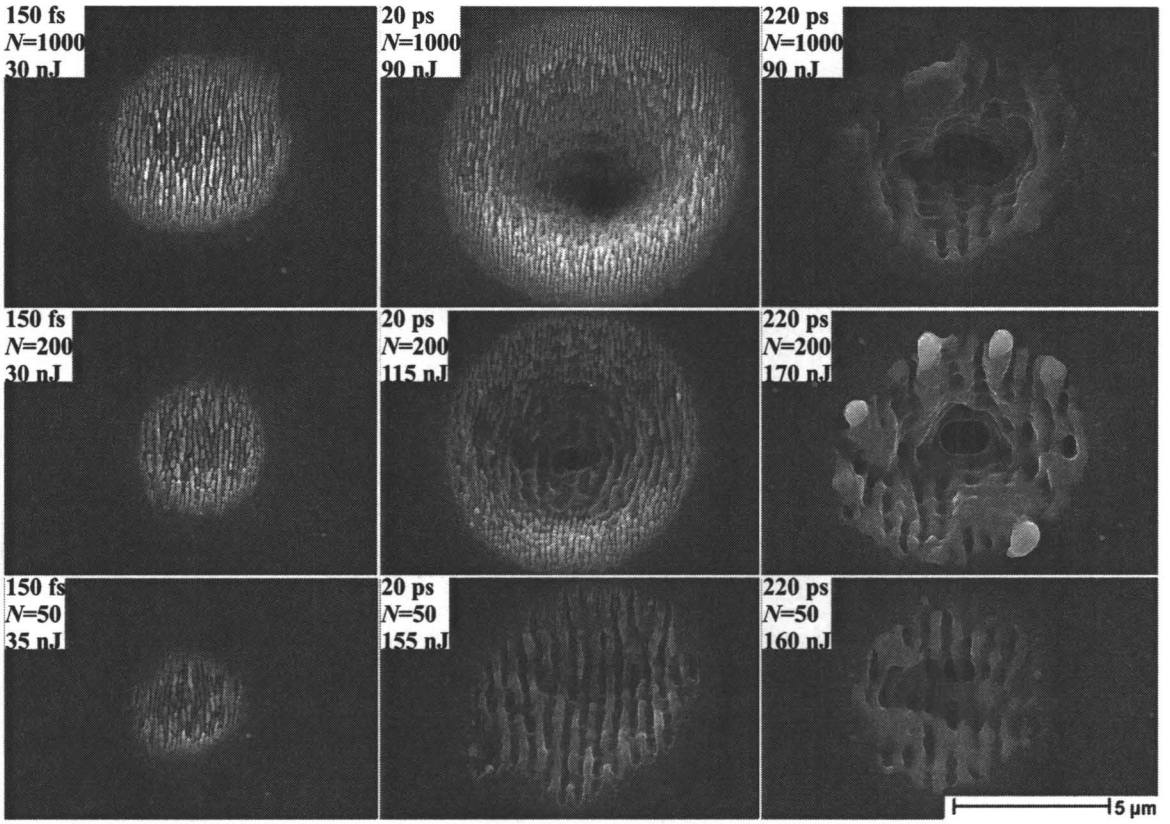

Figure 5.8: SEM images of GaP irradiated at near-threshold conditions for three significantly different pulse durations and for three numbers of pulses (N). These images are from reference [60] and were prepared by E.M. Hsu.

hole walls. On copper (see chapter 8), a microtome provided a relatively straightforward way of cutting a hole along its length for imaging of the hole walls in SEM. This technique could not be used on silicon or GaP due to the much stronger tendency of crystalline semiconductors to cleave and fracture. Application of the focussed ion beam technique to semiconductor holes could allow the imaging of the hole walls in SEM, to get a better view of the wall morphology. Due to the more confined nature of holes compared to grooves, the wall structures may not be the same in the groove and hole cases.

Figure 5.8 shows selected examples of various combinations of pulse durations and numbers of pulses, for GaP irradiated by $\lambda = 800$ nm pulses at energies near the material modification threshold. As the pulse duration increases, the minimum number of pulses for HSFL formation also increases. At a pulse duration of 80 ps, small areas of HSFL were sometimes observed at the periphery of LSFL-dominated sites. For the 130 and 220 ps

cases, only LSFL were formed. Only signs of melting, resolidification and cracking were observed for 7 ns irradiation, with no periodic structures. Near threshold, longer pulse durations tended to produce deeper sites, as can be seen by comparing (for example) the 150 fs and 20 ps cases in figure 5.8. A key result from the investigation of GaP at various pulse lengths [60] is that the HSFL formation was not strongly sensitive to the peak intensity of the pulses. For example, HSFL formed readily at both 150 fs and 20 ps pulse durations, where the fluence for 20 ps was only three times higher than for 150 fs pulse duration. On GaP it was also found that at longer pulse durations (greater than 10 ps) the material removal process becomes less deterministic. For example, when making several irradiation sites using the same number of pulses and pulse energy near the threshold energy, at longer pulse durations it was possible that some sites would show significant damage while no damage was visible on other sites in the group. This behaviour includes cases where femtosecond laser pulses were stretched, and was not just in the 130 ps, 220 ps, and 7 ns cases, so changes in determinism here are not due to changes in how the pulse is generated. Stretched and unstretched pulses would be expected to have similar fluctuations in properties such as pulse energy, so any such fluctuations are unlikely to be affecting the determinism. Similar pulse duration effects have been reported previously for dielectrics (see, e.g. references [108, 109]), however for below-bandgap photon energies in femtosecond irradiation of silicon and GaP, a much more deterministic behaviour was observed.

5.6.2 TEM examinations

Periodic structures on GaP were also examined in cross-section using TEM of FIB-prepared samples. FIB preparation was performed by Fibics, Incorporated, while the TEM imaging was done by Christian Maunders. Knowledge of the sub-surface crystalline configuration could aid in determining the as-yet unresolved cause of substantially sub-wavelength periodic structures. However, cross-sectional TEM additionally provides information on the depths and profiles of structures whose aspect ratios are too high for the AFM probe tip geometry.

For the TEM investigations of GaP, a 75 mm focal length lens was used as the laser focussing element for 150 fs pulses at $\lambda = 800$ nm. Figure 5.9 shows electron microscopy images of a site on GaP irradiated by 100 pulses. LSFL are present in the center region, surrounded by HSFL in the lower-fluence region of the site, again indicating that a lower fluence favors the formation of HSFL. The LSFL and HSFL shown here have periods of $\sim$575 nm and $\sim$185 nm respectively. Figure 5.10 shows a site after 1000 pulses, showing

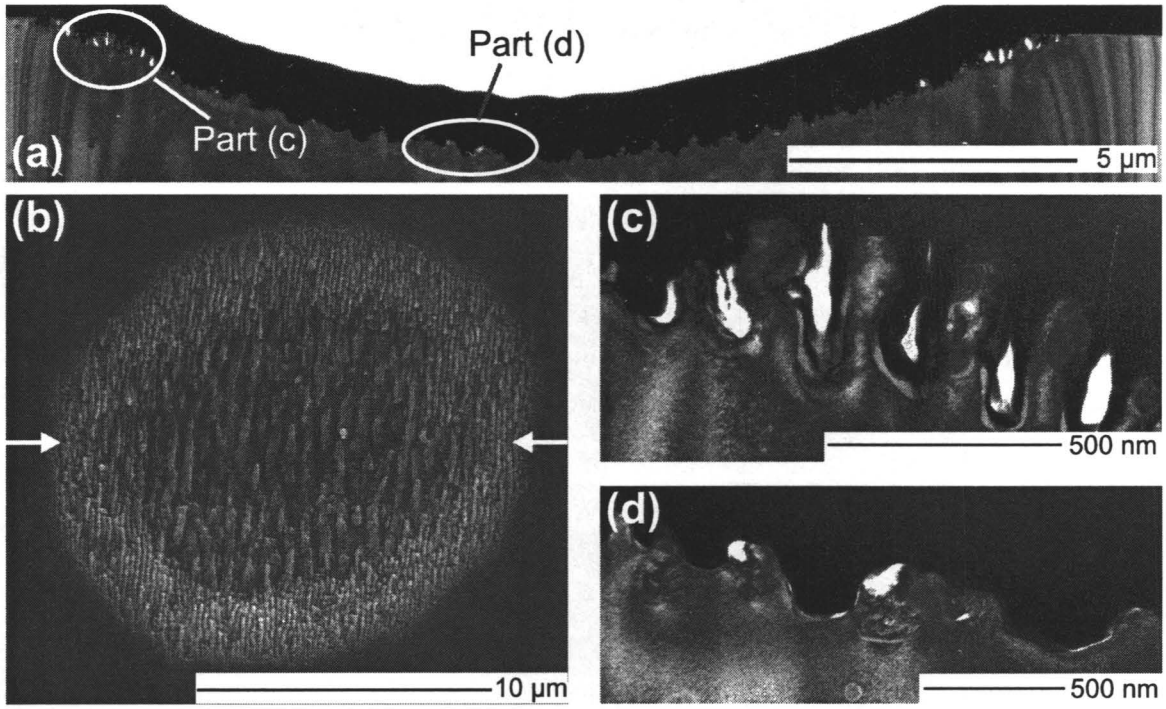

Figure 5.9: SEM and TEM images of GaP irradiated with 100 pulses at a per-pulse energy of ~415 nJ. Part (b) shows an SEM image of a site, while (c) and (d) show higher-magnifications of the TEM image in (a). The arrows in (b) indicate the general location from which the FIB cross-section was taken. These images are from reference [46] and were prepared by E.M. Hsu and C. Maunders.

only HSFL having an average spatial period of ~165 nm. For deeper holes, HSFL form down the walls of the hole, although SEM could not image the bottom of such holes. The HSFL can have a very large height to width ratio, with the tallest protrusion having a height of ~960 nm, while the widths are ~85 nm on average. Such planar-like structures resemble those observed in fused silica by Bhardwaj et al. [62], and are discussed briefly in the silicon structures paper [58] and GaP TEM paper [46]. The approximate depths of the structures on silicon, roughly one hundred nanometres or less, were measured using AFM. In the InP case [43] the FIB sample was not from an optimal location for HSFL observation, but for 20 pulse irradiation the structure height was around a few hundred nanometres.

Many of the possible ripple formation mechanisms discussed in the silicon ripples paper [58] could be applicable to the HSFL formation on GaP and the other III-V materials in reference [59]. The spatial periods of HSFL were larger than the second harmonic wavelength in the bulk material, but smaller than the fundamental wavelength in the bulk (see

references [59, 60]). Electron excitation would be expected to change the refractive index of the material, and thus change the wavelengths within the material. However, the refractive index would vary with time as the density of excited electrons evolves after light absorption, complicating an analysis of this effect. An additional effect [46] not noted in the silicon paper [58] but which would reduce the effective refractive index of the material is the removal of target material after periodic structures start to form. This would be expected to depend on the structure type (shallow structures on silicon in contrast to the much deeper structures on GaP) and the fact that the structure height changes with number of pulses. It should be noted however that any changes in the refractive index might not be particularly relevant if the ripple period is seeded early in the structure formation process.

Electron diffraction patterns from the locations indicated in figure 5.10 reveal that the surface of the structures is capped by a layer of amorphous material, indicated by a ring pattern in the diffraction pattern. The centers of the structures consist of single crystal material (indicated by a pattern of spots in the diffraction pattern) having the same crystal orientation as the substrate. This suggests that the cores of the ripples are not modified. Since amorphous material has different optical constants than crystalline material, changes in crystal structure could affect the structure formation processes [43, 58].

5.6.3 Additional results

The silicon ripples paper [58] and the paper by Borowiec et al. [59] examining HSFL and LSFL formation did not consider irradiation of materials at 400 nm. GaP and sapphire are the two materials presented in reference [59] for which HSFL formed for $\lambda = 800$ nm irradiation. As a follow-up experiment, E.M. Hsu irradiated these two materials with ultrashort $\lambda = 400$ nm pulses [106]. The experimental approach was similar to that used for the other investigations, using a grid of pulse energy and number of pulses. LSFL, running perpendicular to the laser polarization, formed with periods of 320–420 nm on GaP, while no HSFL were observed on GaP. Sapphire, which is one-photon transparent at $\lambda = 400$ nm, exhibited HSFL with a spatial period of $\sim$120 nm, but only for numbers of pulses between approximately 5 and 20, and mostly in a ring-shaped region of the site. Various deep and/or irregular features were frequently observed on sapphire, however no obvious LSFL were observed [106]. The formation and period of HSFL on sapphire and the lack of HSFL for the above-bandgap photon energy on GaP are consistent with the trends reported on other materials [59], namely that below-bandgap photon energies produce HSFL which scale (approximately) with irradiation wavelength. The absence of LSFL on sapphire at

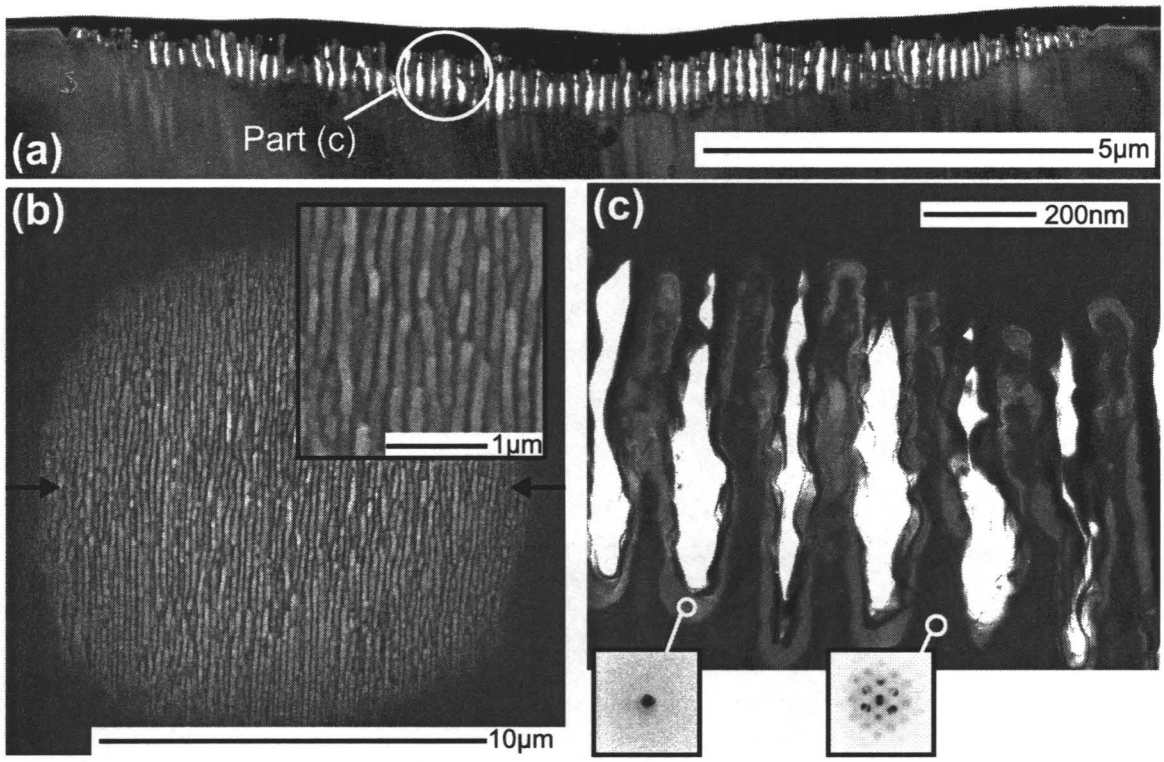

Figure 5.10: SEM and TEM images of GaP irradiated with 1000 pulses at a per-pulse energy of ~190 nJ. Part (b) shows an SEM image of the site, while (c) shows a higher-magnification and electron diffraction patterns of the TEM image in (a). These images are from reference [46] and were prepared by E.M. Hsu and C. Maunders.

this wavelength is unusual, but considering that the HSFL formed for only a small range of conditions at this wavelength, it could be that the conditions for LSFL formation were not used. Although investigation of periodic structures on silicon at 400 nm wavelength was not done, it is expected that LSFL would form but substantially sub-wavelength periodic structures would not do so.

On silicon at ~1300 and ~2100 nm irradiation wavelengths, no experiments were performed with circularly polarized light or with a 'spinning' linear polarization, due mainly to unavailability of appropriate waveplates at the time the experiment was conducted. However, circular and spinning polarization experiments were performed on GaP for 800 nm irradiation wavelength. Both polarization types (circularly polarized and spinning linear polarization) produced large bumps with diameters of ~410–520 nm and small bumps with diameters of ~80–120 nm [106]. These bumps were somewhat randomly distributed, and did not lie on a grid or along lines. Large bumps were formed under pulse energies and

number of pulses conditions which would be expected to produce LSFL for linearly polarized light, while small bumps formed under the conditions under which HSFL would be expected to form [106]. The bumps looked somewhat as if LIPSS had formed overlapping each other at different angles. The main difference between the circular and the spinning polarization was that circularly polarized light generated a mixture of larger and smaller bumps not segregated into separate areas. Since the orientations of LSFL, HSFL, and the various fine silicon structures are related to the direction of linear polarization, a different polarization could give insight into the formation of the structures. One argument against simple 'self-organization' or 'self-assembly' models of periodic structure formation is that they may not intrinsically explain why the laser polarization direction affects the structure formation (as noted in reference [110]).

Grooves in GaP were also prepared by E.M. Hsu, cleaved perpendicular to the length of the grooves, and imaged in SEM [106]. This technique is the same as that done for the silicon grooves presented in chapter 4. The equation for effective number of pulses from section 4.3.2 and the grooves papers [64, 65] [$N_{\text{eff}} = (\sqrt{\pi/2})(\omega_{\circ} f/\upsilon)$] was used to choose a translation speed $\upsilon = 13$ μm/s which yielded $N_{\text{eff}} \approx 1000$. It was possible to make long grooves containing HSFL, as was also found on some III-V materials (unpublished work by A. Borowiec) and as suggested by preliminary results for silicon in section 5.3.4. Periods of HSFL on translated III-V samples were in a similar range as those on stationary samples. On the walls of somewhat deep grooves in GaP, HSFL did not extend perpendicular to the original wafer surface. Instead, they emerged at an angle between the normal to the wafer surface and the normal to the groove wall. In cross-section, debris deposited on the grooves could sometimes be seen with HSFL beneath.

5.7 Irradiation of a germanium (111) surface by various laser wavelengths

Preliminary experiments on undoped Ge(111) (approximately 300 μm thick, with a polished front surface and a rough back surface) were done using the same experimental approach used for Si(100) and Si(111) reported in the silicon ripples paper [58] and in this thesis. At the time these experiments were done, only Ge(111) material was available, and thus no substantially sub-wavelength ripple examinations on Ge(100) were performed. Additionally, only a single experimental run at each of the three irradiation wavelengths (800, ~1300, and ~2100 nm) was produced and imaged in Nomarski DIC microscopy for this investigation, so there has not been extensive work to confirm the repeatability of the

results. However, as presented in chapter 6, multiple experiments were later performed at $\lambda = 800$ nm for the examination of LSFL and larger structures, utilizing generally higher pulse energies and lower numbers of pulses than for the substantially sub-wavelength ripples experiments. Although I had planned to do further investigations on germanium at multiple wavelengths, effort was directed toward several other areas of research, and time constraints meant that I did not end up investigating in more detail the wavelength dependence of structures on germanium. This section of the thesis summarizes the preliminary results. Figure 5.11 shows various examples of periodic structures on germanium, as discussed below.

The LSFL which were observed on silicon and other semiconductors (see, e.g. references [58, 59, 60]) also formed on germanium for all three irradiation wavelengths, and were also aligned perpendicular to the laser polarization. A LSFL period on germanium of 1800 nm for an irradiation wavelength of 2100 nm was reported by Borowiec et al. [59], but other wavelengths on germanium were not used in that work. For all three irradiation wavelengths here, periods on germanium were somewhat less than the wavelength of the laser light, as was the case for all LSFL in references [58, 59]. As noted in chapter 6, germanium showed less tendency than silicon to form LSFL, with LSFL forming predominantly near the edges of substantially roughened areas and deep holes, and typically not covering a large portion of a site. The reduced LSFL prevalence for germanium compared to silicon existed at all three wavelengths investigated.

Germanium exhibited significant differences in behaviour from other semiconductors, with regards to the formation of substantially sub-wavelength structures. On silicon, the intermediate-sized ripples running parallel to the laser polarization formed only for $\sim$1300 and $\sim$2100 nm wavelength irradiation [58]. On germanium, structures with a qualitatively similar appearance and running parallel to the laser polarization also formed on germanium at $\sim$1300 nm and at $\sim$2100 nm, and are shown in figures 5.11(c) and (e). On germanium at $\lambda = 800$ nm, some structures resembling the intermediate-sized ripples formed in rare cases but were very disorganized, lacking long-range coherence (see figure 5.11(a)). The bandgap of germanium corresponds to a wavelength of around 1850 nm, so the formation of these ripples at 800 nm and $\sim$1300 nm irradiation wavelengths does not require a photon energy below the bandgap energy. At $\lambda \approx 2100$ nm, their spacing was roughly 800 nm, while at $\sim$1300 nm their spacing was roughly 750 nm, and the spacing was near 600 nm for 800 nm wavelength irradiation. Thus, unlike for silicon for which the period was roughly half the irradiation wavelength, the period on germanium did not change substantially with wavelength, and is perhaps slightly wavelength dependent. The structures

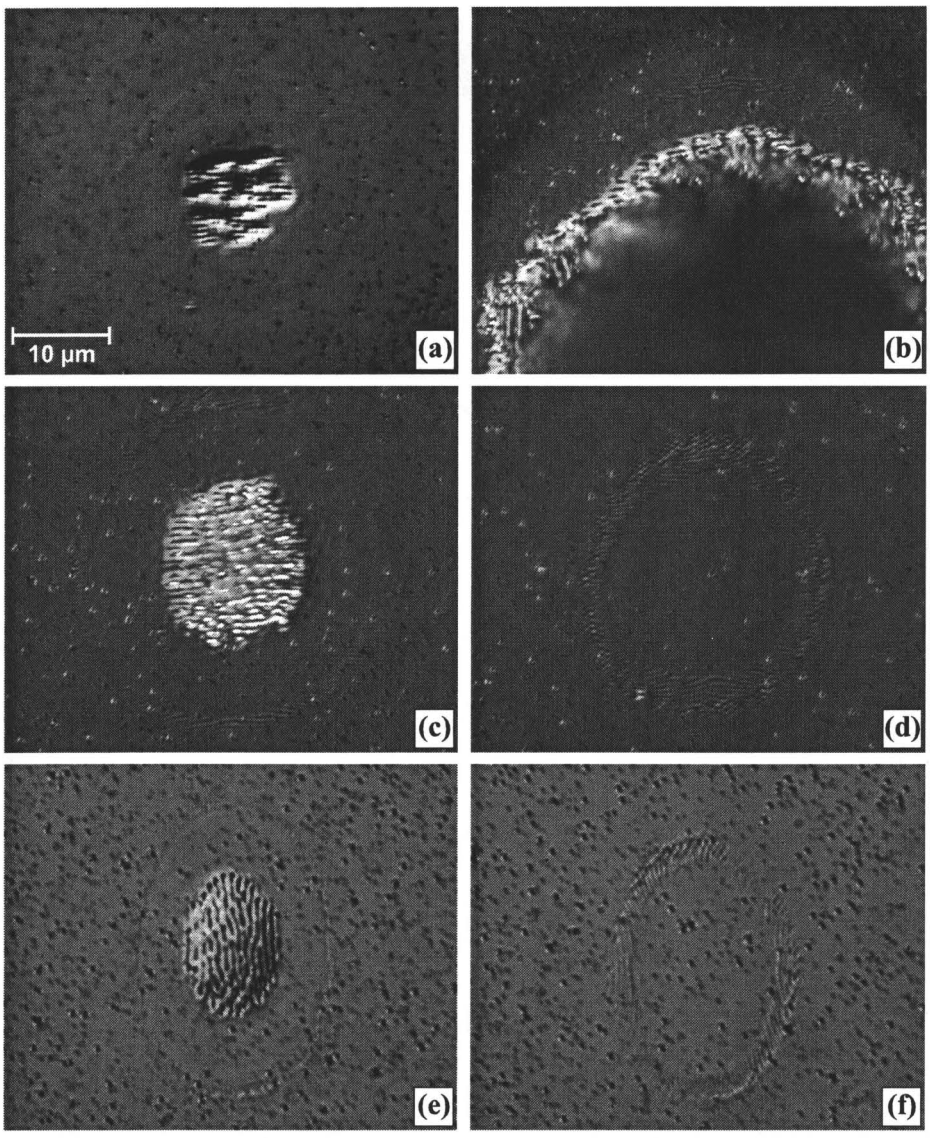

Figure 5.11: Nomarski DIC images of a Ge(111) surface irradiated by femtosecond laser pulses, showing various periodic surface structures. All images show 'fine' ripples at the periphery of the site. Images (a), (c), and (e) show 'intermediate' ripples in the centers of sites for 800, ~1300, and ~2100 nm wavelength irradiation respectively. Image (b) shows fine ripples, and small regions of LSFL near the edge of a deep hole for ~1300 nm wavelength irradiation. Images (d) and (f) (~1300 and ~2100 nm wavelength irradiation respectively) show 'fine' ripples with slight hyperbolic-like curving accompanied by small patches of 'fine bumps'. For the $\lambda = 800$ and ~1300 nm cases, the laser polarization was approximately horizontal in the images, while for the $\lambda \approx 2100$ nm cases the polarization was approximately vertical. The black speckles visible throughout the images are believed to be debris.

shown for $\lambda = 800$ nm are unlikely to be LSFL, since they run parallel to the laser polarization and have a morphology qualitatively similar to 'intermediate' ripples at other wavelengths. Like on silicon, they were present for between approximately 100 and 1000 pulses, and for a narrow fluence range near the single-pulse surface modification threshold.

At all three irradiation wavelengths a type of 'fine' ripples formed aligned parallel to the laser polarization. These structures are shown in parts (a)–(f) in figure 5.11. They all had periods around 350–450 nm, so their period did not seem to change significantly with wavelength. These formed in a wide range of conditions (many different fluences and for a number of pulses typically greater than $\sim$100), but were almost always present in an annular region surrounding the central modified area. When these ripples were long, they tended to curve, so that they formed a slightly hyperbolic shape with the ripple being pulled toward the center of the irradiation site. They seemed somewhat more prevalent for the irradiation wavelength of $\sim$1300 nm. Unlike for silicon, the 'fine' ripples on germanium were present for a wide number of pulses.

On germanium, structures resembling the fine bump arrays on silicon also formed for $\sim$2100 nm and $\sim$1300 nm irradiation wavelengths (see figures 5.11(d) and (f)), but were not observed for 800 nm irradiation. Only Nomarski DIC optical microscopy was used to image these germanium structures, so AFM would be required to determine if their shape is the same as those formed on silicon. When they formed (requiring more than several hundred pulses), their spacing was roughly 300–500 nm, seemingly independent of wavelength. At $\sim$1300 nm, they tended to form in small clumps rather than in larger areas, and were formed at the periphery at fluences lower than those which formed fine ripples. Larger patches of 'fine bump arrays' tended to occur for $\lambda \approx 2100$ nm, particularly near the centers of sites.

Overall, while germanium and silicon showed general similarities in behaviour with regards to LSFL and blunt conical structures, the two materials behaved quite differently in the formation of substantially sub-wavelength structures. In particular, the periods of the 'intermediate-sized' and 'fine' structures on germanium did not vary substantially with irradiation wavelength. In contrast to the other non-metals studied in this thesis, on germanium the bandgap energy relative to the photon energy did not seem to separate two regimes of behaviour. It could be the case that 'self-assembly' mechanisms are dominant on germanium, while other mechanisms are more relevant for the substantially sub-wavelength structures observed on other materials. There are certain differences in physical properties between silicon and germanium which may play a role, in addition to those tabulated in section 6.4. For silicon, some structures had dimensions which were approaching the ex-

pected native oxide thickness, and the possible influence of oxides was noted [58]. Oxide on a germanium surface behaves quite differently from the oxide on silicon. In contrast to SiO_2 used for silicon passivation, germanium surfaces are not effectively passivated with germanium oxides, and the quality is lacking compared to the SiO_2 for silicon technology [111]. Also, while the vaporization temperature of germanium is more than 500 K above that of silicon, it melts nearly 500 K below the melting temperature of silicon [1]. Thus, in germanium an increased melt volume might be expected for similar irradiation conditions. This melt in turn may affect structure formation, particularly at relatively low fluences where the fine structures formed.

An important technical point should be addressed in further investigations of germanium. The silicon surfaces in experiments presented in this thesis were relatively free of particulate matter (as seen in optical microscopy, in the SEM, and from AFM scans), and were cleaned before irradiation as described in other parts of this thesis. However, the germanium did not have a careful cleaning or preparation. For shallow surface structures such as the 'intermediate' ripples and 'fine' structures, the presence of a large number of particles could have affected the structure formation. After irradiation by high numbers of pulses, a region of reduced debris was frequently formed immediately around the irradiation site, suggesting removal of debris via a 'laser cleaning' mechanism (see, e.g. reference [1]) or due to an expanding shock wave (see, e.g. reference [98]). However, it should be noted that substantial particulate matter visible in figure 5.11 is on top of the laser-structured surfaces, suggesting that at least some of it was redeposited from other sites on the samples.

An additional study which could yield useful information on germanium would be to perform cross-sectional TEM imaging. Such work has proven informative on silicon and GaP (presented in several sections of this thesis) and on InP [38, 43]. It would reveal, for example, to what extent germanium oxide is present in and around the various periodic structures. Possible amorphization of germanium after single-pulse irradiation is discussed in section 6.4.3, and TEM could reveal if amorphous material is present in the multiple-pulse cases presented here. The crystallinity of the substantially sub-wavelength structures on germanium, in comparison to those on silicon, could indicate if similar mechanisms are acting on both materials.

In contrast to most materials, silicon and germanium both expand when freezing due to their relatively low atomic packing factor. This expansion could contribute to the formation of structures which were not observed on other materials. Irradiation of other elemental materials which expand upon freezing, such as bismuth and gallium, could be examined

for similar fine structures. However, these materials are not transparent to the laser wavelengths, which would complicate a comparison.

5.8 Conclusions, and suggestions for further investigations

The physical origins of the significantly sub-wavelength periodic structure formation on semiconductors are still an open question. The results presented here have provided some insights, but have still left many opportunities for further investigation. As noted in the 'Conclusions' section of the silicon ripples paper [58], there are several points which would need to be addressed by a complete theory for ripples formation. Additional experiments and analysis methods could help address these points. Ideally, we would have a theory with well defined predictions so that experiments could be designed to test them. The current approach has been to survey a wide parameter space, although this approach has still yielded significant results.

It is not clear why a photon energy less than the bandgap energy is required on silicon [58] and III-V materials [59] for fine structure formation. Jia et al. [61] observed substantially sub-wavelength ripples on ZnSe for 800 nm wavelength irradiation but not for 400 nm wavelength, demonstrating the below-bandgap criterion on a II-VI material. Further investigation of other II-VI materials would examine the 'universality' of the below-bandgap criterion. Multiple II-VI materials have bandgap energies in the visible light range, and thus could be easily examined using a standard Ti:sapphire ultrafast system and second harmonic generation. Experiments using $\lambda = 400$ nm light on GaP showed the continued trend for HSFL formation only for photon energies below the bandgap energy [106]. Such investigations were not performed on germanium or silicon, but would be useful to confirm a similar trend on silicon, and to find if fine ripple formation on germanium also continues for this wavelength. Systematic examination of germanium surfaces would be warranted, to more clearly determine the trends and compare these trends to silicon and the other materials. Several experimental runs with different wavelengths should be done on each material, to show how a structure period scales with wavelength. This would reduce the possibility of a coincidence, where using half the wavelength happens to produce half the period, but due to some other effect (such as a change in optical penetration depth). Additionally, when combining orthogonally polarized collinear 400 and 800 nm wavelength beams, Jia et al. [61] found that the direction of the ripples could be shifted away from the

direction obtained when using only the 800 nm wavelength. Such experiments and other II-VI materials are worthy of further investigation.

Pre-existing surface morphology on graphite has been shown in this thesis chapter to affect the direction of LSFL orientation. The use of pre-patterning on the other III-V or group-IV materials discussed in this thesis could help determine if fine structure formation is affected in the same way. 'Spinning' or circularly polarized light should also be investigated for formation of substantially sub-wavelength structures on silicon. Such investigations could show to what extent light interference effects are relevant to formation of substantially sub-wavelength periods.

As discussed in more detail in reference [60], a wide range of pulse durations produced HSFL on GaP, suggesting that the formation mechanism is not strongly dependent on laser intensity. Although it seems likely that other III-V materials would behave the same way (as the morphologies of HSFL look similar), it is not certain that silicon would exhibit similar results. Pulse stretching techniques could be used on the OPA wavelengths, or different laser type could be used. As noted in the silicon ripples paper [58], various rare-earth-doped fiber and solid state lasers would operate in this wavelength regime, and such lasers could be increasingly popular as fiber and diode-pumped laser systems evolve. In contrast to varying the pulse duration, using two or multiple pulses separated in time by picoseconds to nanoseconds could provide interesting results. For example, two pulses which are each below the threshold for structure formation may produce structures if the time delay does not exceed a particular value. Two pulses of different wavelengths, perhaps either side of the bandgap, may indicate if one pulse seeds a particular period or ripple orientation.

Cross-sectional TEM of femtosecond laser-induced structures on InP [43], GaP [46] and silicon (section 5.4 and chapter 7) has provided information on aspect ratios, material segregation, and crystallographic changes. More extensive work on fine silicon structures would be useful for comparisons. Unusual 'intermediate' and 'fine' structures on germanium have yet to be examined in this way. Chemical analyses, like those performed on InP in the TEM [43] would be useful on silicon and germanium to examine the possible role of oxidation or other atmospheric interactions during irradiation. Laser irradiation in an oxygen-free atmosphere or of an oxide-free target, if it were to affect ripple formation, would also be relevant. Planar-like structures have been observed in bulk fused silica [62] and on GaP [46], and connections between surface structuring and bulk modification should be explored. As dielectrics and III-V materials do not seem to behave the same way as silicon and germanium with regards to significantly sub-wavelength periodic structure formation, planar-like structures on silicon and germanium may be less evident.

The crystalline cores of HSFL shown by TEM in figure 5.10 raise an additional question in structure formation. It is possible that this material was once molten or modified, and regrew epitaxially. The use of some sort of marker layer in the material before irradiation could reveal if this happened. If the marker material diffused into the surrounding material, it would indicate that the semiconductor material melted and regrew epitaxially. However, if the marker layer remained intact, it would be unlikely that the material melted. For example, a very thin layer of some material on GaP (ideally lattice-matched), with several hundred nanometres of crystalline GaP grown on top, would work to allow this investigation since an appropriate 'buried' marker layer would be visible in cross-sectional TEM.

Many materials analysis techniques could be used on laser-irradiated materials. Additionally, many new laser irradiation experiments with various other parameters exist which, when varied, could give insight into the structure formation process. It is still not clear if the causes of HSFL formation on III-V materials are the same, or even related, to the formation of substantially sub-wavelength structures on silicon and germanium. Numerous preliminary investigations have been presented in this thesis, while additional work would be required to more thoroughly explore the phenomenon of substantially sub-wavelength periodic structures.

Chapter 6

Formation of Blunt Conical Structures and Amorphous Material on Silicon and Germanium

6.1 Introduction and motivation

On semiconductors irradiated by ultrashort laser pulses, a variety of surface morphologies have been observed such as annular rings and rims [33, 94], amorphization [34, 45, 46] and periodic ripples [58, 59, 60]. Periodic structures are discussed more extensively in chapters 5 and 8. Along the bottoms of grooves machined in silicon, a coarse modulation in depth was observed in many cases (see reference [65] and chapter 4.) When analyzing the samples used in the ripples experiments on silicon (chapter 5), it was also observed that large coarse non-periodic structures resembling cones were formed for a certain range of pulse energies and numbers of pulses. This range was generally between the conditions which formed periodic structures and the conditions which formed a deep hole. For these coarse structures it was observed that the crystalline orientation of silicon had a significant effect on their tendency to form, with Si(111) producing a much higher density of structures. In the experiments on ripple formation, the (111) surface orientation of silicon was observed to have a greater tendency to produce amorphous material for single-pulse irradiation. While these results were originally going to be included in the silicon periodic surface structures paper [58], it was decided to not include these results in that paper and to focus effort on the characterization of periodic structures. Later in my research, significant time was put into comparing three different crystal orientations of silicon, and also comparing two crystal orientations of germanium to investigate the generality of the behaviour. Cross-sectional TEM was performed on Si(100) and Si(111) samples irradiated under similar conditions, to examine the crystalline composition of LIPSS and the conical structures. The TEM study also enabled comparisons to a large body of cross-sectional TEM work done by the group, such as the multiple-pulse InP [43, 44] and GaP [46], and to the silicon irradiated by low numbers of pulses presented in this thesis (chapter 7).

Cone-like structures have been previously reported on silicon after femtosecond laser irradiation [35, 67], and the irradiation atmosphere has been found to affect their morphology [67]. However, the effect of the target crystalline orientation is generally not considered for structure formation. What is presented here is a systematic extension of these investigations, to examine the effect of the crystallinity. The formation of structures may be detrimental in some applications, possibly limiting the precision or smoothness with which surfaces can be prepared. However, surface roughening can be beneficial in other applications, for instance when an increased surface area is desired [67, 68, 69, 112, 113, 114]. The results presented here are also important to consider when comparing the results from different experiments in the research, since the chemical composition of the target and atmosphere are not the only factors which can influence the final morphology.

In the studies presented in this chapter, I decided the experimental approach, made the decisions as to what aspects to pursue, and did all the sample preparation and laser irradiation. The optical and scanning electron microscopy was done by myself, while Christian Maunders did the majority of the TEM imaging and Fibics, Incorporated did the FIB preparation. I did all the literature review and writing of the results.

6.2 Experimental

The two separate Ti:sapphire laser systems described in chapter 3 were used in these experiments as the pulse sources. These two systems produced linearly polarized ~50 fs and ~150 fs pulses respectively, both operating at a peak wavelength of 800 nm and a pulse repetition rate of 1 kHz. Pulses were focussed using a 12.5 cm or 15.0 cm focal length BK7 plano-convex singlet lens through a 1 mm thick fused silica window onto targets placed in a small sample chamber, evacuated to a rough vacuum atmosphere (less than ~100 mTorr). The Ge(100) and Ge(111) samples were undoped with a thickness of approximately 300 μm each. Samples of Si(100) and Si(111) (phosphorous-doped with 2–6 ohm-cm resistivity, and boron-doped with 7–13 ohm-cm resistivity respectively) were used, each approximately 300 μm thick. The boron-doped Si(110) samples with resistivity of 75–100 ohm-cm in this study were approximately 1000 μm thick. All irradiation targets had a polished front surface and a rough back surface, and were irradiated under similar conditions to allow straightforward comparison between materials. Irradiation proceeded in a similar fashion as for the ripples samples (see chapter 5), whereby a grid of various combinations of number of pulses N and pulse energy E were produced on each sample. The metallic neutral density filters in increments of 0.1 OD (transmission $=10^{-OD}$) allowed

the variation of pulse energy, beginning with 10–15 μJ per pulse and decreasing in steps to well below the sample modification threshold. The numbers of pulses included 1, 5, 10, 25, 50, 100, 200, 350, 500, 650, 750, 850, 1000, 2000, 5000, and 10 000. When fewer than 50 pulses were desired, a mechanical chopper placed in the beam reduced the effective pulse repetition rate to 50 Hz. Some experiments were repeated with the two different laser systems and with different lenses, to check for the possibility that the results were due to an anomaly with particular laser or lens. Nomarski differential interference contrast (DIC) optical microscopy was used for imaging single-pulse irradiation sites. Measurements to the outside of the prominent rims in these sites were used with a D^2 method (see chapter 3) to determine the on-sample spot size ω_o. As in the rest of this thesis, I report incident fluences, not considering the reflectivity of the target surfaces. Scanning electron microscopy was used to image multiple-pulse sites, due primarily to its greater depth of field. Selected sites were prepared via FIB and were imaged in bright-field mode on the Philips CM12 TEM, with a 120 kV acceleration voltage.

6.3 Results

6.3.1 Single-pulse surface analysis

Figure 6.1 shows the five target materials each after irradiation by a single pulse. The Si(100) and Si(110) orientations look very similar, with a thin irregular ring present. This ring has approximately the same size on both silicon crystals, suggesting that the formation threshold does not strongly depend on crystalline orientation. The Si(111) possesses a thin ring of a similar appearance and size, however it is surrounded by a wide annular region of higher optical reflectivity. This brighter annular area is both inside the thin ring, and extends outside a short distance. As discussed in further detail in section 6.4, the higher reflectivity material is likely amorphous silicon. The many small circles distributed randomly on the surface in the Si(111) case are likely due to dust particles created at other irradiation sites redepositing before irradiation of the site shown. In other experimental runs using Si(111) the number of small circles was much smaller than that shown in figure 6.1, correlated with a reduced frequency of dust particles visible outside the irradiated area.

As shown in figure 6.1, the two germanium crystals ((100) and (111)) look very similar after irradiation, with a prominent ring. Unlike silicon, the irradiated Ge(111) did not show a substantially higher reflectivity than the Ge(100). For single and multiple pulse

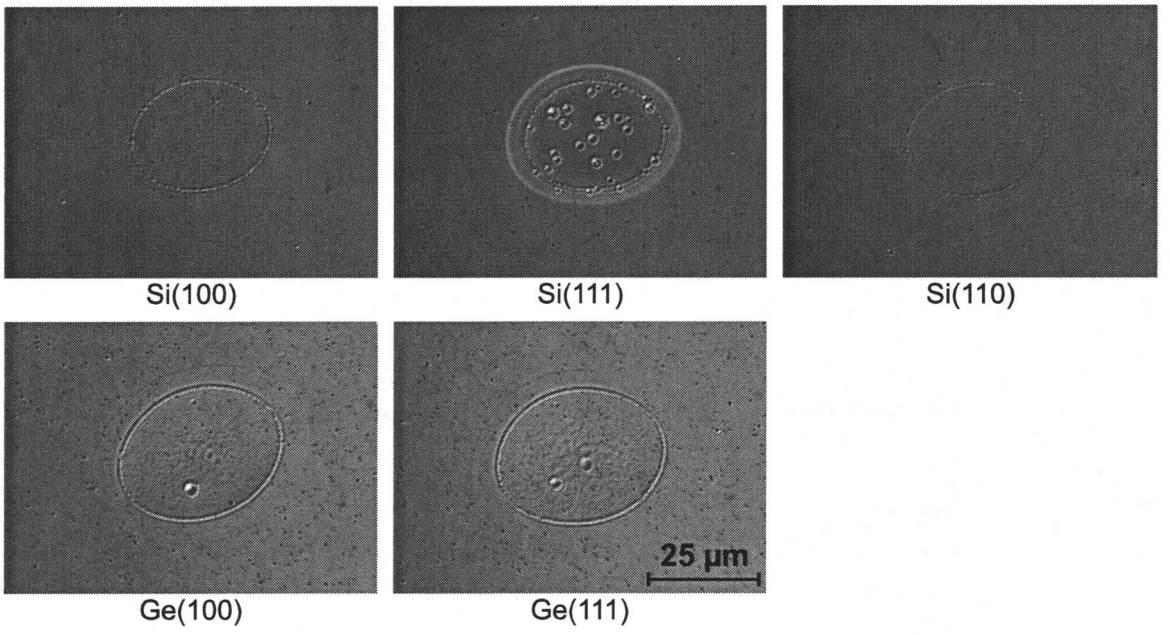

Figure 6.1: Nomarski DIC optical microscope images of Si(100), Si(111), Si(110), Ge(100), and Ge(111) each irradiated by a single pulse with fluence of approximately 1000 mJ/cm^2 (pulse energy 6.3 μJ). For these sites, a 12.5 cm focal length lens was employed with 150 fs pulses. All images use the same scale.

irradiation, germanium could be modified at fluences at which silicon did not show visible change. The irregular ring was larger on germanium than on silicon for the same incident pulse fluence, also consistent with a lower modification threshold for germanium. The single-pulse trends on silicon and germanium described here (sizes of rings and differences in reflectivity) existed for the full range of fluences used in this study.

6.3.2 Multiple-pulse surface analysis

'Classic' low spatial frequency laser-induced periodic surface structures (LSFL) with periods ~70–90% of the irradiation wavelength formed on all samples examined in this chapter. The material composition (silicon or germanium) did not seem to affect the period, nor was the period affected by the crystal orientation. The three types of silicon did not show significant differences in their tendency to form these periodic structures. Germanium showed much lower tendency than silicon to form such LIPSS, although the two crystallographic orientations of germanium did not differ substantially in LIPSS formation. No periodic structures were observed after irradiation by only a single pulse. When pulse

energies near the material modification fluence were used, LIPSS gradually formed with increasing number of pulses over most of the laser-irradiated site. For higher energies and after higher numbers of pulses, they were eroded away in the central area of sites but were still often present in a ring around the site, where the local fluence was low. In an additional experiment performed on the silicon samples (with 50 fs pulses and the 15.0 cm focal length lens), a half-wave plate was placed in the laser beam to rotate the laser polarization $\sim$45° relative to the polarization used in the other experiments. Both with and without this wave plate, the LIPSS formed running perpendicular to the polarization of the light incident on the sample, independent of the surface crystallographic orientation. More discussion of LIPSS is given in chapter 5.

Blunt cone-like structures, with diameters of a few micrometres, can form in the central region of the irradiation sites where the fluence is high enough that the ripples are eroded away. These had a much stronger tendency to form on the materials with (111)-surface orientation than on the materials with (100)-surface orientation. On the (100) surface orientation, they were particularly lacking in the centers of the irradiation sites where the local fluence was highest. Instead of the blunt cones, the central areas of sites on (100) surfaces showed some roughness but minimal large-scale variation in depth. For silicon with a (110) surface orientation, the cone formation tendency was similar to or slightly less than for (111). Experiments on Ge(110) were not performed in this study. For the Si(111), Si(110), and Ge(111), larger but more sparsely spaced cones resulted from higher numbers of incident pulses.

For comparison, figure 6.2 shows the three crystal orientations of silicon and the two orientations of germanium, with each site irradiated by 100 pulses at various pulse energies. Figure 6.3 shows the five materials irradiated by various numbers of pulses, at a per-pulse fluence of approximately 810 mJ/cm^2. The dependence of conical structure formation on surface crystallographic orientation can be seen. The relative occurrence of LIPSS between materials is also shown in figures 6.2 and 6.3, though the magnification used for these images makes the LIPSS difficult to see. For silicon, the differences in the formation of conical structures were most prevalent for between approximately 25 and 850 incident pulses with peak fluences between approximately 500 and 1800 mJ/cm^2. On germanium, these differences were most prevalent for between approximately 25 and 500 pulses and fluences between approximately 250 and 1800 mJ/cm^2. These ranges are approximate, due to the coarseness of the grid and the somewhat subjective nature in comparing different surface morphologies. For fluences below these ranges, the crystallographic orientation did not strongly affect the structure formation. Small cones were gradually replaced with a

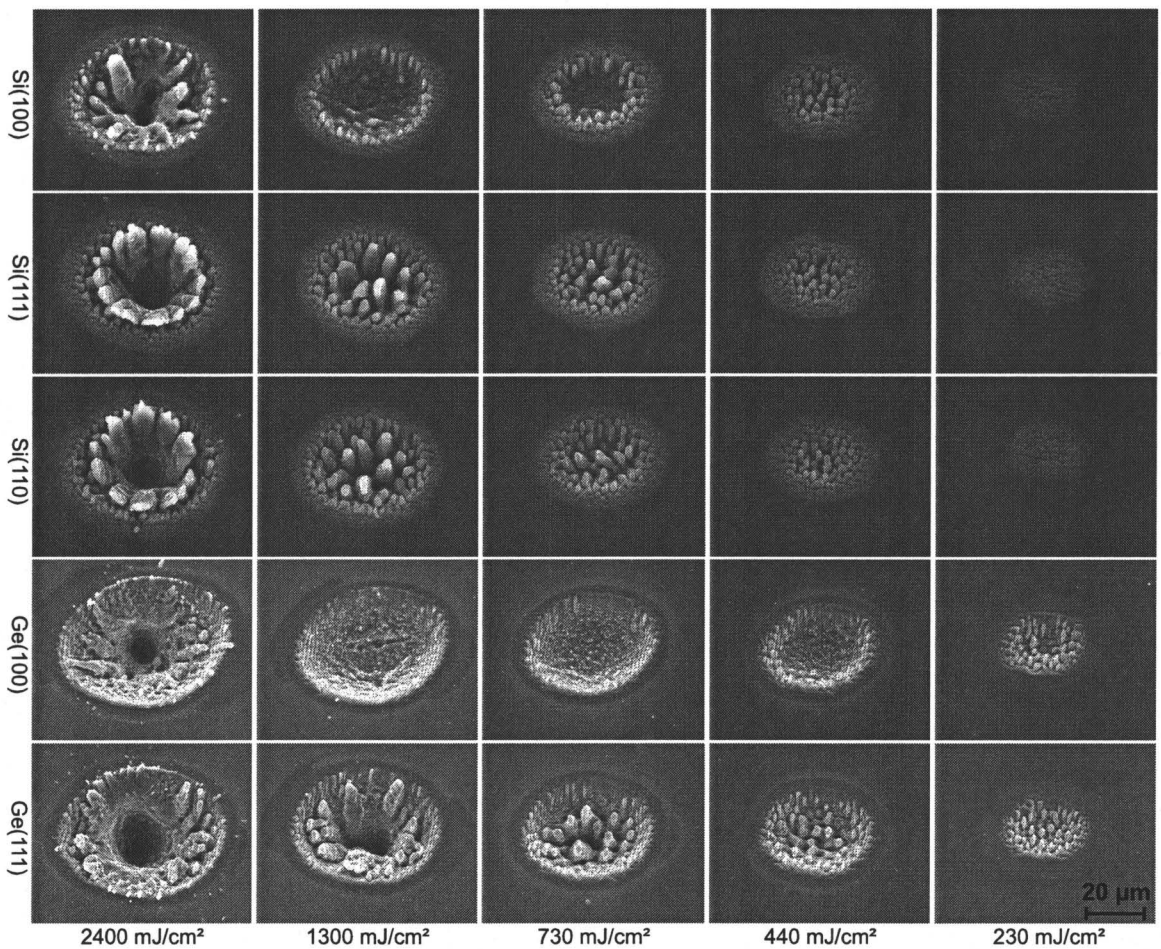

Figure 6.2: SEM images of Si(100), Si(111), Si(110), Ge(100), and Ge(111) irradiated by various pulse fluences. For each case, 100 pulses were used. For these sites, a 12.5 cm focal length lens was employed with 150 fs pulses at $\lambda = 800$ nm. The laser was polarized approximately horizontally in the images. All images use the same scale. The SEM images were taken at a 15° angle relative to the normal. The per-pulse energies corresponding to the indicated fluences are 15, 8.1, 4.6, 2.8, and 1.5 μJ.

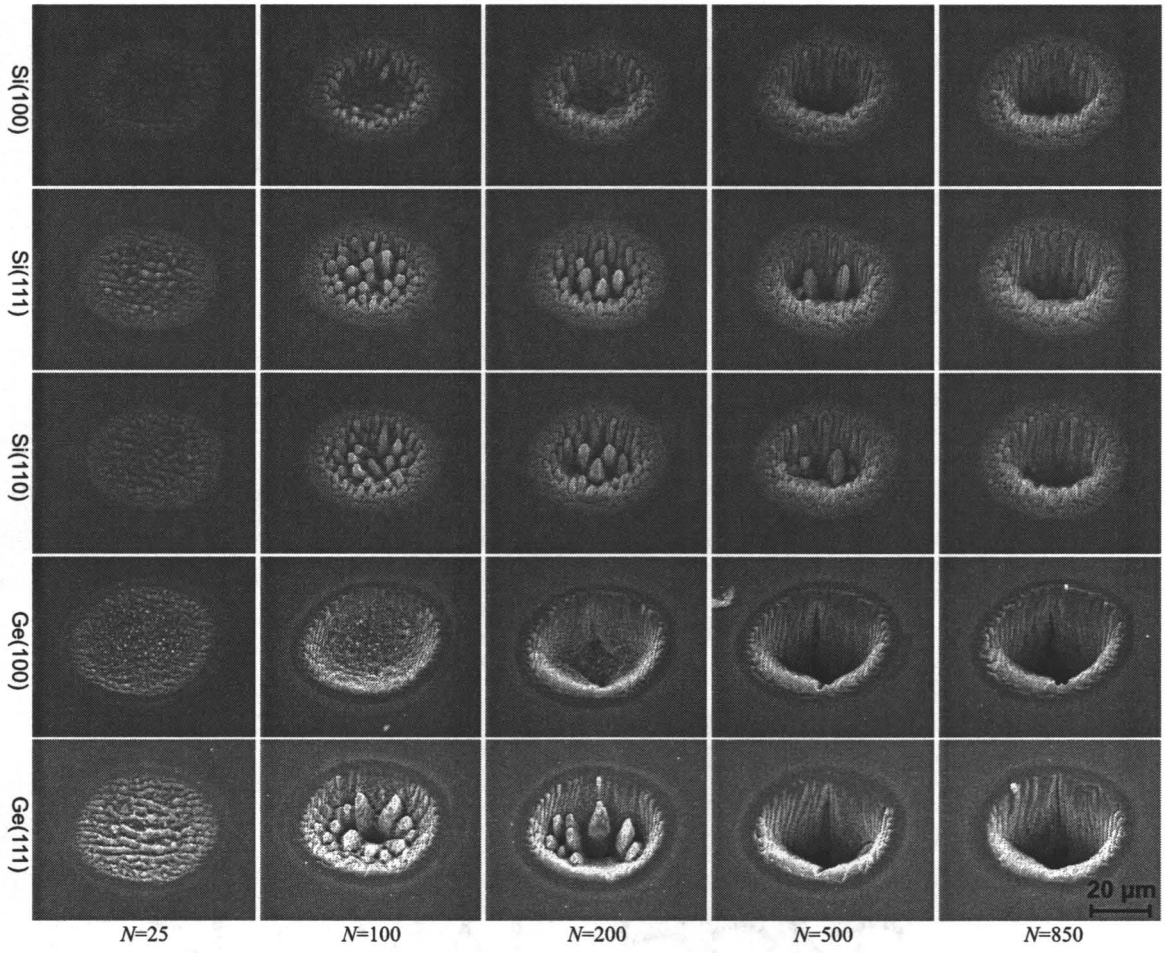

Figure 6.3: SEM images of Si(100), Si(111), Si(110), Ge(100), and Ge(111) irradiated by various numbers of pulses N. Each pulse had a fluence of approximately 810 mJ/cm^2 (pulse energy 5.1 μJ). For these sites, a 12.5 cm focal length lens was employed with 150 fs pulses at $\lambda = 800$ nm. The laser was polarized approximately horizontally in the images. All images use the same scale. The SEM images were taken at a 15° angle relative to the normal.

shallow corrugation, as the fluence was decreased down to the material modification threshold. For fluences greater than the cone-formation fluence range, all investigated materials tended to show a deep hole, with a morphology suggesting strong expulsion of material along the sides of the hole. Above the upper limit of number of pulses, a deep hole formed, and any conical structures which may have been present appeared to have been eroded away. In this study, the upper limits on fluence and number of pulses used were $\sim$2.4 J/cm^2 and 10 000 respectively.

The different tendencies to form large blunt conical structures persist when the sample is translated under the laser beam. Figure 6.4 shows grooves in the five samples for various numbers of passes at a translation speed υ of 1000 μm/s. The numbers of passes are 1, 2, 4, 6, 8, and 10, corresponding to an effective number of pulses per point (as defined in reference [65] and section 4.3.2 as $\sqrt{\pi/2}(\omega_\circ f/\upsilon)$ per pass where $f = 1$ kHz is the pulse repetition rate) of 21, 41, 82, 123, 164, and 205 respectively. The bottoms of the grooves are not smooth. On the silicon (111) and (110) substrates many cones exist along the length of the groove, while the (100) case only shows some sporadic cones at the higher numbers of passes. On Ge(111) the cones look as if they have been flattened somewhat against the sides of the grooves, while Ge(100) does not have these flattened cones. Instead, a coarse periodic modulation appears to be forming after 8–10 passes along the bottom of the groove on Ge(100). This structure may be similar to the corrugation observed on silicon with a more tightly focussed beam (see reference [65] and section 4.7), although more investigation would be required to confirm a connection.

While the results shown in figures 6.2, 6.3, and 6.4 were obtained with the 150 fs laser system, experiments using the 50 fs system on silicon produced similar results. The 50 fs system was not used in experiments on germanium, however it is expected that results would also be similar. The different radii of the laser beams emitted by the two laser systems and the different lens focal lengths affected the on-sample spot size somewhat, however this did not appreciably affect the results. When a half-wave plate was placed in the beam to rotate the on-sample polarization by $\sim$45°, the trends for the formation of conical structures on silicon appeared unaffected. This suggests that the formation of the conical structures does not rely on the laser electric field vector being oriented in a certain direction relative to the crystallographic axes. This effect of rotated polarization was not investigated on germanium samples, although it is likely that the result would be the same. In an additional investigation, $\sim$1300 and $\sim$2100 nm wavelength pulses from an optical parametric amplifier (OPA) pumped by the 50 fs system were focussed on Si(100) and Si(111) surfaces with the 15.0 cm focal length lens. At the two OPA wavelengths

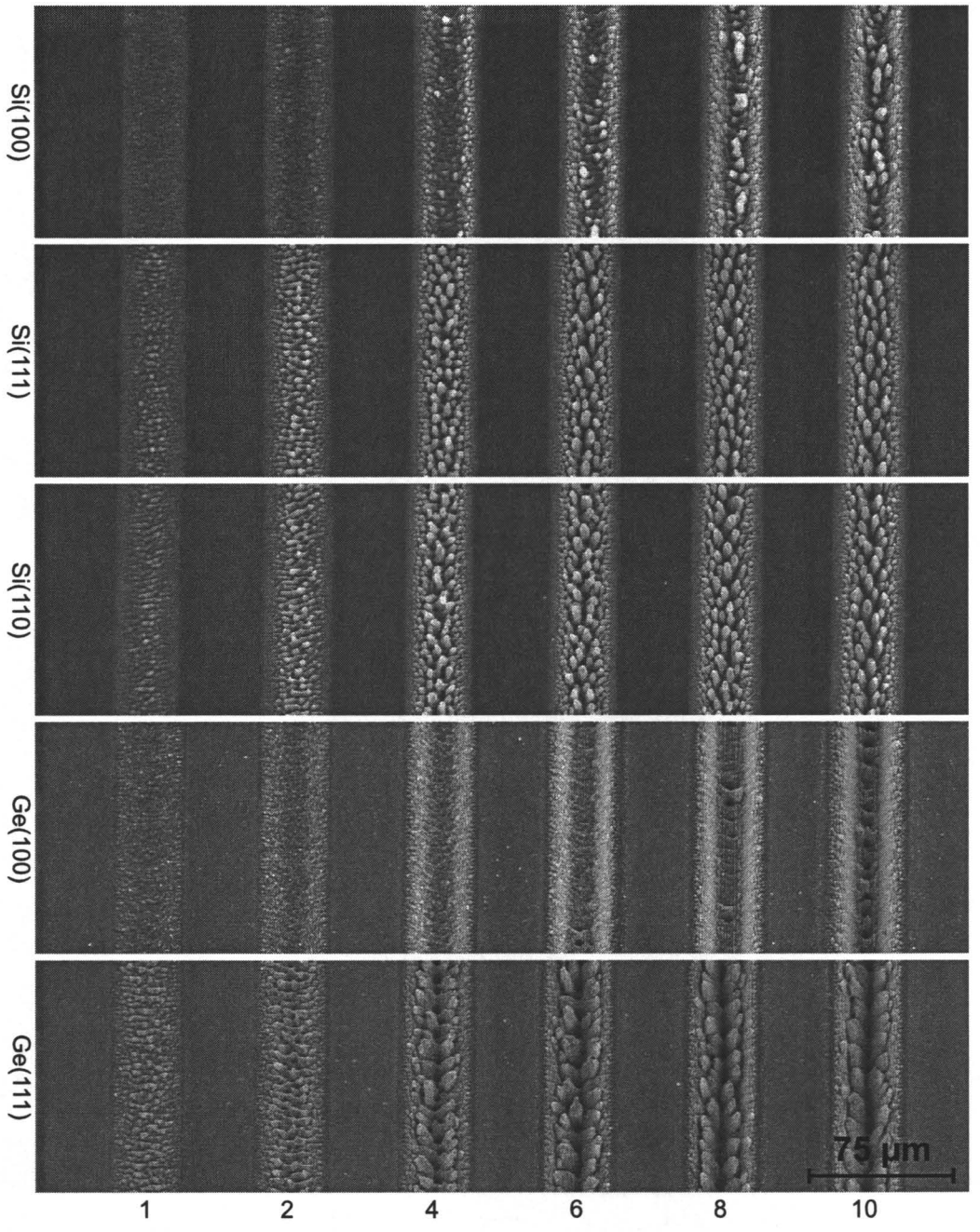

Figure 6.4: SEM images of Si(100), Si(111), Si(110), Ge(100), and Ge(111) translated at 1000 µm/s for a number of passes of 1, 2, 4, 6, 8, and 10 (indicated below the grooves), and pulse energy of 5.1 µJ (fluence 1.2 J/cm^2). A 12.5 cm focal length lens was employed with 150 fs pulses at $\lambda = 800$ nm and a pulse repetition rate of 1 kHz. The laser was polarized approximately horizontally in the images. All images use the same scale, and are taken at a 15° angle relative to the normal.

the trends for blunt conical structure formation were similar to the 800 nm wavelength irradiation, with Si(111) showing a much stronger tendency to form these structures. The OPA wavelengths were not used on a Si(110) surface. As reported previously [58] (and in chapter 5), comparing Si(100) and Si(111) there were no significant differences in the formation of LIPSS or substantially sub-wavelength periodic structures, in contrast to the trends for large conical structures presented here.

6.3.3 Multiple-pulse sub-surface analysis

Cross-sectional TEM allows the direct observation of material crystallinity, but also enables observation of the surface cross-sectional profile. The profile is difficult to obtain using atomic force microscopy when high aspect ratios and depths are present. Figures 6.5 and 6.6 show cross-sections of Si(111) and Si(100) respectively, both irradiated by the same number of pulses and pulse fluence using the 15.0 cm focal length lens. The Si(111) sample possesses large conical structures which are lacking in the Si(100) case. Both cases have small conical structures near the edge of the irradiation site, and LIPSS at the edge running perpendicular to the incident laser polarization. Neither case shows a high density of dislocations or defective material extending deep into the substrate. Bend contours, a TEM artifact visible in crystalline material, are visible in the TEM images.

Figure 6.7 shows a magnified TEM image of a large cone on Si(111). A selected-area diffraction pattern (not shown) taken from the interior of the cone showed that it is primarily single crystal with the same orientation as the substrate. A thin layer of defective material, up to $\sim$500 nm thick, coats most of the large cone. However, no dislocations extended far into the center of the cone. Many small dots, possibly dislocation loops, are present. When tilting the sample in the TEM, bend contours were 'attached' to these dots as if they were sinks or sources of stress.

Figure 6.8 shows cross-sectional TEM images of the small cones and LIPSS present at the side of the Si(100) irradiation site (corresponding to figure 6.6). The small cones, only a couple micrometres wide, contain some defects. They are qualitatively similar to the small cones and LIPSS present on the Si(111) sample (figure 6.5). It can be seen that the LIPSS in this area have a somewhat square profile, with narrow gaps between the material.

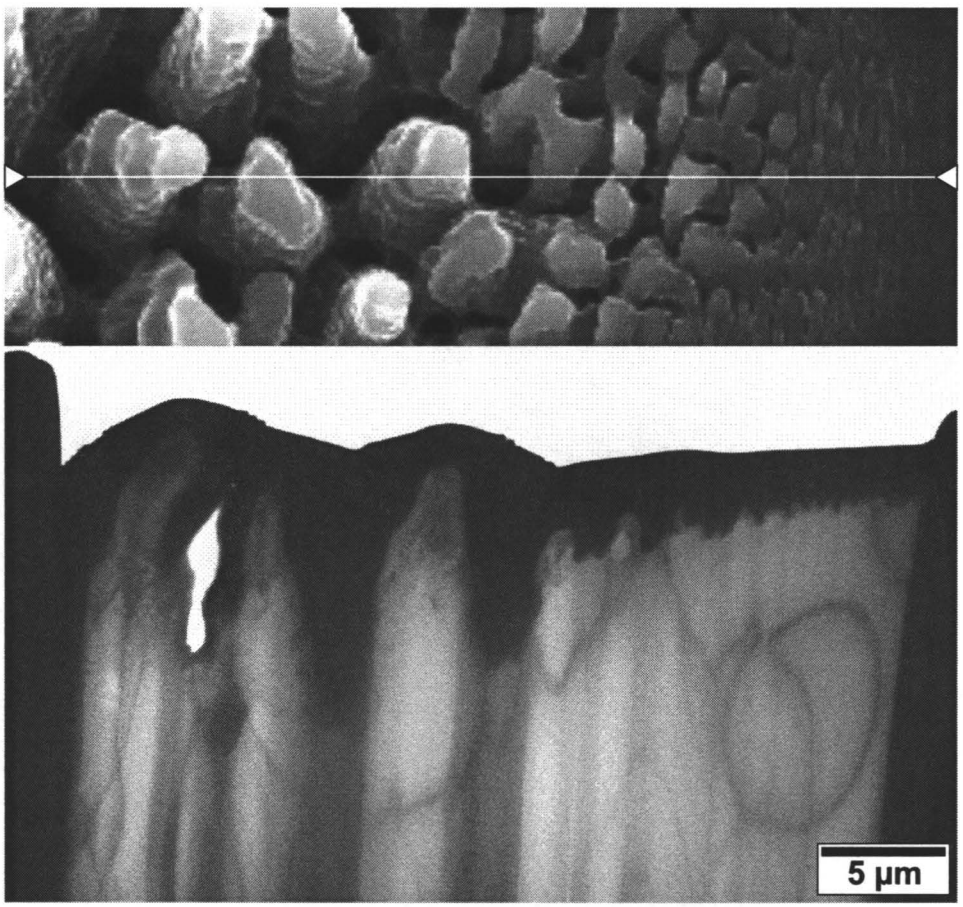

Figure 6.5: Electron microscopy images of a portion of a Si(111) site irradiated by 100 pulses with a peak fluence per pulse of 1.06 J/cm^2 (energy 12.1 μJ per pulse) and $\lambda = 800$ nm. An SEM image of the surface is shown above the corresponding bright-field cross-sectional TEM image, aligned and with the same scale. The white line and triangles in the SEM image show the location of the TEM slice. The black material in the TEM image is protective metal deposited on the sample prior to FIB milling.

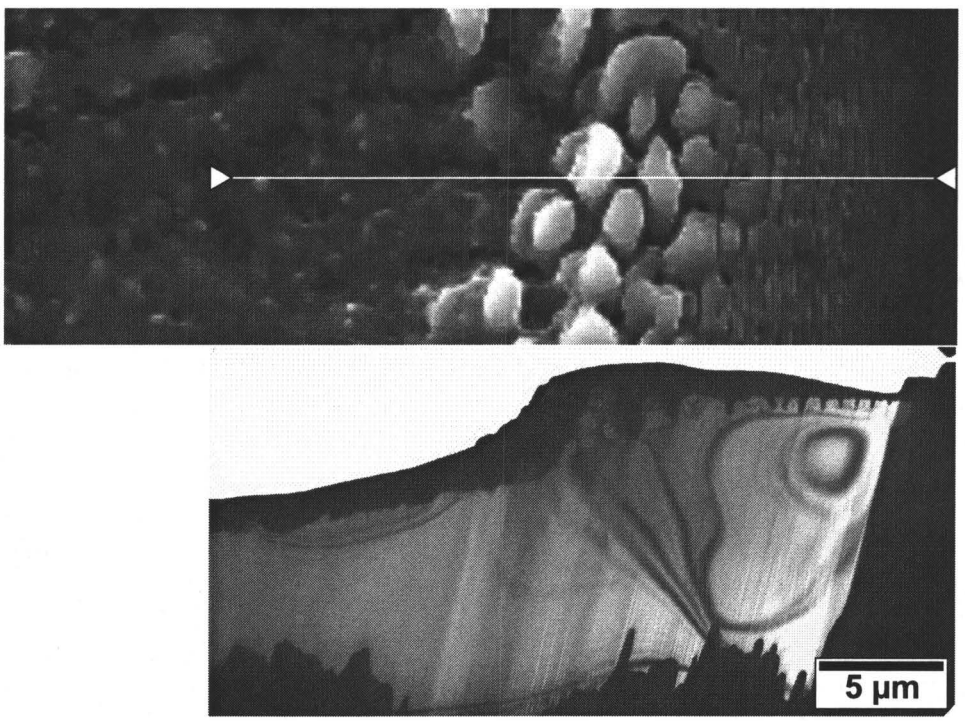

Figure 6.6: Electron microscopy images of a portion of a Si(100) site irradiated by 100 pulses with a peak fluence per pulse of 1.06 J/cm^2 (energy 12.1 µJ per pulse) and $\lambda = 800$ nm. An SEM image of the surface is shown above the corresponding bright-field cross-sectional TEM image, aligned and with the same scale. The white line and triangles in the SEM image show the location of the TEM slice.

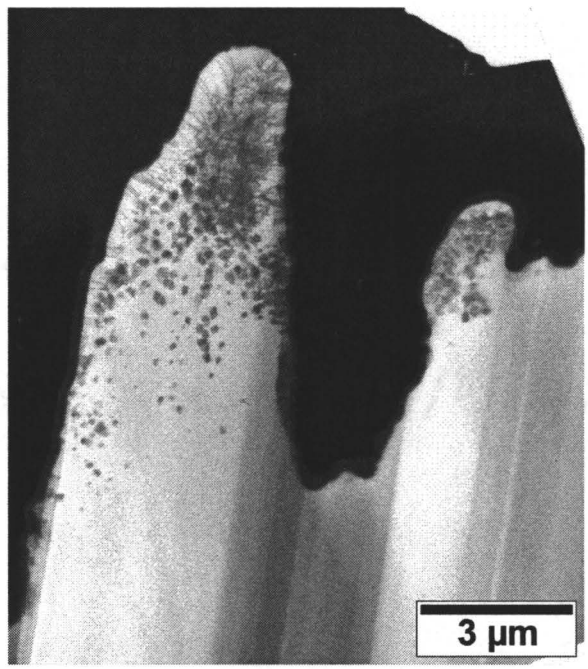

Figure 6.7: Cross-sectional TEM image of a large cone from the Si(111) site shown in figure 6.5.

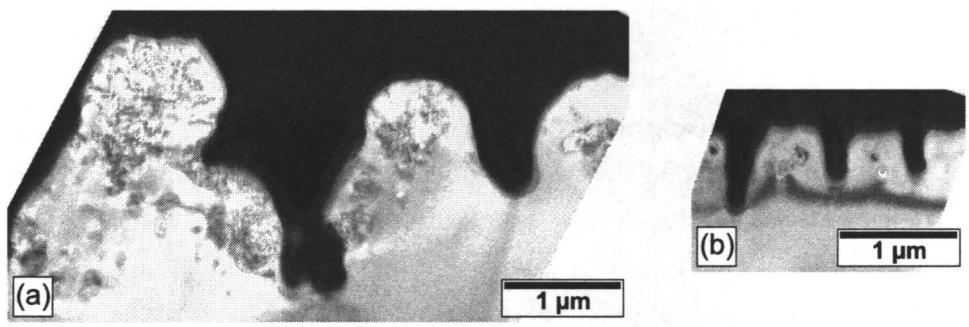

Figure 6.8: Cross-sectional TEM images of (a): small cones and (b): LIPSS from the Si(100) site shown in figure 6.6. Both images have the same scale.

6.4 Discussion

As shown by the trends reported here for blunt conical structure formation and the examination of amorphization on single-pulse silicon sites, there exists different crystal removal and regrowth behaviours after laser irradiation for the different crystalline orientations. It is known that certain chemical solvents have anisotropic etch rates, etching more quickly along one crystallographic axis than another (see, e.g. reference [115] and section 4.10). Thus, it would perhaps not be surprising that different growth or removal behaviours may exist in laser irradiation, since different surface orientations have different densities of surface atoms and potential bonding sites. Section 6.4.3 below discusses reports of differences between different crystalline orientations with regards to amorphization. However, the specific mechanisms which cause differences in the conical structure formation for ultrashort pulse laser irradiation remain an open question.

6.4.1 LIPSS

Similar to the LIPSS shown on silicon in figure 6.8, somewhat square LIPSS were observed on silicon by Coyne et al. [42] after femtosecond pulse irradiation, with crystalline centers and a thin amorphous layer coating the ripples. LIPSS on InP irradiated with femtosecond pulses centered at 2050 nm wavelength also possessed crystalline centers with a resolidified layer [43]. On GaP, high spatial frequency LIPSS (HSFL, see reference [46] and chapter 5) had an amorphous coating on the short-period structures. Similar to the LIPSS shown in this chapter, defects were present within the 'classic' (low spatial frequency) LIPSS on GaP, and the structures had a somewhat rectangular appearance although only a small area of these structures were examined. At the 800 nm irradiation wavelength used in this study, silicon had a stronger tendency than germanium to form LIPSS. As in other studies of semiconductors (see, e.g. references [35, 39, 58, 59, 60, 103]), ripples were not observed for single-pulse irradiation. Table 6.1 summarizes some optical and physical properties of crystalline silicon and germanium. Germanium would be expected to reflect more of the laser light but absorb light over a much smaller depth, although nonlinear absorption would be expected to reduce the absorption depth for both materials. Germanium requires less energy to melt a given volume of material, which correlates with the lower single-pulse threshold observed for surface modification of germanium. Additionally, germanium would be expected to have a lower recrystallization rate due to its lower thermal diffusivity [14]. Young et al. [56] for nanosecond pulse irradiation report similar behavior for LIPSS formation with germanium at 1.06 μm irradiation wavelength as for silicon

Property	Si	Ge	Reference
Reflectivity at 800 nm (%)	33	42	[117]
Linear optical penetration depth at 800 nm (μm)	9.9	0.25	[117]
Melting point (K)	1690	1210	[1]
Boiling point (K)	2650	3100	[1]
Heat capacity at 300 K (J/gK)	0.71	0.32	[1]
Heat capacity at 300 K (J/cm^3K)	1.65	1.71	(calc.)
Melting enthalpy (kJ/cm^3)	4.13	2.72	[1]
Thermal diffusivity at 300 K (cm^2/s)	0.85	0.36	[1]
Thermal conductivity at 300 K (W/cm·K)	1.5	0.6	[1]
Density (g/cm^3)	2.32	5.34	[1]

Table 6.1: Comparison of properties of crystalline silicon and germanium. Note that the diffusivity is the ratio of conductivity to volumetric heat capacity.

at 0.53 μm irradiation wavelength, and draw attention to the fact that the two materials at the respective wavelengths have similar optical absorption coefficients. They also note however difficulty in producing strong ripples with 1.06 μm wavelength light on silicon, stating that this is somewhat expected as the absorption coefficient in silicon at that wavelength is quite small. Wang et al. [116] for femtosecond laser irradiation of Cu, Ag, and Au report a correlation between the morphological clearness of LIPSS and the electron-phonon coupling coefficient. They argue that increased coupling leads to more localized and nonuniform heating of the lattice, and thus the ripples would be more pronounced.

6.4.2 Conical structures

Conical structures qualitatively similar to those in this chapter are reported in the literature, however the effects of target crystallographic dependence are typically not examined. Explanations along the following lines are given by several authors [35, 68, 118, 119] for the formation of columns in general, and such explanations seem applicable to the conical structures presented here. An initial surface corrugation nucleates, and ablation occurs preferentially at the minima (between the columns) of the resulting topology. Semiconductor-rich vapor from the ablation is transported via the vapor plume, and is re-deposited on the protruding features, causing column growth. Increased absorptivity in the valleys leads to increased evaporation there, while the angled surfaces are more reflective. This helps preserve the conical structures. Some structures on laser-irradiated materials resemble the structures which form on sunlight-irradiated snow, for which a similar model has been pro-

posed [120]. In snow, initial depressions are self-amplifying, whereby increased sunlight reflecting to the bottoms of troughs causes more melting and sublimation ("ablation") there, deepening the depression and producing structures up to several metres tall. This general explanation however does not address the orientation dependence of structures, although issues such as the rate of bond formation may be relevant. For the low fluences where LIPSS and small cones formed, the crystal orientation did not have an effect. This suggests that the causes of the crystal orientation dependence are relevant only when significant energy deposition occurs, such as when large quantities of material are being excited.

Columnar structures have been observed on various materials, with different formation tendencies on different materials. Chichkov et al. [2] show an area of blunt cones on femtosecond-irradiated silicon (see their figure 5(b)), with similar but smaller structures on the surface of steel under similar conditions but with an increased number of pulses (see their figure 3(c)). Such structures were not shown in the evolution of Cu and AlN surfaces. In another study [121], columns formed after laser irradiation on Al, Co, Fe, Si, Ti, and the alloy $Fe_{72.3}Si_{14.5}Ru_{7.3}Ga_{5.8}$, while the surfaces of Cu and Au remained flat. Bonse et al. [35] show a (111)-oriented silicon surface as a function of incident fluence (see their figure 9), showing a similar evolution as in the second row of figure 6.2 in this thesis. As with the (111) and (110) crystal orientations presented here, columns in reference [35] were larger for higher fluences, with those in the center of the region being taller, wider, and more sparse than elsewhere. They note some columns protrude above the original sample surface [35], providing evidence for redeposition / recrystallization in this area.

Conical structures were reported on Si(100), Ge(100), and polycrystalline Ti after irradiation by pulses from a copper vapor laser [68] (pulse duration of 20 ns, wavelength of 510.6 nm). They [68] report the tips of cones were more pointed on silicon than on germanium, although images in that work show tips which are more pointed than those in this thesis chapter. For 60–90° angles of incidence the structures grew toward the laser beam axis. They note [68] that a wide range of pressures (from 1 Pa to 10^5 Pa air) did not affect the obtained structures, and this suggests negligible chemical interaction between the vapors and the atmosphere for those structures. In this thesis, comparing silicon and germanium with the same crystal orientation the conical structures did not exhibit significantly different shapes. Further studies of the structures in this chapter, such as varying the angle of incidence and performing experiments in a different pressure such as that of ambient air, would be informative. It would be beneficial to test for the presence of oxygen in the surface of the conical structures, such as in the layer seen in figure 6.7.

Chemical species in the irradiation atmosphere have been shown to have a significant effect on the formation of certain structures. In SF_6 and Cl_2 atmospheres, femtosecond pulse irradiation of silicon produced sharp spikes, while vacuum, N_2 and He atmospheres produced blunt spikes [67]. These blunt spikes closely resemble the cones observed on (111) and (110)-oriented materials in this thesis (compare figures 6.2 and 6.3 to figure 2(b) in reference [67]). Spike formation appeared independent of dopant concentration [67], and were produced pointing toward the incident laser beam direction [112]. Nanosecond laser irradiation has also been used to produce spikes on silicon in SF_6 atmosphere [118, 122]. The spikes from femtosecond irradiation in SF_6 (see references [112, 122]) were found to be crystalline with the same crystallographic orientation as the substrate, and with a < 1 μm thick highly disordered layer seen via bright-field TEM [122]. This bears some similarity to the crystal structures observed in the Si(111) cone from irradiation in rough vacuum atmosphere (figure 6.7), although the disordered layer in reference [122] (see their figure 3(a)) appears much more disordered than the layer observed in figure 6.7. A ~500 nm or thinner layer is observed here, with a rather sharp interface between the disordered material (possessing lines running approximately perpendicular to the cone surface) and the central mainly-crystalline material.

6.4.3 Amorphization

In ultraviolet nanosecond-pulse laser-irradiation studies on various semiconductors, the crystallographic orientation of the substrate has been found to significantly affect the extent of material amorphization. For example, in reference [123] a significantly greater amorphous layer thickness was found for silicon crystal surfaces oriented within 15° of the [111] direction, compared to other surface orientations including (110) and (100). The maximum solidification velocity for which crystalline regrowth (rather than amorphization) occurs on silicon was found to be similar for (110) and (100) surface orientations, but less for (111) orientation [30, 123]. If the resolidification front is driven above this velocity, amorphous material will form [14, 30, 123, 124]. On germanium, GaP, and GaAs at a temperature of 77 K, materials with (111) crystal orientations could easily be rendered amorphous, while no amorphous material was observed on the (100) forms of germanium and GaAs, and only a very thin amorphous layer could be formed on (100)-oriented GaP [124].

In figure 6.1, the higher reflectivity (brighter) area on Si(111) which is absent on Si(100) and Si(110) after single pulse femtosecond laser irradiation is likely due to amorphous material on the surface. Amorphous silicon has a higher reflectivity than crystalline silicon

throughout the visible spectrum [117]. However, thin film interference effects (due to the oxide and amorphous layer on a crystalline substrate) would affect the observed reflectivity. Knowledge of these can give a measurement of the amorphous layer thickness [14, 33, 34]. On Si(111) irradiated by a single ultrashort pulse of fluence 0.42 J/cm^2, the amorphous material was reported to have a maximum thickness of approximately 60 nm [34]. However, previous work using cross-sectional TEM on femtosecond laser-irradiated Si(100) (see reference [45] and chapter 7) revealed no amorphous material for a single pulse with a fluence of 1.5 J/cm^2 or of 33 J/cm^2, and only up to a few tens of nanometres thick for a 11 J/cm^2 single-pulse site. Similar TEM work on the (111) and (110) orientations to confirm the presence or absence of amorphous material would be informative, and would provide information on any other crystallographic changes such as within the rim.

The optical properties of crystalline and amorphous germanium differ substantially from those of silicon. For visible wavelengths amorphous germanium is less reflective than crystalline material between approximately 500 and 650 nm but is more reflective otherwise [117], so simple visual imaging with white light (as done here) might not readily indicate the presence of amorphous material. Over much of the visible spectrum, the optical penetration depths of amorphous and crystalline germanium differ by less than a factor of two [117], while for silicon more than an order of magnitude difference exists [117]. Bonse et al. [14] calculated the reflectivity change as a function of amorphous film thickness on a crystalline germanium substrate. From reflectivity measurements on a Ge(100) surface they did not observe any permanent change in reflectivity, and concluded that there was no evidence of the formation of an amorphous layer. From simple optical microscope images in this thesis chapter, no substantial change in reflectivity was observed between the irradiated area and the surrounding material, both for Ge(100) and for Ge(111) and at all single-pulse fluences used in this study. In contrast to silicon, this preliminary test suggests that no substantial amorphous material formed on the Ge(111) substrate after single-pulse femtosecond laser irradiation, despite the increased expectation of such on a (111) surface. In the study on germanium, GaP, and GaAs [124], the thinnest amorphous layers on (111) materials were on GaAs. Materials like GaAs, which has a relatively low thermal conductivity, would have a lower recrystallization rate and thus be less likely to attain the critical velocity for amorphous material formation [14, 124]. GaP, with a higher thermal conductivity than germanium and GaAs, was the only (100) material able to be amorphized in reference [124] with ultraviolet, nanosecond pulses. The thermal diffusivity and conductivity of germanium are lower than for silicon (see table 6.1), which would predict less likelihood of amorphous material formation in germanium than for silicon [14]. Among silicon, germanium, GaAs, and GaP, based solely on heat conductivity arguments silicon should

be the easiest to amorphize. Beyond the simple optical microscopy presented here, other techniques such as micro-Raman spectroscopy [33], cross-sectional TEM [124], or light microscopy with selected wavelengths (such as in scanning laser microscopy [33, 34]), would be needed to determine if amorphous germanium is present or more prevalent on one particular germanium substrate after femtosecond laser irradiation. External heating or cooling of the target, as in reference [124], could be used to change the solidification interface velocity and thus the likelihood of amorphous material formation.

In previous work using cross-sectional TEM on Si(100) (see reference [45] and chapter 7), for only five pulses at a per-pulse fluence of 1.3 J/cm^2 small regions of amorphous material were observed near the edge of the irradiation site with no evidence of amorphous material or a high density of dislocations at the center. In both of the 100-pulse irradiation sites shown in figures 6.5 and 6.6, defects which extend significantly into the bulk are relatively lacking. This is also seen toward the center of the Si(100) case (figure 6.6), which has a relatively slowly-varying depth for the central region but few defects below that region. In the TEM images shown here 100 pulses were used at a somewhat lower pulse fluence (1.06 J/cm^2), but the much higher number of pulses still did not result in a significant presence of defects despite substantial removal of material.

6.5 Potential future work

Several further investigations are proposed, which would increase our understanding of the mechanisms of femtosecond laser-material interactions. Cross-sectional TEM of the single-pulse sites would directly reveal the depth of the amorphous layer on Si(111) as well as any structure within the irregular ring. Examination of germanium with cross-sectional TEM would also be informative, to test for the presence of amorphous material and defects below the surface. This would also enable comparisons to be made between silicon and germanium, to see to what extent the sub-surface evolution depends on material properties in these group-IV materials. The smaller spot size used in our previous TEM work might affect the defect formation tendency, so this should also be considered in comparisons to earlier work. Femtosecond laser irradiation studies on other crystalline materials with various orientations (such as a III-V material like GaP) could give insight as to how universal the cone formation is, with perhaps an indication of how readily epitaxy of non-single-element materials (like compound semiconductors) occurs. For nanosecond, ultraviolet pulse irradiation [124], no evidence was seen for gallium segregation from GaP and GaAs, although for femtosecond irradiation [43] of InP a phosphorus-deficient material was ob-

served with indium-rich particles. Irradiation in other atmospheres such as Cl_2 and SF_6 could be performed, to determine the effect of chemical species, and to see if sharp spike formation (in contrast to blunt cone formation) can be affected by the underlying substrate crystalline orientation.

Translation of Si(111), Si(110), and (to a lesser extent) Ge(111) samples in this work has resulted in a ~20–25 μm wide groove containing a large quantity of blunt conical structures along the length of the groove. The use of a larger focal spot size and raster scanning of multiple adjacent grooves could potentially enable the fabrication of large areas of blunt conical structures. Femtosecond laser irradiation of a metal has been suggested for producing a mold for transferring a microstructure to a polymer to increase its hydrophobic properties [69]. Other applications such as improving adhesion of other materials [67], and low-reflectivity [68] or highly-absorbing surfaces [112] could require large areas of highly structured material. If crystalline semiconductors are to be used in these or related applications, the results in this chapter suggest that the use of (111) or (110) surface orientations would be advantageous. The parameter space (in terms of pulse fluence and number of pulses) for large conical structures is larger for (111) and (110) orientations, and atmospheres such as SF_6 may not be necessary if the high sharpness of spikes is not needed.

Chapter 7

Cross-sectional Transmission Electron Microscopy Examinations of Femtosecond Laser-irradiated Silicon

7.1 Introduction and motivation

For femtosecond irradiation, the effect of single and low numbers of pulses on the crystal structure of semiconductors is a relatively unexplored area. The conditions for formation of defects and amorphous material are of interest since they can limit the use of femtosecond laser machining in practical applications. After pulsed laser irradiation, sufficiently rapid cooling of molten semiconductor will result in amorphous material being formed [30, 33, 34, 35, 123]. For ultrashort pulse irradiation, high transient pressures from a few to hundreds of GPa, have been reported [125, 126] and predicted by simulations [9, 20, 127, 128, 129]. Sustained pressures of only a few gigapascals are expected to produce defects in semiconductors [37, 38]. Surface analysis techniques such as optical (light) microscopy, scanning electron microscopy (SEM), and atomic force microscopy provide significant information on the final state of laser-irradiated material. However, while showing the surface topology, they generally do not provide significant information on crystallographic changes below the surface, or indicate the presence of different chemical compositions or crystalline phases. Transmission electron microscopy (TEM) can provide this additional information.

Plan-view TEM studies of silicon, InP, and GaAs irradiated by femtosecond pulses (in which imaging was along the same axis as the laser pulse was incident) were previously performed by Andrzej Borowiec et al. [37, 38]. While this provided some information on the crystalline nature of the irradiated material, it left some unanswered questions. For example, if a thin amorphous layer was present, it could not be easily identified in the plan-view orientation. The possibility of an amorphous layer on silicon was mentioned [37] but could not be confirmed. Imaging a cross-section of laser-irradiated material, rather than

a plan-view sample, allows improved selectivity and level of detail in the observations. Focussed ion beam milling (FIB) allows the precise removal of material, and can be used to prepare a thin electron-transparent specimen suitable for imaging in transmission electron microscopy.

An additional material configuration which is not easily examined by plan-view studies is the effect of additional layers, such as metal or thermally-grown oxide, on the laser-material interaction process. Oxides, metals, and semiconductors have significantly different optical, thermal, and mechanical properties, which can affect the material evolution. Silicon covered with oxide and metal layers is used extensively in the electronics industry, and provides a more complex configuration than a simple bulk substrate. Given the emergence of femtosecond laser machining applications in this industry, it is important to understand the effects of such pulses on these layers. Laser pulses could potentially be used to selectively remove the metallization, but the resulting substructure and the possibility of damage below the surface should be understood. Such damage may not be apparent from surface imaging techniques.

In the summers of 2003 and 2004, Junji Yamanaka began the cross-sectional TEM examinations of silicon and multilayer material irradiated by small numbers of $\lambda = 800$ nm, femtosecond laser pulses. A multilayer sample, consisting of Au/Pt/Ti/SiO_2 with thicknesses of approximately 240/50/25/250 nm on a 300 μm thick Si(100) wafer, had been previously prepared by myself with the assistance of Michael Brennan and Peter Jonasson. This was also irradiated by $\lambda = 800$ nm femtosecond laser pulses, and imaged in cross-sectional TEM by Junji Yamanaka. In 2007, additional sites from the $\lambda = 800$ nm multilayer sample were prepared by FIB and imaged in TEM. The original $\lambda = 800$ nm TEM samples were re-imaged at that time, to verify that the material had not evolved over the preceding years due to 'annealing' at room-temperature. An additional set of multilayer sample irradiations was performed using $\lambda = 400$ nm pulses in 2007 by Eugene Hsu, and were subsequently imaged in TEM after FIB preparation. These further examinations allowed the comparison of irradiation by different pulse energies, and the comparison of the effects of two different wavelengths.

In this work, I performed the laser irradiation of all samples, with the exception of the $\lambda = 400$ nm irradiation which was performed by Eugene Hsu. I did the Nomarski optical microscope imaging. Scanning electron microscopy of the samples (before FIB milling) and energy-dispersive x-ray spectroscopy (EDXS) of the multilayer samples was performed by myself, with the exception of the multilayer samples irradiated by 400 nm wavelength pulses, for which the SEM and EDXS were performed by Eugene Hsu. Fibics

Incorporated, located in Ottawa, Canada, performed the focussed ion beam milling of the samples after laser irradiation, with the exception of certain non-multilayer sites which had the FIB preparation performed by Junji Yamanaka at the University of Yamanashi in Japan. The FIB samples prepared in Japan can be identified by a protective carbon deposition layer which was not used on the samples by Fibics.

In addition to the various TEM techniques performed by Junji Yamanaka on the silicon and multilayer samples, some bright-field TEM imaging of additional multilayer sample sites was performed by Christian Maunders and Gianluigi Botton. Some TEM brightfield and darkfield images and diffraction patterns of the five-pulse multilayer sample were obtained by myself (with the assistance of Fred Pearson) as part of the MATLS 731/732 course taught by Gianluigi Botton. I performed EDXS within the TEM on the multilayer samples, to confirm the elemental compositions of various locations.

The preliminary results for the non-multilayer work were written by Junji Yamanaka. However, I did the majority of the writing and literature review for the rest of the non-multilayer work and for all of the multilayer submission. Most of the silicon and multilayer work presented in this chapter was published in two journal publications:

- T.H.R. Crawford, J. Yamanaka, G.A. Botton, H.K. Haugen: *High-Resolution Observations of an Amorphous Layer and Sub-Surface Damage Formed by Femtosecond Laser Irradiation of Silicon*, Journal of Applied Physics **103**, 053104 (2008) [45]

- T.H.R. Crawford, J. Yamanaka, E.M. Hsu, G.A. Botton, H.K. Haugen: *Femtosecond Laser Irradiation of Metal and Thermal Oxide Layers on Silicon: Studies Utilising Cross-sectional Transmission Electron Microscopy*, Applied Physics A **91**, 473 (2008) [47]

Substantial portions of this thesis chapter come from the above two articles, with some text taken nearly verbatim[1]. Before the publication of these two papers, I presented some results in the following conference contributions:

- J. Yamanaka, T.H.R. Crawford, G.A. Botton, H.K. Haugen: *Electron microscopy observations of an amorphous layer formed by femtosecond laser irradiation*, 8th International Conference on Laser Ablation (COLA) 2005, Poster presentation TuPO24

[1] See appendices C and F for copyright and permission information.

- J. Yamanaka, T.H.R. Crawford, G.A. Botton, H.K. Haugen: *Cross-sectional transmission electron microscopy observations of silicon after femtosecond laser irradiation*, 5th International Conference on Photo-Excited Processes and Applications (ICPEPA) 2006, Poster presentation C-5080

7.2 Experimental

The general technique for producing the samples did not differ significantly from that used for other samples in this thesis. Irradiation was performed with the $5\times$ objective, with targets situated in a rough vacuum. For irradiation of multilayer samples with $\lambda = 400$ nm, this wavelength of light was generated by placing a 500 μm thick AR-coated BBO crystal after the half wave plate and polarizer described in section 3.2. In this case the residual transmitted 800 nm wavelength light was removed by a series of three dielectric mirrors highly reflective at $\lambda = 400$ nm. Uncertainties in the pulse energy ($\pm 5\%$) and spot size lead to an uncertainty in fluence of approximately $\pm 30\%$. Reported fluences are those incident at the sample surface, as the amount light reflected at that surface was not measured. Some of the fluences used in this section are significantly higher than those from the group's previous works (e.g., [37, 38, 43, 64]). At these higher fluences, phenomena such as pressure wave generation may be expected to play a more significant role. Single and low numbers of pulses were used, rather than high numbers of pulses, as the simpler configuration may help in clarifying the fundamental physical processes underlying ultrashort pulse laser-material interaction.

The target in non-multilayer experiments was the polished side of phosphorous-doped Si(100) wafers (resistivity 2-6 ohm-cm, thickness 300 μm, with rough back surface). These targets were previously cleaned by submersion in ~90°C acetone then in ~90°C methanol, each for approximately seven minutes, followed by deionized water rinse, submersion in 49% HF solution for two minutes, deionized water rinse, and nitrogen blow dry. The silicon substrates in the multilayer experiments were of (100) surface orientation, approximately 300 μm thick, with phosphorous doping (quoted resistivity 12 ohm-cm), a polished front surface and rough back surface. The wafers were cleaned using a standard cleaning procedure involving boiling H_2SO_4/H_2O_2, boiling H_2O_2/HCl, and an HF solution. (This procedure is from the September 2000 version of the Engineering Physics 4U4 course notes, and was not used for any other samples in this thesis.) Within approximately one hour of cleaning, an oxide layer was thermally grown on the wafer by placing it inside a thermal oxidation furnace at approximately 1100°C. Oxygen was bubbled through ~95°C water

before entering the furnace at one end. An oxide thickness on the order of 250 nm was estimated via comparisons to a thin-film colour chart. An ultrahigh vacuum electron beam evaporator with a quartz crystal thickness monitor was used to deposit ~25 nm of titanium, ~50 nm of platinum, and ~240 nm of gold on the oxide. The titanium and platinum layers improve adhesion of the gold and reduce possible migration of the gold into the substrate. On the rough back surface, ~25 nm of titanium and ~200 nm of gold were deposited. The back surface preparation was done because there was concern of charge build-up in the SEM, and the back metallization would help drain any accumulating charge.

After irradiation but before FIB preparation, some sites were imaged with brightfield optical microscopy, Nomarski differential interference contrast microscopy, and/or the secondary electron imaging mode of scanning electron microscopy (Philips SEM515). For multilayer samples, EDXS was used in the SEM to help identify the elemental composition of various locations on the sample surface. The EDXS examination was primarily used to determine if metals or oxide were remaining in the centers of irradiation sites. In order to protect the laser-irradiated surfaces, before FIB preparation the specimens were coated by protection layers including a platinum-palladium alloy, tungsten, and in some cases an initial layer of carbon. After the FIB preparation, the microstructure of the specimens was observed using TEM. Three transmission electron microscopes were utilized for the examination of non-multilayer samples. A Philips CM12 operating at 120 kV obtained images and diffraction patterns (selected-area diffraction patterns and NBD (nanobeam diffraction)). HAADF (high-angle annular dark-field) and STEM (scanning TEM) brightfield imaging at 200 kV was performed using a Hitachi HD-2300C. A JEOL 2010F was equipped with a Gatan imaging filter for HREM (high-resolution electron microscopy) and electron energy loss spectroscopy, and an Oxford Instruments Inca system for EDXS analysis. For the multilayer samples, only the CM12 TEM was used for cross-sectional imaging and EDXS.

The structures observed in this work could not have been induced by the process of FIB sample preparation. Although FIB milling can induce lattice damage, this would be present on the thin TEM foil surface and not at specific sites as discussed below. The protective coatings deposited before FIB milling avoid ion-beam damage along the original sample surface. Additionally, the final ion-beam polishing is done with a low beam current to minimize potential artifacts.

Light micrographs	Number of pulses	Filter OD	Pulse energy (μJ)	Spot size (μm)	Fluence per pulse (J/cm^2)	TEM and EDXS results
Figure 7.1(a)	1	1.3	0.622	5.2	1.5	Figure 7.2
Figure 7.1(b)	1	0.4	4.43	5.2	11	Figure 7.3
Figure 7.1(c)	1	0.6	3.32	4.4	11	Figures 7.4–7.6
Figure 7.1(d)	1	-	10.1	4.4	33	Figure 7.10
Figure 7.1(e)	5	1.4	0.404	4.4	1.3	Figures 7.7–7.9
-	4	0.6	3.32	4.4	11	Figure 7.11

Table 7.1: Table of laser irradiation conditions, TEM and EDXS results of specimens in the cross-sectional TEM study of non-multilayer silicon samples. Pulse energies have an uncertainty of approximately ±5%, and fluences have an uncertainty of approximately ±30%.

Number of pulses	Fluence per pulse (J/cm^2)	Amorphous present?	Defects present?	Other notes	Figures
1	1.5	No	No	Very shallow	7.1(a), 7.2
1	11	No	No	500 nm deep	7.1(b), 7.3
1	11	Rim	No	Not oxide	7.1(c), 7.4, 7.5, 7.6
1	33	No	Center	Significant twinning	7.1(d), 7.10
5	1.3	Rim	Some	Not oxide	7.1(e), 7.7, 7.8, 7.9
4	11	No	Center	Resolidified layer	7.11

Table 7.2: Summary of results for cross-sectional TEM of non-multilayer silicon irradiated by single and low numbers of femtosecond pulses.

7.3 Results

7.3.1 Silicon targets: single and multiple pulses

The laser irradiation conditions of the specimens lacking the thermal oxide and metal layers are presented in table 7.1, and table 7.2 summarizes the results. A series of plan-view Nomarski differential interference contrast light micrographs of laser-irradiated targets are shown in figure 7.1. These images give a preliminary understanding of how craters were formed, along with information regarding dimensions and surface morphology. Figures 7.1(a) to 7.1(d) present single-pulse craters, illustrating how the morphologies of the craters change with fluence. Using a laser fluence of 1.5 J/cm^2, a very shallow crater is obtained, as illustrated in figure 7.1(a). The craters in figures 7.1(b) and 7.1(c), obtained with a much higher fluence of 11 J/cm^2, exhibit smooth rims. Substantial ejected mate-

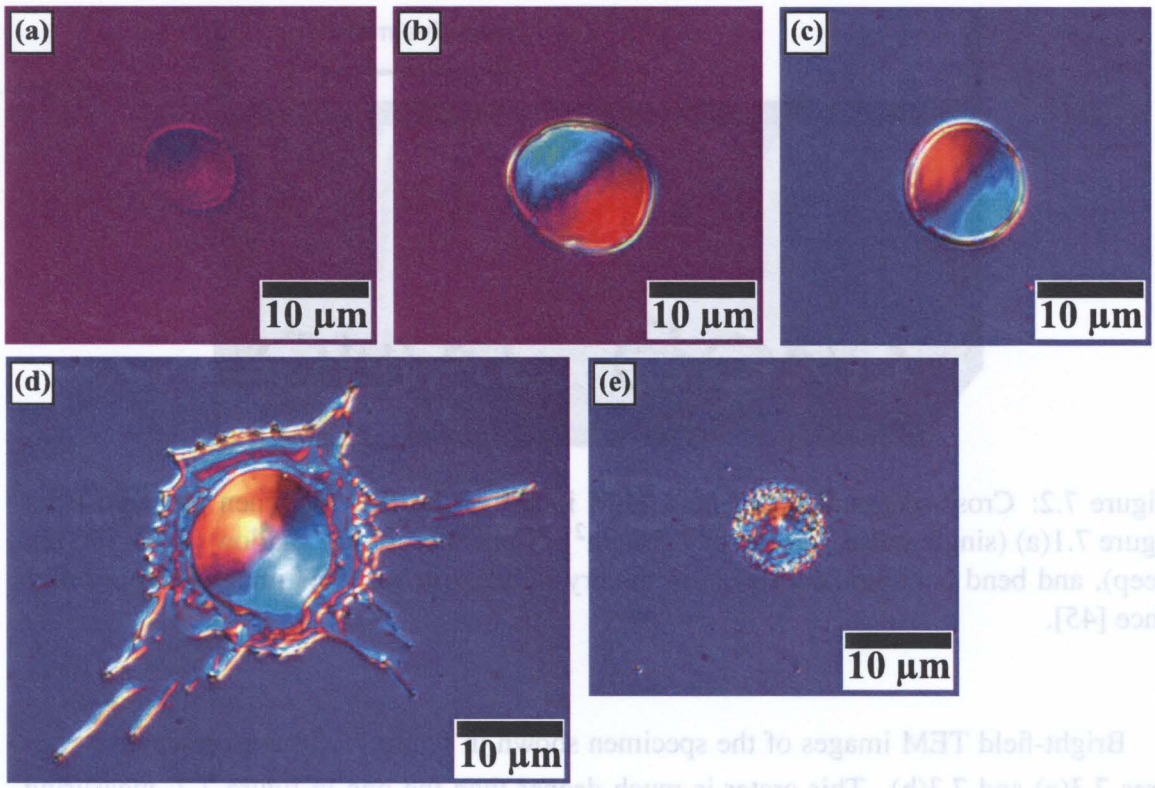

Figure 7.1: Plan-view Nomarski light micrographs of silicon irradiated by femtosecond laser pulses, prior to FIB preparation. (a): Single pulse with fluence of 1.5 J/cm^2. (b): Single pulse with fluence of 11 J/cm^2. (c): Single pulse with fluence of 11 J/cm^2, with similar conditions as those for the specimen shown in figure 7.1(b). (d): Single pulse with fluence of 33 J/cm^2. (e): Five pulses, each with a fluence of 1.3 J/cm^2. These images are from reference [45].

rial is obtained in the case of the crater of figure 7.1(d) which was formed under a laser irradiation fluence of 33 J/cm^2. A five-pulse irradiation case using a moderate fluence of 1.3 J/cm^2 per pulse is shown in figure 7.1(e).

Figure 7.2 presents a cross-sectional overall TEM image of the specimen shown in figure 7.1(a) (fluence of 1.5 J/cm^2). This bright-field image reveals that the crater is very shallow as is suspected from the plan-view light micrograph observation (figure 7.1(a)). Due to the large width-to-depth ratio of this crater, it is difficult to accurately measure the ~50–100 nm depth from the TEM image. There is no evidence of dislocations or other lattice defects. Only bend contours (a TEM imaging effect due to the very thin and slightly bent sample) can be seen in the crystalline material.

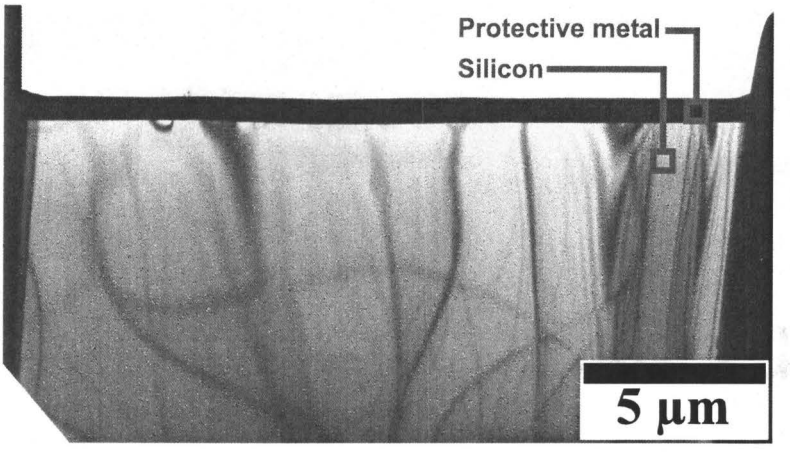

Figure 7.2: Cross-sectional bright-field TEM image of the FIB specimen prepared from figure 7.1(a) (single pulse, fluence of 1.5 J/cm^2). The crater is very shallow (~50–100 nm deep), and bend contours are visible in the crystalline silicon. This image is from reference [45].

Bright-field TEM images of the specimen shown in figure 7.1(b) are presented in figures 7.3(a) and 7.3(b). This crater is much deeper than the one in figure 7.2, measuring approximately 500 nm below the original substrate at its center. Figure 7.3(a) shows a bright-field image of the overall area of the crater, while figure 7.3(b) provides a higher magnification image of the rim of the crater. The morphological change is clear but there is no evidence of lattice defects. The bend contours extend to the very top of the sample, clearly indicating that the sample is crystalline up to the surface of the crater.

Figure 7.4 gives electron microscopy images of the specimen from figure 7.1(c). The laser irradiation conditions are almost identical to those corresponding to figures 7.1(b) and 7.3. The overall image shown in figure 7.4(a) (obtained in STEM mode) is quite similar to the micrograph of figure 7.3(a), however, a different characteristic was found in and near the rim portion of this specimen. Figures 7.4(b) and 7.4(c) respectively display a bright-field STEM image which exhibits diffraction contrast, and an HAADF image which exhibits Z-contrast (atomic-number contrast). The carbon protective layer can be easily identified from the bright field image as a bright band under the (dark) protective metal and as the dark band under the (bright) protective metal in the HAADF image. Only in the bright-field image (figure 7.4(b)) can a difference between the surface and inner part of the specimen be seen with modulations in contrast at the interface with carbon. This means that the surface layer just below the carbon protective film is silicon but its crystallographic structure is not the same as that of the silicon substrate. In order to confirm that the surface

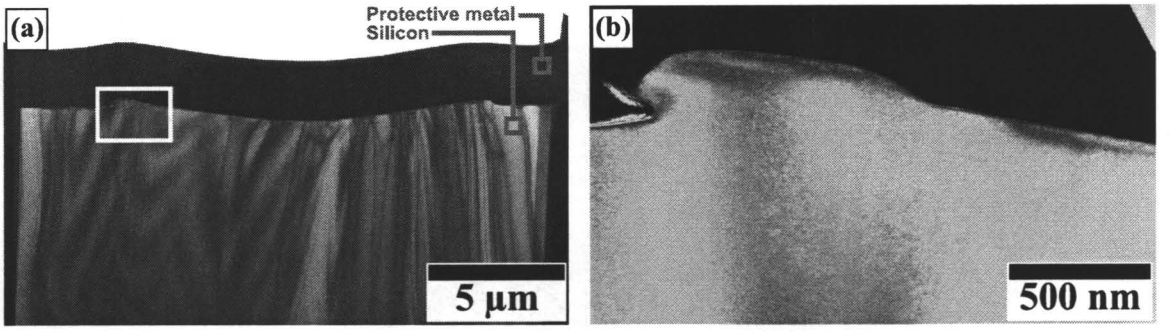

Figure 7.3: TEM images of the specimen shown in figure 7.1(b) (single pulse, fluence of 11 J/cm^2). (a): Bright-field image of the overall cross-section. (b): Bright-field image of the rim part indicated by the rectangle in figure 7.3(a). These images are from reference [45].

layer and substrate are both silicon, EDXS analysis was performed. The positions where the EDXS spectra were obtained are indicated in figure 7.4(b).

Figures 7.5(a) and 7.5(b) present the EDXS spectra from the inner part of the specimen and the surface region, respectively. No differences can be discerned in these spectra. Moreover, there are no oxygen peaks both in EDXS analysis and in electron energy loss spectroscopy. Therefore, both areas are composed of pure silicon and they are not oxides. The small peak corresponding to copper is due to the ring on which the FIB sample was mounted. Additionally, the high-resolution image in figure 7.6 demonstrates that the surface layer is amorphous. Measurements of figures 7.4 and 7.6 suggest that the amorphous material is up to a few tens of nanometres thick, and the center of the crater itself is approximately 500 nm below the original substrate surface. While amorphous material was found near the rim, the central area of the crater and part of the rim was still perfectly crystalline without a change in crystalline orientation.

Similar phenomena were observed in a multiple-pulse crater. Figure 7.7(a) shows an STEM bright-field image of the overall cross-section of the five-pulse crater from figure 7.1(e). Bright-field and Z-contrast images of the rim part of the five-pulse crater are illustrated in figures 7.7(b) and 7.7(c), respectively, and indicate that there are two different structures of pure silicon. The EDXS spectra presented in figures 7.8(a) and 7.8(b) also demonstrate that both inner and surface areas are pure silicon. In order to clarify crystallographic structure, nanobeam diffraction (NBD) was carried out. The inset in figure 7.8(a) is an NBD pattern from the inner part of the silicon, revealing that the inner part is a single crystal. However, the inset diffraction pattern of figure 7.8(b) obtained from the surface area shown in figure 7.7(b), demonstrates that this region is amorphous. The NBD beam size

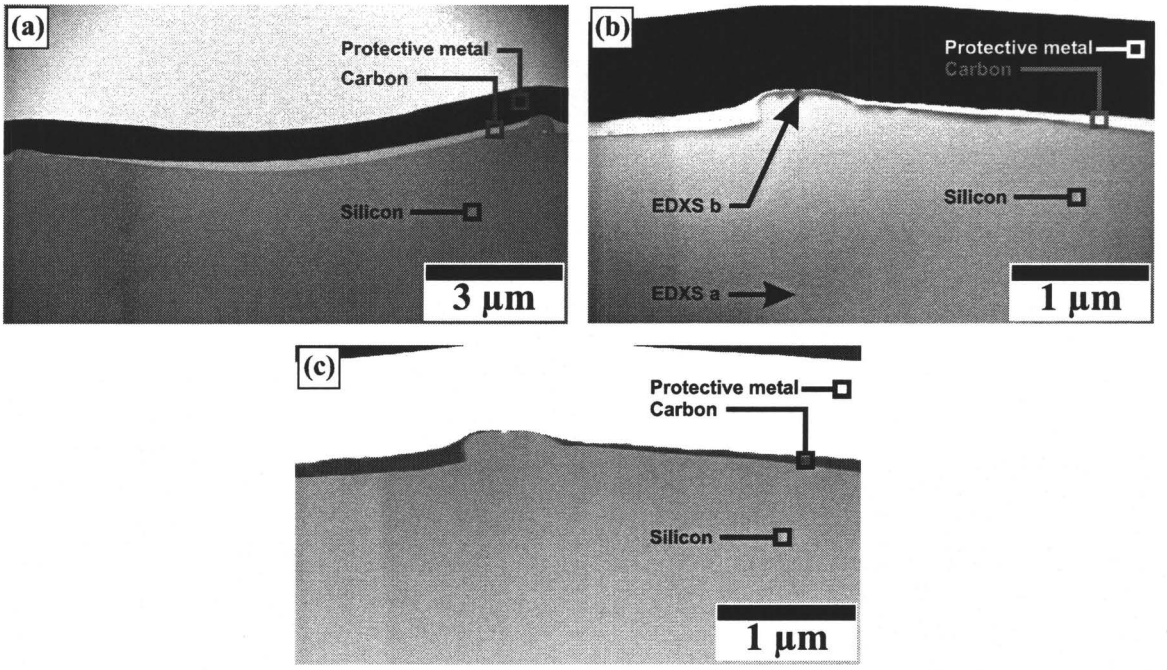

Figure 7.4: TEM images of the specimen shown in figure 7.1(c) (single pulse, fluence of 11 J/cm^2). (a): STEM bright-field image of the overall cross-section. (b): STEM bright-field image of the rim part, exhibiting diffraction contrast. Two arrows indicate positions where EDXS spectra were taken (see figure 7.5). The HREM image in figure 7.6 was taken near the location indicated by "EDXS b". (c): HAADF image (exhibiting atomic number contrast) of the area shown in figure 7.4(b). These images are from reference [45].

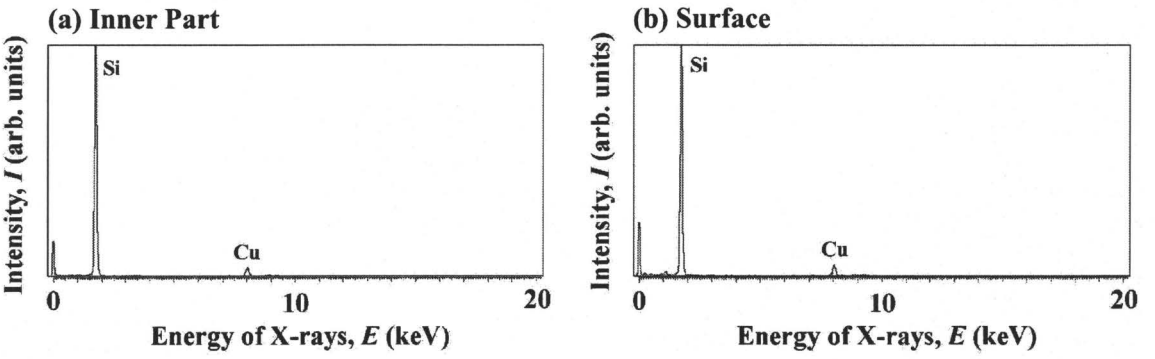

Figure 7.5: EDXS spectra of the specimen shown in figures 7.1(c) and 7.4 (single pulse, fluence of 11 J/cm^2), with analyzed positions indicated in figure 7.4b. (a): Spectrum of the inner region. (b): Spectrum of the surface region. Only silicon peaks can be seen except for copper peaks (which came from the sample mount) and zero strobe reference peaks at 0 keV. These graphs are from reference [45].

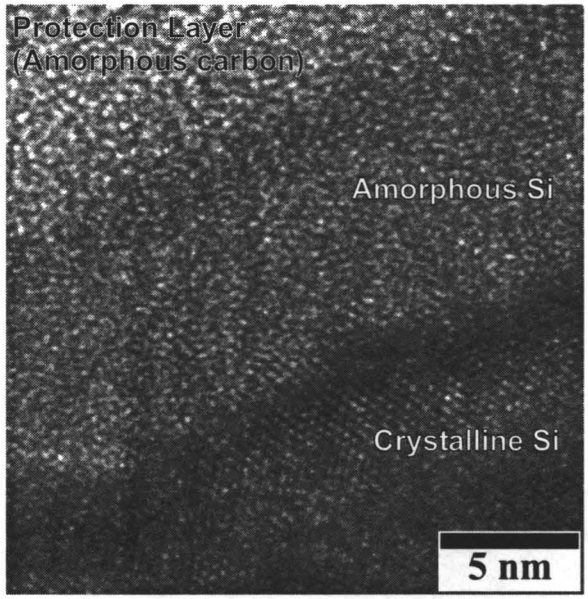

Figure 7.6: HREM image of the rim part shown in figure 7.4 (single pulse, fluence of 11 J/cm^2). Amorphous silicon is present between the crystalline substrate and the FIB preparation coating. This image is from reference [45].

was approximately 10 nm so it was sufficiently small to investigate this amorphous layer. The high-resolution image shown in figure 7.9, taken at the right edge of the area where EDXS and NBD were taken, also establishes this fact very clearly. From these results it can be concluded that the surface layer in this five-pulse-irradiated crater is an amorphous phase of pure silicon. At the center of this multiple-pulse crater (figure 7.7(a)), there was no evidence of a high density of dislocations, stacking faults, or amorphous material.

Figure 7.10 shows a TEM image of the center of the highest-energy single-pulse case (fluence of 33 J/cm^2), which was presented in figure 7.1(d). A TEM result for the highest-energy multiple-pulse condition in this study is seen in figure 7.11. In this case, the fluence was approximately 11 J/cm^2 per pulse and four pulses were used. For both the samples illustrated in figures 7.10 and 7.11, dislocations were observed but there was no evidence of an amorphous phase of silicon. Significant twinning is observed in addition to the dislocations in figure 7.10. In the low fluence case (figure 7.11), a ~300 nm thick resolidified layer showing many dislocations is present. The dislocations under the layer are only present near the center of the site.

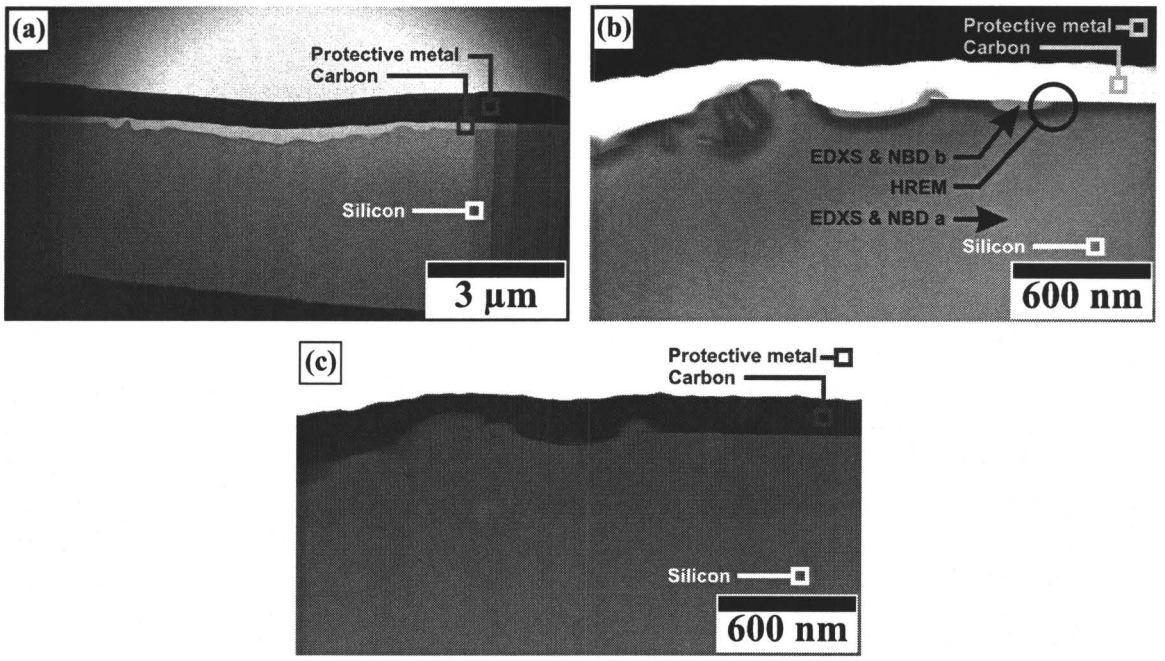

Figure 7.7: TEM images of the specimen shown in figure 7.1(e) (five pulses, fluence of 1.3 J/cm^2). (a): Bright-field STEM image of the overall cross-section. (b): Bright-field STEM image of the rim part. Two arrows indicate positions where EDXS spectra and NBD were taken (see figure 7.8), while the circle indicates the location of the HREM image (see figure 7.9). (c): HAADF image of the area shown in figure 7.7(b). These images are from reference [45].

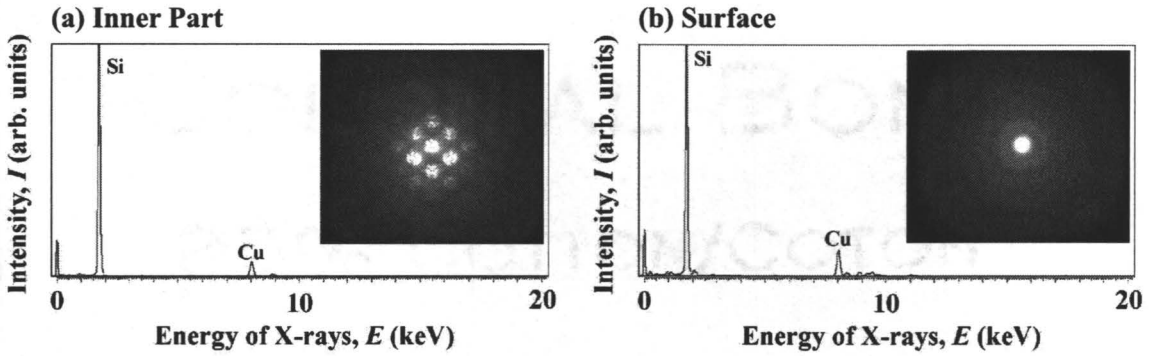

Figure 7.8: EDXS spectra and *(inset)* NBD patterns from the specimen shown in figures 7.1(e) and 7.7 (five pulses, fluence of 1.3 J/cm^2), with analyzed positions indicated in figure 7.7(b). (a): Spectrum and diffraction pattern from the inner unmodified region. (b): Spectrum and diffraction pattern of the laser-modified surface region. Only silicon peaks can be seen in the spectra except for copper peaks (from the sample mount) and zero strobe reference peaks at 0 keV. These graphs and images are from reference [45].

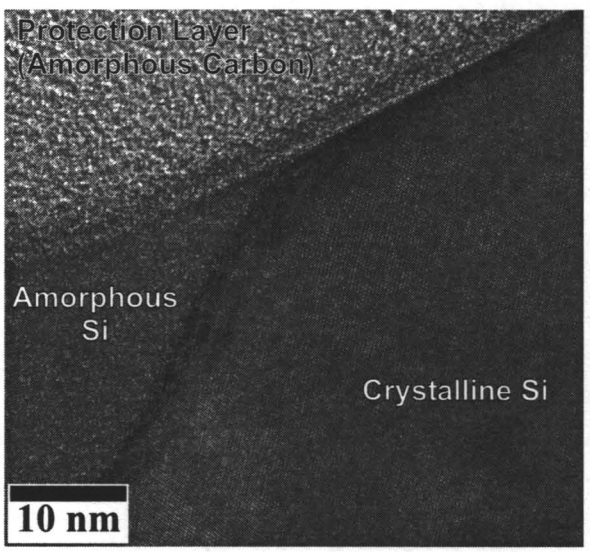

Figure 7.9: HREM image of the amorphous part shown in figures 7.1(e) and 7.7 (five pulses, fluence of 1.3 J/cm^2). The location of the HREM site is indicated in figure 7.7(b). This image is from reference [45].

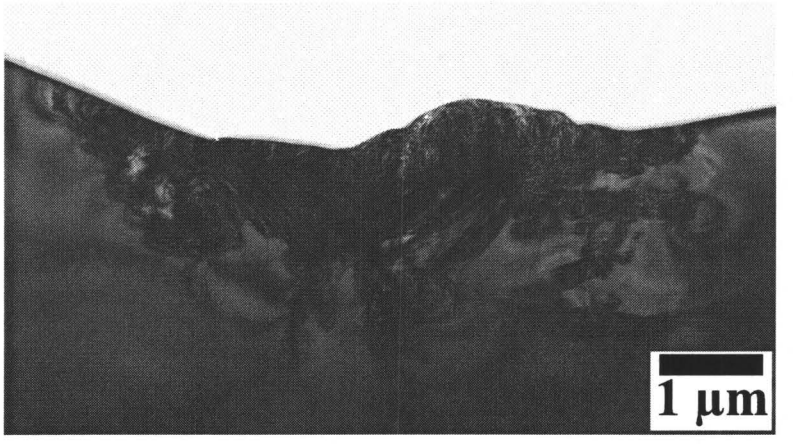

Figure 7.10: Cross-sectional bright-field TEM image of the specimen irradiated by a single high-fluence (33 J/cm^2) pulse, shown in figure 7.1(d). This image is from reference [45].

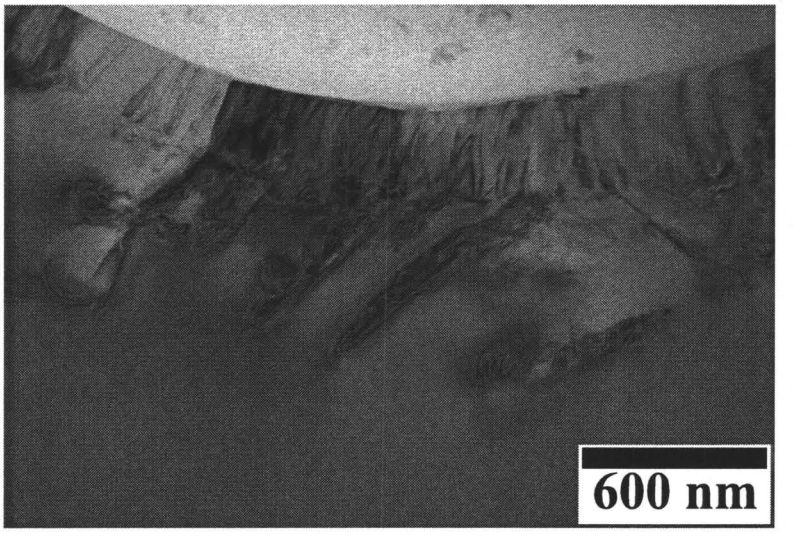

Figure 7.11: Cross-sectional bright-field TEM image of the silicon specimen irradiated by four laser pulses (fluence of 11 J/cm^2 each). This image is from reference [45].

Figures	λ (nm)	Filter OD	Number of pulses	Pulse energy (μJ)	Fluence (J/cm^2)	Result
7.12(a), 7.13	800	0.0	1	5.01	10.5	Defects 2–3 μm deep
7.12(b), 7.16(a)	800	0.3	1	2.76	5.75	No defects visible
7.12(c), 7.16(b)	800	0.5	1	1.73	3.60	No defects visible
7.12(d), 7.14	400	0.5	1	3.42	10.1	Defects 4–5 μm deep
7.12(e)	400	0.8	1	1.86	5.49	Defects 2–3 μm deep
7.12(f), 7.15	400	1.5	1	0.358	1.06	No defects visible
7.17, 7.18	800	0.0	5	5.01	10.5	Deep crater
7.19(b)	400	1.8	2	0.200	0.592	No defects visible

Table 7.3: Summary of results from irradiation of the multilayer sample. In all cases the oxide was not deformed or visibly thinned, with the exception of the 5-pulse 800 nm case (oxide and silicon removed) and the 400 nm 10.1 J/cm^2 case (oxide deformed). Pulse energies have an uncertainty of approximately $\pm$5%, and fluences have an uncertainty of approximately $\pm$30%.

7.3.2 Multilayer targets: single pulse irradiation

For laser irradiation of the multilayer samples, the conditions and a brief summary of the key observations are given in table 7.3. Figure 7.12 shows plan-view SEM images of the multilayer sample, with each site irradiated by a single pulse. A rather sharp boundary exists between the darker central area of the sites and the brighter material covering the rest of the sample. The SEM images suggest that the titanium/platinum/gold layer was removed in the central (darker) area of the sites, as the lower atomic number elements (silicon and oxygen) produce a lower secondary electron signal in the microscope. EDXS spectra taken in the SEM at the centers of sites in figure 7.12 possessed prominent silicon and oxygen peaks with no significant peaks at energies corresponding to the three metals, indicating that the metal layer was removed there.

Below a peak pulse fluence between $\sim$2.6 and $\sim$3.2 J/cm^2 for 800 nm wavelength irradiation, the gold layer was not completely removed in the center of the site. A thin protruding shell-like feature, appearing as a bright outer ring in figure 7.12, can be observed at a radius larger than that at which the oxide is visible. This shell was seen under SEM for the 800 nm case for fluences above $\sim$1.1–1.5 J/cm^2.

For single-pulse 400 nm wavelength irradiation, figures 7.12(d) and (f) show the approximate fluence extrema at which the oxide was exposed but the underlying silicon was still covered. Slightly above this fluence range silicon was partially exposed, and below

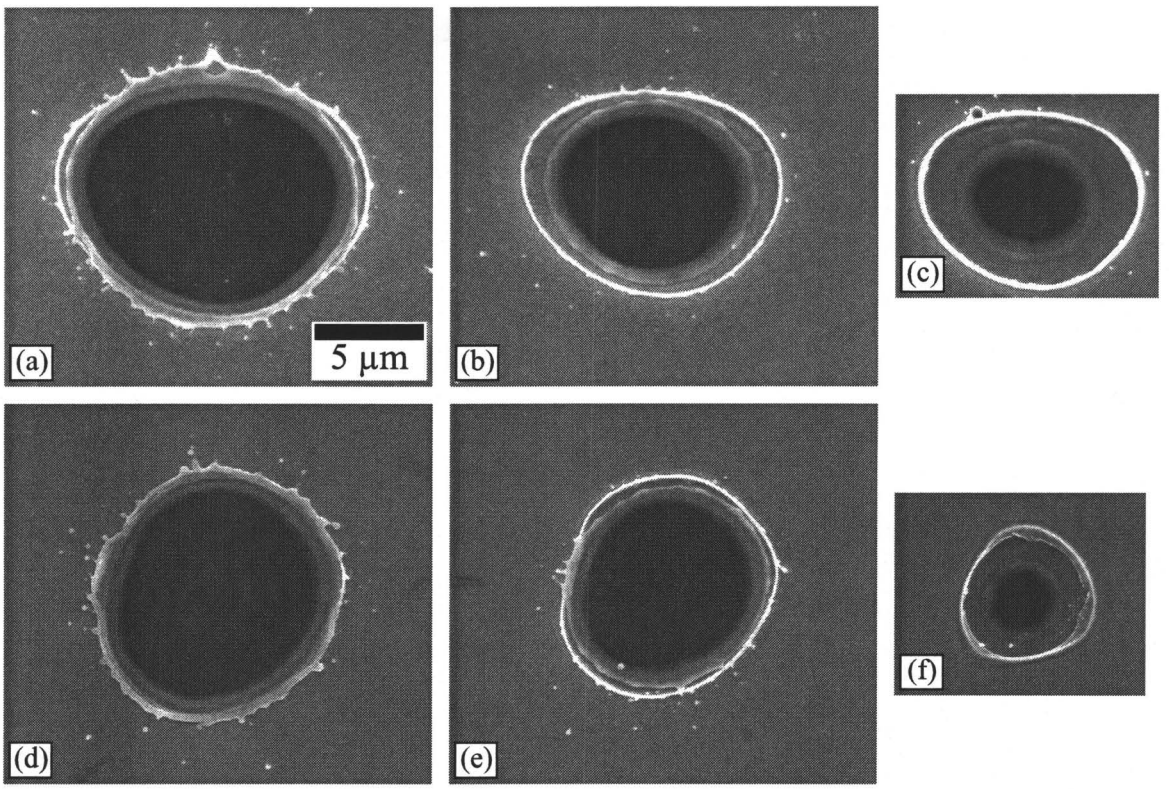

Figure 7.12: SEM plan-view images of the multilayer sample irradiated by a single pulse. The sites in images (a)–(c) are from 800 nm wavelength irradiation, while (d)–(f) are from 400 nm irradiation. The images all have the same scale. The incident energies and fluences at the material surface are: (a): 5.01 μJ (10.5 J/cm^2). (b): 2.76 μJ (5.75 J/cm^2). (c): 1.73 μJ (3.60 J/cm^2). (d): 3.42 μJ (10.1 J/cm^2). (e): 1.86 μJ (5.49 J/cm^2). (f): 0.358 μJ (1.06 J/cm^2). These images are from reference [47].

fluences of ~0.9–1.1 J/cm^2 the gold was still present at the center. The shell-like feature was seen under SEM for fluences above ~0.41–0.47 J/cm^2 for the 400 nm wavelength case.

Figure 7.13 shows the bright-field TEM cross-section of the 10.5 J/cm^2, $\lambda = 800$ nm site (shown in figure 7.12(a)). Bend contours are visible throughout the crystalline silicon. The oxide layer, approximately 230 nm thick, is present along the entire cross-section with little variation in thickness. However, despite the relative lack of apparent change in the oxide, the silicon below the oxide at the irradiation site possesses significant crystalline damage. In a selected area electron diffraction pattern taken from the damaged silicon region there were no $\langle 111 \rangle$ streaks which would be a feature of stacking faults and twin boundaries. Thus, the straight lines in the bright-field TEM image (figure 7.13) are predominantly dislocations. The dislocations after laser irradiation lie on the $\{111\}$ plane, as

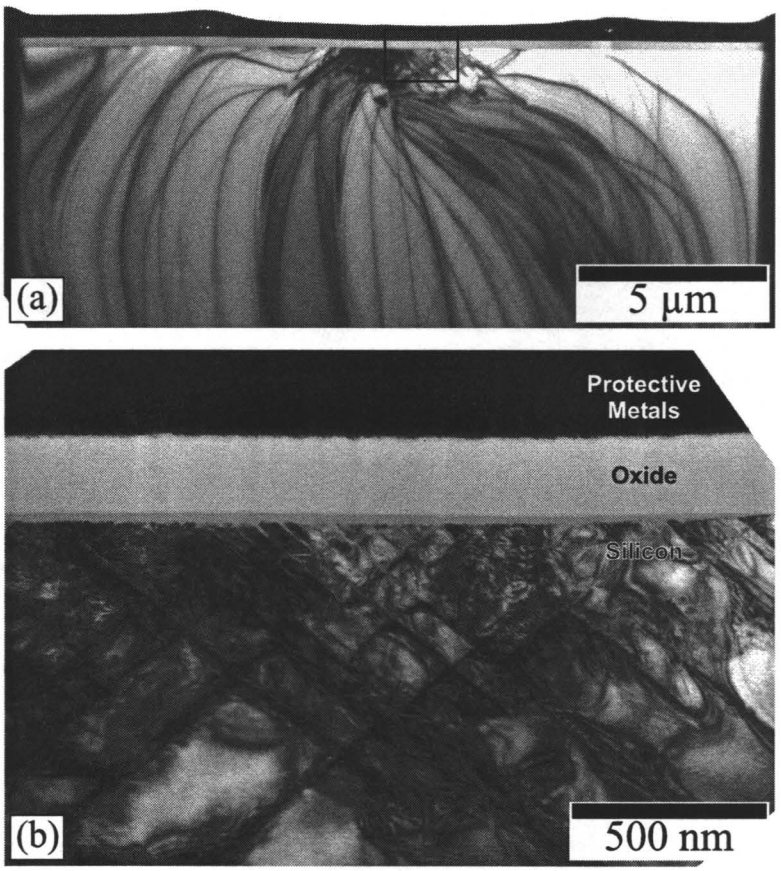

Figure 7.13: Bright-field TEM images of a cross-section of the multilayer sample irradiated by a single $\lambda = 800$ nm, 5.01 μJ (10.5 J/cm^2) pulse. Image (b) shows a higher magnification of the area indicated by the rectangle in (a). These images are from reference [47].

is typical for silicon in general. Due to the thickness of the FIB samples and the high atomic numbers of the metals, in bright-field 120 kV TEM images it was difficult to discriminate between the protective Pd and W metals for FIB preparation and the original Ti, Pt, and Au layers.

In contrast to the 10.5 J/cm^2 case shown in figures 7.12(a) and 7.13, TEM imaging of the $\lambda = 800$ nm sites produced by single 5.75 J/cm^2 and 3.60 J/cm^2 pulses (figures 7.12(b) and (c)) did not show any crystallographic damage in the silicon. For all three cases, the gold layer was removed and the oxide layer was not visibly thinned by the laser pulse irradiation. The use of cross-sectional TEM provides a significant advantage over surface SEM imaging, as the presence or absence of defects in the silicon substrate was not apparent from surface SEM imaging.

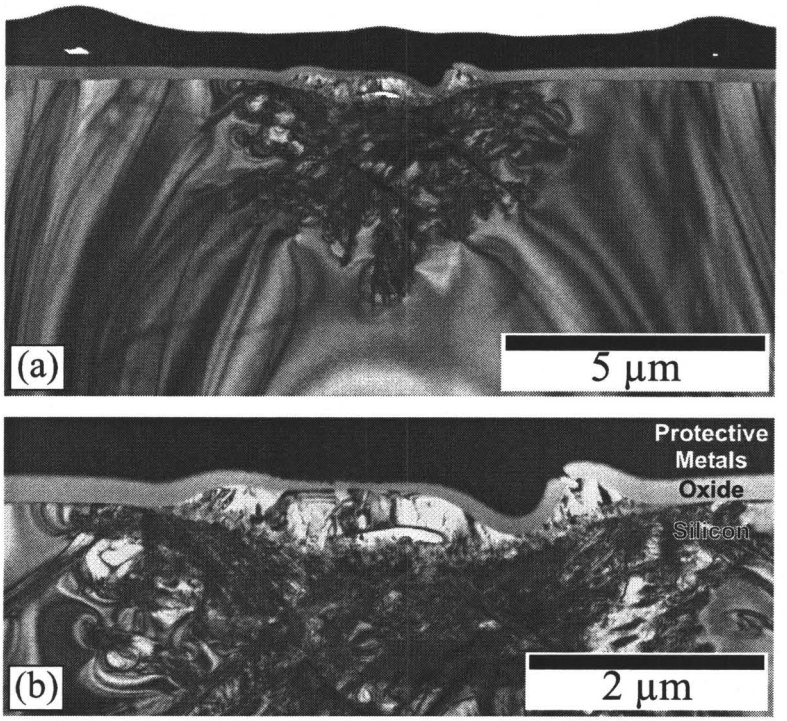

Figure 7.14: Bright-field TEM images of a cross-section of the multilayer sample irradiated by a single $\lambda = 400$ nm, 3.42 μJ (10.1 J/cm^2) pulse. Image (b) shows a higher magnification of the deformed oxide in (a). These images are from reference [47].

The cross-sectional TEM image in figure 7.14 shows the highest-energy $\lambda = 400$ nm single-pulse site (10.1 J/cm^2). As suggested by the corresponding SEM image (shown in figure 7.12(d)), the oxide layer has been deformed but is still continuous except for a small crack. Crystallographic defects extend up to ~4 μm below the surface, roughly double the depth as for the $\lambda = 800$ nm case with similar incident pulse fluence (see figure 7.13). Bend contours are visible throughout the crystalline silicon. Cross-sectional TEM imaging of the $\lambda = 400$ nm site irradiated by a single 5.49 J/cm^2 pulse (SEM image shown in figure 7.12(e)) also revealed significant crystallographic defects up to ~2 μm below the oxide. However, the oxide was not visibly thinned or deformed in this case. The presence of defects at this fluence is in contrast with irradiation with a single 800 nm wavelength pulse of similar incident fluence (see figure 7.12(b)), for which no defects were observed. For the lowest-fluence single-pulse 400 nm irradiation site (1.06 J/cm^2, see figure 7.12(f)), no changes in the oxide or crystallographic changes in the silicon were seen in cross-sectional TEM. This case is shown in figure 7.15, which is qualitatively similar to the single-pulse $\lambda = 800$ nm irradiations at 5.75 J/cm^2 and 3.60 J/cm^2 (not shown).

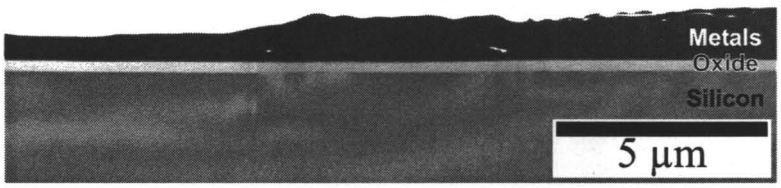

Figure 7.15: Bright-field TEM image of a cross-section of the multilayer sample irradiated by a single $\lambda = 400$ nm, 0.358 μJ (1.06 J/cm^2) pulse, with no damage visible in the crystalline silicon. This image is from reference [47].

A small void (appearing as a white spot in TEM images) is usually present in the FIB samples on either side of the irradiation site within the metal layer, and is visible in figures 7.13(a), 7.14(a), and 7.15. The voids are seen just inside the protruding shell-like feature seen in SEM images (see figure 7.12), adjacent to the gold and the protective metal layer deposited for FIB milling. The shell-like feature, which extends a few hundred nanometres above the original gold layer, likely caused shadowing in the process of depositing the protective FIB metals, thus forming the void. It was difficult to observe the shell feature in 120 kV TEM due to the high atomic numbers of the gold and protective metals. Figure 7.16 shows cross-sectional TEM images of shell areas, after using image-editing software to rescale the brightness range. The silicon, oxide, and area near the top of the FIB metal have had their visibility obscured by this rescaling. The gold layer thickness drops abruptly within the shell area, and decreases gradually to zero nearer the center of the irradiation site. EDXS mapping would be a good alternative for identifying the locations of the various metals. Only discrete points were analyzed in some EDXS measurements in the TEM of certain samples, due to time and equipment availability constraints. The titanium 4.5 keV $K\alpha$ x-ray line was found to be particularly useful, since it does not occur near the x-ray emission lines of the other elements present, and thus indicates the region along the oxide over which the Ti/Pt/Au layer was removed.

7.3.3 Multilayer targets: multiple pulse irradiation

Figure 7.17 shows an SEM image and figure 7.18 shows cross-sectional bright-field TEM images of the site on the multilayer target irradiated by five $\lambda = 800$ nm pulses. Each pulse had a fluence of 10.5 J/cm^2, the same as for the highest-fluence single-pulse 800 nm site. Bend contours are visible in the crystalline silicon area of the TEM images,

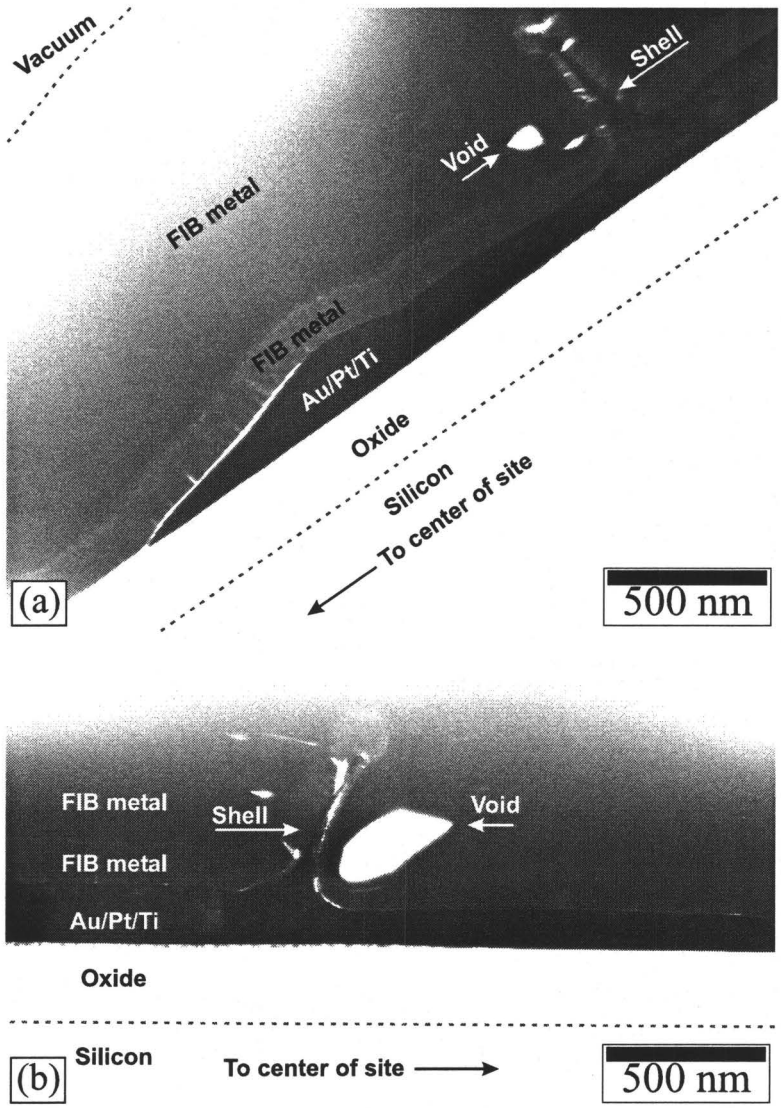

Figure 7.16: Bright-field TEM images of a cross-section of the multilayer sample irradiated by a single $\lambda = 800$ nm pulse, emphasizing the protruding shell and void features. The brightness range has been strongly scaled in order to make the different metals discernible. Image (a) is for a 2.76 μJ (5.75 J/cm^2) pulse, while (b) is for a 1.73 μJ (3.60 J/cm^2) pulse.

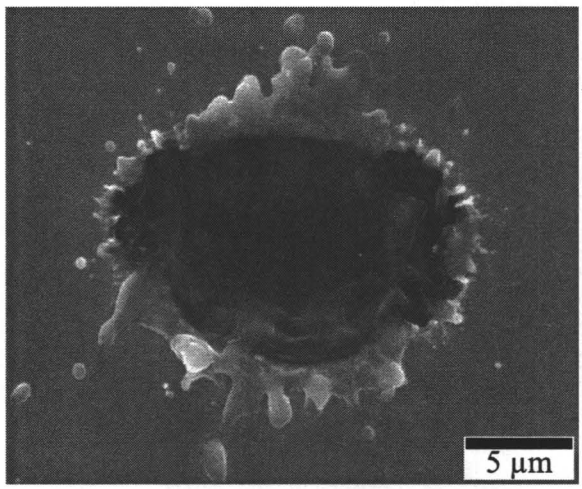

Figure 7.17: SEM image of the multilayer sample irradiated by five $\lambda = 800$ nm pulses (5.01 μJ per pulse, 10.5 J/cm^2 per pulse). This image is from reference [47].

along with significant crystallographic damage near the irradiated surface. The oxide is cut quite sharply, while near the cut, the metal layer protrudes above the original metal surface somewhat. The metal and oxide serve as a useful marker to delineate between the original substrate and material which was perturbed by the laser pulses. On the right side of the site, a significant amount of material has been deposited on top of the metal layer. Less material is visible on the left side (see figure 7.18(b)), which could be due to the rather uneven distribution of protruding material observed in the SEM image (figure 7.17). A continuous region of silicon exists from the central region to the area on top of the metal layer, suggesting that it either flowed or was redeposited from the substrate to the top surface. Electron diffraction patterns obtained from the deposited layer above the metal in figure 7.18(a) and (b) indicate that it is polycrystalline. Two approximately-linear features in the silicon, extending roughly normal to the exposed silicon surface and intersecting the bend contours, are visible in figures 7.18(a) and (b). These are periodic dislocation loops. Within the crystalline silicon substrate, dislocations extend up to $\sim$3 μm.

At an irradiation wavelength of 400 nm and incident pulse fluence of 0.59 J/cm^2 (energy 0.20 μJ), a single pulse did not completely remove the gold layer although the shell-like structure was still formed. Two pulses, each of the same fluence (0.59 J/cm^2), exposed oxide. Three or more pulses resulted in the exposure of the underlying silicon substrate. SEM images of this evolution are shown in figure 7.19. Cross-sectional TEM of the two-pulse site showed an approximately uniform oxide thickness. Additionally, there were no

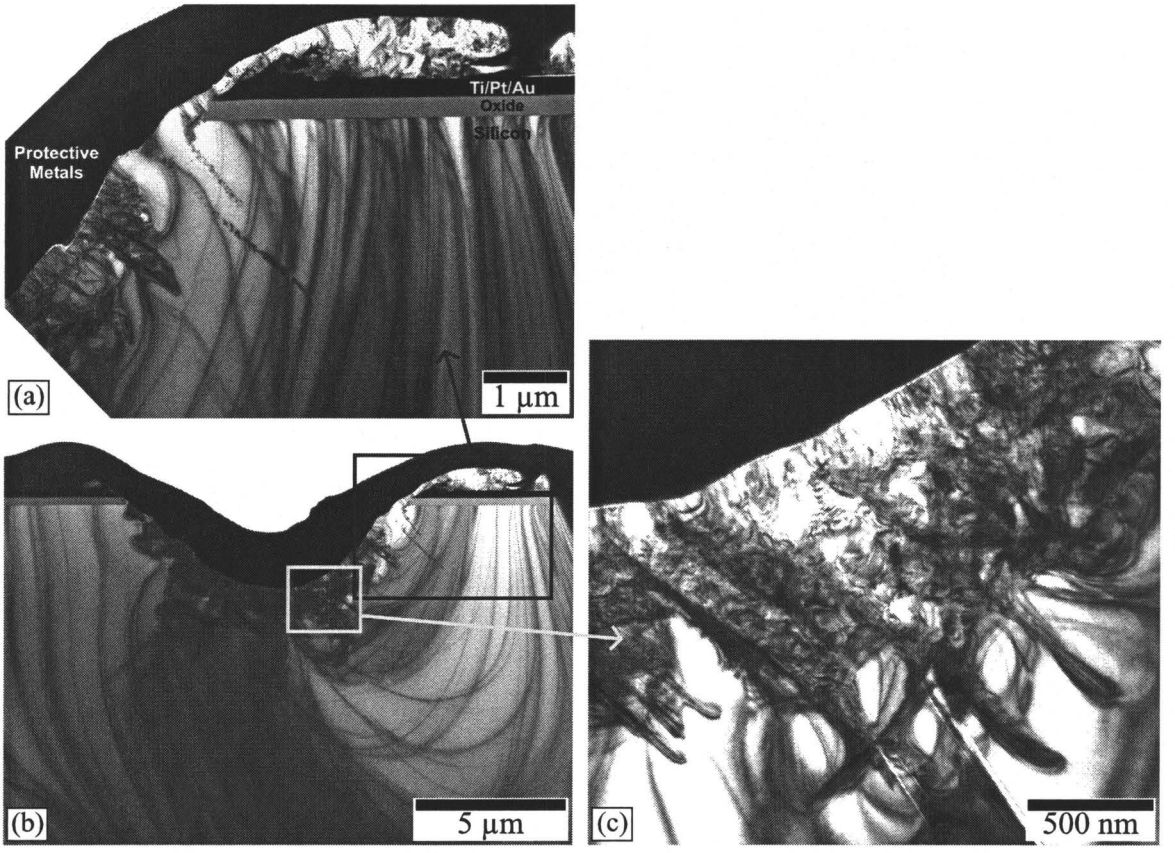

Figure 7.18: Bright-field TEM images of a cross-section of the multilayer sample irradiated by five $\lambda = 800$ nm pulses (5.01 μJ per pulse, 10.5 J/cm^2 per pulse). The thick uneven black layer at the top of the images is the protective metal layer deposited in FIB preparation. Images (a) and (c) show higher magnifications of the areas indicated in (b). These images are from reference [47].

crystallographic defects seen in the silicon beneath the two-pulse irradiation location. The lack of defects is perhaps not surprising, as the fluence was very low compared to the cases where defects formed. For sufficiently high pulse fluences, the second and subsequent pulses begin removal of the oxide followed by the silicon substrate, as was suggested by selected SEM-EDXS examinations.

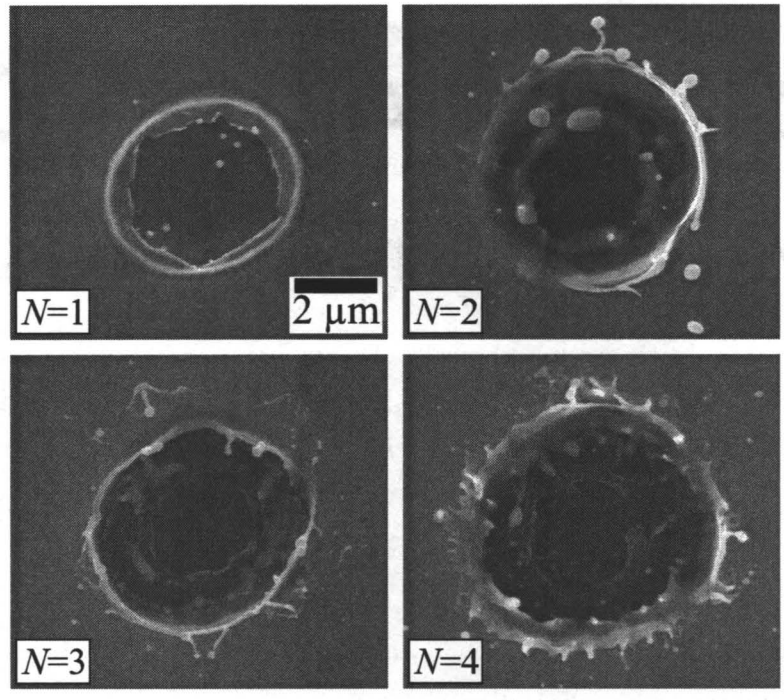

Figure 7.19: SEM plan-view images of the multilayer sample irradiated by one to four $\lambda = 400$ nm pulses. The images all have the same scale. The incident per-pulse energy was 0.20 μJ (fluence 0.59 J/cm^2). EDXS at the center of the $N = 1$ has a prominent gold peak, the center of $N = 2$ has an oxide peak, and $N = 3$ and 4 lack oxide and gold peaks.

7.4 Discussion

7.4.1 Amorphization

A significant conclusion which could not be made by Borowiec et al. [37] in previous work on silicon using plan-view TEM is that the silicon amorphous phase was formed by femtosecond laser irradiation. In the results presented here, amorphous material is readily observed under certain circumstances (see figures 7.4, 7.6, 7.7, and 7.9). The results indicate that amorphization is a result of the rapid quench of silicon melts. The amorphous phase was found only on or around the rim, and in these cases perfect crystallinity existed in the central part of the craters. In specimens where solidified phases existed in the central portions of the craters (figures 7.10 and 7.11), they were found not to be amorphous but rather composed of crystalline phases with many dislocations.

Other authors have reported studies of amorphization of semiconductors under ultrashort pulse irradiation. Izawa et al. [41] observed different amorphous layer thicknesses on (100) silicon for three different ultrashort pulse wavelengths. At a fluence of $\sim$0.2 J/cm^2 with 800 nm irradiation wavelength, a minimum of six pulses was reported to be required before amorphous material was produced [41]. This fluence is substantially below the fluences used in the cross-sectional TEM work presented here on silicon, and the reported absence of an amorphous layer after single-pulse 800 nm irradiation at low fluence is consistent with the observations presented here. On a Si/SiO_2/Si target, Jia et al. [40] show in the crystalline silicon film an amorphous layer up to 60 nm thick caused by processing with five ultraviolet laser pulses, while no crystalline defects are shown. Substantial differences in the irradiation conditions exist between the work presented here and the work of Jia et al. [40], for example a much lower single-pulse fluence and a shorter wavelength. Additionally, the $\sim$200 nm thick oxide underlying the $\sim$180 nm c-Si target film in reference [40] could affect the heat flow and solidification behavior.

Using micro-Raman techniques and scanning laser microscopy, Bonse et al. [33, 34] observed an amorphous silicon layer some tens of nanometres thick on Si(111) irradiated by a single pulse at 0.42 J/cm^2 fluence, with polycrystalline silicon forming at a somewhat higher fluence. A slower resolidification of material in the central higher fluence region of the Gaussian laser spot was argued to lead to formation of crystalline or polycrystalline material there [33]. The experiments of Bonse et al. [33, 34] used lower fluences than in the TEM work here and used a different silicon surface orientation ((111) vs. (100)). Furthermore, factors such as ambient atmosphere, substrate temperature, and the total volume of melt may affect the cooling rate.

In early studies using short nanosecond ($\leq$3 ns) pulse irradiation of silicon, energy density thresholds were observed above which amorphous material did not form [30, 32, 123]. These thresholds were dependent on the crystallographic orientation of the silicon. Irradiation of silicon with a sufficiently high energy density pulse has produced an amorphous ring with a crystalline center [29, 123], the centers of the irradiation sites having higher local fluences where amorphous material no longer formed. These observations are for shorter wavelengths and longer pulse lengths than those in the present study. However, they are also qualitatively consistent with the observation here of amorphous material near the outer edge of the single-pulse 11 J/cm^2 crater (figure 7.4), and not at its center.

7.4.2 Deformation, pressure waves, and defects

In the cases of single-pulse irradiation on a silicon surface, the surface morphology revealed by light micrographs exhibited relatively smooth rims (see figures 7.1(a)–7.1(d)). Particularly in the case of high-energy irradiation (figure 7.1(d)), the flow of molten silicon is observed. In general, not only solidification of the melts on the substrates but also plastic deformation of the substrates themselves could form a smooth rim. If the rims were formed by plastic deformation, there would be dislocations. However, there is no evidence of lattice defects in the TEM images of the low-fluence cases (see figures 7.2–7.4), so it can be concluded that these rims are epitaxially solidified layers of melts. Other reports have noted the existence of amorphous material and the protrusion of material above the original substrate surface, and have concluded that a liquid phase exists for part of the material modification process (see, e.g. references [40, 42]).

Coyne et al. [42] studied the effects of laser irradiation of Si(100) with 150 fs duration 775 nm pulses in air for a fluence range of 0.43–14 J/cm^2. They reported evidence of damage far from the ablated region when the laser fluence reached 10 J/cm^2. For a fluence of 11.5 J/cm^2 and with 1000 pulses, extensive damage was observed near the base of a laser-machined hole [42]. These studies, conducted in air and under different irradiation conditions, are consistent with the work presented here. The study of Izawa et al. [41] using relatively low laser fluences was primarily aimed at the study of amorphous layer formation, and did not reveal sub-surface damage.

A laser pulse incident on a surface will produce a pressure wave which propagates into the material and can lead to lattice disorder. Very large magnitudes of transient pressures can be generated near the surface by femtosecond laser irradiation. For example, on an aluminum film a maximum value of 95 $\pm$ 15 GPa has been deduced [125] for femtosecond irradiation conditions comparable to the 11 J/cm^2 non-multilayer and the 10.1 J/cm^2 and 10.5 J/cm^2 multilayer cases presented here. A pressure of 255 $\pm$ 50 GPa [125] was deduced for conditions comparable to the 33 J/cm^2 non-multilayer case. Computer modeling of various materials irradiated by $\leq$1 ps pulses has been reported (see, e.g. references [13, 20, 127, 128]), with pressures of hundreds of GPa predicted for high fluences (see, e.g. references [9, 129]). It has been previously estimated that a (sustained) pressure of a few GPa would be required to nucleate defects in semiconductors [37, 38]. Although much larger transient pressures are expected to be generated at the higher fluences used in the work presented here, it is the magnitude of the pressure wave in the affected sub-surface region which is relevant. The strength of the pressure wave launched into the crystalline bulk (see, e.g. reference [13]) is expected to decrease with propagation distance into the

material. Pressures at depths of a micrometre or more are also relevant to some results presented here, as the defected region extends this far below the original substrate surface. In part due to the computational power required, computer modeling studies have typically not examined material evolution more than a few hundred nanometres below the irradiated surface (see, e.g. references [23, 127, 129]). In addition, the dynamics of melting and recrystallization, along with the heat transported into the bulk, could play a substantial role in inducing crystallographic changes.

It is evident from cross-sectional TEM observations of silicon lacking metal and thermal oxide layers that multiple-pulse irradiation produces damage more readily than single-pulse irradiation. Isolated defects on silicon were observed at a low fluence (1.3 J/cm^2) for five-pulse irradiation (see figures 7.1(e) and 7.7–7.9), while for nearly ten times the fluence, a single pulse produced no observable defects and only a thin amorphous region (figures 7.1(b), 7.1(c), and 7.3–7.6). After the first pulse, subsequent pulses are incident on material with potentially different chemical, structural, and optical properties [44]. An incubation effect, in which the modification threshold fluence decreases with increased number of pulses, has been reported for various crystalline materials [39, 130] including silicon [35]. It has been proposed that incubation could arise from the storage of energy by changes of a mechanical (stress-strain) [35, 130], chemical [35, 39], or crystallographic [39] nature. For the lower fluence single-pulse site (1.5 J/cm^2, see figures 7.1(b) and 7.2), the only observed modification was a change in surface profile, and not in the form of substantial crystallographic changes such as amorphization or defect generation.

7.4.3 Effects of multiple layers

For the five-pulse irradiation site on the multilayer sample (fluence 10.5 J/cm^2), substantial defects were observed in the silicon (see figure 7.18). In the cross-sectional TEM work on uncoated silicon, four ultrashort laser pulses with a similar fluence (11 J/cm^2) and same wavelength also produced dislocations. Comparing these two multiple-pulse cases, the presence of the films did not substantially affect the final outcome. For a single pulse fluence of 11 J/cm^2 on the non-multilayer sample, crystalline defects did not form. The single pulse fluence used on the multilayer sample is similar (10.5 J/cm^2) and was at the same wavelength (800 nm), yet the presence of the metal and oxide layers resulted in significant defects. It is conceivable that differing degrees of thermal expansion among the materials, in addition to the enhanced pressure wave due to strong absorption in the metal, led to stresses sufficient to cause defects.

The results of multilayer sample irradiation with 400 nm and 800 nm wavelength pulses with similar incident fluences are not expected to be the same. For example, the reflectance of gold differs significantly between the two wavelengths [99]. In a study on copper [79], the surface reflectance has been shown to affect the ablation threshold for 800 nm irradiation. From SEM observations, incident fluence thresholds for the gold removal and shell formation were lower for 400 nm irradiation than for 800 nm irradiation. The spot size was somewhat smaller for the shorter wavelength, so although the spot size itself may influence structure formation, the use of peak fluences rather than pulse energies allows a more fair comparison. The cross-sectional TEM observation of greater damage effects for $\lambda = 400$ nm compared with 800 nm radiation (for similar incident fluences) is expected based on the higher absorption of incident light at the shorter wavelength. Although only three different fluences were examined for each wavelength in single-pulse multilayer irradiation, there appears to be a fluence threshold below which crystallographic damage in the silicon does not occur. This threshold is higher for the longer wavelength, and is consistent with the gold-removal and shell-formation thresholds mentioned earlier being higher for the $\lambda = 800$ nm case.

McDonald et al. [131] irradiated various thicknesses of thermal oxide films on silicon with femtosecond laser pulses. A bubble or blister was observed resulting from the delamination and expansion of the film from the substrate. Although the oxide thickness on the multilayer samples reported in this thesis was within the range used in reference [131] and a similar wavelength is used, a much lower single pulse fluence was employed in reference [131]. The fact that the oxide film on the multilayer sample remained intact implies that the metal film played a major role in the single-pulse irradiation process. In reference [131], the pulses were expected to pass through the oxide without depositing much energy into it, and thus deposit the laser energy into the underlying silicon. In the case presented here however, the pulse fluences are near or significantly above the damage threshold of bulk silicon dioxide (see, e.g. reference [132]).

While Jia et al. [40] reported amorphous silicon on an $Si/SiO_2/Si$ sample, in this thesis crystalline damage, rather than an amorphous layer, was observed for the five-pulse multilayer case. As noted earlier however, a much lower fluence and shorter wavelength were used in reference [40]. Additionally, in the case presented in this thesis the oxide and substantial underlying silicon were removed while in reference [40] the oxide was not exposed. The underlying oxide in reference [40] could have influenced the heat flow and pressure wave propagation, thus affecting crystallographic changes.

7.5 Additional considerations for future work

For nanosecond-duration excimer laser irradiation, Giust and Sigmon [133] deposited polycrystalline silicon on silicon oxide of various thicknesses. A thinner oxide provided less thermal resistance between the polycrystalline silicon and the substrate under the oxide, affecting the cooling of the polysilicon. As a follow-up experiment to the work presented in this thesis, examination of the crystallographic structure under various oxide thicknesses after femtosecond laser irradiation would be valuable. A thicker oxide layer could reduce the heat reaching the oxide-silicon interface and delay its arrival. Sufficiently thick oxide could also somewhat attenuate the generated pressure waves before they reach the silicon substrate.

Additional studies with other thicknesses or compositions of the overlying metal film could indicate the role of the absorbing material above the oxide. In gold, the linear optical penetration depth is $\sim$12.5 nm [99] (at 800 nm wavelength), but the effective penetration depth of the laser energy is much larger [23, 134], on the scale of the metal film thickness on the multilayer sample used here. The damage threshold fluence depends on the thickness of the film when the film is thinner than a certain critical value. This value is strongly dependent on the strength of electron-phonon coupling [135]. Noble metals, such as gold, have a much slower electron-phonon relaxation compared to transition metals, and thus the molten phase in noble metals exists longer [136]. Compared to nickel, for example, gold has a larger effective penetration depth of excited electrons [23], and a larger critical film thickness [135]. Differences in the properties of selected metal overlayers could play a significant role in the extent to which the underlying substrate becomes damaged under femtosecond laser irradiation of such layered samples.

Concerning incubation effects, more studies of two-, three-, and four-pulse sites at low fluences, possibly with different methods of analysis in TEM, would be useful to examine the surface and sub-surface crystallographic evolution. In particular, careful examinations at fluences near and below the single-pulse threshold could reveal the extent to which defects are formed after the first and subsequent pulses, and thus indicate the extent to which formation of defective material is related to incubation behaviour. Such investigations could conceivably show the pulse-to-pulse sub-surface evolution. Similar work could be done on the multilayer samples. For example, while FIB was done on the two-pulse $\lambda = 400$ nm low-fluence sample, additional FIB work on the 1-, 3-, and 4-pulse cases (for which SEM images are shown in figure 7.19) of the same wavelength and fluence would complement the 2-pulse TEM results. Currently, only the evolution visible under SEM has been observed.

In the growth and deposition of thermal oxide and metals for the fabrication of the multilayer target, additional silicon wafers were prepared possessing the thermal oxide without the metal deposition, and possessing the metal without an underlying thermal oxide. These additional possibilities remain to be examined. For example, the lack of oxide under a metal film may result in reduced defects if thermal expansion mismatch is the primary cause of defect generation. Alternately, more defects might be expected if pressure waves do not have a large region of oxide in which to dissipate. Irradiation of the thermal oxide coating could allow significant absorption of laser light in the silicon, similar to the cases presented by McDonald et al. [131].

Further TEM studies on silicon could be done using selected laser wavelengths, such as those at which silicon is single-photon transparent, and with targets of various crystal orientations. This would build upon the results shown in chapters 5 and 6. Different densities or types of defects may be produced depending on the direction of compression relative to the crystalline axes. With multilayer targets, the use of longer pulses could affect the magnitude of the pressure wave without substantially changing the thermal deposition, more clearly identifying the relative effects of thermal expansion mismatch and pressure wave propagation. Similar experiments on the non-multilayer samples would also be useful, to understand the relative effects of varying pulse intensity without varying the pulse energy and fluence. Studies using various pulse durations on copper and on gallium phosphide have been performed with the same laser system as the one used in this thesis chapter, and the results are reported in chapters 5 and 8.

Some additional technical details deserve comment and would be worthy of further investigation. Due to the nature of regenerative amplification in femtosecond laser systems (see section 3.1 for details), a train of pre-pulses and post-pulses exists, the magnitude of which depends on the system design and operation conditions. For the laser system used in this study, the pre-pulses have an energy of up to ~0.05–0.2% of the main pulse energy and could lead to minor heating of the target. For the post-pulse an energy of roughly 0.7–1% of the main pulse is expected. These 'satellite' pulses are spaced approximately 7 ns apart. Due to the nonlinear nature of second harmonic generation, such pulses will be greatly attenuated in the case of 400 nm wavelength irradiation. The nonlinear processes in optical parametric amplification will also greatly attenuate these satellite pulses in studies where ~1300 and ~2100 nm wavelengths are used. For the highest fluence $\lambda = 800$ nm irradiation presented in this thesis section (33 J/cm^2), the fluence of a 1% post-pulse is near the single-pulse modification threshold of silicon (around a few hundred mJ/cm^2, see, e.g. reference [33]). The post-pulse would be incident on material which is still experi-

encing surface evolution as suggested by studies using time-resolved ultrafast imaging [5]. The effect of such a pulse on sub-surface crystallinity for the bare silicon irradiation and multilayer sample remains to be investigated. In addition, the reflective metallic neutral density filters used in this experiment are expected to lead to weak satellite pulses delayed approximately 10 ps with respect to the main pulse. Although these technical aspects are not expected to significantly influence the key findings presented here, a comprehensive set of follow-up experiments exploring the effects of additional pulses incident within a picosecond and nanosecond time frame would be of definite interest.

7.6 Conclusions

Cross-sectional TEM examinations of single-pulse and multiple-pulse femtosecond laser-irradiated silicon and Au/Pt/Ti/SiO_2/Si were performed. The conditions for formation of defects and amorphous material are of interest since they can limit the application of femtosecond laser machining in practical applications. Substantial sub-surface damage on the silicon-only sample was only observed under the single-pulse irradiation condition at a fluence of 33 J/cm^2, and under four-pulse irradiation at 11 J/cm^2. The amorphous phase of pure silicon was found in the case of a single-pulse irradiation of silicon with a fluence of 11 J/cm^2 and in the case of five-pulse irradiation with a fluence of 1.3 J/cm^2. Irradiation with a single pulse of 1.5 J/cm^2 produced neither amorphous material nor lattice defects. It is observed that multiple-pulse irradiation produces crystallographic damage more readily than a single pulse.

On the multilayer targets, a range of pulse energies in single-pulse irradiation exists for which the metal film was removed but the oxide was not appreciably thinned. For a sufficiently high pulse energy within this range, substantial defects were observed in the underlying silicon. This behaviour exists for irradiation by $\lambda = 400$ nm and 800 nm wavelength pulses, though with different incident fluence thresholds at different irradiating wavelengths. Although the metallization can be removed by the laser pulses, care should be taken to consider the potential damage, not apparent from simple surface observations, of the underlying substrate covered by the insulating layer. Five infrared pulses of a relatively high fluence created significant defects, as well as producing polycrystalline material on top of the original oxide and metal.

Chapter 8

Laser Drilling of High Aspect Ratio Holes in Metal Foils

8.1 Introduction and motivation

This chapter of the thesis details the work done on the drilling of high aspect ratio holes in copper sheets. The work was performed in collaboration with Arnaud Weck. The results were published in the following papers:

- A. Weck, T.H.R. Crawford, A. Borowiec, D.S. Wilkinson, J.S. Preston: *Femtosecond laser-based fabrication of a new model material to study fracture*, Applied Physics A **86**, 55 (2007) [74]
- A. Weck, T.H.R. Crawford, D.S. Wilkinson, H.K. Haugen, J.S. Preston: *Ripple formation during deep hole drilling in copper with ultrashort laser pulses*, Applied Physics A **89**, 1001 (2007) [75]
- A. Weck, T.H.R. Crawford, D.S. Wilkinson, H.K. Haugen, J.S. Preston: *Laser drilling of high aspect ratio holes in copper with femtosecond, picosecond, and nanosecond pulses*, Applied Physics A **90**, 537 (2008) [76]

Additionally, I presented this work in the following conference contribution:

- A. Weck, D.S. Wilkinson, T.H.R. Crawford, H.K. Haugen, J.S. Preston: *Femtosecond laser drilling of high aspect ratio holes in copper sheets*, 9th International Conference on Laser Ablation (COLA) 2007, Poster PMO-31

In the experiments, I was responsible for some modification of the machining apparatus and setting up the photodiode acquisition electronics. Myself and A. Weck jointly machined the majority of the samples for the ripples and photodiode experiments. A. Weck

did the majority of the machining for the ductile fracture experiments, and did all the microscopy work. The microtome work was performed by Marcia Reid at the Integrated Microscopy Facility in the Health Science Center at McMaster University. The initial proof-of-principle experiment showing the feasibility of recording data from a below-sample photodiode was performed by A. Borowiec. For the paper writing, my role was in the contribution of some details from the laser-material interaction literature, some discussion and interpretation of some physical phenomena, and contributing specific details of the experimental setup. The outlines and initial drafts of the papers, and preparation of the figures, were done by A. Weck. Unless otherwise noted, the images and graphs in this portion of the thesis were generated by A. Weck, and were also presented in one of the papers [74, 75, 76][1].

The ductile fracture process consists of the nucleation, growth, and coalescence of voids in the material [74]. It is difficult to observe the coalescence event, but understanding of this event is important for developing predictive models of ductility [74]. The initial motivation for the use of femtosecond lasers in copper drilling was to fabricate a 'model material' for the study of fracture. A single metal sheet possessing an array of laser-drilled holes could be placed in a tensile testing apparatus within an SEM, for observation of the coalescence with pulling. A foil possessing holes could be diffusion bonded between hole-free sheets, producing a bar with encased voids. These could be pulled while observing in situ in a synchrotron x-ray beamline. X-ray computed tomography could then be used to obtain three-dimensional images of the coalescence event. This work was presented in reference [74]. The technique can be applied to a variety of materials, for example to compare those with different crystal structures (hexagonal close packed for titanium as opposed to face centered cubic in copper and aluminum), or heat capacity and heat conductivity (stainless steel as opposed to copper and aluminum). The computer-controlled translation stages on which the machining chamber is mounted allow for a wide variety of possible drilling patterns (rectangular or hexagonal grids, pseudo-randomly distributed holes, etc.), while different focussing elements allow a range of hole diameters.

In the process of determining optimal laser parameters for the model material preparation (pulse energy, polarization, focussing element, pulse duration, number of pulses, irradiation atmosphere) a variety of observations were made, such as the entrance and exit hole diameters and surface morphology. After much of the ductile fracture work was completed, it was decided to systematically measure the effects of these parameters and publish the results. In the literature most studies of laser-irradiated materials only look near the surface,

[1] See appendices C and F for copyright and permission information.

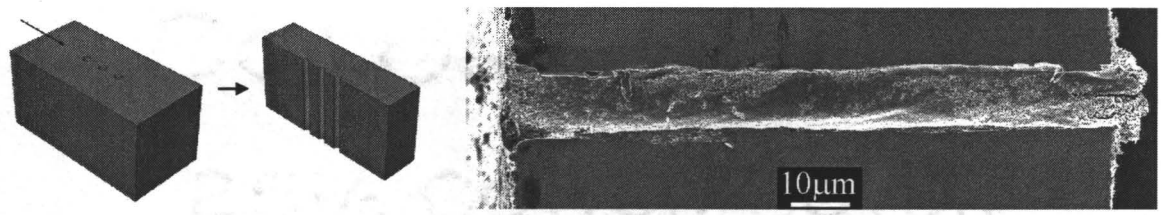

Figure 8.1: Schematic of the process of making a microtome cut, and an SEM image of an entire laser-drilled hole in copper cut with the microtome. These images are from reference [76].

although there have been some studies on deep holes (see, e.g. references [2, 71, 72, 73] for metals and semiconductors). Systematic variation of parameters such as pulse duration, polarization, and energy were generally lacking, and few reports provided examination of the hole wall.

For the preparation of most samples in this section of the thesis, a spinning half-wave plate, placed in the beam and rotating $\sim$15° per millisecond (the time between pulses at the standard operating condition of 1 kHz), was used. This produced a 'spinning' linear polarization, and provided approximately circular entrance and exit holes. Non-'spinning' linearly polarized pulses tended to produce elliptical entrance and exit profiles, which were undesirable. A 5$\times$ microscope objective was usually used, with irradiation in air atmosphere unless otherwise noted. Irradiation however was performed inside a steel vacuum chamber equipped with a 1 mm thick fused silica window, but without the vacuum pump turned on. Performing the irradiation inside the chamber helped contain debris and attenuate x-rays generated by the machining.

Using a microtome (equipped with an atomically sharp diamond knife), a cross-section of the hole was obtained for observation in SEM; a schematic and example are shown in figure 8.1. A large-area photodiode ($\sim$1 cm^2) mounted a few millimetres below the foil recorded the laser signal as a function of number of pulses, and this was done at a wide range of pulse durations and pulse energies. The results of the microtome, SEM, and photodiode work were published in the subsequent papers [75, 76].

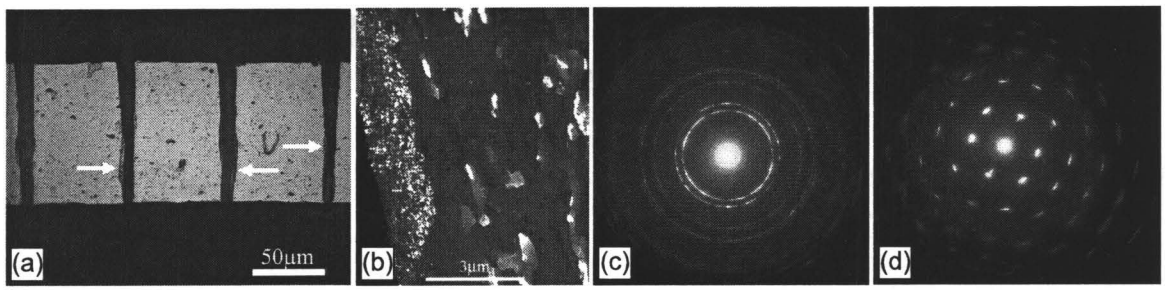

Figure 8.2: (a): Light microscopy image of laser-drilled holes in aluminum, cut with a microtome. (b): Dark-field TEM image showing (from left to right) a hole in aluminum, a nano-grains region, and the unmodified material. (c), (d): Electron diffraction patterns of the nano-grains region (in (c)) and the unmodified material (in (d)). These images are from reference [74].

8.2 Analysis of the heat-affected zone in laser-drilled holes

A heat affected zone, while usually small for short laser pulses, is produced by the heating of the target. Previous work in our research group [44, 48] on grooves in indium phosphide revealed a heat affected zone, and it was proposed that stresses were due to solidification of a molten layer. Figure 8.2(a) shows a series of holes in an aluminum foil cut with a microtome [74]. The taper of the holes (from $\sim$10 μm diameter at the top where the laser entered to $\sim$8 μm at the bottom) can be seen, with evidence of a remelted layer indicated by the arrows. A TEM sample of high purity aluminum was prepared with the microtome, and a darkfield TEM image is shown in figure 8.2(b). The solid black region on the left is the hole. Adjacent to it is the heat-affected zone consisting of nano-grains. This region was found to have a thickness from 300 nm to 2 μm. The central to right portion of the figure is the unmodified material. Figures 8.2(c) and (d) show diffraction patterns from the nano-grains region and the unmodified material respectively. The rings in figure 8.2(c) are characteristic of nano-grains.

Nanoindentation is a technique by which the hardness of a material can be estimated. It is shown schematically in figure 8.3(a), whereby the indent-deformed region overlaps with the heat-affected zone. Since the deformed region is roughly three times the diameter of the indent, an indent width of approximately 2 μm was chosen, and indents were placed about 3 μm from the edge of the laser-drilled holes [74]. This allowed the deformed zone to extend approximately to the edge of the hole and thus interact with the heat affected zone. Indents were also placed far from the holes, to estimate the relative hardness of the

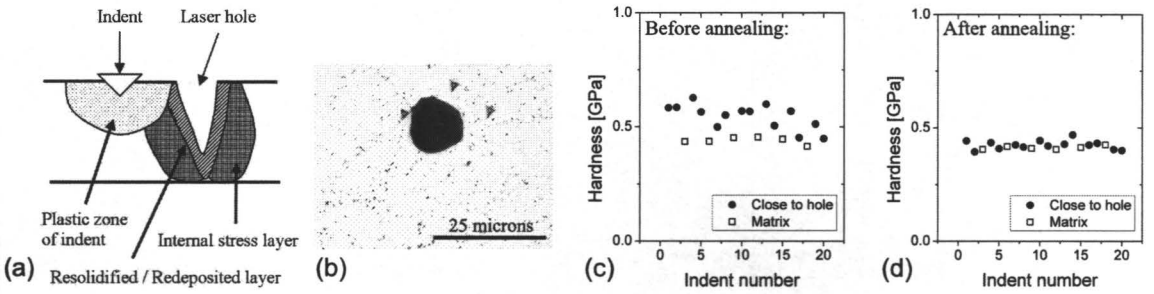

Figure 8.3: Nanoindentation of commercial purity aluminum. (a): Schematic of the nanoindentation process. (b): Optical micrograph of a laser-drilled hole, with three indents near the hole. (c): Results of nanoindentation close to the hole, and far from the hole (labeled 'Matrix') before heat treatment. (d): Results of nanoindentation after heat treatment. These images are from reference [74].

original material. Figure 8.3(b) shows an optical microscope image of commercial purity (99.99%) aluminum with three indents. Figure 8.3(c) shows the approximate hardness of many sites on commercial purity aluminum chosen close to the hole, and also far from the hole (labeled 'Matrix' in the figure). Multiple indents were performed, and the variability in the exact position of an indent relative to a laser-drilled hole is reflected in the scatter in the values for 'Close to hole'. While these results are fairly qualitative, there is clearly an increased hardness near a laser-drilled hole. After annealing the material, the nanoindentation test was repeated. The results, shown in figure 8.3(d) show that the hardness near the hole is similar to the unmodified material after annealing [74]. The exact mechanism which reduces the hardness after annealing was not investigated. It is possible that internal stresses generated in laser drilling are being relieved by the annealing. Dislocations could be greatly reduced by the annealing, or small crystal grains produced by laser irradiation could grow into large grains. Further work would be needed to more clearly identify the relevant processes. However, a key result from this work is that the femtosecond laser drilling of deep holes produces a heat affected zone which can be reduced by heat treatment. A conclusion for metals is qualitatively similar as for InP [44, 48]: femtosecond laser drilling with multiple pulses is not entirely 'damage-free'. While the results presented in this section are for aluminum, similar experiments on aluminum alloy 5052 and stainless steel yielded qualitatively similar results.

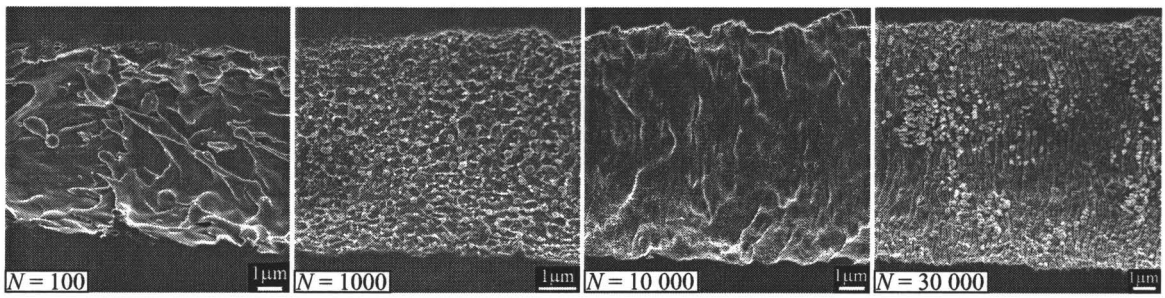

Figure 8.4: Evolution of the wall of copper holes with number of pulses N. SEM images are taken from approximately the center of the hole, and are representative of the structures observed along the length of the hole. These images are from reference [75].

8.3 Ripple formation in deep holes in copper

After drilling of a hole, the microtome can be used to slice the hole along its length, and the side walls of the hole can then be observed using SEM. In some applications the wall morphology may play an important role. For example, smooth walls may be desired for microfluidic applications while rough walls may be desired for improving the adhesion of other materials. Laser-induced periodic surface structures (LIPSS) may also form on laser-irradiated surfaces. For laser radiation incident on a surface at normal incidence, LIPSS generally have a period near the in-air laser wavelength. These have been reported extensively for a variety of materials and pulse durations [1, 24, 25, 35, 53, 56, 58, 59, 63, 103, 130, 137, 138, 139], including metals such as copper (see, e.g. reference [79]). For an angle of incidence θ, the LIPSS period Λ has frequently been found [24, 53, 54, 56, 137] to obey the equation:

$$\Lambda = \frac{\lambda}{1 \pm \sin(\theta)}, \tag{8.1}$$

where λ is the laser wavelength. As $\theta \rightarrow 90°$, the period $\Lambda \rightarrow \lambda/2$ (when using the $+$ in equation 8.1, which was the case observed in the results on copper presented here). For femtosecond laser irradiation of materials, the LIPSS period is frequently reported to be near but less than the laser wavelength. This trend is discussed more extensively in chapter 5.

Figure 8.4 shows the evolution of the hole wall morphology of copper as a function of number of pulses. A spinning polarization was used, with a pulse duration of 150 fs, center laser wavelength of 800 nm, pulse energy 10 μJ (peak fluence ~22 J/cm^2), 5× focussing objective and air atmosphere. The copper foils used in these experiments were of 99.999%

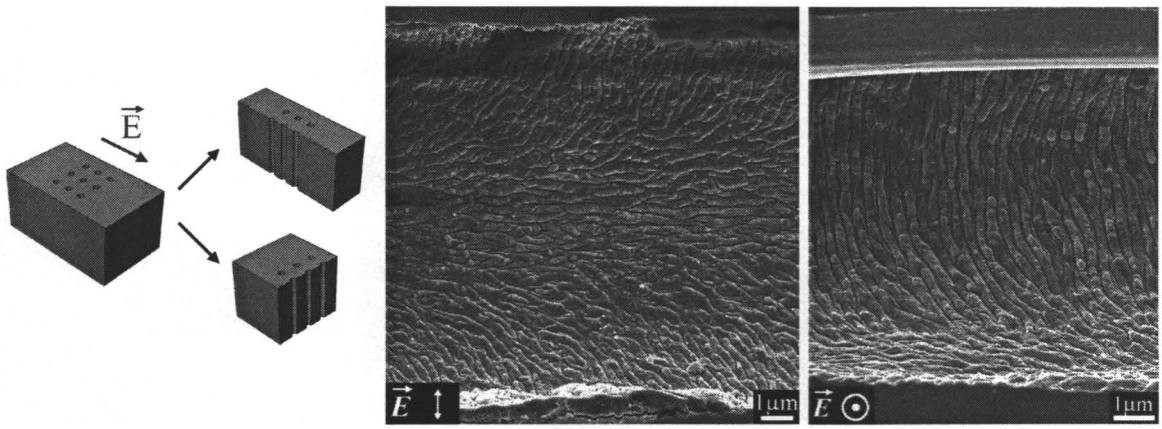

Figure 8.5: Schematic diagram of holes cut with the microtome parallel and perpendicular to the laser polarization, and SEM images of the wall of such holes. In this case, 30 000 pulses were used, with a pulse duration of ~10 ps. These images are from reference [75].

or 99.9999% purity, 100 μm thick, and annealed before laser irradiation. The annealing led to a grain size around a couple hundred micrometres, so that holes (diameters less than ~20 μm) were typically within single crystal material. After 100 pulses, the surface is very rough with large features which look as if they came from molten material. The foil required ~160 pulses before the hole completely passed through it. After 1000 pulses, the surface looks as if many small droplets have impinged on the surface. With 10 000 pulses the surface is smoother, and shows some evidence of a periodic structure. Finally, after 30 000 pulses prominent ripples are present on the walls of the hole. The ripples resemble stacked rings, with their centers along a common axis down the center of the hole. The ripple spacing is approximately 300 nm, somewhat less than half the wavelength of the laser light. Further experiments (see reference [76] and results presented later in this thesis chapter) showed that the period does not depend strongly on pulse duration. Once 10 000–30 000 pulses have been incident on the sample, the hole is in somewhat of a steady-state condition where the hole entrance and exit diameters are not increasing substantially. The spatial edges of the pulses incident on the surface have too low a fluence to remove further material. Ripples formed only when the hole was approaching its steady state condition, as the laser energy incident on the walls of the holes is rather low at that stage.

Cross-sections of a hole drilled with non-spinning linearly polarized light in air are shown in figure 8.5. The ripples are curved, running perpendicular to the length of the hole where the polarization is parallel to the normal to the hole wall, and running parallel to the length of the hole where the polarization is perpendicular to the normal of the wall.

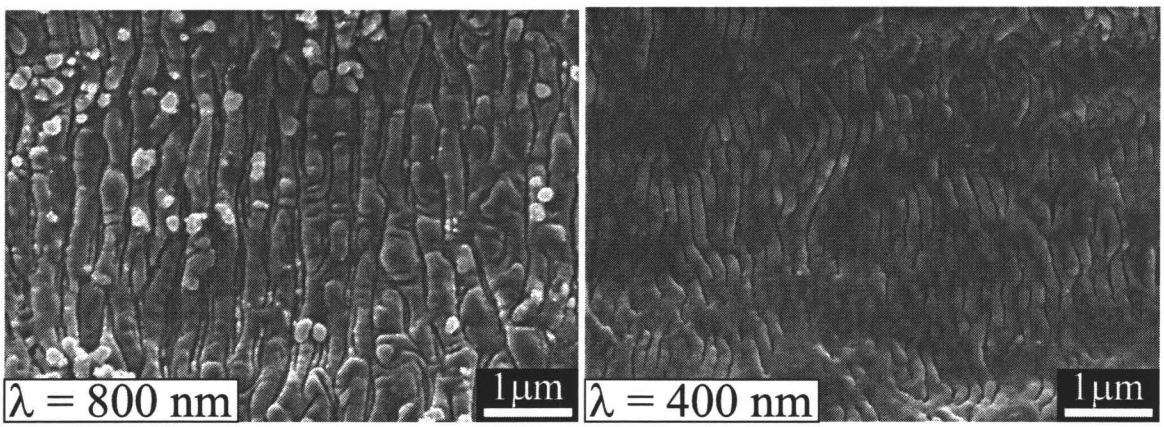

Figure 8.6: SEM images of the wall of holes drilled with *(left)* $\lambda = 800$ nm pulses, and *(right)* $\lambda = 400$ nm pulses. In each case, 30 000 pulses were used. These images are from reference [75].

Overall the ripples generally run perpendicular to the incident laser light polarization. This strongly suggests that the ripples arise from interference effects. The two SEM images in figure 8.5, for which non-spinning polarization was used are in contrast to the case shown in figure 8.4, for which a spinning polarization was used. With the spinning polarization, the ripples formed rings along the same central axis, and in no location curved to travel along the length of the hole as seen in the non-spinning case.

As a final test to determine if ripples in high aspect ratio copper holes are consistent with interference effects, a different laser wavelength (400 nm, produced by sending 150 fs, 800 nm wavelength pulses through a 150 μm thick BBO crystal) was used. If interference effects are the cause, the period would be expected to vary with wavelength. Figure 8.6 shows holes drilled by 30 000 pulses of 10 μJ energy per pulse, with two different wavelengths in an air atmosphere. The ripple period in the 400 nm case is around ~160 nm, compared to ~300 nm for the 800 nm case. The ~50% reduction in period with 50% reduction in wavelength supports the theory that the ripples originate from light interference effects. The 400 nm case has a less prominent ripple structure, overall being smoother as if more molten material had been present. For normal incidence, copper has a much higher reflectance at $\lambda = 800$ nm than at 400 nm [99], so more energy would be absorbed for the shorter wavelength. The reflectances would both approach 1.0 for angle of incidence of 90° however, so simple comparisons cannot be easily made. Throughout the discussion of ripple formation on the walls of holes, the possible waveguiding effects which can occur in small diameter holes in metals have been neglected.

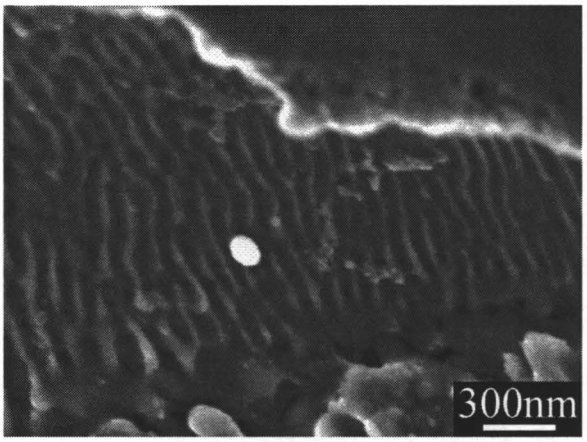

Figure 8.7: SEM image of the entrance of a hole drilled with 30 000 pulses, 30 ps pulse duration, $\lambda = 800$ nm, and spinning polarization in air. This image is from reference [75].

A very fine ripple structure was observed with SEM at the entrance of a laser hole. This is shown in figure 8.7. The ripple period is approximately 75 nm, which is roughly 1/10 of the laser wavelength. It is noteworthy, since although substantially sub-wavelength ripple periods have been reported frequently in the literature for non-metals (see chapter 5), they not been reported extensively in the literature on metals (the one occurrence we are aware of being reference [139]). The general lack of substantially sub-wavelength ripples on metals could provide insight into the formation mechanisms. The ripples observed in figure 8.7 were not common, and further work would be needed to more fully understand their formation conditions and causes for formation. It could be the case that these fine ripples on copper are not due to light interference effects, in contrast to the LIPSS observed more frequently on the hole walls.

Since the pulse duration of the Ti:sapphire-based laser system can be adjusted, the wall morphology in copper sheets could be examined as a function of pulse duration. For durations up to ~35 ps, the amount of pulse recompression after the chirped pulse amplification step could be changed. The physical layout of the compressor enclosure set this upper limit. Pulses of ~220 ps duration were obtained by bypassing the compressor, and a duration of ~7 ns was obtained by not seeding the amplifier. For the determination of the pulse duration of the unseeded amplifier, a communications signal analyzer and fast InGaAs photodiode (manufacturer-quoted impulse response 18.5 ps) were used. For measurement of the shorter pulse durations, a non-collinear second-order autocorrelator with a

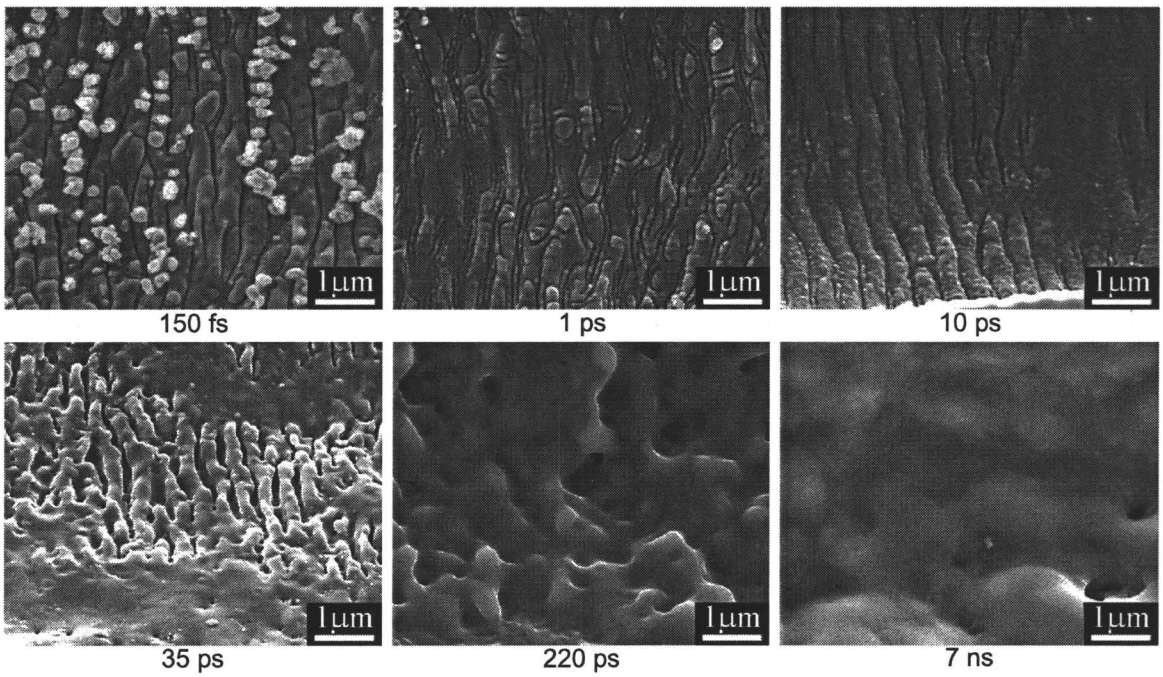

Figure 8.8: SEM images of the walls of holes drilled with 30 000 pulses, $\lambda = 800$ nm, per-pulse energy of 10 μJ, and spinning polarization with various pulse lengths in air atmosphere. These images are from reference [76].

500 μm thick KDP crystal was used. More details on pulse length configuration are given in chapter 3.

Figure 8.8 shows, for irradiation of copper foil in air with spinning polarization, the wall morphologies at various pulse durations. For durations up to 10 ps, prominent ripples formed, with the ripple spacing of ~300 nm not strongly affected by pulse duration. However, at 10 ps and particularly at 35 ps, ripples began to be replaced with a structure which appeared to have come from molten material. At 220 ps, a random-looking structure with bumps on the order of a few micrometres was present. At 7 ns, a smooth morphology was present, which looked as if it had previously been molten. The entrances of holes drilled in air atmosphere are shown in figure 8.9. In those images, significant fine debris is present in the 150 fs and 1 ps cases (as well as in 300 fs and 600 fs cases, not shown here), while for longer pulse durations the amount of debris is reduced and more evidence of molten material is visible. In particular, a 'chimney'-shaped structure formed in the 220 ps and 7 ns cases (and small in the 35 ps case), which appeared as if it had been formed by molten material depositing on the edge of the hole.

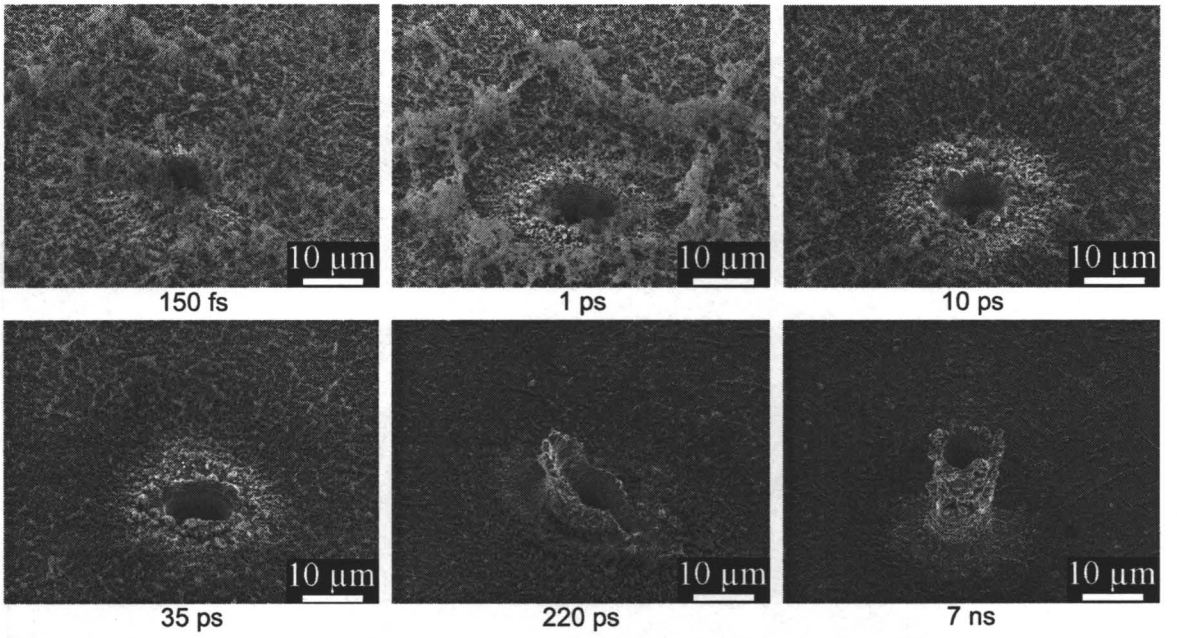

Figure 8.9: SEM images of the entrances of holes drilled with 30 000 pulses, $\lambda = 800$ nm, per-pulse energy 6.8 μJ, and spinning polarization with various pulse durations in air. These images are from reference [76].

In examining the wall morphology as a function of pulse duration, an additional set of holes was prepared with irradiation in a rough vacuum atmosphere. The results are shown in figure 8.10. The ripples which formed in air atmosphere were not present for vacuum irradiation. Instead, for pulse durations up to 10 ps, the surface looked as if small droplets with diameters on the order of 200 nm impinged upon the surface. For 35 ps pulses the droplets were on the order of ~350 nm wide, increasing to more than 3 μm for 7 ns pulse duration. Irradiation in air and vacuum atmospheres was also investigated with regard to the surface near the entrance of the hole. These, shown in figure 8.11, show a greater amount of debris on the sample surface for irradiation in air. The debris contains small copper particles trapped in a fine nanostructured foam.

In short pulse laser interaction with metals, the laser energy is initially absorbed by the conduction band electrons. This occurs on a very short time scale, and the electrons then begin to diffuse through the material and transfer their energy to the lattice via electron-phonon coupling. This electron-phonon coupling affects the material melting and/or vaporization, and in copper, occurs after a time scale on the order of a few picoseconds [128, 140]. It is expected that a transition in behavior would be observed for pulse

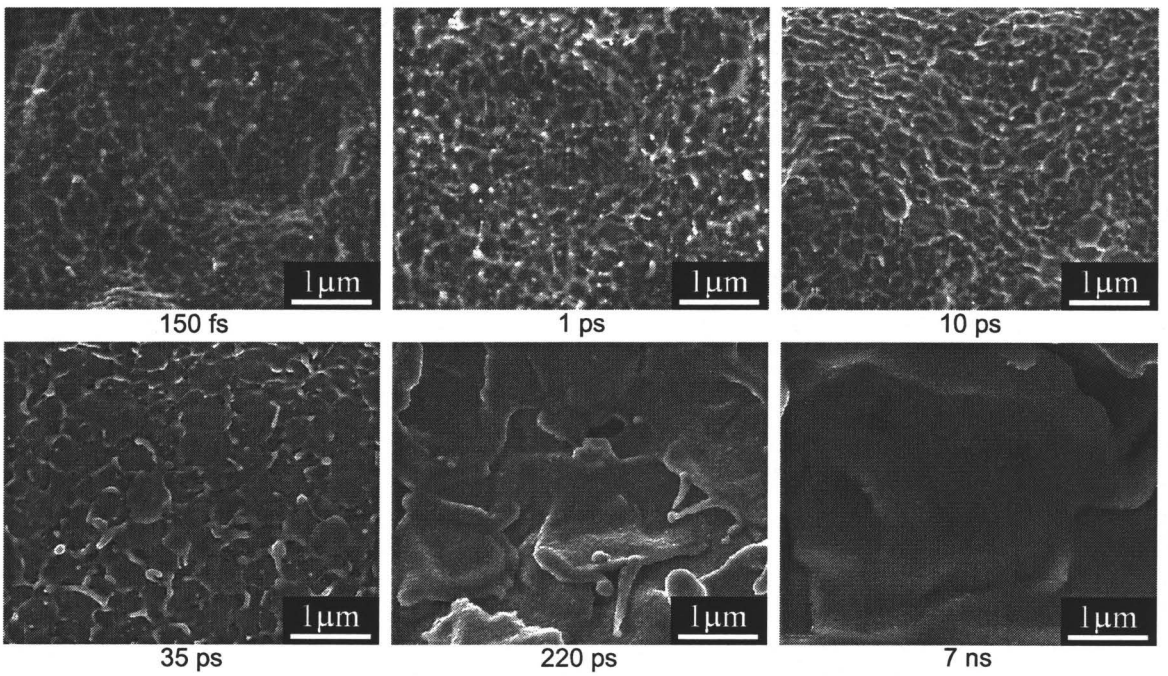

Figure 8.10: SEM images of the walls of holes drilled with 30 000 pulses, $\lambda = 800$ nm, per-pulse energy of 10 μJ, and spinning polarization with various pulse durations in a rough vacuum ($<\sim$100 mTorr). These images are from reference [76].

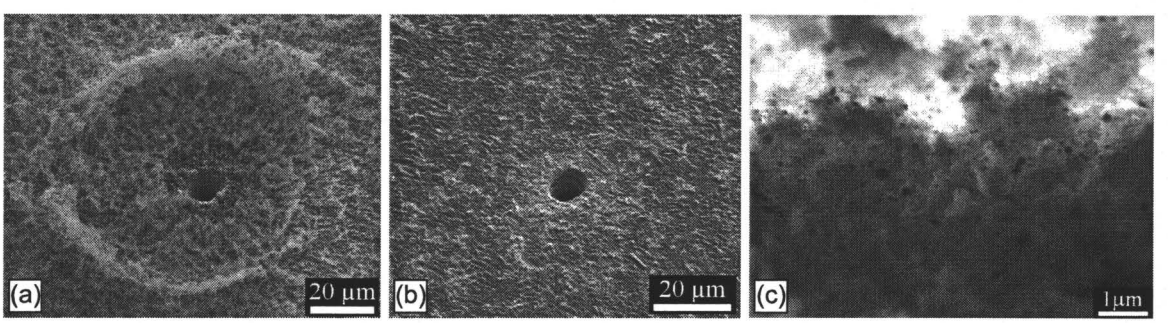

Figure 8.11: SEM images of the surfaces of holes drilled in (a) air and (b) vacuum with 1000 pulses, pulse duration of 150 fs, and per-pulse energy of 0.89 μJ. Image (c) is a higher-resolution image of debris produced near a hole drilled in air with 10 ps pulses. These images are from reference [76].

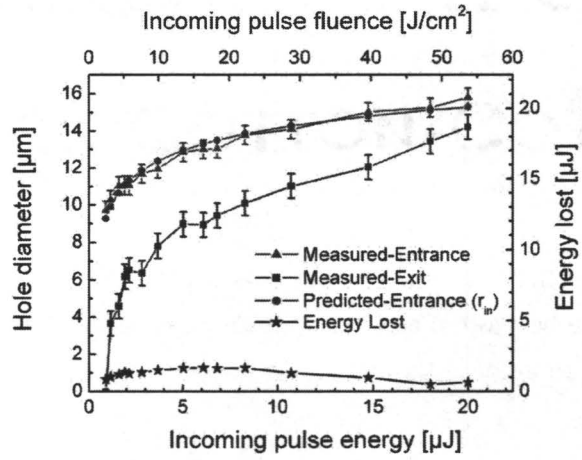

Figure 8.12: Experimentally measured entrance and exit hole diameters, curve fit to the entrance diameter, and measurement of pulse energy lost by the laser passing through the hole. All holes were drilled with 30 000 pulses each, with 150 fs pulse duration and $\lambda = 800$ nm. This graph is from reference [76].

durations near this time. In the two-temperature model for laser irradiation of metals (see chapter 2), the nature of the material evolution changes depending on whether the pulse duration is longer or shorter than the electron-phonon coupling time. A change in final morphology of the holes near pulse durations of $\sim$10 ps (such as the increased evidence of a molten phase shown in figures 8.8, 8.9 and 8.10) is consistent with this model.

8.4 Hole diameters

Entrance and exit hole diameters of holes drilled with 30 000 pulses (with spinning polarization, 800 nm wavelength, 5$\times$ focussing objective, in air atmosphere) were measured using optical (light) microscopy, and are shown in figure 8.12. By 30 000 pulses the hole has reached an approximately steady state condition, where the diameter is no longer changing appreciably (based on photodiode measurements presented in section 8.5). The entrance hole diameter is larger than the exit for a given energy, and higher pulse energy results in a larger diameter. The difference in diameters between entrance and exit is smaller for higher pulse energies, suggesting that high pulse energies should be used when nearly-cylindrical (rather than conical) hole profiles are desired.

For a Gaussian spatial laser beam profile, the fluence ϕ at a radius r is

$$\phi = \phi_\circ \exp\left(\frac{-2r^2}{\omega_\circ^2}\right), \tag{8.2}$$

where $\phi_\circ$ is the fluence at the center of the beam and $\omega_\circ$ is the radius at which the intensity has decreased to $1/e^2$ of its peak. Using the D^2 method described in section 3.5 the beam radius $\omega_\circ$ was found be be approximately 5 μm. By rearranging equation 8.2, the hole diameter ($2r$) can be plotted as a function of peak incident fluence $\phi_\circ$, with ϕ as a fit parameter. This fit parameter is the threshold fluence for material removal at the edge of a hole, when the fitting is to the hole diameter data presented in figure 8.12. For the entrance hole diameters, a value ϕ of 0.39 J/cm^2 was found as the threshold fluence. Despite the assumption that the beam profile is Gaussian (particularly in the wings of the profile, where the threshold fluence typically lies), the fit is reasonably good. A fit to the exit hole diameters was not done, due to the complexity of beam propagation down a metal hole and the resulting non-Gaussian nature of the beam at the exit.

The threshold value of 0.39 J/cm^2 can be compared to other values in the literature, however a direct comparison is complicated by many factors. Single-pulse modification thresholds are typically given for smooth flat surfaces, in contrast to the rough hole edge here. The reflectance of the surface, which can be affected by roughness or oxidation [79], affects the absorbed fluence. Additionally, incubation effects exist whereby the the damage threshold for multiple pulses is lower than the single-pulse damage threshold [35, 39, 79, 105, 130]. Our value is somewhat higher than those reported in the literature for copper in multiple pulse conditions and similar wavelength and pulse duration. A threshold near 0.2 J/cm^2 for 1000 pulses was reported in reference [79], 170 mJ/cm^2 for a 10–30 μm deep hole (number of pulses not specified) in reference [141], and less than 0.32 J/cm^2 for 3000 pulses in reference [142]. Some difference could be related to where exactly near the hole surface the diameter is measured, since there is some taper even near the hole entrance.

Also shown in figure 8.12 is the energy lost by a laser pulse after propagating through the hole after 30 000 pulses, as a function of pulse energy incident at the hole entrance. More details on the photodiode setup are given in section 8.5, but briefly, a reverse-biased large area photodiode was first exposed to defocussed pulses such that a voltage signal was recorded for each pulse energy. Then, the photodiode voltage was recorded for pulses after they passed through the steady-state hole. The reduction in photodiode signal corresponds to the energy loss. It was found that the energy lost is approximately 1–1.5 μJ per pulse, not strongly dependent on the incoming pulse energy.

8.5 Photodiode results

A large-area photodiode (approximately square with lateral dimensions of ~1 cm per side) could be placed a short distance (~5 mm) below a target. It can detect any laser light which passes through the target, or exits from the bottom of a hole. In studies using copper, the foil thickness was 100 μm while the optical penetration depth of 800 nm light is much smaller (roughly 12 nm [99]), so it is assumed that all photodiode signal is due to light passing through a drilled hole. For a set of machining experiments, the photodiode was reverse-biased and connected to a boxcar integrator. This allowed the recording of the photodiode signal for each pulse using the data acquisition computer, as a function of pulse energy and pulse duration. From calculations assuming an Airy diffraction pattern of $\lambda = 800$ nm light exiting a circular aperture, almost all of the exiting light should be incident on the photodiode for holes with a diameter of more than ~2 μm. The exit hole diameter was generally larger than this (see, e.g. figure 8.12). Results from the photodiode measurements are shown in figure 8.13.

For all pulse durations examined, higher pulse energies result in a higher photodiode signal since more energy reaches the photodiode. Higher pulse energies typically result in the hole being drilled with a lower number of pulses, as indicated by the rise in photodiode signal from zero near the start of the drilling. The 150 fs data is shown on a logarithmic scale (with number of pulses) in figure 8.14(a), more clearly showing the rise from zero signal for each pulse energy.

Early in the drilling process in the 10 ps, 35 ps, and 220 ps cases one or more 'spike' features are frequently observed in the photodiode data. These are where the photodiode signal rises from zero and remains non-zero for multiple pulses, before dropping to zero again. This may occur multiple times before the signal rises permanently for the rest of the drilling. Spikes in the 35 ps case are shown more clearly in figure 8.14(b), which is a magnified image of the plot shown for 35 ps in figure 8.13. By blocking the laser while a spike was occurring and using optical microscopy in light-transmission mode, it was confirmed that the hole passed through the material at the occurrence of a spike. Thus, the spikes are not a data acquisition glitch or other technical error. The spike behavior could be due to material being removed from the hole wall and lodging at the bottom of the hole, blocking light until subsequent pulses have removed the lodged debris. The data suggests that once a spike has formed, many more pulses are then required to permanently open the hole.

A prominent feature in the data shown in figure 8.13 is the 'noise' or brief signal drops in the 10 ps, 35 ps, and (to a lesser extent) the 220 ps case. These occur when the hole

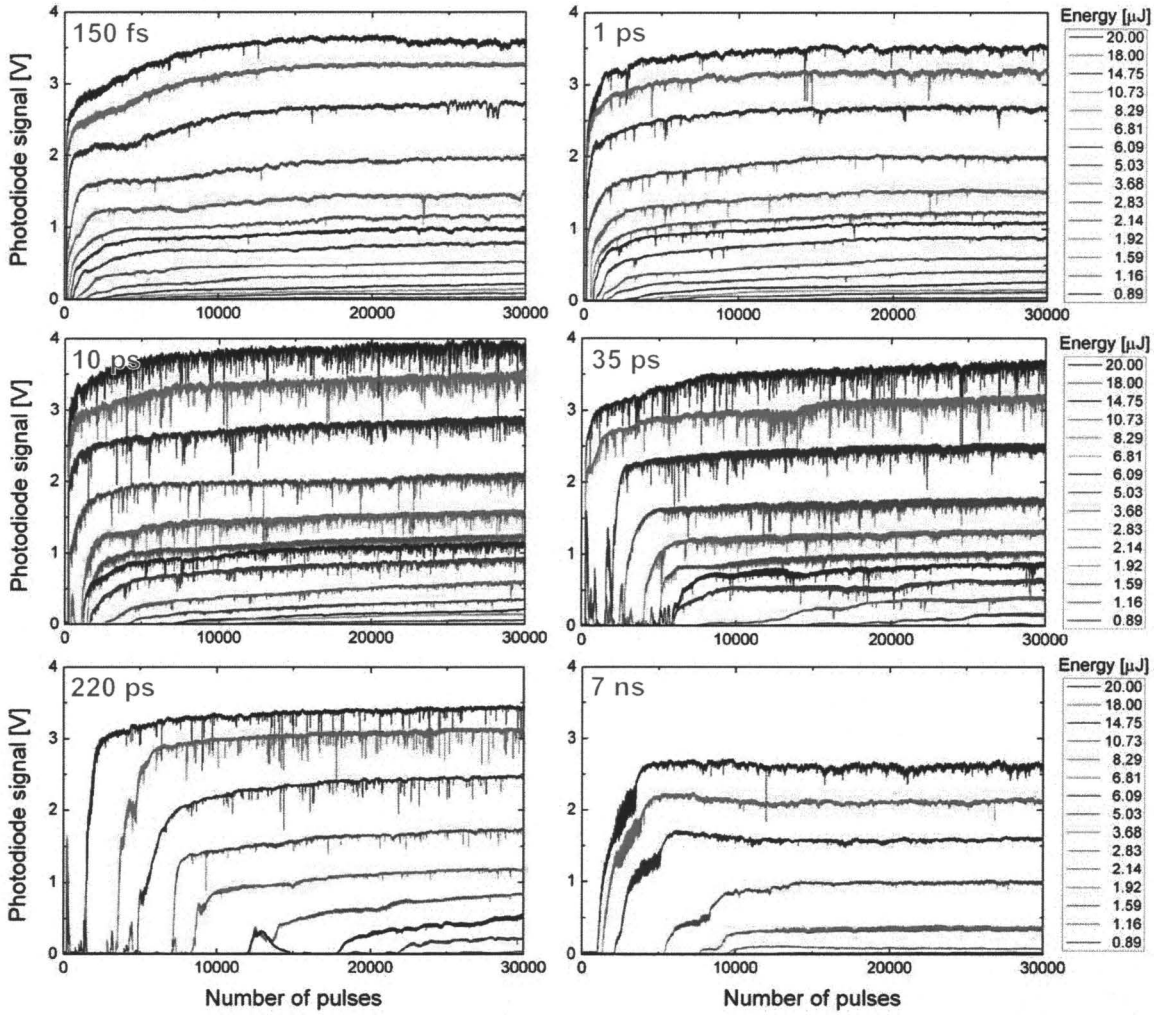

Figure 8.13: Data from a photodiode placed below a 100 μm thick copper foil, for six different pulse durations and various pulse energies in air atmosphere. In all cases, $\lambda = 800$ nm. The graphs are from reference [76].

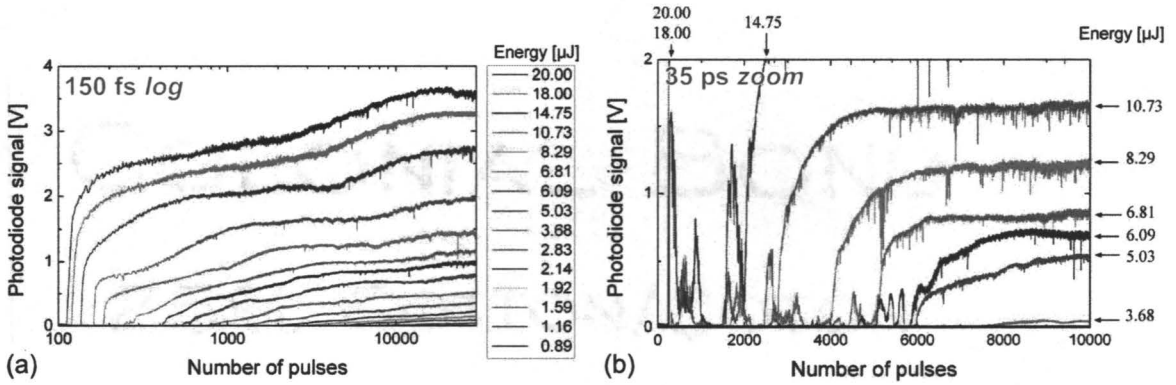

Figure 8.14: Data from a photodiode placed below a 100 μm thick copper foil, more clearly showing the signal near the start of drilling of the holes for (a) 150 fs and (b) 35 ps. The graphs show the same data as is shown in figure 8.13. The graphs are from reference [76].

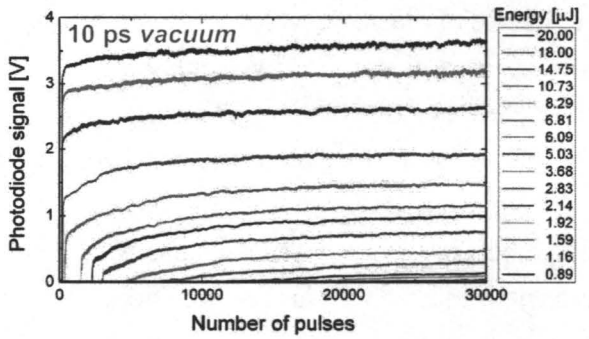

Figure 8.15: Data from a photodiode placed below the copper foil, with irradiation in rough vacuum atmosphere with 10 ps pulses. This data lacks the signal-drop noise observed for the same pulse duration in air atmosphere (see figure 8.13). This is graph is from reference [76].

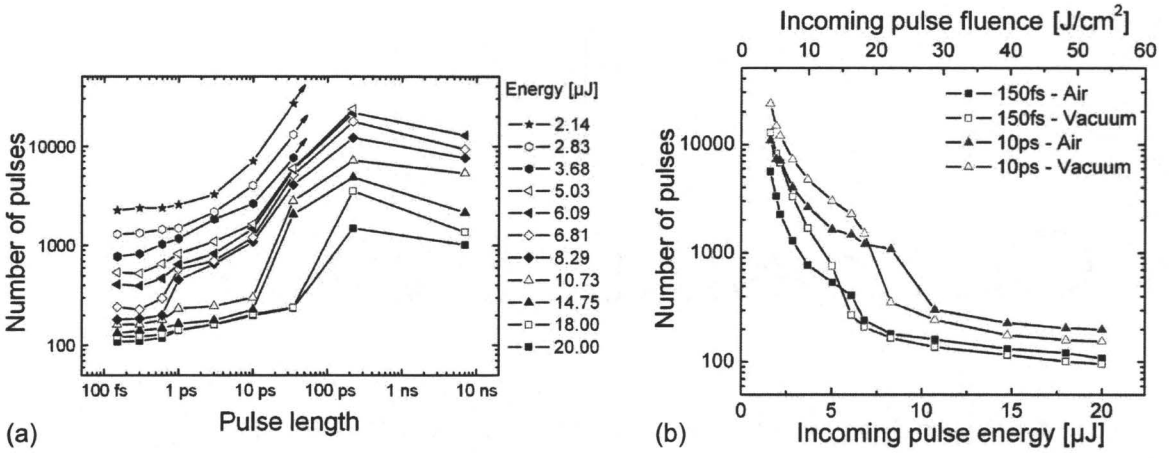

Figure 8.16: Number of pulses required for the laser to completely drill through a 100 μm thick copper foil, as a function of (a) pulse duration and energy in air, and (b) for two pulse durations in air and vacuum. These graphs are from reference [76].

diameter is no longer rapidly changing. The air atmosphere in which material irradiation occurred plays a role in this noise. Figure 8.15 shows photodiode data for 10 ps irradiation under similar conditions as the 10 ps case in figure 8.13, but with irradiation performed in a rough vacuum of less than ~100 mTorr. Comparing the air and vacuum cases, the dropout noise is absent in the vacuum case. The specific causes of the noise are uncertain, however one possibility is plasma formation. For example, Mao et al. [143, 144] for ~35 ps pulses on copper have shown evidence of plasma development in the early stages of the irradiation process, and they did not observe plasma at lower pressures. The induced air plasma was initiated by the ejection of electrons from the target surface [143] via the interaction of the light, air, and electrons. In the results presented here, the drops in signal could potentially be due to the interaction of part of the pulse with the plasma, while for sufficiently short pulses the pulse has passed before significant plasma has been generated. Sufficiently long pulses could lack the intensity required for plasma induction. More study would be required to more conclusively determine the causes of the noise drops.

The number of pulses required to completely penetrate the foil under various conditions can be easily extracted from the photodiode data by finding the data point at which a sharp rise in photodiode signal begins. Figure 8.16(a) shows this data as a function of pulse duration for various pulse energies. The data is for a permanent opening in the foil, as the 'spikes' in the 10–220 ps cases are not considered. For lower pulse energies, more pulses are required. Longer pulses also typically require the use of more pulses to penetrate the

foil. At the higher pulse energies a sharp jump in number of pulses is observed, with the jump occurring at shorter pulse durations for lower energies. The jump could be related to the causes of the spikes. For example, at 35 ps the two highest pulse energies required few pulses to penetrate, while the other pulse energies required a large number of pulses. Looking at figure 8.14(b) for 35 ps, the two highest energies did not show spikes. At 220 ps, all pulse energies showed spikes, and all pulse energies required a large number of pulses. At 10 ps, the four lowest energies required a small number of pulses, and the four lowest energies did not show spikes. It could be the case that redeposited debris in the lower pulse energy cases needs to be removed by subsequent laser pulses, and thus more pulses are required in those cases.

Figure 8.16(b) shows the number of pulses required to penetrate a copper sheet, for two pulse durations (150 fs and 10 ps) in two different drilling atmospheres (air and rough vacuum of under $\sim$100 mTorr). As in figure 8.16(a) the shorter pulse duration generally requires fewer pulses. However, it is observed that for high pulse energy, fewer pulses are required in vacuum than in air. For low pulse energies, fewer pulses are required in air atmosphere. This behavior is consistent with results reported for aluminum and stainless steel [70].

8.6 Conclusions

Substantial information was obtained from the studies on copper. Femtosecond laser drilling of metals was found to be a good method for producing model materials in the examination of ductile fracture. An increased hardness near femtosecond laser-drilled holes was measured, and annealing was shown to reduce this hardness to a level similar to the unmodified material.

Laser-induced periodic surface structures were observed along the lengths of laser-drilled holes in copper. Varying the polarization and wavelength produced results which strongly suggest that the periodic structures were formed by light interference effects. An unusual size of ripple on metal, with a period of approximately $\lambda/10$ was also observed, which is particularly interesting due to the relative lack of observations of significantly sub-λ ripples on metals in the literature.

Placing a photodiode below the target is a straightforward technique which provides a variety of data in addition to the number of pulses required for drilling through the foil under various conditions. Some results remain to be explained fully, such as the mechanism

of the signal drops ('noise') for certain pulse durations, or how the atmosphere affects the drilling rate differently for high and low pulse energies.

The morphologies of the hole walls and surface were examined as a function of pulse duration. These results can provide useful information on the time scales of various physical processes. A particularly useful result is the identification of a range of pulse durations for which the physical material changes do not vary appreciably. While femtosecond laser systems may be expensive and complicated, lasers producing short picosecond pulses could be used to provide similar results in some laser drilling applications with increased simplicity and reduced cost (see, e.g. references [145, 146]). Additionally, the increased pulse duration reduces the peak intensity, which in turn reduces the yield of x-rays which are generated in laser-material interaction [87, 88].

Chapter 9

Summary and Suggestions for Future Work

In this thesis, the effects of ultrashort laser pulses on the surface and sub-surface structure of materials were examined, with particular emphasis put on semiconductors. Two major thrusts in this work were to characterize periodic surface structures formed under a variety of irradiation conditions, and to examine the sub-surface crystallinity after short pulse irradiation. Some work was done to compare the effects of femtosecond laser pulses to those from longer pulse durations. There are still many unresolved issues however, and the experiments and results presented here serve as a good foundation for future investigations.

9.1 Summary

In the first set of experiments in this thesis, femtosecond laser pulses were used for the machining of grooves in silicon. The pulse energy, translation speed, and number of passes were systematically varied, and the effects on groove depth and morphology were measured. Both silicon and indium phosphide obeyed the same qualitative trends for depth as a function of these machining parameters, for $\lambda = 400$ nm and for $\lambda = 800$ nm irradiation, though the $\lambda = 400$ nm light generally produced narrower and deeper grooves. More scatter in the depth data was generally observed for the $\lambda = 800$ nm silicon case than for the other cases. The scatter in data points could be related to a depth modulation or corrugation which was observed along the bottom of grooves. The corrugation depended somewhat on the laser irradiation parameters, and did not appear to be related to the laser-induced periodic surface structures (LIPSS) which had periods which scaled with laser wavelength. Qualitatively similar corrugation was observed for multiple irradiation wavelengths, spot sizes, materials (silicon and germanium), and target crystalline orientations.

The laser polarization relative to the translation direction affected the cross-sectional profile of deep grooves, with similar effects for 400 and 800 nm irradiation wavelengths. Two different morphologies were observed on the walls of grooves, with a periodic pattern on the upper half and a rough appearance on the lower half. Grooves machined for non-

normal incidence angle of the laser are possible, and by appropriate target positioning V-shaped structures have been made.

On silicon, LIPSS with periods substantially less than the wavelength were observed after irradiation by hundreds of ultrashort pulses with photon energies below the bandgap energy of silicon. These ripples had a period of roughly half the laser wavelength, or were shaped like fine lines or grids of bumps with spacings of ~20–25% of the irradiation wavelength. The silicon structures did not have the same surface morphology as the high spatial frequency LIPSS (HSFL) previously reported on various III-V semiconductors for femtosecond laser irradiation below the bandgap energy of the respective material. On the III-V materials the structures had periods ~4–5 times smaller than the irradiation wavelength, and were prominent after much fewer pulses than was the case for short-period structures on silicon. On GaP, the short-period ripple formation was not strongly dependent on pulse duration, forming for durations up to several tens of picoseconds. Cross-sectional TEM of GaP HSFL showed planar-like structures with a height-to-width ratio of roughly 10, with an amorphous coating and crystalline cores having the same crystalline orientation as the substrate.

Low spatial frequency LIPSS (LSFL) were observed on Si(100), Si(111), and Ge(111) for three different irradiation wavelengths, and had periods around ~80% of the irradiation wavelength. Si(110) and Ge(100) showed a similar spacing as the other Si and Ge samples, though only $\lambda = 800$ nm was used on these targets. Silicon had a stronger tendency to form LSFL compared to germanium, which generally did not produce large regions of LSFL. GaP(100) had a LSFL spacing of around ~65–85%, with the period decreasing somewhat with increasing number of pulses. The evolution of structures with increasing number of pulses was different for silicon and GaP. On silicon, fine structures were easily eroded and would be replaced by a deep hole, while on GaP with increasing number of pulses HSFL would form readily, including on the walls of deepening holes. Structures deep within holes on semiconductors were not characterized due to the difficulty of imaging them. After irradiation with several thousand ultrashort pulses in air atmosphere, the walls of holes in copper foils developed a periodic ripple structure. The orientation of the ripples depended on the laser polarization, and the period scaled with wavelength (as $\lambda/2$), suggesting that the ripples were due to light interference effects. A small area of ripples on copper with a period of ~75 nm was observed, though the mechanism for this formation is not clear.

On GaP irradiated by circularly polarized light or for a spinning polarization, bumps were formed with similar dimensions as would be expected for the two types of LIPSS, as if LIPSS had formed at multiple angles overlapping each other. No HSFL were observed

on GaP with 400 nm irradiation wavelength, consistent with the general trend that only below-bandgap photon energies produce significantly sub-wavelength structures. Sapphire irradiated with 400 nm wavelength pulses also produced HSFL but only for a small region of the focal area and for a small range of numbers of pulses. No LSFL were observed on sapphire for $\lambda = 400$ nm.

In a preliminary experiment, $\lambda/2$ ripples, small areas of fine bump arrays, and fine lines could be produced on germanium. Under optical microscopy these resembled the significantly sub-wavelength structures observed on silicon. However, these structures were formed on Ge(111) for irradiation wavelengths above and below the germanium bandgap, with periods not strongly affected by the irradiation wavelength. This was an exception to the wavelength-dependent periods observed on other materials.

Calculations for silicon suggest that sample heating and localized heating are small for the 1 kHz laser repetition rate, and thus would not be expected to significantly affect the periodic structure formation. From calculations it is expected that increasing the repetition rate to 100 kHz would not significantly affect the processes on silicon (from thermal considerations for the same number of pulses), but the increased repetition rate would have a significant influence on materials like glass which have a much lower thermal diffusivity.

In none of the studies in this thesis on silicon and germanium did the material crystal orientation appear to affect the formation, morphology, or period of periodic structures. However, coarse structuring was observed for which the two materials with (111) surface orientations exhibited a much higher density of conical structures than the materials with (100) orientations. Examinations using cross-sectional TEM revealed a thin modified layer coating the conical structures and the LIPSS, but minimal defects near the center of a site despite irradiation by 100 pulses. Amorphous material after single-pulse irradiation of silicon was only observed on the (111) orientation, and not on the (100) or (110) orientations. Dependencies on surface crystalline orientation are important to consider when comparing the various Si(100) results in this thesis to other reported results, such as the Si(111) examined by J. Bonse. Such differences could also be relevant in defect generation, as observed in cross-sectional TEM.

Cross-sectional TEM results were obtained for ultrashort pulse irradiation of a multiple-layer target, consisting of metals on a thermally-grown oxide, on a silicon (100) substrate. Substantial defects could be produced in the silicon substrate for pulse fluences which removed the metal layer but did not visibly thin the oxide layer. Within the range of pulse fluences which could cleanly remove the metal, there appeared to be a fluence threshold above which defects would be produced in the silicon. This result is important where

femtosecond laser machining is to be used for machining of electronics, since multiple-layer structures are common. Lower fluence thresholds for the production of defects and other morphological features were observed on the multiple-layer sample when using the 400 nm irradiation wavelength, compared to the 800 nm wavelength.

Comparisons were made between the multiple-layer sample and an uncoated silicon target. Notably, for a single pulse which produced substantial defects on the multiple-layer sample, no defects were present on the silicon-only sample after irradiation by a single pulse of similar fluence. This suggested that the overlying layer significantly affects the material evolution. Amorphous material was directly observed by cross-sectional TEM after femtosecond pulse irradiation of (non-multilayer) silicon for various pulse conditions. Amorphous material was found only near the rims of the craters, while defects were predominantly near the centers. For single-pulse irradiation, no amorphous material was present for the lowest and highest pulse fluence sites, but was present for a moderate fluence site. It should be noted that the moderate and high fluence sites had fluences substantially above those typically used in the other experiments presented in this thesis. Substantial defects were present for the highest-fluence single-pulse case, however it was found that multiple pulse irradiation at a given per-pulse fluence damages silicon more readily than single pulse irradiation at a higher fluence. For example, five-pulse irradiation at a particular fluence produced defects while a single pulse at roughly ten times the fluence did not produce defective material.

Femtosecond laser machining has been shown to be capable of making a 'model material' for ductile fracture experiments. Material near laser-drilled holes in metals had a higher hardness than the material far from the holes, however subsequent annealing after irradiation reduced the hardness to that of the original material. Measuring light penetration using a large area photodiode below a copper foil gave information such as the number of pulses required to penetrate the foil under various conditions. For low pulse energies, penetration of a foil occurred more quickly for irradiation in air, while for high pulse energies, penetration was quicker in vacuum.

For the machining of holes in copper foils several observations were made as a function of pulse duration, namely the amount of laser light transmitted through the hole while drilling, the morphology of the walls of the hole, and the surface surrounding the entrance of the hole. These all suggested a change in the material modification phenomena for pulse durations between 10 and 35 picoseconds. Below these pulse durations, changing the pulse duration did not have a major effect. The change in material evolution at these pulse durations is expected to be related to the electron-phonon relaxation, which occurs

on a similar time scale. Ripples on hole walls were not observed for pulse durations longer than a few tens of picoseconds, for low numbers of pulses, or for irradiation in a vacuum atmosphere. A more molten appearance with large nonperiodic structure was observed for lower number of pulses and for longer pulse durations. Longer pulse durations and lower pulse energies required higher numbers of pulses to penetrate the foil. A major conclusion is that lasers producing short picosecond pulses could give as good results for machining applications as femtosecond lasers, but without the higher complexity, cost, higher x-ray yield and potential undesired nonlinear effects associated with femtosecond systems.

9.2 Suggestions for future work

With the diversity of experimental possibilities in femtosecond laser irradiation of materials, there remains a wide variety of experiments which could be performed. The following subsections outline some logical extensions of the work already done, in particular, experiments which could help expand our understanding of the underlying phenomena of various laser-material interactions. Preliminary experiments have already been performed for many of the cases, and further experiments would expand upon the body of research presented in this thesis. Most of these possibilities would be implementable using the equipment and facilities available at McMaster. Some of these investigations are discussed in more detail in the thesis chapters where the relevant experimental results were presented.

9.2.1 Multiple-layer and buried layer studies

In contrast to irradiation of homogeneous targets, irradiation of materials incorporating multiple layers is a rather unexplored area of research. Carefully chosen configurations can be used to examine specific aspects of the irradiation process and material evolution. In the cross-sectional TEM results presented in this thesis, it is unknown how much of the material was molten and simply recrystallized epitaxially on the substrate since such material is indistinguishable from the unmodified crystal substrate. A useful experiment to identify the extent of the molten material would be to have one or more thin layers of material of a different chemical composition within the target. Similar configurations have been epitaxially grown on a substrate by molecular beam epitaxy at McMaster for diode laser substrates (see, e.g. reference [147]). A buried layer several nanometres thick would be thick enough to be easily observable in cross-sectional TEM, particularly if it had a higher average atomic number than the surrounding material. If the molten material were

to reach a buried layer, the materials would mix and a sharply-defined buried layer would no longer be observed under TEM. On GaP, HSFL were found to have crystalline cores. If the buried layer was observed within the ripple cores, this would indicate that the crystalline cores had never melted. Presumably, such an experiment would require that the bandgaps of the substrate and layer were both greater than the incident photon energy. In the case of the blunt conical structures, the additional layer would tell if epitaxial regrowth or selective material removal are the cause of the structures. Experiments would need to confirm that a buried layer does not significantly affect the material modification. Conceivably, a layer with the same elemental composition as the surrounding material but containing a different isotope would not affect structure formation, but the preparation and analysis of such a sample could be particularly challenging.

Thin metal films irradiated by laser pulses behave differently than the bulk metal (see, e.g. references [79, 135]). Semiconductor films warrant examination, particularly in the study of periodic structure formation where the film thickness approaches the dimensions of the structures. For example, an attempt should be made to produce fine periodic structures on a thin transparent semiconductor layer on a thicker opaque layer or an insulating layer. This would help identify if the ripple formation mechanism is a surface effect (perhaps similar to that suggested by Kautek et al. [148]), a bulk phenomenon (such as in the nanoplasmonics model suggested by Bhardwaj et al. [62]), or due to thermal effects. Silicon-on-insulator, which consists of a silicon substrate, an oxide layer, and a thin silicon top layer, would be a convenient target for examining the role of thermal effects. In my thermal diffusion simulations (see appendix A), reducing the silicon thickness to 300 μm did not have a significant effect on heat diffusion. The use of a much thinner silicon layer (or a thin silicon wafer) would cause more heat confinement, and thus would be expected to affect the amorphization and possibly the structure formation. Simulations have shown that pressure wave propagation, and thus potentially the formation of defects, is affected by film thickness [23].

While the ability to selectively remove metal from a dielectric has been demonstrated (see section 7.3.2 and the M.A.Sc. thesis of E.M. Hsu [106]), the ability to selectively remove metals from silicon could be useful from an industrial point of view, particularly if the silicon is not damaged. As described in further detail in chapter 7, different thicknesses of metal and oxide material, and different metal compositions, could provide insight into the role of the speed of electron-phonon coupling, pressure wave generation and propagation, and thermal expansion mismatch. Varying the pulse duration would affect the pulse intensity, and would be expected to affect the degree of defect formation. For oxide-on-silicon

samples without an original metal layer, examination of the underlying silicon for pulse fluences which did not damage the oxide would be interesting, particularly in comparison to cases in this thesis where metal was removed but the oxide remained. However, a technique would be needed to accurately locate the laser irradiation sites for later examination, since the oxide would not have been visibly modified. Finally, silicon and germanium with their native oxides removed prior to irradiation would indicate what role the native oxide plays, if any, particularly for fine ripple and shallow structure formation.

9.2.2 Comparisons of group-IV materials

As shown in this thesis, different materials can behave differently under similar femtosecond laser irradiation conditions. Insight could be provided by comparing materials and conditions specifically chosen to emphasize particular characteristics. Although germanium has been used in some of the experiments presented in this thesis, there is still much to be explored on germanium. As discussed in chapter 5, preliminary experiments indicated that germanium does not demonstrate the same trend for significantly sub-wavelength period formation as other semiconductors (specifically, the need for below-bandgap photon energy). More carefully prepared samples and the use of detailed surface analysis techniques (AFM, TEM, etc.) could yield valuable information. It could be the case that fine germanium structures have a different morphology than those on silicon, but they look similar under the limited resolution of optical microscopy. The different oxidation properties of germanium compared to silicon could play a role in the germanium structure formation. The chemical composition of small structures on germanium and silicon could be examined, as the structures were very shallow and could contain significant oxide composition. During laser irradiation the use of a different ambient gas, particularly a noble gas, could indicate the role of oxidation or other chemical modification in the silicon and germanium work.

It is not known if $\lambda = 400$ nm irradiation of germanium would produce the same type of structures as formed other wavelengths, although substantially sub-wavelength periodic structures on silicon would be unexpected for this wavelength. As the (linear) optical penetration depth of 400 nm wavelength light is less than at 800 nm, a different extent of amorphization and defect generation may be produced. These could be checked using cross-sectional TEM. Since the morphologies of silicon and germanium differ from those on GaP, the morphologies might arise from different phenomena, and thus it is not clear if they would obey the same pulse duration-dependent trends. Pulse stretching of OPA

wavelength pulses would allow the investigation of the trend. Translating a GaP target under a focussed laser beam produced short-period structures extending coherently along the irradiation path. More systematic work on silicon and germanium could indicate the role of irradiation site morphology on periodic structure production, for example, translation of the target to determine if the $\lambda/2$ structures rely on scattering from the crater walls.

A variety of experiments were performed on silicon, such as the characterization of groove cutting rates, and examination of crystalline damage under the surface of single- and multiple-pulse irradiation sites. While these results were compared to those from InP studies, these experiments could also be performed on germanium, diamond, and other materials. This would allow a comparison of different material types with regards to amorphization and defect generation, as well as being a useful characterization for industrial applications. Different densities, hardnesses, and crystal orientations could significantly affect defect generation. While preliminary work on graphite surface features has been presented, examination of the crystallographic changes within graphite would be informative. Work has begun on electron microscopy examinations of diamond irradiated by femtosecond laser pulses, with HSFL observed in preliminary tests. Alloys of multiple group-IV materials, like SiC and $Si_{1-x}Ge_x$, also have various industrial applications, with some work reported for ripple formation on SiC (see, e.g. reference [148]). A requirement of below-bandgap photon energy has been recently observed for ZnSe [61], and work on other II-VI materials would indicate to what extent the short period structuring is a 'universal' phenomenon.

9.2.3 Bulk modification

In contrast to the machining of parallel lines on silicon-on-insulator for production of a rib waveguide (discussed in section 4.10), a waveguide for telecom wavelengths has been produced by focussing $\lambda \approx 2400$ nm pulses below the surface of silicon coated by a thermally-grown oxide [81]. This waveguiding was not due to removal of surface material. Bhardwaj and co-workers have reported the formation of parallel planes within glass for femtosecond pulses focussed into the bulk material [62]. The possibility of periodic material modification in the bulk material below the periodic surface structures on semiconductors should be considered. The features reported here on GaP, which resembled planes extending into the bulk material, could have a similar origin. Recent work has begun in the lab with focussed ion beam milling and electron microscopy examination of dielectrics, for which the laser pulses have been focussed within the bulk. This has revealed

parallel planes in crystal quartz. Similar studies are also possible for semiconductors, both for pulses focussed within the bulk, and for any modifications extending below a modified surface.

9.2.4 Focussed ion beam milling and cross-sectional TEM investigations

There are many possibilities for further research using FIB milling and cross-sectional TEM, and these experiments would build upon a substantial body of prior work in the group. J. Bonse has performed studies of Si(111) using spatially resolved reflectivity at multiple wavelengths [33, 34] and micro-Raman studies [33] to estimate the thickness of the amorphous layer on a single-pulse site. However, these are indirect techniques for determining the thickness. Cross-sectional TEM of a FIB-prepared site under these conditions would provide a useful point for comparison. Minimal TEM studies of germanium have been reported in the literature, although Bonse et al. [14] have not observed amorphization on Ge(100) using surface reflectivity measurements. While most of the TEM work in this thesis is on material with a (100) surface orientation, cross-sectional TEM of sites on other material crystal orientations would be useful for providing a direct comparison of similar fluences. For example, it would directly reveal the depth of amorphization on Si(111). With cross-sectional TEM, minimal defects were observed on Si(100) and Si(111) for 100-pulse sites. However, for all TEM examinations in this thesis, silicon samples irradiated by a low number of pulses had a (100) surface orientation. In these (100)-oriented cases dislocations tended to lie on the $\{111\}$ plane. Irradiation of silicon with a different surface crystalline orientation could be expected to produce different dislocation morphology, and is worthy of further investigation.

A FIB-prepared cross-sectional sample of the fine bump arrays on silicon was prepared. Unfortunately, the exact position and orientation of the cross-section on the irradiation site is unknown, and the metal protective layer may have been masking some features, so only some very general conclusions could be drawn. To gain a better understanding, additional ripple sites should be prepared and imaged under TEM, with the locations carefully chosen and characterized. Care would need to be taken to ensure that a FIB slice is taken from an accurately known location, through the structures of interest. Since structure formation is affected by the irradiation wavelength, sub-surface structuring and modification may also sensitive to wavelength. Further experiments with TEM analysis would reveal such differences, since the majority of TEM investigations presented in this thesis were for $\lambda = 800$ nm irradiation. It would be illustrative to do cross-sectional TEM on the cor-

rugation structures which formed in the centers of multiple-pass grooves on silicon. This could help identify their origin, and could be compared to the cross-sectional results of large conical structures found from stationary irradiation sites.

A tripod polishing technique was successfully employed for examining cross-sections of grooves in silicon. It is a promising technique which should also be considered for the inexpensive, simultaneous preparation of TEM samples containing many different irradiation conditions on the same sample. Even as a tool for preliminary examination, it could be used to identify laser conditions worthy of further examination via other techniques. The sub-surface evolution of crystallographic changes could be observed as a function of number of pulses, in particular to examine the role of defects in the incubation phenomena with fluences near the material modification threshold. This would require several FIB samples to be prepared, each for a different number of laser pulses. However, various 'effective' numbers of pulses are attainable by translating the sample. This could be used with the tripod polishing technique as a simple way to examine defects as a function of number of pulses.

Focussed ion beam milling allows the very precise removal of small quantities of material, and is not solely a preparation technique for TEM samples. As material removal rates in FIB are typically low, material removal using a femtosecond pulse laser could be useful as an alternative to FIB milling in cases where moderate amounts of material are to be removed. The technique could be used in conjunction with FIB milling, in which the laser removes a large volume and the FIB does final finishing of the surface. Alternately, the precision of FIB milling could be used to mill shallow depressions or other patterns for pre-patterning of targets before laser irradiation. Pre-patterning would give insight into the ripple formation origins. On graphite, flake edges were shown in this thesis to affect LSFL formation, and other forms of pre-patterning have been previously reported to affect ripple formation. If short-period structures like HSFL were to form parallel to a scratch, this could suggest light interference plays an important role, although it is possible the scratch would seed other phenomena. In experiments on polycrystalline materials, irradiation near grain boundaries should be checked for the possibility that these affect material evolution.

9.2.5 Deep hole drilling, and comparisons involving metals

While much of the work in this thesis was on semiconductors, the examinations of metals allow for comparisons between substantially different materials. In the drilling of deep holes in copper sheets, it was argued that the nature of material modification changes at a

pulse length near the electron-phonon relaxation time. Similar work could be done to compare materials with significantly different electron-phonon relaxation times, for example, nickel and gold [23]. In the drilling of deep holes on copper, some ripples with a period of ~75 nm were observed near the entrance of a particular site. More microtomy or hole wall imaging may reveal previously unobserved structures.

In some cases periodic structuring or roughness on the walls of holes or grooves may be undesirable. While FIB milling may be used to produce smoother features, it may be possible to reduce the roughness using appropriate laser parameters or scanning approaches. No attempt was made to decrease the roughness of laser-machined features in this thesis. Certain features could not be imaged with atomic force microscopy, due to the geometry of the sample and AFM tip. However, in a preliminary experiment a polymer was deposited on silicon regions raster-scanned with the laser, and subsequent removal of the polymer provided an inverse replica of the machined area. It was proposed that polymer could be examined by AFM to measure the roughness, particularly in cases where the geometry of the sample and AFM tip prevent direct AFM imaging of the original surface.

9.2.6 Additional pulse parameters to investigate

Investigation of irradiation by double or multiple pulses closely separated in time would be a valuable topic for further study. E.M. Hsu did preliminary experiments on silicon using two pulses temporally separated using a Michelson interferometer [106]. Two pulses of approximately equal energy separated by a few hundred picoseconds produced a more uneven 'splash' appearance near the rim, compared to pulses separated by under a few tens of picoseconds, a single pulse, and two pulses separated by 1 ms. However, some aspects of the experiment, such as the spatial overlap, should be technically improved. More detailed experiments are possible, for example by extending the range of delays used, adjusting the ratio of pulse energies between the first and second pulses, and by using two pulses of different wavelengths. The effect of a secondary weak pulse would be particularly worthy of investigation, as the regenerative amplifier and certain optics produce weak secondary pulses. Care would need to be taken in the experiments, as the weak pulses may be difficult to characterize and the effects may not be immediately obvious. From time-resolved reflectivity experiments on InP, J. Bonse has observed that the weak post-pulse from a regenerative amplifier can cause a sudden decrease in reflectivity when it interacts with the evolving material, however germanium seemed much less sensitive to the post-pulse [149]. When varying the ratio of pulse energies in 400 nm and 800 nm wavelengths simultane-

ously incident on ZnSe, Jia et al. [61] found the direction of periodic structures was affected by the ratio. Similar experiments, particularly with a time delay between pulses, would be useful for the examination of ripple formation conditions on other materials. With the photon energies of the two pulses on either side of the bandgap energy for example, it could be the case that one pulse seeds a period which is enhanced by the other pulse, while a single pulse would not otherwise have sufficient pulse energy to produce structuring.

Various other pulse parameters, such as the amount of pulse front tilt, pulse duration, spatial profile, and spot size could be varied in examinations of laser-material interaction. For example, a much larger spot size could be used to machine much deeper grooves, since less shielding of the light by the walls of the grooves is expected. Wider grooves are shown in chapter 6, and while some coarse corrugation along the length of the groove was observed in certain cases, it might be avoided more easily with wider grooves. A sufficiently small spot size would be expected to affect the heat dissipation and anisotropy of pressure wave propagation [23], having a more 3D-like character than a 2D-like character. This could affect amorphization and formation of defects. A Bessel-shaped beam, which can maintain a small transverse size over long propagation distances, has been used to produce linear features in dielectrics along the direction of laser propagation [150]. This and other beam profiles could be explored as an option for semiconductor and metal machining. Based on work by A. Borowiec on InP [44], different pulse durations would be expected to produce substantial differences in the sub-surface crystallinity. Longer pulse durations would be expected to produce a weaker pressure wave, which would affect defect generation, and a longer duration would also be expected to produce more melting.

Varying the angle of incidence was used in the machining of grooves and showed promise for larger-quantity material removal and cantilever fabrication. For an increased understanding of the physical mechanisms of laser-material interaction, irradiation of stationary targets at various angles of incidence would be valuable in the examination of blunt cone formation and periodic structure formation. The origins of HSFL on compound materials and fine structures on silicon and germanium are currently unknown, however a dependence on laser incident angle would strongly suggest light interference effects as part of the cause. Due to the design of the vacuum chamber in use at the time, angled irradiation in a vacuum atmosphere was not possible, although it is possible with the current chamber.

No clear explanation for the substantially sub-wavelength ripple periods and their orientation has been found which explains the necessary irradiation conditions. More theoretical analyses, such as incorporating nonlinear phenomena into the theory of Sipe et al. [54], or exploration of the nanoplasmonic model presented by Bhardwaj et al. [62], would be use-

ful. The optical properties of the material are expected to change due to significant electron excitation by the pulse, and this could play a role in various theories. The relative lack of reports of short-period structures on metals deserves consideration as part of proposed theories. Additionally, throughout this research and in a large number of published reports on various materials, the periods of LSFL after ultrashort pulse irradiation were found to be somewhat shorter than the wavelength of the laser light. This also warrants further examination.

9.2.7 Materials analysis from adaptations of the machining apparatus

In addition to being an apparatus for material modification, the laser machining equipment used in this work could be used to provide various materials analysis possibilities. In an experiment performed by Florent Lefevre-Schlick, Ognian Marinov, and myself, we measured the transient change in resistivity of a thin platinum film irradiated by a single 800 nm laser pulse. The results are described in the Ph.D thesis of F. Lefevre-Schlick. The devices and associated electronics are available to be used for shorter pulse experiments.

Work by A. Borowiec in collaboration with D.M. Bruce and D.T. Cassidy (see reference [48]) produced a map of the photoluminescence of InP on the cleaved facet around a laser-machined groove. Analysis of the polarization of the photoluminescence gave a measurement of strains and stresses, and suggested the presence of defects [44]. While a red HeNe laser was used in reference [48] to produce photoluminescence, in preliminary work by A. Shiner with the $\lambda = 800$ nm mode-locked oscillator a photoluminescence signal was obtained on zinc sulfide. The laser irradiation apparatus in which my samples were machined could be easily converted into a spatially-resolved two-photon photoluminescence mapper with minimal extra components. Additionally, while the photoluminescence from indirect bandgap materials such as silicon and germanium is weak, the high peak intensities of femtosecond pulses however might be able to produce sufficient photoluminescence for mapping. Porous or ion-implanted silicon from recent silicon photonics research at McMaster could be examined. With slight modification, a reflectivity microscope could easily be achieved with essentially the same setup. Rather than the photoluminescence signal, the power of the reflected beam would be recorded. A similar setup was used by J. Bonse [33, 34] to obtain a map of the reflectivity of a sample surface at different wavelengths, allowing determination of the depth profile of amorphous material on silicon.

9.3 Concluding remarks

Femtosecond laser pulses can be used for a variety of scientific and technological applications. The application presented here was the modification of semiconductors and metals, with particular emphasis on silicon and copper. A variety of analysis techniques were used to examine the surface morphology and sub-surface crystallinity after irradiation. The experiments presented in this thesis serve as a good foundation for future research in the field of ultrashort pulse laser-material interaction. However, for the scientific and industrial community further research will prove valuable. Additional experiments, irradiation configurations, and analysis techniques along with additional theoretical work would lead to a more complete understanding of the underlying physical phenomena.

Appendix A

Thermal Calculations and Discussion

A sample will be heated by incident laser pulses. It is possible that structure formation or other material modification processes are affected by a temperature increase due to the accumulation of heat from previous laser pulses. Properties such as the specific heat capacity and thermal diffusivity vary somewhat with temperature. As such, it is possible that heating by one pulse will produce a material with different thermal properties at the time the next pulse is incident. This is separate from the changes in surface area and morphology, chemical composition, and crystallographic conditions. In this appendix an estimate is made of the temperature increases in short pulse laser irradiation, to determine if these would be expected to significantly affect the material properties. Two cases are presented. In the first case, the energy input to the sample from the laser is assumed to dissipate throughout the sample, uniformly raising the temperature of the entire sample. In the second case, local heating at the irradiation site is considered, using equations for heat conduction.

A.1 Whole-sample heating

The quantity $\mathcal{Q}$ of energy transferred to a material of mass m and specific heat capacity c as it undergoes a temperature change ΔT is given by

$$\mathcal{Q} = mc\Delta T \tag{A.1}$$

provided the material does not undergo a phase change, and assuming the heat capacity is constant. Using equation A.1, the temperature increase of a sample irradiated by laser pulses can be estimated. In this calculation, the input energy is distributed evenly throughout the sample. As a worst-case scenario, it will be assumed that all this energy was absorbed by the sample to produce heating, and that no energy was lost to reflection, material removal, radiation, conduction to the sample holder or atmosphere, or other processes such as phase changes. At a temperature of 300 K, crystalline silicon has a density $\rho = 2.32$ g/cm^3, specific heat $c = 0.71$ J/gK, and thermal diffusivity $D = 0.85$ cm^2/s (see

appendix C in reference [1]). In a typical single-shot run consisting of a single pulse irradiation at each of the energies obtained from the neutral density filter set, starting with a maximum pulse energy of 10 μJ at an OD of 0.0, a total laser energy of approximately 50 μJ per run was used. These energies were typical of runs using a 12.5 or 15.0 cm focal length lens. Experiments using the 5× microscope objective generally used less energy due to the smaller spot size and thus higher fluence for the same pulse energy. In an experiment for the observation of sub-wavelength ripples and structures, the equivalent of approximately 20 000 single-shot runs was used per sample. This is the summation of runs consisting of 10, 25, 50, 100, 200, 350, 500, 650, 750, 850, 1000, 2000, 5000, and 10 000 pulses per hole. This results in approximately one joule of incident energy per sample. Given the approximate dimensions of a sample (300 μm thick and several mm per lateral dimension in the case of the ripples experiments), the maximum possible temperature increase of the whole sample is estimated to be approximately 30–50 K. This suggests that overall heating of the sample is not likely to have changed the material properties appreciably during the course of the experiment.

A.2 Local heating

Local heating occurs due to the finite time required for heat at the irradiation site to diffuse. A higher pulse repetition rate will mean less time for heat diffusion before another pulse is incident on the sample. This repetition-rate effect has been reported for the femtosecond irradiation of dielectrics [151, 152].

A.2.1 Equations

For an instantaneous point source of heat at time $t = 0$, the temperature increase T is given by [1, 153]:

$$T = \frac{Q}{8(\pi D t)^{3/2}} \mathrm{e}^{-r^2/4Dt} \tag{A.2}$$

where r is the distance from the point source. The 'strength' Q of the source (units of $\mathrm{K{\cdot}m^3}$) is considered to be "the temperature to which the amount of heat liberated would raise unit volume of the substance" [153], and thus the energy liberated is ρc times the strength of the source. Equation A.2 describes three-dimensional heat flow in an infinite, isotropic medium, assuming ρ, c, and D are all independent of temperature and direction. The 'characteristic' heat diffusion length ℓ_T, which defines the $1/\mathrm{e}$ spatial decay distance,

is $\ell_T = 2\sqrt{Dt}$. For room temperature silicon, after 1 ms (the time between pulses when the laser regenerative amplifier is operating at its usual repetition rate of 1 kHz), $\ell_T \approx 580$ μm.

Equation A.2 can be used to derive equations describing heat diffusion from various shapes of sources. The temperature increase for an instantaneous disk-shaped source of heat for a disk radius a with the disk in the plane $z = 0$ can be derived. The instantaneous point in time at which heat is released is at $t = 0$. The z axis extends perpendicular to the surface of the material, with $z = 0$ at the material surface. A strength of $qr'dr'd\theta'$ is used in equation A.2, and the equation is integrated for $\theta' = 0$ to 2π, and $r' = 0$ to a. The mathematics is simplified by restricting the points of interest to those lying on the z axis. The temperature T on the z-axis at a distance z from the origin is then given by [153]:

$$T = \frac{q}{2(\pi Dt)^{1/2}}\left[1 - e^{-a^2/4Dt}\right]e^{-z^2/4Dt} \tag{A.3}$$

where $q\pi a^2 \rho c$ units of heat are liberated (the source strength is equivalently $q\pi a^2$ after integration). Equation A.3 is for an infinite solid. When the disk radius a is small compared to $\ell_T = 2\sqrt{Dt}$ (i.e. for small disks or after a long time), this approaches the equation for temperature due to an instantaneous point source of heat (equation A.2).

Using a similar approach, I have derived an equation for temperature increase with an instantaneous Gaussian-shaped source at time $t = 0$, Gaussian $1/e^2$ radius $\omega_\circ$, and for the two-dimensional Gaussian in the plane $z = 0$. A strength $qe^{-2r'^2/\omega_\circ^2}r'dr'd\theta'$ is used, and the integration of equation A.2 is for $\theta' = 0$ to 2π and $r' = 0$ to $+\infty$. The resulting temperature equation is:

$$T = \frac{q}{2(\pi Dt)^{1/2}}\left[\frac{1}{1 + 8Dt/\omega_\circ^2}\right]e^{-z^2/4Dt} \tag{A.4}$$

where $(q\pi\omega_\circ^2/2)\rho c$ units of heat are liberated (the source strength is equivalently $q\pi\omega_\circ^2/2$ after integration). When $\omega_\circ$ is small compared to $\ell_T = 2\sqrt{Dt}$, equation A.4 approaches the equation for the instantaneous point source (equation A.2).

The previous equations were for sources of heat within an infinite solid, however laser irradiation in this work typically occurs on the surface of a substrate. If there are planes at $z = 0$ and $z = \ell$ and no heat flow can occur across these planes, the equation for temperature increase due to an instantaneous point source at the origin is [153]:

$$T = \frac{Q}{8(\pi Dt)^{3/2}}e^{-(x^2+y^2)/4Dt} \times 2\sum_{n=-\infty}^{\infty} e^{-(2n\ell - z)^2/4Dt}. \tag{A.5}$$

For the point $(x,y,z) = (0,0,0)$, this reduces to equation A.2 but with a multiplicative factor $2\sum e^{-n^2\ell^2/Dt}$. When $\ell \gg \sqrt{Dt}$ with $z = 0$ (approximating a point on a surface, when the surface is infinite in the $\pm x$ and $\pm y$ directions, and infinite in the $+z$ direction), the sum is approximately equal to one, and equation A.5 approaches $2\times$ equation A.2.

A.2.2 Calculations

These calculations are intended to be a simple first-order estimate, to determine if more detailed studies are warranted. The equations in the previous section can be used to estimate the increase in temperature at the center of the irradiation site due to a single laser pulse. As with the case of whole-sample heating (see section A.1), the 'worst-case' scenario of the entire pulse energy converting solely into heat will be assumed in these calculations, as well as assuming the material properties are constant. Additionally, the instantaneous point, disk, and Gaussian equations can be compared, to determine if the source shape plays a major role in the temperature evolution for the given parameters.

As a representative example, I used a pulse energy of 5 μJ with a disk radius a of 20 μm and a Gaussian radius $\omega_\circ$ of 20 μm. The differences in temperatures for a time $t = 1$ ms after the pulse at the center of the irradiation site ($z = 0$) are very small: 2.7497, 2.7481, and 2.7481 mK respectively for the point, disk, and Gaussian sources (equations A.2, A.3, and A.4). Thus, for the material properties of silicon given and the 1 ms time frame, the differences in the three models are negligible.

Equations A.2, A.3, and A.4 are plotted in figure A.1 as a function of time (for the point of interest at $z = 0$), and as a function of distance along the z-axis from the center of the heat source (at a time $t = 1$ ms). These calculations used a disk radius and Gaussian $1/e^2$ radius of 20 μm, and the results from the three equations differ very slightly. When a much larger disk and Gaussian radius (300 μm) are used, the difference is larger. This case is shown in figure A.2. The temperatures at $z = 0$, $t = 1$ ms are 2.7497 mK, 2.4158 mK, and 2.4283 mK for the point, disk, and Gaussian sources respectively. It is logical that the larger sources would produce a lower temperature, as more energy is deposited in the xy plane away from $(x,y) = (0,0)$. At larger distances along the z-axis, the difference between the three source shapes becomes small.

Temperature distributions from instantaneous point, disk, and Gaussian sources on silicon can be compared to other materials, such as glass (a-SiO_2). The thermal diffusivity of glass is roughly two orders of magnitude less than that of silicon, and so heat accumulation will be a more significant issue for glass. For glass (a-SiO_2), $D = 0.009$ cm^2/s,

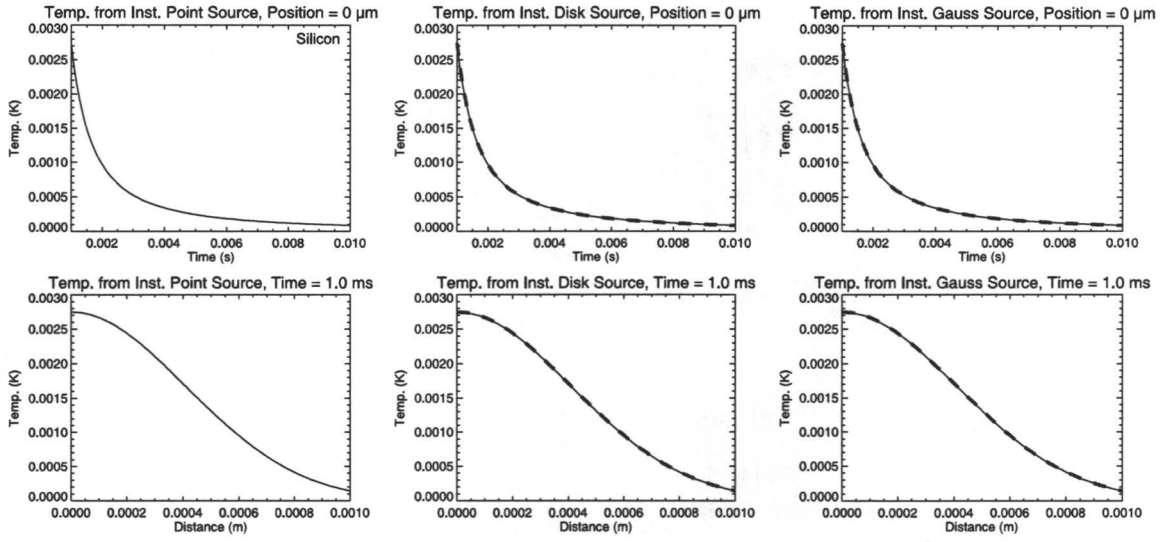

Figure A.1: Temperature evolution for silicon, assuming material properties of $T = 300$ K silicon, for instantaneous point, disk ($a = 20$ μm), and Gaussian ($\omega_\circ = 20$ μm) sources (*left*, *center*, and *right* respectively). The top row shows the temperature at the center of the site as a function of time, while the bottom row shows temperature as a function of depth, 1 ms after the pulse. The dashed line on the disk and Gaussian plots is of the point source calculation, for comparison.

$\rho = 2.2$ g/cm^2, and $c = 0.72$ J/gK [1]. Figure A.3 shows the temperature distribution for the same time and distance ranges shown in figure A.1. The temperature at $z = 0$ for a time 1 ms after the pulse is calculated to be 2.624 K for the point source, and 2.484 K and 2.486 K for the disk and Gaussian sources, all much higher than for the silicon case. As would be expected, the temperature at $t = 1$ ms drops much more rapidly as a function of depth than for silicon.

As a representative example of a pulse incident on the surface of a bounded material (planes at $z = 0$ and $z = 300$ μm, approximating a 300 μm thick silicon wafer), I use a pulse of energy 5 μJ and treat the pulse as an instantaneous point source. Based on these rough approximations and equation A.5, the temperature increase 1 ms after a single pulse is approximately 9.5 mK at the position $z = 0$. Two and three milliseconds after a single pulse, the temperature increase is 4.7 mK and 3.2 mK respectively. Figure A.4 shows the temperature evolution with time and depth. As noted earlier, a material infinite only in the $+z$ direction (using equation A.5) would be expected to have a temperature distribution $2\times$ that of a material infinite in both $\pm z$ directions (using equation A.2). To aid in the comparison, the dashed line in figure A.4 shows $2\times$ equation A.2. The dotted line shows

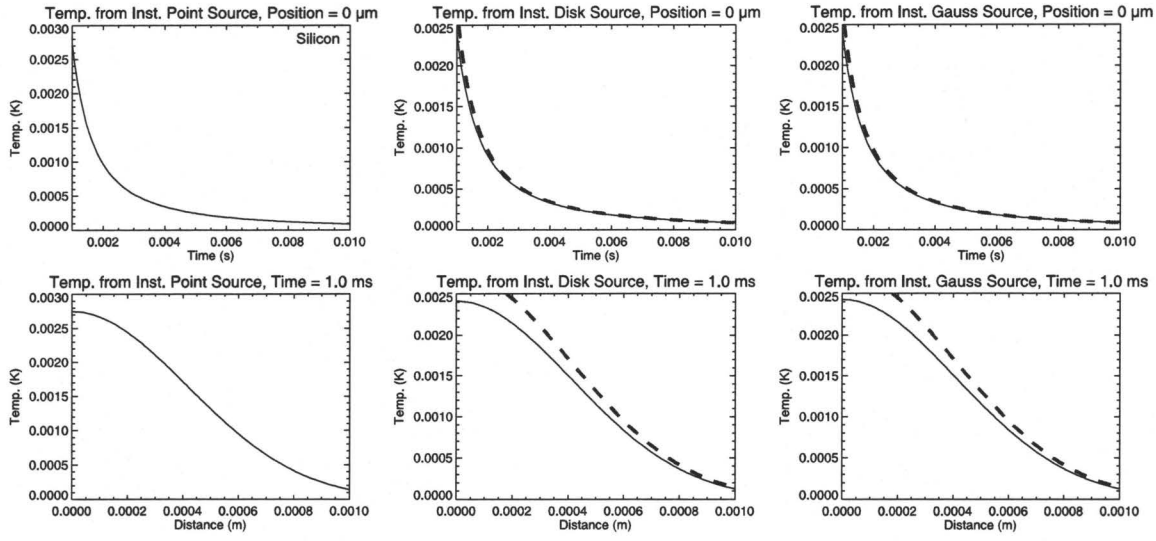

Figure A.2: Temperature evolution for silicon, assuming material properties of $T = 300$ K silicon, for instantaneous point, disk ($a = 300$ μm), and Gaussian ($\omega_o = 300$ μm) sources (*left*, *center*, and *right* respectively). The top row shows the temperature at the center of the site as a function of time, while the bottom row shows temperature as a function of depth, 1 ms after the pulse. The dashed line on the disk and Gaussian plots is of the point source calculation, for comparison.

equation A.2 unmodified, while the solid line shows equation A.5. For 300 μm thick silicon after 1 ms, a significant difference can be seen between the bounded and 2× unbounded case: the bounded and 2× unbounded cases differ by a factor of approximately 1.7, equal to the sum in equation A.5. The condition $\ell \gg \sqrt{Dt}$ mentioned earlier is not satisfied, since for an $\ell \approx 300$ μm thick silicon wafer at room temperature after 1 ms, $\ell \approx \sqrt{Dt}$.

The same calculation for a 300 μm thick glass sample however (figure A.5) shows minimal difference between the bounded case and 2× the unbounded case. It can be seen that after 1 ms, the temperature at 300 μm into the material is nearly unchanged, i.e. the heat has not yet reached that location. Thus, it is not surprising that the two models give nearly the same result. In additional calculations, it was observed that as the temperature at 300 μm begins to rise, equation A.5 begins to deviate from 2× equation A.2.

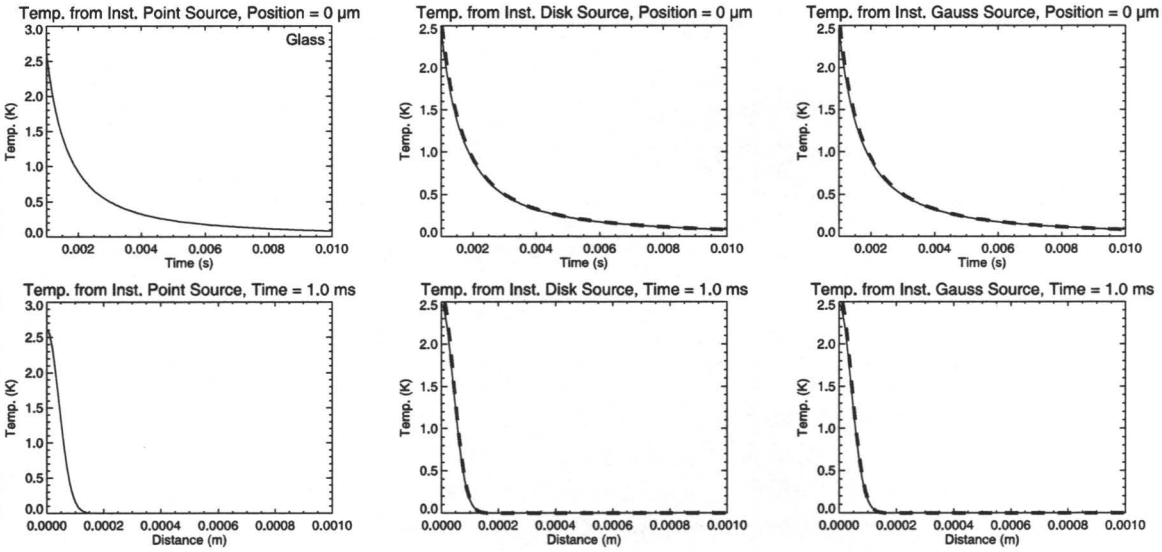

Figure A.3: Temperature evolution for glass (a-SiO_2), assuming material properties of $T =$ 300 K glass, for instantaneous point, disk ($a = 20$ μm), and Gaussian ($\omega_o = 20$ μm) sources (*left*, *center*, and *right* respectively). The top row shows the temperature at the center of the site as a function of time, while the bottom row shows temperature as a function of depth, 1 ms after the pulse. The dashed line on the disk and Gaussian plots is of the point source calculation, for comparison.

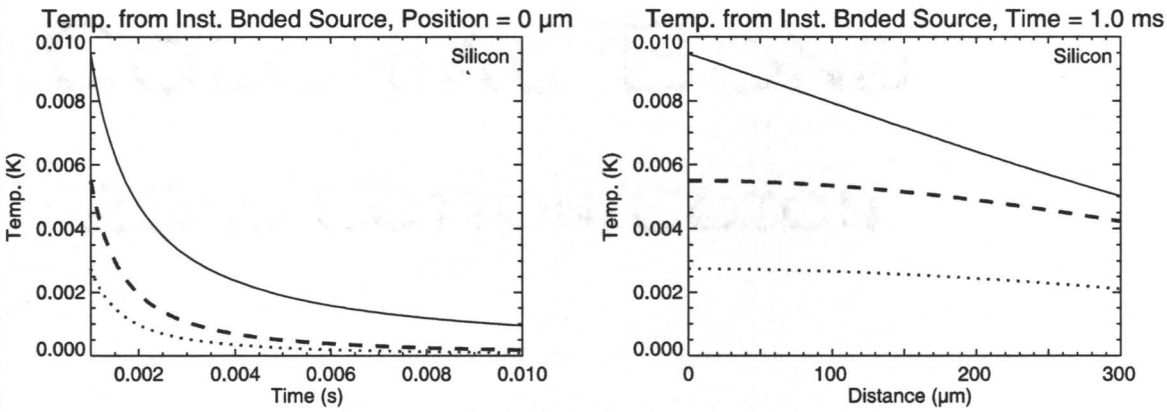

Figure A.4: Temperature distribution for silicon, assuming material properties of $T =$ 300 K silicon, for an unbounded (infinite material) and bounded (300 μm thick material) instantaneous point source, as a function of time (at $z = 0$) and depth (at $t = 1$ ms). The solid line indicates the bounded calculation, the dotted line indicates the unbounded calculation, and the dashed line indicates $2\times$ the unbounded calculation.

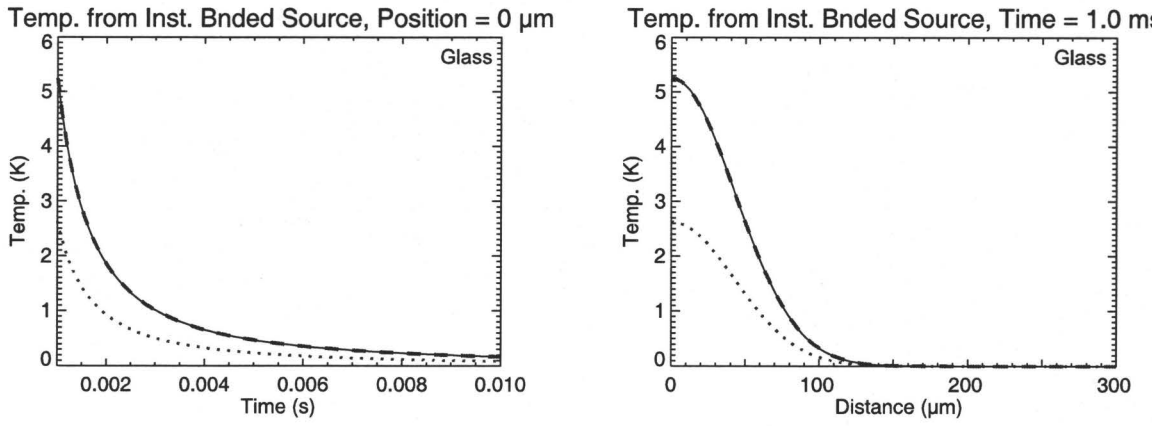

Figure A.5: Temperature distribution for glass, assuming material properties of $T = 300$ K glass, for an unbounded (infinite material) and bounded (300 μm thick material) instantaneous point source, as a function of time (at $z = 0$) and depth (at $t = 1$ ms). The solid line indicates the bounded calculation, the dotted line indicates the unbounded calculation, and the dashed line indicates $2\times$ the unbounded calculation.

A.2.3 Summing

The temperature increase due to many pulses each separated by 1 ms can be calculated. This is done by adding together the temperature after 1 ms, 2 ms, 3 ms, and so on. Summing the temperature increases due to ten thousand pulses each with an energy of 5 μJ and separated by 1 ms yields for silicon a net temperature increase of approximately 92 mK (1 ms after the final pulse). The 10 001st pulse is incident on silicon which is 92 mK warmer than the material exposed to the first pulse. Thus from this rough estimate, it can be concluded that local heat accumulation does not significantly change the material parameters encountered by each pulse. The evolution of temperature with time (data points calculated for 1 ms after each pulse) is graphed in figure A.6. The temperature increase for a-SiO_2 glass is also shown in figure A.6. The temperature increase for glass under the same simulation is 17.2 K. This suggests that at 1 kHz laser repetition rate, the properties of glass would not be greatly changed. The bounded calculation and $2\times$ the unbounded calculation show a larger (percentage) difference for silicon than for glass, as would be expected from the lower thermal diffusivity of glass. Since the diffusivity of glass is lower, heat is more strongly held near the irradiated surface and the second surface has less of an influence at the time frame shown.

To compare the possible effects of repetition rate on machining, a calculation was done for a laser repetition rate of 100 kHz. Some newer femtosecond laser systems marketed

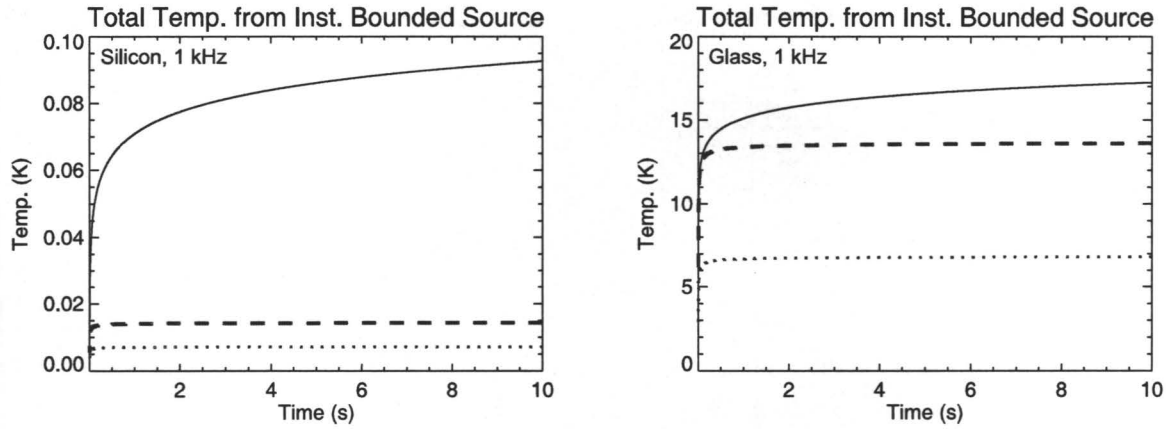

Figure A.6: Temperature evolution determined by summing the temperature increases due to multiple pulses for a bounded (solid line) and unbounded (dotted line) material, for a pulse repetition of 1 kHz. The dashed line is 2× the dotted line, for comparison between models. The bounded material is 300 μm thick, while the unbounded material is infinitely thick. *(left):* Evolution for silicon. *(right):* Evolution for glass. The data points are calculated 1 ms after each incident pulse.

for laser machining can operate around this repetition rate (see, e.g. reference [154]). For industrial manufacturing, a high repetition rate allows a higher translation speed and thus faster processing time [152, 154]. Figure A.7 shows the temperature evolutions of silicon and glass for the bounded and unbounded cases, similar to those in figure A.6. For silicon, the temperature increase in the bounded case after 0.01 s (1000 pulses) is 15.7 K. This suggests that increasing the laser repetition rate to 100 kHz on silicon would likely not significantly change the thermal properties of the material being irradiated. However, the simulation for glass shows a rapid increase in temperature to more than 13 000 K, for a 100 kHz repetition rate and 1000 pulses. This is a somewhat unphysical result, as the glass vaporizes significantly below this temperature (near 2500 K [1]). However it does indicate that at 100 kHz the machining of glass would be significantly different than at 1 kHz. Other experimental works (see, e.g. reference [152]) have reported this effect on dielectrics.

Amorphous silicon has a thermal diffusivity of 0.0097 cm^2/s at room temperature [1], which is 1–2 orders of magnitude less than that of crystalline silicon. However, since any amorphous layers would be expected to be thin, amorphization would not be expected to have a major effect with regard to heat transport. Any crystalline material adjacent to warm amorphous material would be expected to rapidly conduct heat away from the interface.

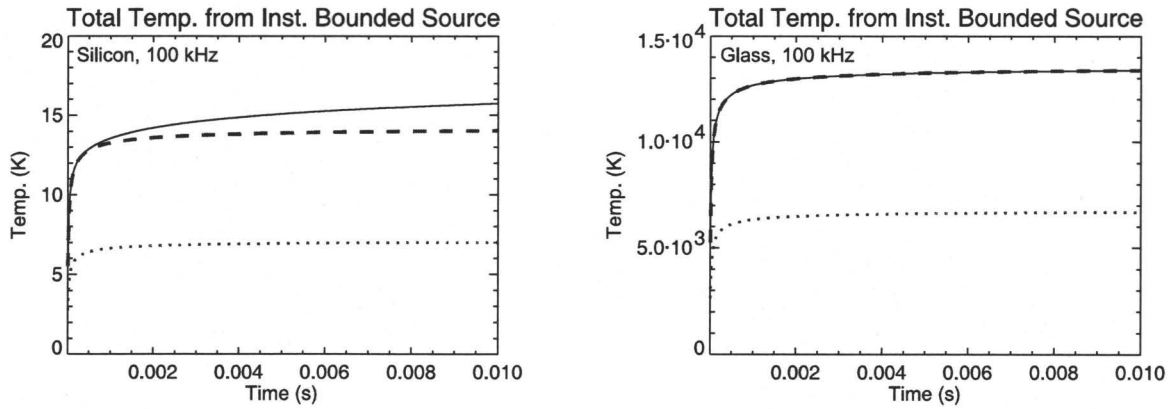

Figure A.7: Temperature evolution determined by summing the temperature increases due to multiple pulses for a bounded (solid line) and unbounded (dotted line) material, for a pulse repetition rate of 100 kHz. The dashed line is 2× the dotted line, for comparison between models. The bounded material is 300 μm thick, while the unbounded material is infinitely thick. *(left):* Evolution for silicon. *(right):* Evolution for glass. The data points are calculated 0.01 ms after each incident pulse.

For the short periodic surface structures presented in this thesis, less energy was typically used than in these estimates, and mechanisms such as reflectivity of incident light at the sample surface are expected to reduce the amount of energy which would be available to heat the sample. The structures of interest on silicon are typically destroyed after more than a few thousand pulses. Pulse-to-pulse changes in the surface morphology and (possibly) changes in composition and crystallinity will present each incident pulse with a situation which is somewhat different than for the previous pulse. Such issues likely play a much greater role than the sample heating in the case of the conditions presented here.

A.3 Conclusions

The calculations presented here strongly suggest that sample heating, either by accumulation of heat via multiple pulses, after a single pulse, or distributed throughout the entire sample, did not have a significant effect on the material properties and thus the laser-material interaction. The calculations also suggest however that for a sufficiently high repetition rate, or sufficiently low thermal diffusivity (i.e. for materials like glass), these processes would have a greater effect.

Appendix B

Sipe Theory Calculations and Discussion

B.1 Calculations

In the theory of Sipe et al. [54], a function η is developed which describes the efficacy with which inhomogeneous energy absorption occurs at the surface of a material irradiated by laser light. For nanosecond pulse irradiation, very good semiquantitative agreement with the positions of peaks in η and the spatial periods Λ of structures on various materials was reported [56]. In several later papers the efficacy factor was calculated and compared to experimental results (see, e.g. references [103, 113, 155]).

Of particular relevance to my work on semiconductors, Bonse et al. [103] have used the theory of Sipe et al. [54] to predict the periods of ripples formed on InP by femtosecond laser irradiation. The plot of η for InP (figure 7 in reference [103]) predicted for normal incidence ripples with $\lambda/\Lambda = 3.0$–3.5 oriented parallel to the laser polarization [103], where Λ is the structure period and λ is the in-air laser wavelength. The peak on the plot of η as a function of λ/Λ was rounded and such ripples were not observed experimentally [103].

Using the formalism presented in the Bonse work [103], I have made plots of the efficacy factor η for silicon under various conditions. The equations presented in reference [103] were implemented in the 'IDL' programming language. Values of the 'shape factor' $s = 0.4$ and 'filling factor' $F = 0.1$ were used, as in references [56, 103, 113, 155]. My calculations are for normal incidence, as this is the condition I used in the majority of my work on ripples. Due to the shallow profiles of the silicon irradiation sites, the angle of incidence does not vary appreciably across the site. The complex refractive index $n = n_\circ + \imath k$ of silicon at 400, 800, 1300, and 2100 nm wavelengths is $n \approx 5.57 + 0.39\imath$, $\approx 3.69 + 0.01\imath$, $\approx 3.51 + 0.00\imath$, and $\approx 3.45 + 0.00\imath$ respectively [99] (where $\imath^2 \equiv -1$). For silicon at the two OPA wavelengths, the linear absorption is approximately zero (i.e. $k \approx 0$), while silicon is not transparent at $\lambda = 400$ nm and 800 nm (i.e. $k > 0$). In the calculations, a variable kappa or κ is used, with the definition $\kappa = \lambda/\Lambda$. The graphs of the efficacy factor

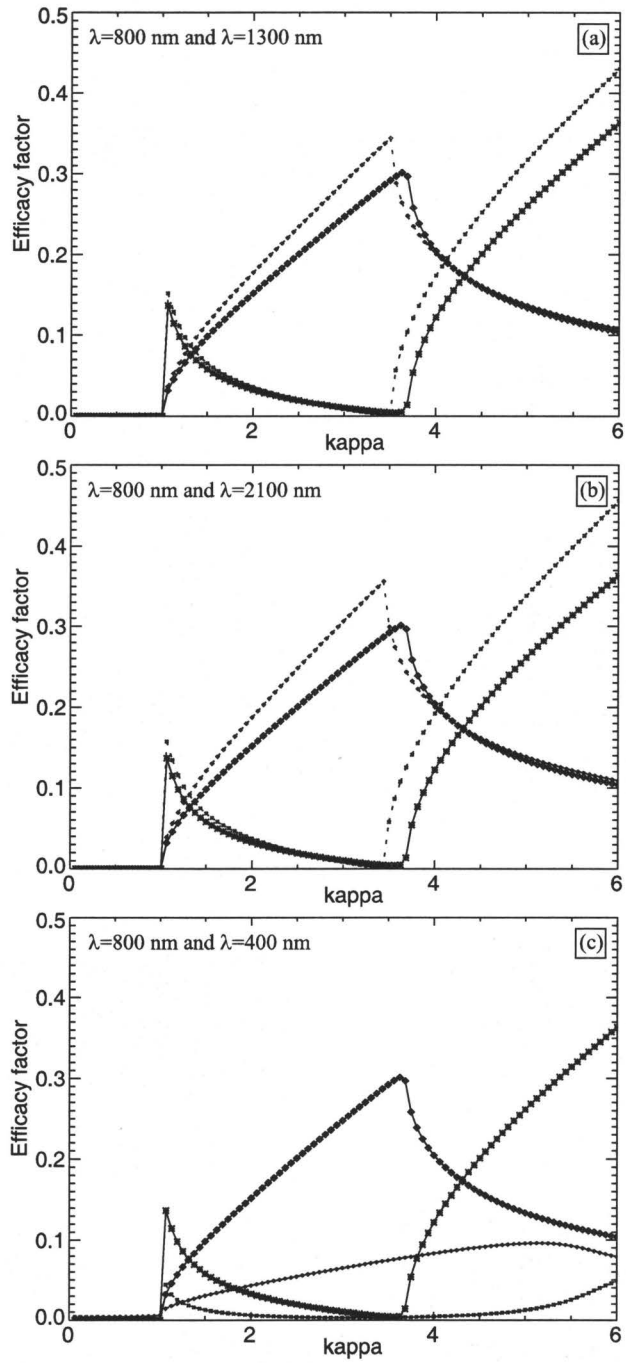

Figure B.1: Calculation of efficacy factor as a function of kappa (λ/Λ) for 800 nm wavelength (large symbols and solid line on all three graphs), in comparison to (a) 1300, (b) 2100, and (c) 400 nm wavelengths (small symbols with dashed line). Diamonds indicate ripples with their wave vector perpendicular to the incoming light polarization, while stars indicate ripples with their wave vector parallel to the polarization.

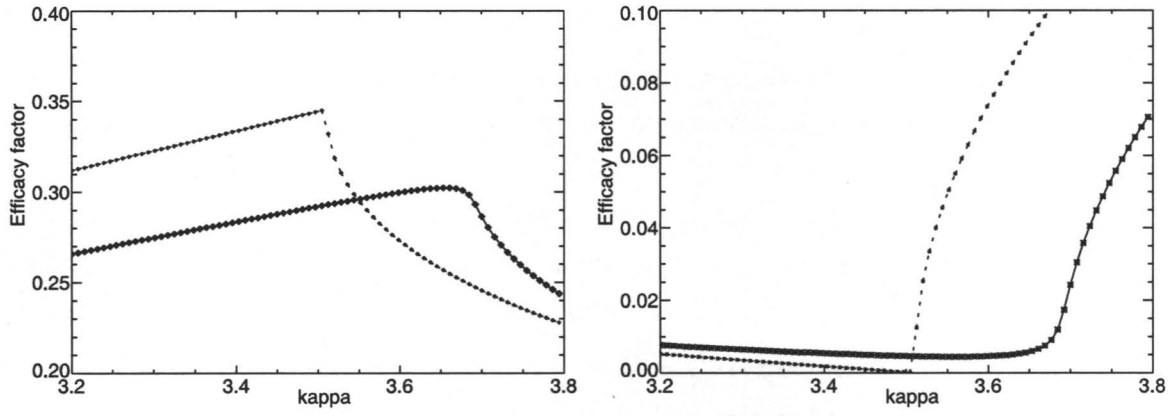

Figure B.2: Zoom of figure B.1(a) for the 800 nm and 1300 nm wavelength cases, showing the difference in smoothness of the traces of efficacy factor, near kappa of 3.5. The zoom for a wavelength of 2100 nm (not shown) is qualitatively similar to the 1300 nm case.

η as a function of κ for these four wavelengths are shown in figure B.1, with a magnified portion of the 1300 and 800 nm graphs shown in figure B.2.

At all wavelengths used in the calculations, a sharp asymmetric peak in η was present at $\lambda \approx \Lambda$ (i.e. $\kappa \approx 1$) for light polarization parallel to the ripple wave vector (i.e. ripples running perpendicular to the light polarization). The efficacy factor drops rapidly toward zero for kappa slightly less than one. For kappa slightly greater than one (Λ slightly less than λ), the efficacy factor decreases more slowly. Bonse et al. [103] present a similar feature on their graphs for InP, and note this is consistent with their observation of ripples with periods between 600 and 800 nm. Many reports of 'classic' LSFL having periods somewhat less than the irradiating wavelength (see reference [58] and related discussion in chapter 5) may also be related to asymmetric peaks in η plots near $\kappa = 1$.

For the three infrared wavelengths, the plot for light polarization parallel to the ripples (i.e. ripple wave vector perpendicular to polarization direction) has a peak near $\Lambda \approx \lambda / n_o$. The peak is slowly increasing from the low-κ side, but has an initial rapid drop on the high-κ side of the peak. For 800 nm, the peak is somewhat less sharp than those at 1300 and 2100 nm, and is approximately ~85–90% the height of the peaks for 1300 and 2100 nm. The peak for $\lambda = 400$ nm is very broad in comparison to the peak at other wavelengths. It reaches its maximum near $\kappa = 5.2$, slightly less than the real part of the refractive index.

Figure B.2 shows a region of the efficacy plot near $\kappa = 3.5$, allowing a closer (higher resolution calculation) look at the smoothness of the plot near the peak for 800 and 1300 nm

wavelength irradiation. In my work on substantially sub-wavelength structures on silicon, such structures formed after irradiation by $\lambda \approx 1300$ nm and ≈ 2100 nm pulses, but not for pulses centered at $\lambda = 800$ nm. Possibly, the greater roundedness of the peak for the $\lambda = 800$ nm case reduced the tendency of substantially sub-wavelength periodic structures to form at that wavelength. A rounded peak with an absence of corresponding ripples was obseved by Bonse et al. [103]. Ripples with a period near Λ of $\sim \lambda/3.5$ were not observed in my work. Possible reasons for the difference in period between this and the observed $\sim \lambda/4$–$\lambda/5$ and $\sim \lambda/2$ periods are discussed later.

In simulations where the real part $n_\circ$ of the refractive index n was varied while the imaginary part k was held at zero and all other parameters were held constant, the peak in the efficacy factor occurred at $\kappa \approx n_\circ$. As $n_\circ$ is increased, the peak decreases in height and its position moves to larger κ. Figure B.3 shows plots of the efficacy factor for various values of k, with $n_\circ$ held constant at the arbitrary value of 3.5. As k is increased from zero, the peak near $\kappa \approx n_\circ$ becomes more rounded, and lower in height. The position of the peak also shifts to somewhat lower values of κ. In semiconductors, the bandgap arises in part due to the periodic nature of the crystal lattice. As the crystal loses order (i.e. becomes amorphous), a bandgap is less well defined. For the wavelengths used in this study, amorphous silicon has a larger value of k than for the crystalline material, including at the wavelengths where crystalline silicon has $k \approx 0$ (see, e.g. reference [99]). At 400, 800, 1300, and 2100 nm, the refractive indices of amorphous silicon are $n \approx 4.3 + 2.2\imath$, $\approx 3.9 + 0.17\imath$, $\approx 3.5 + 0.023\imath$, and $\approx 3.4 + 0.003\imath$ respectively [99], although it should be noted that these values are sensitive to preparation conditions [99]. Amorphous InP has larger real and imaginary values of refractive index compared to crystalline InP, and Bonse et al. showed that the peak in η for amorphous InP shifted to a larger λ/Λ and was flatter and lower [103]. It could be that the laser-induced amorphization of a sample surface tends to inhibit the formation of short-period structures, although this neglects the possibility that a structure, once it has begun to form, tends to enhance its own growth. The following section discusses some of these possibilities.

B.2 Discussion

In general, for optical wavelengths the imaginary part of the refractive index is small for photon energies less than the bandgap energy, while it is larger for above-bandgap energies. This may be an important point to consider, since in multiple cases sub-bandgap photon energies have been required for substantially sub-wavelength periodic structure for-

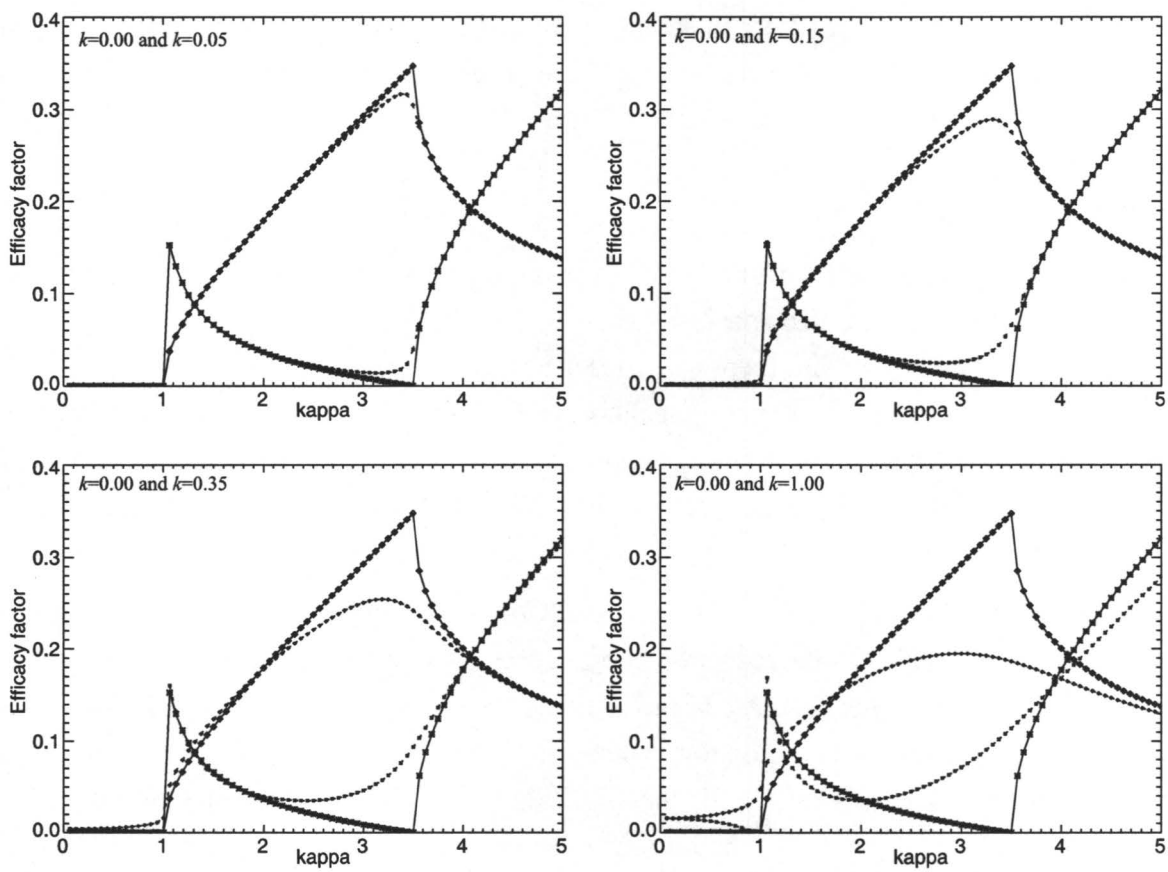

Figure B.3: Calcuation of efficacy factor as a function of kappa (λ/Λ) for a material with $n_o = 3.5$ and k of 0.00, 0.05, 0.15, 0.35, and 1.0. The $k = 0.00$ case is plotted (as large symbols and solid line) on all four graphs, for comparison to the other k values (small symbols with dashed line). Diamonds indicate ripples with their wave vector perpendicular to the incoming light polarization, while stars indicate ripples with their wave vector parallel to the polarization.

mation [58, 59, 61, 106]. Young et al. [56] note that damage mechanisms are complex and nonlinear so complete quantitative agreements should not be expected, and that it is difficult to extract quantitative information about η. They state that they simply demonstrate that experimentally observed results are similar to the gross features represented by peaks in η [56]. There is a question concerning to what extent a peak contributes to material damage at that wave vector [56]. The theory [54] does not include the role of feedback mechanisms, which could affect the tendency of certain structures to form [56, 155]. The difference between the predicted periods and the observed periods in the work presented in this thesis still remains to be explained.

As noted in the silicon ripples paper [58], the theory of Sipe et al. [54] indicates that structures with these predicted $\lambda/n_\circ$ periods are strongly suppressed when the absorption of the light is large. In the work in this thesis, the predicted periods are larger than the observed periods of fine structures, but smaller than the intermediate-sized structures. A thorough analysis using the theory of Sipe and co-workers for femtosecond irradiation should consider how the material optical constants change under high electron excitation. Formation of amorphous material could affect the calculations, as the optical properties of amorphous silicon differ from those of crystalline silicon and depend on the preparation conditions [99].

For substantially sub-wavelength ripples and the possibility of second harmonic generation, Jia et al. [61] discuss the reduction of refractive index with increase in electron number density. They argue this decrease in refractive index $n_\circ$ induced by the intense laser light could raise the value of $\lambda/2n_\circ$ up to the measured ripple period. A similar argument could be used in the calculations using the theory of Sipe et al. [54]. The calculations presented here and typically presented in the literature use the refractive indices of non-excited materials. An additional difficulty is the transient nature of the electron number density and refractive index, as they change during irradiation and subsequent material evolution.

B.3 Conclusions

The calculations presented here show that the theory given by Sipe et al. [54] predicts that the formation of substantially sub-wavelength ripple periods is possible. The predicted periods are near $\Lambda \approx \lambda/n_\circ$, particularly for the case when the material is transparent to the laser irradiation. The situation however is complicated by various factors, such as the complexity of damage mechanisms, neglection of feedback effects, formation of amorphous material, and transient changes in the refractive index.

Appendix C

List of Published Research

Note that permission for the reproduction of copyrighted material is provided in appendix F. The footnotes in this list are present to comply with the permission requirements.

C.1 Refereed journal contributions

- *Femtosecond laser micromachining of grooves in silicon with 800 nm pulses*, T.H.R. Crawford, A. Borowiec, H.K. Haugen, Appl. Phys. A **80**, 1717–1724 (2005). ©Springer-Verlag 2004.
  DOI:10.1007/s00339-004-2941-2

- *Sub-wavelength surface structures on silicon irradiated by femtosecond laser pulses at 1300 and 2100 nm wavelengths*, T.H.R. Crawford, H.K. Haugen, Appl. Surf. Sci. **253**, 4970–4977 (2007). ©2006 Elsevier B.V. All rights reserved[1].
  DOI:10.1016/j.apsusc.2006.11.004

- *Femtosecond laser-based fabrication of a new model material to study fracture*, A. Weck, T.H.R. Crawford, A. Borowiec, D.S. Wilkinson, J.S. Preston, Appl. Phys. A **86**, 55–61 (2007). ©Springer-Verlag 2006.
  DOI:10.1007/s00339-006-3730-x

- *Ripple formation during deep hole drilling in copper with ultrashort laser pulses*, A. Weck, T.H.R. Crawford, D.S. Wilkinson, H.K. Haugen, J.S. Preston, Appl. Phys. A **89**, 1001–1003 (2007). ©Springer-Verlag 2007.
  DOI:10.1007/s00339-007-4203-6

- *Laser drilling of high aspect ratio holes in copper with femtosecond, picosecond, and nanosecond pulses*, A. Weck, T.H.R. Crawford, D.S. Wilkinson, H.K. Haugen,

[1]This article was published in Applied Surface Science, volume 253, T.H.R. Crawford, H.K. Haugen, "Sub-wavelength surface structures on silicon irradiated by femtosecond laser pulses at 1300 and 2100 nm wavelengths", Pages 4970–4977, Copyright Elsevier (2006).

J.S. Preston, Appl. Phys. A **90**, 537–543 (2008). ©Springer-Verlag 2007.
DOI:10.1007/s00339-007-4300-6

- *High-resolution observations of an amorphous layer and subsurface damage formed by femtosecond laser irradiation of silicon*, T.H.R. Crawford, J. Yamanaka, G.A. Botton, H.K. Haugen, J. Appl. Phys. **103**, 053104-1–7 (2008). ©2008 American Institute of Physics[2].
DOI:10.1063/1.2885111

- *Femtosecond laser irradiation of metal and thermal oxide layers on silicon: studies utilising cross-sectional transmission electron microscopy*, T.H.R. Crawford, J. Yamanaka, E.M. Hsu, G.A. Botton, H.K. Haugen, Appl. Phys. A **91**, 473–478 (2008). ©Springer-Verlag 2008.
DOI:10.1007/s00339-008-4433-2

- *Periodic surface structures on gallium phosphide after irradiation with 150 fs – 7 ns laser pulses at 800 nm*, E.M. Hsu, T.H.R. Crawford, H.F. Tiedje, H.K. Haugen, Appl. Phys. Lett. **91**, 111102-1–3 (2007). ©2007 American Institute of Physics[3].
DOI:10.1063/1.2779914

- *Cross-sectional study of periodic surface structures on gallium phosphide induced by ultrashort laser pulse irradiation*, E.M. Hsu, T.H.R. Crawford, C. Maunders, G.A. Botton, H.K. Haugen, Appl. Phys. Lett. **92**, 221112-1–3 (2008). ©2008 American Institute of Physics[4].
DOI:10.1063/1.2936865

C.2 Conference contributions

- *Femtosecond laser micromachined grooves cut in silicon with 400 nm and 800 nm pulses*, T.H.R. Crawford, A. Borowiec, H.K. Haugen, CLEO/QELS (Conference on Lasers and Electro-Optics / Quantum Electronics & Laser Science Conference) 2003, Oral presentation CFF6

[2]Reprinted with permission from the Journal of Applied Physics. Copyright 2008, American Institute of Physics.

[3]Reprinted with permission from Applied Physics Letters. Copyright 2007, American Institute of Physics.

[4]Reprinted with permission from Applied Physics Letters. Copyright 2008, American Institute of Physics.

- *Femtosecond laser micromachining of silicon at 400 nm and 800 nm wavelengths* T.H.R. Crawford, A. Borowiec, H.K. Haugen, CAP (Canadian Association of Physicists) Annual Congress, June 2003, Oral presentation WE-A1-5

- *Sub-wavelength surface structures on silicon irradiated by femtosecond laser pulses*, T.H.R. Crawford, A. Borowiec, H.K. Haugen, CLEO/IQEC and PhAST (Conference on Lasers and Electro-Optics / International Quantum Electronics Conference and Photonic Applications Systems Technologies) 2004, Poster presentation CTuP40

- *Electron microscopy observations of an amorphous layer formed by femtosecond laser irradiation*, J. Yamanaka, T.H.R. Crawford, G.A. Botton, H.K. Haugen, 8th International Conference on Laser Ablation (COLA) 2005, Poster presentation TuPO24

- *Cross-sectional transmission electron microscopy observations of silicon after femtosecond laser irradiation*, J. Yamanaka, T.H.R. Crawford, G.A. Botton, H.K. Haugen, 5th International Conference on Photo-Excited Processes and Applications (ICPEPA) 2006, Poster presentation C-5080

- *Femtosecond laser drilling of high aspect ratio holes in copper sheets*, A. Weck, D.S. Wilkinson, T.H.R. Crawford, H.K. Haugen, J.S. Preston, 9th International Conference on Laser Ablation (COLA) 2007, Poster presentation PMO-31

- *Near and sub-wavelength ripples on gallium phosphide irradiated at various laser pulse durations*, E.M. Hsu, T.H.R. Crawford, H.F. Tiedje, H.K. Haugen, 9th International Conference on Laser Ablation (COLA) 2007, Poster presentation PTU-65

- *Deep hole drilling in copper with ultrashort laser pulses*, A. Weck, T.H.R. Crawford, D.S. Wilkinson, H.K. Haugen, J.S. Preston, 19th Canadian Materials Science Conference (CMSC) 2007, Poster presentation

- *AFM, SEM, and cross-sectional TEM examinations of semiconductors irradiated by femtosecond laser pulses*, T.H.R. Crawford, J. Yamanaka, A. Borowiec, M. Couillard, E.M. Hsu, E.M. Griswold, J.S. Preston, G.A. Botton, H.K. Haugen, 19th Canadian Materials Science Conference (CMSC) 2007, Poster presentation

- *Femtosecond laser machining of quartz*, M. Budiman, T. Snyder, E. Hsu, T.H.R. Crawford, H.F. Tiedje, H.K. Haugen, G.A. Botton, 19th Canadian Materials Science Conference (CMSC) 2007, Poster presentation

Appendix D

List of Abbreviations

AFM	Atomic force microscope; Atomic force microscopy
AR	Anti-reflection
BBO	Beta barium borate (crystal)
CCD	Charge-coupled device (camera)
CPA	Chirped pulse amplifier; Chirped pulse amplification
DIC	(Nomarski) Differential interference contrast (OM)
DVE	Depth vs. energy
DVN	Depth vs. number of passes
DVS	Depth vs. translation speed
EDXS	Energy-dispersive x-ray spectroscopy
FIB	Focussed ion beam
HAADF	High-angle annular dark-field (electron microscopy)
HF	Hydrogen fluoride; Hydrofluoric acid
HREM	High-resolution electron microscopy
HSFL	High spatial frequency LIPSS
HWP	Half-wave plate
KDP	Potassium dihydrogen phosphate (crystal)
LIPSS	Laser-induced periodic surface structures
LSFL	Low spatial frequency LIPSS
MD	Molecular dynamics
NBD	Nanobeam (electron) diffraction
ND	Neutral density
OD	Optical density (transmission $= 10^{-\mathrm{OD}}$)
OM	Optical (light) microscopy
OPA	Optical parametric amplifier; Optical parametric amplification
QWP	Quarter-wave plate
SDG	Synchronization and delay generator
SEM	Scanning electron microscope; Scanning electron microscopy
SOI	Silicon on insulator
STEM	Scanning TEM
TEM	Transmission electron microscope; Transmission electron microscopy

Appendix E

List of Symbols

d	Depth
D	Crater diameter
E	Pulse energy
f	Pulse repetition frequency; Focal length
$\imath$	Imaginary unit defined by $\imath^2 \equiv -1$
k	Extinction coefficient (imaginary part of refractive index n)
n	Refractive index ($n_\circ + \imath k$)
$n_\circ$	Real part of refractive index n
N	Number of pulses
t	Time
T	Temperature
υ	Translation velocity
Z	Atomic number
α	Absorption coefficient ($\alpha^{-1} = \lambda/(4\pi k)$)
η	Efficacy factor for energy absorption
θ	Angle of incidence
κ	Ratio of λ to Λ
λ	Center wavelength of a laser pulse (measured in air or in vacuum)
Λ	Periodic structure period
τ	Pulse duration
ϕ, φ	Fluence (energy per unit area)
$\phi_\circ$	Peak fluence (at center of Gaussian profile)
$\omega_\circ$	Focussed laser spot size, radius to $1/e^2$ of peak intensity

Appendix F

Permission to Reproduce Copyrighted Material

Below is the permission from the American Institute of Physics, Elsevier, and Springer-Verlag for reproduction of copyrighted journal articles or portions of these articles. The full information for the original publications is given in appendix C.

F.1 Permission from the American Institute of Physics

Date: Wed, 25 Jun 2008 09:59:33 -0400
From: RIGHTS <Rights@aip.org>
To: Travis Crawford <crawftr@mcmaster.ca>
Subject: Re: Permission request for reproduction of articles in a Ph.D thesis

Dear Dr. Crawford:

This permission clarifies the conditions for inclusion of the following material in your Ph.D thesis entitled "Examination of surface morphology and sub-surface crystallographic changes of Si, Cu, GaP, and Ge after ultrashort laser pulse irradiation:"

"High-resolution observations of an amorphous layer and subsurface damage formed by femtosecond laser irradiation of silicon", T.H.R. Crawford, J. Yamanaka, G.A. Botton, H.K. Haugen, J. Appl. Phys. v.103, p.053104 (2008)

"Periodic surface structures on gallium phosphide after irradiation with 150 fs - 7 ns laser pulses at 800 nm", E.M. Hsu, T.H.R. Crawford, H.F. Tiedje, H.K. Haugen, Appl. Phys. Lett. v.91, p.111102 (2007)

"Cross-sectional study of pericdic surface structures on gallium phosphide induced by ultrashort laser pulse irradiation", E.M. Hsu, T.H.R. Crawford, C. Maunders, G.A. Botton, H.K. Haugen, Appl. Phys. Lett. v.92, 221112 (2008)

It is understood that your intention is to include most of the figures and some of the text from the original articles, but not to reprint the entire article verbatim. We also grant a nonexclusive license to McMaster University and to the National Library of Canada to reproduce this material as a part of the thesis.

Please let us know if you have any questions.

Sincerely,
Susann Brailey

~~~~~~~~~~
Office of the Publisher, Journals and Technical Publications
Rights & Permissions
American Institute of Physics
Suite 1NO1
2 Huntington Quadrangle
Melville, NY 11747-4502
516-576-2268 TEL
516-576-2450 FAX
rights@aip.org

>>> Travis Crawford <crawftr@mcmaster.ca> 06/20/08 5:34 PM >>>
Dear Madam/Sir,

I recently received the following permissions for inclusion of material from AIP articles in my Ph.D thesis. I am a co-author of the articles. The license numbers are:

- 1973161095178
- 1973171153184
- 1973240543622

The third licence is intended to replace 1973170870129, for which an incorrect "title of your work" field was present.

I would like to confirm with you two details about the licence:

- Although the "Type of use" is listed as "Republish Entire Article", my requested use is to include most of the figures and some of the text from the original articles, but not to reprint the entire article verbatim. Is this permission given by the licenses above?
~~~~~~~~~~

- I request that you grant irrevocable, nonexclusive license to McMaster University and to the National Library of Canada to reproduce this material as a part of the thesis. Is this permission included as part of the licenses above?

Thank-you for your time,

Travis Crawford

Ph.D. Candidate
Department of Engineering Physics
McMaster University
1280 Main Street West
Hamilton, Ontario, Canada
L8S 4L7

Phone: 905-525-9140 ext. 24859
Fax: 905-527-8409

On Fri, 20 Jun 2008, RIGHTS wrote:

> Dear Requestor:
>
> Thank you for requesting permission to reuse copyrighted material from the
> American Institute of Physics, AVS The Science & Technology Society, or the
> Acoustical Society of America.
>
> AIP has streamlined its permission process with the implementation of
> Rightslink(R), a service of Copyright Clearance Center, Inc. With Rightslink, you
> can now obtain permission yourself online instantly in just a few simple steps.
>
>
> We have processed your recent request through Rightslink and an account has
> been established for you. The Copyright Clearance Center will send you several
> confirmation e-mails regarding your account and the reuse license. We invite you
> to try the Rightslink system the next time you seek permission to reuse our
> material.
>
> To begin the process, simply locate the article containing the material you
> wish to use by accessing it online at http://journals.aip.org/ (for AIP
> articles) or http://scitation.aip.org/ (for AVS and ASA articles). In the
> abstract view of the article, click on the "Permissions for Reuse" link in
> the upper right-hand corner. You'll be guided through the process quickly and
> easily from there.
>
> Keep in mind that when asked for the publication date of your work, an
> estimated or expected date of publication is fine. And if you don't have a
> purchase order number (PO number), fill in the box with the word "Pending."
>
> To learn more about Rightslink, read our press release at
> http://www.aip.org/press_release/rightslink.html
> or visit www.copyright.com. If you have any questions about the order that was
> processed for you, contact customercare@copyright.com.
>
> We hope you will benefit from the speed and ease of use Rightslink provides in
> obtaining the permissions you need. As always, feel free to contact us with any
> questions, concerns, or comments you may have.
>
> AIP Office of Rights and Permissions
>
> ~~~~~~~~~~
> Office of the Publisher, Journals and Technical Publications
> Rights & Permissions
> American Institute of Physics
> Suite 1NO1
> 2 Huntington Quadrangle
> Melville, NY 11747-4502
> 516-576-2268   TEL
> 516-576-2450   FAX
> rights@aip.org
>
> >>> Travis Crawford <crawftr@mcmaster.ca> 06/18/08 12:40 PM >>>
> Dear Madam/Sir
>
> I am completing a Ph.D thesis at McMaster University entitled "Examination
> of surface morphology and sub-surface crystallographic changes of Si, Cu,
> GaP, and Ge after ultrashort laser pulse irradiation.". I would like your
> permission to reproduce substantial portions of the the following journal
> articles in my thesis:
>
> "High-resolution observations of an amorphous layer and subsurface damage
> formed by femtosecond laser irradiation of silicon", T.H.R. Crawford, J.
> Yamanaka, G.A. Botton, H.K. Haugen, J. Appl. Phys. v.103, p.053104 (2008)
>
> "Periodic surface structures on gallium phosphide after irradiation with
> 150 fs - 7 ns laser pulses at 800 nm", E.M. Hsu, T.H.R. Crawford, H.F.
> Tiedje, H.K. Haugen, Appl. Phys. Lett. v.91, p.111102 (2007)
>
> "Cross-sectional study of periodic surface structures on gallium phosphide
> induced by ultrashort laser pulse irradiation", E.M. Hsu, T.H.R. Crawford,
> C. Maunders, G.A. Botton, H.K. Haugen, Appl. Phys. Lett. v.92, 221112
> (2008)
>
> Please note that I am a coauthor of these works.
>
> I would also like to request that you grant irrevocable, nonexclusive
> license to McMaster University and to the National Library of Canada to
> reproduce this material as a part of the thesis. Proper acknowledgement of
> your copyright of the reprinted material (including the authors, title,
> date and publisher) will be given in the thesis.
>
> If these arrangements meet with your approval please let me know. Thank
> you very much.
>
>
> Travis Crawford
>
> Ph.D. Candidate
> Department of Engineering Physics
> McMaster University
> 1280 Main Street West
> Hamilton, Ontario, Canada
> L8S 4L7
>
> Phone: 905-525-9140 ext. 24859
> Fax: 905-527-8409

AMERICAN INSTITUTE OF PHYSICS LICENSE
TERMS AND CONDITIONS

Jun 20, 2008

This is a License Agreement between Travis Crawford ("You") and American Institute of Physics ("American Institute of Physics"). The license consists of your order details, the terms and conditions provided by American Institute of Physics, and the payment terms and conditions.

License Number	1973161095178
License date	Jun 20, 2008
Licensed content publisher	American Institute of Physics
Licensed content title	High-resolution observations of an amorphous layer and subsurface damage formed by femtosecond laser irradiation of silicon
Licensed content author	T. H. R. Crawford, J. Yamanaka, G. A. Botton, and H. K. Haugen
Type of Use	Republish Entire Article
Requestor Type	Author
Title of your work	Examination of surface morphology and sub-surface crystallographic changes of Si, Cu, GaP, and Ge after ultrashort laser pulse irradiation
Publisher of your work	McMaster University
Publication date of your work	12/01/2008
PO Number	pending
Promotion code	
Total	$0.00

Terms and Conditions

American Institute of Physics -- Terms and Conditions: Permissions Uses

American Institute of Physics ("AIP") hereby grants to you the non-exclusive right and license to use and/or distribute the Material according to the use specified in your order, on a one-time basis, for the specified term, with a maximum distribution equal to the number that you have ordered. Any links or other content accompanying the Material are not the subject of this license.

1. You agree to include the following copyright and permission notice with the reproduction of the Material: "Reprinted with permission from [FULL CITATION]. Copyright [PUBLICATION YEAR], American Institute of Physics." For an article, the copyright and permission notice must be printed on the first page of the article or book chapter. For photographs, covers, or tables, the copyright and permission notice may appear with the Material, in a footnote, or in the reference list.
2. If you have licensed reuse of a figure, photograph, cover, or table, it is your responsibility to ensure that the material is original to AIP and does not contain the copyright of another entity, and that the copyright notice of the figure, photograph, cover, or table does not indicate that it was reprinted by AIP, with permission, from another source. Under no circumstances does AIP, purport or intend to grant permission to reuse material to which it does not hold copyright.
3. You may not alter or modify the Material in any manner. You may translate the Material into another language only if you have licensed translation rights. You may not use the Material for promotional purposes. AIP reserves all rights not specifically granted herein.
4. The foregoing license shall not take effect unless and until AIP or its agent, Copyright Clearance Center, receives the Payment in accordance with Copyright Clearance Center Billing and Payment Terms and Conditions, which are incorporated herein by reference.
5. AIP or the Copyright Clearance Center may, within two business days of granting this license, revoke the license for any reason whatsoever, with a full refund payable to you. Should you violate the terms of this license at any time, AIP, American Institute of Physics, or Copyright Clearance Center may revoke the license with no refund to you. Notice of such revocation will be made using the contact information provided by you. Failure to receive such notice will not nullify the revocation.
6. AIP makes no representations or warranties with respect to the Material. You agree to indemnify and hold harmless AIP, American Institute of Physics, and their officers, directors, employees or agents from and against any and all claims arising out of your use of the Material other than as specifically authorized herein.
7. The permission granted herein is personal to you and is not transferable or assignable without the prior written permission of AIP. This license may not be amended except in a writing signed by the party to be charged.
8. If purchase orders, acknowledgments or check endorsements are issued on any forms containing terms and conditions which are inconsistent with these provisions, such inconsistent terms and conditions shall be of no force and effect. This document, including the CCC Billing and Payment Terms and Conditions, shall be the entire agreement between the parties relating to the subject matter hereof.

This Agreement shall be governed by and construed in accordance with the laws of the State of New York. Both parties hereby submit to the jurisdiction of the courts of New York County for purposes of resolving any disputes that may arise hereunder.

AMERICAN INSTITUTE OF PHYSICS LICENSE
TERMS AND CONDITIONS

Jun 20, 2008

This is a License Agreement between Travis Crawford ("You") and American Institute of Physics ("American Institute of Physics"). The license consists of your order details, the terms and conditions provided by American Institute of Physics, and the payment terms and conditions.

License Number	1973240543622
License date	Jun 20, 2008
Licensed content publisher	American Institute of Physics
Licensed content title	Periodic surface structures on gallium phosphide after irradiation with 150 fs--7 ns laser pulses at 800 nm
Licensed content author	E. M. Hsu
Type of Use	Republish Entire Article
Requestor Type	Author
Title of your work	Examination of surface morphology and sub-surface crystallographic changes of Si, Cu, GaP, and Ge after ultrashort laser pulse irradiation
Publisher of your work	McMaster University
Publication date of your work	12/01/2008
PO Number	Pending
Total	$0.00

Terms and Conditions

American Institute of Physics -- Terms and Conditions: Permissions Uses

American Institute of Physics ("AIP") hereby grants to you the non-exclusive right and license to use and/or distribute the Material according to the use specified in your order, on a one-time basis, for the specified term, with a maximum distribution equal to the number that you have ordered. Any links or other content accompanying the Material are not the subject of this license.

1. You agree to include the following copyright and permission notice with the reproduction of the Material: "Reprinted with permission from [FULL CITATION]. Copyright [PUBLICATION YEAR], American Institute of Physics." For an article, the copyright and permission notice must be printed on the first page of the article or book chapter. For photographs, covers, or tables, the copyright and permission notice may appear with the Material, in a footnote, or in the reference list.
2. If you have licensed reuse of a figure, photograph, cover, or table, it is your responsibility to ensure that the material is original to AIP and does not contain the copyright of another entity, and that the copyright notice of the figure, photograph, cover, or table does not indicate that it was reprinted by AIP, with permission, from another source. Under no circumstances does AIP, purport or intend to grant permission to reuse material to which it does not hold copyright.
3. You may not alter or modify the Material in any manner. You may translate the Material into another language only if you have licensed translation rights. You may not use the Material for promotional purposes. AIP reserves all rights not specifically granted herein.
4. The foregoing license shall not take effect unless and until AIP or its agent, Copyright Clearance Center, receives the Payment in accordance with Copyright Clearance Center Billing and Payment Terms and Conditions, which are incorporated herein by reference.
5. AIP or the Copyright Clearance Center may, within two business days of granting this license, revoke the license for any reason whatsoever, with a full refund payable to you. Should you violate the terms of this license at any time, AIP, American Institute of Physics, or Copyright Clearance Center may revoke the license with no refund to you. Notice of such revocation will be made using the contact information provided by you. Failure to receive such notice will not nullify the revocation.
6. AIP makes no representations or warranties with respect to the Material. You agree to indemnify and hold harmless AIP, American Institute of Physics, and their officers, directors, employees or agents from and against any and all claims arising out of your use of the Material other than as specifically authorized herein.
7. The permission granted herein is personal to you and is not transferable or assignable without the prior written permission of AIP. This license may not be amended except in a writing signed by the party to be charged.
8. If purchase orders, acknowledgments or check endorsements are issued on any forms containing terms and conditions which are inconsistent with these provisions, such inconsistent terms and conditions shall be of no force and effect. This document, including the CCC Billing and Payment Terms and Conditions, shall be the entire agreement between the parties relating to the subject matter hereof.

This Agreement shall be governed by and construed in accordance with the laws of the State of New York. Both parties hereby submit to the jurisdiction of the courts of New York County for purposes of resolving any disputes that may arise hereunder.

AMERICAN INSTITUTE OF PHYSICS LICENSE
TERMS AND CONDITIONS

Jun 20, 2008

This is a License Agreement between Travis Crawford ("You") and American Institute of Physics ("American Institute of Physics"). The license consists of your order details, the terms and conditions provided by American Institute of Physics, and the payment terms and conditions.

License Number	1973171153184
License date	Jun 20, 2008
Licensed content publisher	American Institute of Physics
Licensed content title	Cross-sectional study of periodic surface structures on gallium phosphide induced by ultrashort laser pulse irradiation
Licensed content author	E. M. Hsu, T. H. R. Crawford, C. Maunders, G. A. Botton, and H. K. Haugen
Type of Use	Republish Entire Article
Requestor Type	Author
Title of your work	Examination of surface morphology and sub-surface crystallographic changes of Si, Cu, GaP, and Ge after ultrashort laser pulse irradiation
Publisher of your work	McMaster University
Publication date of your work	12/01/2008
PO Number	pending
Promotion code	
Total	$0.00

Terms and Conditions

American Institute of Physics -- Terms and Conditions: Permissions Uses

American Institute of Physics ("AIP") hereby grants to you the non-exclusive right and license to use and/or distribute the Material according to the use specified in your order, on a one-time basis, for the specified term, with a maximum distribution equal to the number that you have ordered. Any links or other content accompanying the Material are not the subject of this license.

1. You agree to include the following copyright and permission notice with the reproduction of the Material: "Reprinted with permission from [FULL CITATION]. Copyright [PUBLICATION YEAR], American Institute of Physics." For an article, the copyright and permission notice must be printed on the first page of the article or book chapter. For photographs, covers, or tables, the copyright and permission notice may appear with the Material, in a footnote, or in the reference list.
2. If you have licensed reuse of a figure, photograph, cover, or table, it is your responsibility to ensure that the material is original to AIP and does not contain the copyright of another entity, and that the copyright notice of the figure, photograph, cover, or table does not indicate that it was reprinted by AIP, with permission, from another source. Under no circumstances does AIP, purport or intend to grant permission to reuse material to which it does not hold copyright.
3. You may not alter or modify the Material in any manner. You may translate the Material into another language only if you have licensed translation rights. You may not use the Material for promotional purposes. AIP reserves all rights not specifically granted herein.
4. The foregoing license shall not take effect unless and until AIP or its agent, Copyright Clearance Center, receives the Payment in accordance with Copyright Clearance Center Billing and Payment Terms and Conditions, which are incorporated herein by reference.
5. AIP or the Copyright Clearance Center may, within two business days of granting this license, revoke the license for any reason whatsoever, with a full refund payable to you. Should you violate the terms of this license at any time, AIP, American Institute of Physics, or Copyright Clearance Center may revoke the license with no refund to you. Notice of such revocation will be made using the contact information provided by you. Failure to receive such notice will not nullify the revocation.
6. AIP makes no representations or warranties with respect to the Material. You agree to indemnify and hold harmless AIP, American Institute of Physics, and their officers, directors, employees or agents from and against any and all claims arising out of your use of the Material other than as specifically authorized herein.
7. The permission granted herein is personal to you and is not transferable or assignable without the prior written permission of AIP. This license may not be amended except in a writing signed by the party to be charged.
8. If purchase orders, acknowledgments or check endorsements are issued on any forms containing terms and conditions which are inconsistent with these provisions, such inconsistent terms and conditions shall be of no force and effect. This document, including the CCC Billing and Payment Terms and Conditions, shall be the entire agreement between the parties relating to the subject matter hereof.

This Agreement shall be governed by and construed in accordance with the laws of the State of New York. Both parties hereby submit to the jurisdiction of the courts of New York County for purposes of resolving any disputes that may arise hereunder.

F.2 Permission from Elsevier

Date: Tue, 24 Jun 2008 11:10:42 +0100
From: "Smith, Stephanie (ELS-OXF)" <ST.Smith@elsevier.com>
To: crawftr@mcmaster.ca
Subject: RE: Permission request for reproduction of article in a Ph.D thesis

Dear Mr Crawford

We hereby grant you permission to reprint the material detailed below at no charge in your thesis subject to the following conditions:

1. If any part of the material to be used (for example, figures) has appeared in our publication with credit or acknowledgement to another source, permission must also be sought from that source. If such permission is not obtained then that material may not be included in your publication/copies.

2. Suitable acknowledgment to the source must be made, either as a footnote or in a reference list at the end of your publication, as follows:

"This article was published in Publication title, Vol number, Author(s), Title of article, Page Nos, Copyright Elsevier (or appropriate Society name) (Year)."

3. Your thesis may be submitted to your institution in either print or electronic form.

4. Reproduction of this material is confined to the purpose for which permission is hereby given.

5. This permission is granted for non-exclusive world English rights only. For other languages please reapply separately for each one required. Permission excludes use in an electronic form. Should you have a specific electronic project in mind please reapply for permission.

6. This includes permission for the Library and Archives of Canada to supply single copies, on demand, of the complete thesis. Should your thesis be published commercially, please reapply for permission.

Help us improve our service! Please take 3 minutes to complete our customer service survey at [LINK]

Yours sincerely

Steph Smith

Rights Assistant
Elsevier Ltd
The Boulevard
Langford Lane
Kidlington
Oxford OX5 1GB

-----Original Message-----
From: Travis Crawford [mailto:crawftr@mcmaster.ca]
Sent: 23 June 2008 16:25
To: Parker, Kerry (ELS-OXF)
Subject: RE: Permission request for reproduction of article in a Ph.D thesis

Hello,

I have an additional question about the license to reproduce an article in a Ph.D thesis. I obtained the following license:

Licensee: Travis Crawford

License Date: Jun 23, 2008
License Number: 1974810605401
Publication: Applied Surface Science
Title: Sub-wavelength surface structures on silicon irradiated by femtosecond laser pulses at 1300 and 2100 nm wavelengths
Type Of Use: Thesis / Dissertation

Total: 0.00 USD

However, I need to confirm that this licence also grants irrevocable, nonexclusive license to McMaster University and to the National Library of Canada to reproduce this material as a part of the thesis.

Thank-you for your time,

Travis Crawford

Ph.D. Candidate
Department of Engineering Physics
McMaster University
1280 Main Street West
Hamilton, Ontario, Canada
L8S 4L7

Phone: 905-525-9140 ext. 24859
Fax: 905-527-8409

On Mon, 23 Jun 2008, Parker, Kerry (ELS-OXF) wrote:

> Dear Travis
>
> Elsevier is pleased to announce our partnership with Copyright
> Clearance Center's Rightslink service. With Rightslink (r) it's faster
> and easier than ever before to obtain permission to use and republish
> material from Elsevier.
>
> In order to get permission for the material you have requested please
> follow the link [LINK] which will launch you into
> the Rightslink application and then follow the steps below.
>
> 1. Select the way you would like to reuse the content 2. Create an
> account if you haven't already 3. Accept the terms and conditions and
> you're done
>
> For future requests simply visit: http://www.sciencedirect.com/ ,
> locate your desired content, open the abstract or summary and then
> click on the 'Request Permission' button to open the following page:
>
> Please contact Rightslink Customer Care with any questions or comments
> concerning this service:
>
> Copyright Clearance Center
> Rightslink Customer Care
> Tel (toll free): 877/622-5543
> Tel: 978/777-9929
> E-mail: customercare@copyright.com
> Web: http://www.rightslink.com
>
>
> Kind regards
>
> Kerry Parker
>
> Rights Assistant

> Elsevier Ltd.
> Tel: +44 (0) 1865 843280
> Fax: +44 (0) 1865 843950
>
>
>
> -----Original Message-----
> From: Travis Crawford [mailto:crawftr@mcmaster.ca]
> Sent: 18 June 2008 17:41
> To: Rights and Permissions (ELS)
> Subject: Permission request for reproduction of article in a Ph.D
> thesis
>
> Dear Madam/Sir
>
> I am completing a Ph.D thesis at McMaster University entitled
> "Examination of surface morphology and sub-surface crystallographic
> changes of Si, Cu, GaP, and Ge after ultrashort laser pulse
> irradiation.". I would like your permission to reprint the following
> journal article in my thesis:
>
> "Sub-wavelength surface structures on silicon irradiated by
> femtosecond laser pulses at 1300 and 2100 nm wavelengths", T.H.R. Crawford, H.K.
> Haugen, Appl. Surf. Sci. v.253, p.4970 (2007)
>
> Please note that I am a coauthor of this work.
>
> I would also like to request that you grant irrevocable, nonexclusive
> license to McMaster University and to the National Library of Canada
> to reproduce this material as a part of the thesis. Proper
> acknowledgement of your copyright of the reprinted material (including
> the authors, title, date and publisher) will be given in the thesis.
>
> If these arrangements meet with your approval please let me know.
> Thank you very much.
>
> Travis Crawford
>
> Ph.D. Candidate
> Department of Engineering Physics
> McMaster University
> 1280 Main Street West
> Hamilton, Ontario, Canada
> L8S 4L7
>
> Phone: 905-525-9140 ext. 24859
> Fax: 905-527-8409
>
>
> This email is from Elsevier Limited, a company registered in England
> and Wales with company number 1982084, whose registered office is The
> Boulevard, Langford Lane, Kidlington, Oxford, OX5 1GB, United Kingdom.
>

ELSEVIER LIMITED LICENSE
TERMS AND CONDITIONS

Jun 23, 2008

This is a License Agreement between Travis Crawford ("You") and Elsevier Limited ("Elsevier Limited"). The license consists of your order details, the terms and conditions provided by Elsevier Limited, and the payment terms and conditions.

Supplier	Elsevier Limited The Boulevard,Langford Lane Kidlington,Oxford,OX5 1GB,UK
Registered Company Number	1982084
Customer name	Travis Crawford
Customer address	Department of Engineering Physics Hamilton, ON L8S 4L7
License Number	1974810605401
License date	Jun 23, 2008
Licensed content publisher	Elsevier Limited
Licensed content publication	Applied Surface Science
Licensed content title	Sub-wavelength surface structures on silicon irradiated by femtosecond laser pulses at 1300 and 2100â€‰nm wavelengths
Licensed content author	T.H.R. Crawford and H.K. Haugen
Licensed content date	30 March 2007
Volume number	253
Issue number	11
Pages	8
Type of Use	Thesis / Dissertation
Portion	Full article
Format	Both print and electronic
You are an author of the Elsevier article	Yes
Are you translating?	No
Purchase order number	
Expected publication date	Sep 2008
Elsevier VAT number	GB 494 6272 12
Permissions price	0.00 USD
Value added tax 0.0%	0.00 USD
Total	0.00 USD

Terms and Conditions

INTRODUCTION

1. The publisher for this copyrighted material is Elsevier. By clicking "accept" in connection with completing this licensing transaction, you agree that the following terms and conditions apply to this transaction (along with the Billing and Payment terms and conditions established by Copyright Clearance Center, Inc. ("CCC"), at the time that you opened your Rightslink account and that are available at any time at <http://myaccount.copyright.com>).

GENERAL TERMS

2. Elsevier hereby grants you permission to reproduce the aforementioned material subject to the terms and conditions indicated.

3. Acknowledgement: If any part of the material to be used (for example, figures) has appeared in our publication with credit or acknowledgement to another source, permission must also be sought from that source. If such permission is not obtained then that material may not be included in your publication/copies. Suitable acknowledgement to the source must be made, either as a footnote or in a reference list at the end of your publication, as follows:

â€œReprinted from Publication title, Vol /edition number, Author(s), Title of article / title of chapter, Pages No., Copyright (Year), with permission from Elsevier [OR APPLICABLE SOCIETY COPYRIGHT OWNER].â€ Also Lancet special credit - â€œReprinted from The Lancet, Vol. number, Author(s), Title of article, Pages No., Copyright (Year), with permission from Elsevier.â€

4. Reproduction of this material is confined to the purpose and/or media for which permission is hereby given.

5. Altering/Modifying Material: Not Permitted. However figures and illustrations may be altered/adapted minimally to serve your work. Any other abbreviations, additions, deletions and/or any other alterations shall be made only with prior written authorization of Elsevier Ltd. (Please contact Elsevier at permissions@elsevier.com)

6. If the permission fee for the requested use of our material is waived in this instance, please be advised that your future requests for Elsevier materials may attract a fee.

7. Reservation of Rights: Publisher reserves all rights not specifically granted in the combination of (i) the license details provided by you and accepted in the course of this licensing transaction, (ii) these terms and conditions and (iii) CCC's Billing and Payment terms and conditions.

8. License Contingent Upon Payment: While you may exercise the rights licensed immediately upon issuance of the license at the end of the licensing process for the transaction, provided that you have disclosed complete and accurate details of your proposed use, no license is finally effective unless and until full payment is received from you (either by publisher or by CCC) as provided in CCC's Billing and Payment terms and conditions. If full payment is not received on a timely basis, then any license preliminarily granted shall be deemed automatically revoked and shall be void as if never granted. Further, in the event that you breach any of these terms and conditions or any of CCC's Billing and Payment terms and conditions, the license is automatically revoked and shall be void as if never granted. Use of materials as described in a revoked license, as well as any use of the materials beyond the scope of an unrevoked license, may constitute copyright infringement and publisher reserves the right to take any and all action to protect its copyright in the materials.

9. Warranties: Publisher makes no representations or warranties with respect to the licensed material.

10. Indemnity: You hereby indemnify and agree to hold harmless publisher and CCC, and their respective officers, directors, employees and agents, from and against any and all

claims arising out of your use of the licensed material other than as specifically authorized pursuant to this license.

11. No Transfer of License: This license is personal to you and may not be sublicensed, assigned, or transferred by you to any other person without publisher's written permission.

12. No Amendment Except in Writing: This license may not be amended except in a writing signed by both parties (or, in the case of publisher, by CCC on publisher's behalf).

13. Objection to Contrary Terms: Publisher hereby objects to any terms contained in any purchase order, acknowledgment, check endorsement or other writing prepared by you, which terms are inconsistent with these terms and conditions or CCC's Billing and Payment terms and conditions. These terms and conditions, together with CCC's Billing and Payment terms and conditions (which are incorporated herein), comprise the entire agreement between you and publisher (and CCC) concerning this licensing transaction. In the event of any conflict between your obligations established by these terms and conditions and those established by CCC's Billing and Payment terms and conditions, these terms and conditions shall control.

14. Revocation: Elsevier or Copyright Clearance Center may deny the permissions described in this License at their sole discretion, for any reason or no reason, with a full refund payable to you. Notice of such denial will be made using the contact information provided by you. Failure to receive such notice will not alter or invalidate the denial. In no event will Elsevier or Copyright Clearance Center be responsible or liable for any costs, expenses or damage incurred by you as a result of a denial of your permission request, other than a refund of the amount(s) paid by you to Elsevier and/or Copyright Clearance Center for denied permissions.

LIMITED LICENSE

The following terms and conditions apply to specific license types:

15. **Translation**: This permission is granted for non-exclusive world **English** rights only unless your license was granted for translation rights. If you licensed translation rights you may only translate this content into the languages you requested. A professional translator must perform all translations and reproduce the content word for word preserving the integrity of the article. If this license is to re-use 1 or 2 figures then permission is granted for non-exclusive world rights in all languages.

16. **Website**: The following terms and conditions apply to electronic reserve and author websites:
Electronic reserve: If licensed material is to be posted to website, the web site is to be password-protected and made available only to bona fide students registered on a relevant course if:
This license was made in connection with a course,
This permission is granted for 1 year only. You may obtain a license for future website posting,
All content posted to the web site must maintain the copyright information line on the bottom of each image,
A hyper-text must be included to the Homepage of the journal from which you are licensing at http://www.sciencedirect.com/science/journal/xxxxx or the Elsevier homepage for books at http://www.elsevier.com, and
Central Storage: This license does not include permission for a scanned version of the material to be stored in a central repository such as that provided by Heron/XanEdu.

17. **Author website** for journals with the following additional clauses:
This permission is granted for 1 year only. You may obtain a license for future website posting,
All content posted to the web site must maintain the copyright information line on the bottom of each image, and
The permission granted is limited to the personal version of your paper. You are not allowed to download and post the published electronic version of your article (whether PDF or HTML, proof or final version), nor may you scan the printed edition to create an electronic version,
A hyper-text must be included to the Homepage of the journal from which you are licensing at http://www.sciencedirect.com/science/journal/xxxxx , or the Elsevier homepage for books at http://www.elsevier.com and
Central Storage: This license does not include permission for a scanned version of the material to be stored in a central repository such as that provided by Heron/XanEdu.

18. **Author website** for books with the following additional clauses:
Authors are permitted to place a brief summary of their work online only.
A hyper-text must be included to the Elsevier homepage at http://www.elsevier.com
This permission is granted for 1 year only. You may obtain a license for future website posting,
All content posted to the web site must maintain the copyright information line on the bottom of each image, and
The permission granted is limited to the personal version of your paper. You are not allowed to download and post the published electronic version of your article (whether PDF or HTML, proof or final version), nor may you scan the printed edition to create an electronic version,
A hyper-text must be included to the Homepage of the journal from which you are licensing at http://www.sciencedirect.com/science/journal/xxxxx , or the Elsevier homepage for books at http://www.elsevier.com and
Central Storage: This license does not include permission for a scanned version of the material to be stored in a central repository such as that provided by Heron/XanEdu.

19. **Website** (regular and for author): â€œA hyper-text must be included to the Homepage of the journal from which you are licensing at http://www.sciencedirect.com/science/journal/xxxxx.â€

20. **Thesis/Dissertation**: If your license is for use in a thesis/dissertation your thesis may be submitted to your institution in either print or electronic form. Should your thesis be published commercially, please reapply for permission. These requirements include permission for the Library and Archives of Canada to supply single copies, on demand, of the complete thesis and include permission for UMI to supply single copies, on demand, of the complete thesis. Should your thesis be published commercially, please reapply for permission.

v1.2

21. **Other conditions:**

None

F.3 Permission from Springer-Verlag

Date: Fri, 20 Jun 2008 12:06:36 +0200
From: "Schmidt-Loeffler, Barbara, Springer DE"
<Barbara.Schmidt-Loeffler@springer.com>
To: crawftr@mcmaster.ca
Subject: AW: Permission request for reproduction of article in a Ph.D thesis

Dear Mr. Crawford,

Thank you for your e-mail.

With reference to your request (copy herewith) to re-use material on which Springer controls the copyright, our permission is granted free of charge, on the following condition:

* full credit (journal title, volume, year of publication, page, article title, name(s) of author(s), figure number(s), original copyright notice) is given to the publication in which the material was originally published.

With best regards,

-
Barbara Schmidt-Löffler
Springer
Rights and Permissions
-
Tiergartenstr. 17 | 69121 Heidelberg | Germany
permissions@springer.com
www.springeronline.com
-

-----Ursprüngliche Nachricht-----
Von: Schmidt-Loeffler, Barbara, Springer DE Im Auftrag von Permissions Heidelberg, Springer DE
Gesendet: Donnerstag, 19. Juni 2008 10:46
An: Schmidt-Loeffler, Barbara, Springer DE
Betreff: WG: Permission request for reproduction of article in a Ph.D thesis

-----Ursprüngliche Nachricht-----
Von: Travis Crawford [mailto:crawftr@mcmaster.ca]
Gesendet: Mittwoch, 18. Juni 2008 18:42
An: Permissions Heidelberg, Springer DE
Betreff: Permission request for reproduction of article in a Ph.D thesis

Dear Madam/Sir

I am completing a Ph.D thesis at McMaster University entitled "Examination of surface morphology and sub-surface crystallographic changes of Si, Cu, GaP, and Ge after ultrashort laser pulse irradiation.". I would like your permission to reprint the following journal article in my thesis:

"Femtosecond laser micromachining of grooves in silicon with 800 nm pulses", T.H.R. Crawford, A. Borowiec, H.K. Haugen, Appl. Phys. A v.80, p.1717 (2005)

Additionally, I would like to reproduce substantial portions of the following articles in the thesis:

"Femtosecond laser-based fabrication of a new model material to study fracture", A. Weck, T.H.R. Crawford, A. Borowiec, D.S. Wilkinson, J.S. Preston, Appl. Phys. A v.86, p.55 (2007)

"Ripple formation during deep hole drilling in copper with ultrashort laser pulses", A. Weck, T.H.R. Crawford, D.S. Wilkinson, H.K. Haugen, J.S. Preston, Appl. Phys. A v.89, 1001 (2007)

"Laser drilling of high aspect ratio holes in copper with femtosecond, picosecond, and nanosecond pulses", A. Weck, T.H.R. Crawford, D.S. Wilkinson, H.K. Haugen, J.S. Preston, Appl. Phys. A v.90, 537 (2008)

"Femtosecond laser irradiation of metal and thermal oxide layers on silicon: studies utilising cross-sectional transmission electron microscopy", T.H.R. Crawford, J. Yamanaka, E.M. Hsu, G.A. Botton, H.K. Haugen, Appl. Phys. A v.91, 473 (2008)

Please note that I am a coauthor of these works.

I would also like to request that you grant irrevocable, nonexclusive license to McMaster University and to the National Library of Canada to reproduce this material as a part of the thesis. Proper acknowledgement of your copyright of the reprinted material (including the authors, title, date and publisher) will be given in the thesis.

If these arrangements meet with your approval please let me know.
Thank you very much.

Travis Crawford

Ph.D. Candidate
Department of Engineering Physics
McMaster University
1280 Main Street West
Hamilton, Ontario, Canada
L8S 4L7

Phone: 905-525-9140 ext. 24859
Fax: 905-527-8409

Bibliography

[1] D. Bäuerle: *Laser Processing and Chemistry, Third Edition* (Springer-Verlag, Berlin, 2000)

[2] B.N. Chichkov, C. Momma, S. Nolte, F. von Alvensleben, A. Tünnermann: Appl. Phys. A **63**, 109 (1996)

[3] S.-S. Wellershoff, J. Hohlfeld, J. Güdde, E. Matthias: Appl. Phys. A **69 [Suppl.]**, S99 (1999)

[4] B.H. Christensen, K. Vestentoft, P. Balling: Appl. Surf. Sci. **253**, 6347 (2007)

[5] D. von der Linde, K. Sokolowski-Tinten: Appl. Surf. Sci. **154-155**, 1 (2000)

[6] B. Rethfeld, K. Sokolowski-Tinten, D. von der Linde, S.I. Anisimov: Appl. Phys. A **79**, 767 (2004)

[7] K. Sokolowski-Tinten, J. Bialkowski, A. Cavalleri, D. von der Linde, A. Oparin, J. Meyer-ter-Vehn, S.I. Anisimov: Phys. Rev. Lett. **81**, 224 (1998)

[8] P.R. Herman, A. Oettl, K.P. Chen, R.S. Marjoribanks: Proc. SPIE **3616**, 148 (1999)

[9] M.D. Perry, B.C. Stuart, P.S. Banks, M.D. Feit, V. Yanovsky, A.M. Rubenchik: J. Appl. Phys. **85**, 6803 (1999)

[10] D. von der Linde, K. Sokolowski-Tinten, J. Bialkowski: Appl. Surf. Sci. **109-110**, 1 (1997)

[11] N. Bärsch, K. Körber, A. Ostendorf, K.H. Tönshoff: Appl. Phys. A **77**, 237 (2003)

[12] G. Mourou: Appl. Phys. B **65**, 205 (1997)

[13] P. Lorazo, L.J. Lewis, M. Meunier: Phys. Rev. B **73**, 134108 (2006)

[14] J. Bonse, G. Bachelier, J. Siegel, J. Solis: Phys. Rev. B **74**, 134106 (2006)

[15] J. Bonse, S.M. Wiggins, J. Solis: Appl. Surf. Sci. **248**, 151 (2005)

[16] W.G. Roeterdink, L.B.F. Juurlink, O.P.H. Vaughan, J. Dura Diez, M. Bonn, A.W. Kleyn: Appl. Phys. Lett. **82**, 4190 (2003); See also Appl. Phys. Lett. **85**, 694 (2004) and Appl. Phys. Lett. **85**, 696 (2004) for comment and response

[17] D. Perez, L.J. Lewis: Phys. Rev. Lett. **89**, 255504 (2002)

[18] H. Dachraoui, W. Husinsky, G. Betz: Appl. Phys. A **83**, 333 (2006)

[19] D. Perez, L.J. Lewis: Phys. Rev. B **67**, 184102 (2003)

[20] P. Lorazo, L.J. Lewis, M. Meunier: Phys. Rev. Lett. **91**, 225502 (2003)

[21] T.E. Itina, F. Vidal, Ph. Delaporte, M. Sentis: Appl. Phys. A **79**, 1089 (2004)

[22] D.S. Ivanov, L.V. Zhigilei: Phys. Rev. Lett. **91**, 105701 (2003)

[23] E. Leveugle, D.S. Ivanov, L.V. Zhigilei: Appl. Phys. A **79**, 1643 (2004)

[24] D.C. Emmony, R.P. Howson, L.J. Willis: Appl. Phys. Lett. **23**, 598 (1973)

[25] N.R. Isenor: Appl. Phys. Lett. **31**, 148 (1977)

[26] A. Penzkofer, D. von der Linde, A. Laubereau, W. Kaiser: Appl. Phys. Lett. **20**, 351 (1972)

[27] D. Strickland, G. Mourou: Opt. Comm. **56**, 219 (1985)

[28] H.J. Leamy, G.A. Rozgonyi, T.T. Sheng, G.K. Celler: Appl. Phys. Lett. **32**, 535 (1978)

[29] P.L. Liu, R. Yen, N. Bloembergen, R.T. Hodgson: Appl. Phys. Lett. **34**, 864 (1979)

[30] A.G. Cullis, N.G. Chew, H.C. Webber, D.J. Smith: J. Crystal Growth **68**, 624 (1984)

[31] P.M. Fauchet, A.E. Siegman: Appl. Phys. Lett. **40**, 824 (1982)

[32] A.G. Cullis, H.C. Webber, N.G. Chew, J.M. Poate, P. Baeri: Phys. Rev. Lett. **49**, 219 (1982)

[33] J. Bonse, K.-W. Brzezinka, A.J. Meixner: Appl. Surf. Sci. **221**, 215 (2004)

[34] J. Bonse: Appl. Phys. A **84**, 63 (2006)

[35] J. Bonse, S. Baudach, J. Krüger, W. Kautek, M. Lenzner: Appl. Phys. A **74**, 19 (2002)

[36] R. Tsu, R.T. Hodgson, T.Y. Tan, J.E. Baglin: Phys. Rev. Lett. **42**, 1356 (1979)

[37] A. Borowiec, M. MacKenzie, G.C. Weatherly, H.K. Haugen: Appl. Phys. A **76**, 201 (2003)

[38] A. Borowiec, M. MacKenzie, G.C. Weatherly, H.K. Haugen: Appl. Phys. A **77**, 411 (2003)

[39] J. Bonse, J.M. Wrobel, J. Krüger, W. Kautek: Appl. Phys. A **72**, 89 (2001)

[40] J. Jia, M. Li, C.V. Thompson, Appl. Phys. Lett. **84**, 3205 (2004)

[41] Y. Izawa, Y. Izawa, Y. Setsuhara, M. Hashida, M. Fujita, R. Sasaki, H. Nagai, M. Yoshida: Appl. Phys. Lett. **90**, 044107 (2007)

[42] E. Coyne, J.P. Magee, P. Mannion, G.M. O'Connor, T.J. Glynn: Appl. Phys. A **81**, 371 (2005)

[43] M. Couillard, A. Borowiec, H.K. Haugen, J.S. Preston, E.M. Griswold, G.A. Botton: J. Appl. Phys. **101**, 033519 (2007)

[44] A. Borowiec, M. Couillard, G.A. Botton, H.K. Haugen: Appl. Phys. A **79**, 1887 (2004)

[45] T.H.R. Crawford, J. Yamanaka, G.A. Botton, H.K. Haugen: J. Appl. Phys. **103**, 053104 (2008)

[46] E.M. Hsu, T.H.R. Crawford, C. Maunders, G.A. Botton, H.K. Haugen: Appl. Phys. Lett. **92**, 221112 (2008)

[47] T.H.R. Crawford, J. Yamanaka, E.M. Hsu, G.A. Botton, H.K. Haugen: Appl. Phys. A **91**, 473 (2008)

[48] A. Borowiec, D.M. Bruce, D.T. Cassidy, H.K. Haugen: Appl. Phys. Lett. **83**, 225 (2003)

[49] M. Birnbaum: J. Appl. Phys. **36**, 3688 (1965)

[50] M. Oron, G. Sørensen: Appl. Phys. Lett. **35**, 782 (1979)

[51] A.K. Jain, V.N. Kulkarni, D.K. Sood, J.S. Uppal: J. Appl. Phys. **52**, 4882 (1981)

[52] H.M. van Driel, J.E. Sipe, J.F. Young: Phys. Rev. Lett. **49**, 1955 (1982)

[53] Z. Guosheng, P.M. Fauchet, A.E. Siegman: Phys. Rev. B **26**, 5366 (1982)

[54] J.E. Sipe, J.F. Young, J.S. Preston, H.M. van Driel: Phys. Rev. B **27**, 1141 (1983)

[55] J.F. Young, J.E. Sipe, J.S. Preston, H.M. van Driel: Appl. Phys. Lett. **41**, 261 (1982)

[56] J.F. Young, J.S. Preston, H.M. van Driel, J.E. Sipe: Phys. Rev. B **27**, 1155 (1983)

[57] J.F. Young, J.E. Sipe, H.M. van Driel: Phys. Rev. B **30**, 2001 (1984)

[58] T.H.R. Crawford, H.K. Haugen: Appl. Surf. Sci. **253**, 4970 (2007)

[59] A. Borowiec, H.K. Haugen: Appl. Phys. Lett. **82**, 4462 (2003)

[60] E.M. Hsu, T.H.R. Crawford, H.F. Tiedje, H.K. Haugen: Appl. Phys. Lett. **91**, 111102 (2007)

[61] T.Q. Jia, H.X. Chen, M. Huang, F.L. Zhao, J.R. Qiu, R.X. Li, Z.Z. Xu, X.K. He, J. Zhang, H. Kuroda: Phys. Rev. B **72**, 125429 (2005)

[62] V.R. Bhardwaj, E. Simova, P.P. Rajeev, C. Hnatovsky, R.S. Taylor, D.M. Rayner, P.B. Corkum: Phys. Rev. Lett. **96**, 057404 (2006)

[63] G. Dumitru, V. Romano, H.P. Weber, M. Sentis, W. Marine: Appl. Phys. A **74**, 729 (2002)

[64] A. Borowiec, H.K. Haugen: Appl. Phys. A **79**, 521 (2004)

[65] T.H.R. Crawford, A. Borowiec, H.K. Haugen: Appl. Phys. A **80**, 1717 (2005)

[66] S. Ameer-Beg, W. Perrie, S. Rathbone, J. Wright, W. Weaver, H. Champoux: Appl. Surf. Sci. **127-129**, 875 (1998)

[67] T.-H. Her, R.J. Finlay, C. Wu, S. Deliwala, E. Mazur: Appl. Phys. Lett. **73**, 1673 (1998)

[68] S.I. Dolgaev, S.V. Lavrishev, A.A. Lyalin, A.V. Simakin, V.V. Voronov, G.A. Shafeev: Appl. Phys. A **73**, 177 (2001)

[69] M. Groenendijk, J. Meijer: *Microstructuring using femtosecond pulsed laser ablation*, Proceedings of ICALEO 2005, Paper M408 (2005)

[70] A.E. Wynne, B.C. Stuart: Appl. Phys. A **76**, 373 (2003)

[71] S. Juodkazis, H. Okuno, N. Kujime, S. Matsuo, H. Misawa: Appl. Phys. A **79**, 1555 (2004)

[72] A. Luft, U. Franz, A. Emsermann, J. Kaspar: Appl. Phys. A **63**, 93 (1996)

[73] S. Bruneau, J. Hermann, G. Dumitru, M. Sentis, E. Axente: Appl. Surf. Sci. **248**, 299 (2005)

[74] A. Weck, T.H.R. Crawford, A. Borowiec, D.S. Wilkinson, J.S. Preston: Appl. Phys. A **86**, 55 (2007)

[75] A. Weck, T.H.R. Crawford, D.S. Wilkinson, H.K. Haugen, J.S. Preston: Appl. Phys. A **89**, 1001 (2007)

[76] A. Weck, T.H.R. Crawford, D.S. Wilkinson, H.K. Haugen, J.S. Preston: Appl. Phys. A **90**, 537 (2008)

[77] D. Day, M. Gu: Opt. Exp. **14**, 10753 (2006)

[78] E. Dupont, X. Zhu, S. Chiu, S. Moisa, M. Buchanan, M. Gao, H.C. Liu, P.B. Corkum: Semicond. Sci. Technol. **15**, L15 (2000)

[79] S.E. Kirkwood, A.C. van Popta, Y.Y. Tsui, R. Fedosejevs: Appl. Phys. A **81**, 729 (2005)

[80] M. Li, K. Mori, M. Ishizuka, X. Liu, Y. Sugimoto, N. Ikeda, K. Asakawa: Appl. Phys. Lett. **83**, 216 (2003)

[81] A.H. Nejadmalayeri, P.R. Herman, J. Burghoff, M. Will, S. Nolte, A. Tünnermann: Opt. Lett. **30**, 964 (2005)

[82] Spectra-Physics Lasers, Inc., *User's Manual: Millennia V - Diode-pumped, cw Visible Laser*, Part number 0000-245A, Rev. B, November 1997.

[83] Spectra-Physics Lasers, Inc., *User's Manual: Tsunami Mode-locked Ti:Sapphire Laser*, Part Number 0000-232A, Rev. B, December 1999.

[84] E.B. Treacy: IEEE. J. Quant. Electron. **5**, 454 (1969)

[85] Spectra-Physics Lasers, Inc., *User's Manual: Spitfire Multikilohertz Pulsed Ti:Sapphire Amplifier with Pulse Stretcher and Compressor* [LCX version]

[86] Spectra-Physics Lasers, Inc., *User's Manual: OPA Ultrafast kHz Optical Parametric Amplifier*, Part number 0000-249A, Rev. 2, June 1997.

[87] J. Thøgersen, A. Borowiec, H.K. Haugen, F.E. McNeill, I.M. Stronach: Appl. Phys. A **73**, 361 (2001)

[88] C.G. Serbanescu, J.A. Chakera, R. Fedosejevs: Rev. Sci. Instrum. **78**, 103502 (2007)

[89] P. O'Shea, M. Kimmel, X. Gu, R. Trebino: Opt. Lett. **26**, 932 (2001)

[90] Z. Sacks, G. Mourou, R. Danielius: Opt. Lett. **26**, 462 (2001)

[91] G. Pretzler, A. Kasper, K.J. Witte: Appl. Phys. B **70**, 1 (2000)

[92] M. Pluta: Proc. SPIE **1846**, 10 (1994)

[93] J.M. Liu: Opt. Lett. **7**, 196 (1982)

[94] A. Borowiec, H.F. Tiedje, H.K. Haugen: Appl. Surf. Sci. **243**, 129 (2005)

[95] T.H.R. Crawford, A. Borowiec, H.K. Haugen: *Femtosecond Laser Micromachined Grooves Cut in Silicon with 400 nm and 800 nm Pulses*, CLEO/QELS 2003 Technical Digest on CD-ROM (The Optical Society of America, Washington, DC, 2003), Oral presentation CFF6

[96] A. Borowiec, Ph.D Thesis (Department of Engineering Physics, McMaster University, 2004, supervisor H.K. Haugen)

[97] W. Kautek, J. Krüger: Mater. Sci. Forum **173-174**, 17 (1995)

[98] S. Singh, M. Argument, Y.Y. Tsui, R. Fedosejevs: J. Appl. Phys. **98**, 113520 (2005)

[99] E.D. Palik (Ed.): *Handbook of Optical Constants of Solids* (Academic Press, Inc., Boston, 1985)

[100] J. Yamanaka, *Report of TEM work during the 2003 Summer*, December 2003 (Internal report)

[101] M.J.H. Luttikhof, T.H.R. Crawford, M. Couillard, J.S. Preston, G.A. Botton, H.K. Haugen, *Transmission electron microscopy (TEM) of laser grooves in silicon*, Poster presentation for the Brockhouse Institute for Materials Research, Summer 2004.

[102] T.H.R. Crawford, A. Borowiec, H.K. Haugen: CLEO/IQEC and PhAST 2004 Technical Digest on CD-ROM (The Optical Society of America, Washington, DC, 2004), Poster presentation CTuP40

[103] J. Bonse, M. Munz, H. Sturm: J. Appl. Phys. **97**, 013538 (2005)

[104] M.S. Trtica, B.M. Gaković: Appl. Surf. Sci. **205**, 336 (2003)

[105] P.T. Mannion, J. Magee, E. Coyne, G.M. O'Connor, T.J. Glynn: Appl. Surf. Sci. **233**, 275 (2004)

[106] E.M. Hsu, M.A.Sc. Thesis (Department of Engineering Physics, McMaster University, 2007)

[107] A.-C. Tien, S. Backus, H. Kapteyn, M. Murnane, G. Mourou: Phys. Rev. Lett. **82**, 3883 (1999)

[108] M. Lenzner, J. Krüger, W. Kautek, F. Krausz: Appl. Phys. A **68**, 369 (1999)

[109] X. Liu, D. Du, G. Mourou: J. Quant. Electron. **33**, 1706 (1997)

[110] J. Reif, F. Costache, M. Henyk, S.V. Pandelov: Appl. Surf. Sci. **197-198**, 891 (2002)

[111] J. Oh, J.C. Campbell: J. Elec. Mater. **33**, 364 (2004)

[112] T.-H. Her, R.J. Finlay, C. Wu, E. Mazur: Appl. Phys. A **70**, 383 (2000)

[113] Q. Wu, Y. Ma, R. Fang, Y. Liao, Q. Yu, X. Chen, K. Wang: Appl. Phys. Lett. **82**, 1703 (2003)

[114] A.M. Ozkan, A.P. Malshe, T.A. Railkar, W.D. Brown, M.D. Shirk, P.A. Molian: Appl. Phys. Lett. **75**, 3716 (1999)

[115] O. Powell, H.B. Harrison: J. Micromech. Microeng. **11**, 217 (2001)

[116] J. Wang, C. Guo: Appl. Phys. Lett. **87**, 251914 (2005)

[117] S. Adachi: *Optical Constants of Crystalline and Amorphous Semiconductors - Numerical Data and Graphical Information* (Kluwer Academic Publishers, Norwell, MA, 1999)

[118] A.J. Pedraza, J.D. Fowlkes, D.H. Lowndes: Appl. Phys. Lett. **74**, 2322 (1999)

[119] D.H. Lowndes, J.D. Fowlkes, A.J. Pedraza: Appl. Surf. Sci. **154-155**, 647 (2000)

[120] M.D. Betterton: Phys. Rev. E **63**, 056129 (2001)

[121] E. van de Riet, C.J.C.M. Nillesen, J. Dieleman: J. Appl. Phys. **74**, 2008 (1993)

[122] C.H. Crouch, J.E. Carey, J.M. Warrender, M.J. Aziz, E. Mazur, F.Y. Génin: Appl. Phys. Lett. **84**, 1850 (2004)

[123] J.A. Yater, M.O. Thompson: Phys. Rev. Lett. **63**, 2088 (1989)

[124] A.G. Cullis, H.C. Webber, N.G. Chew: Appl. Phys. Lett. **42**, 875 (1983)

[125] R. Evans, A.D. Badger, F. Falliès, M. Mahdieh, T.A. Hall, P. Audebert, J.-P. Geindre, J.-C. Gauthier, A. Mysyrowicz, G. Grillon, A. Antonetti: Phys. Rev. Lett. **77**, 3359 (1996)

[126] K. Sokolowski-Tinten, C. Blome, C. Dietrich, A. Tarasevitch, M. Horn von Hoegen, D. von der Linde, A. Cavalleri, J. Squier, M. Kammler: Phys. Rev. Lett. **87**, 225701 (2001)

[127] C. Cheng, X. Xu: Appl. Phys. A **79**, 761 (2004)

[128] C. Schäfer, H.M. Urbassek, L.V. Zhigilei: Phys. Rev. B **66**, 115404 (2002)

[129] T.E. Itina, J. Hermann, Ph. Delaporte, M. Sentis: Thin Solid Films **453-454**, 513 (2004)

[130] Y. Jee, M.F. Becker, R.M. Walser: J. Opt. Soc. Am. B **5**, 648 (1988)

[131] J.P. McDonald, V.R. Mistry, K.E. Ray, S.M. Yalisove, J.A. Nees, N.R. Moody: Appl. Phys. Lett. **88**, 153121 (2006)

[132] T.Q. Jia, Z.Z. Xu, X.X. Li, R.X. Li, B. Shuai, F.L. Zhao: Appl. Phys. Lett. **82**, 4382 (2003)

[133] G.K. Giust, T.W. Sigmon: Appl. Phys. Lett. **70**, 3552 (1997)

[134] J. Koch, F. Korte, T. Bauer, C. Fallnich, A. Ostendorf, B.N. Chichkov: Appl. Phys. A **81**, 325 (2005)

[135] J. Güdde, J. Hohlfeld, J.G. Müller, E. Matthias: Appl. Surf. Sci. **127-129**, 40 (1998)

[136] F. Korte, J. Koch, B.N. Chichkov: Appl. Phys. A **79**, 879 (2004)

[137] N. Tsukada, S. Sugata, Y. Mita: Appl. Phys. Lett. **42**, 424 (1983)

[138] P. Rudolph, W. Kautek: Thin Solid Films **453-454**, 537 (2004)

[139] N. Yasumaru, K. Miyazaki, J. Kiuchi: Appl. Phys. A **81**, 933 (2005)

[140] H.E. Elsayed-Ali, T.B. Norris, M.A. Pessot, G.A. Mourou: Phys. Rev. Lett. **58**, 1212 (1987)

[141] S. Nolte, C. Momma, H. Jacobs, A. Tünnermann, B.N. Chichkov, B. Wellegehausen, H. Welling: J. Opt. Soc. Am. B **14**, 2716 (1997)

[142] K. Furusawa, K. Takahashi, H. Kumagai, K. Midorikawa, M. Obara: Appl. Phys. A **69 [Suppl.]**, S359 (1999)

[143] S.S. Mao, X.L. Mao, R. Greif, R.E. Russo: Appl. Phys. Lett. **76**, 31 (2000)

[144] S.S. Mao, X.L. Mao, R. Greif, R.E. Russo: Appl. Phys. Lett. **77**, 2464 (2000)

[145] J. Kleinbauer, R. Knappe, R. Wallenstein: Appl. Phys. B **80**, 315 (2005)

[146] A. Fürbach, X. Peng, L. Turi, F. Krausz: Appl. Phys. B **78**, 261 (2004)

[147] M.J. Brennan, A.J. Budz, B.J. Robinson, P. Mascher, H.K. Haugen: IEEE Phot. Tech. Lett. **16**, 1798 (2004)

[148] W. Kautek, P. Rudolph, G. Daminelli, J. Krüger: Appl. Phys. A **81**, 65 (2005)

[149] J. Bonse, Private communication

[150] A. Marcinkevičius, S. Juodkazis, S. Matsuo, V. Mizeikis, H. Misawa: Jpn. J. Appl. Phys. **40**, L1197 (2001)

[151] G. Seifert, M. Kaempfe, F. Syrowatka, C. Harnagea, D. Hesse, H. Graener: Appl. Phys. A **81**, 799 (2005)

[152] C.B. Schaffer, J.F. García, E. Mazur: Appl. Phys. A **76**, 351 (2003)

[153] H.S. Carslaw, J.C. Jaeger: *Conduction of Heat in Solids, Second Edition*, (Clarendon Press, Oxford, 1959)

[154] F. Yoshino, J. Bovatsek, A. Arai, Y. Uehara, Z. Liu, G. Cho: J. Laser Micro/Nanoeng. **1**, 258 (2006)

[155] S.E. Clark, D.C. Emmony: Phys. Rev. B **40**, 2031 (1989)